Stony Brook University

A study of Vector Boson Scattering process in the semi-leptonic final state and limits on anomalous quartic gauge coupling

A Dissertation presented

by

Aungshuman Zaman

to

The Graduate School

in Partial Fulfillment of the

Requirements

for the Degree of

Doctor of Philosophy

in

Physics

Stony Brook University

August 2016

Stony Brook University

The Graduate School

Aungshuman Zaman

We, the dissertation committe for the above candidate for the

Doctor of Philosophy degree, hereby recommend

acceptance of this dissertation

Dmitri Tsybychev
Professor, Dept. of Physics

Patrick Meade
Professor, Dept. of Physics

Michael Rijssenbeek
Professor, Dept. of Physics

Marc-Andre Pleier
Physicist, Brookhaven National Lab

This dissertation is accepted by the Graduate School

Nancy Goroff
Interim Dean of the Graduate School

Abstract of the Dissertation

by

Aungshuman Zaman

Doctor of Philosophy

in

Physics

Stony Brook University

2016

In this dissertation we look into the vector boson scattering process in the semi-leptonic channel using 20.2 fb^{-1} of 2012 proton-proton collision data at $\sqrt{s} = 8$ TeV coming from the Large Hadron Collider. The final state considered is WVjj (V=W,Z) where the W decays into a charged lepton (electron or muon) and a neutrino and the other vector boson decays hadronically. The analysis requires one charged lepton, missing transverse energy and four jets, two of which are forward jets with a large invariant mass. Expected limits on the anomalous quartic gauge coupling (aQGC) parameters were estimated using Whizard+Pythia8 Monte Carlo samples for signal. The observed limits on the aQGC coefficients α_4 and α_5 are $[-0.030, 0.034]$ and $[-0.033, 0.038]$ respectively at 95% confidence level.

To my parents.

List of Figures

List of Tables

Contents

Acknowledgements

I would like to express my sincerest gratitude to my advisor and mentor Professor Dmitri Tsybychev. He has been a tremendous support both at and outside work. Research at doctoral level is not easy emotionally and intellectually. He has been a source of encouragement and inspiration, patiently nudging my research in the right direction. I would also like to thank Brian Lindquist who has been my go-to man all these years and without whose help I may not have come this far.

I would like to acknowledge my dissertation committee members; Professors Michael Rijssenbeek, Patrick Meade and Marc-Andre Pleier who provided useful comments and suggestions to guide my research. I would like to thank Professors John Hobbs under who I started research during my first summer, and Dean Scamberger who has been a constant presence, rescuing me numerous times from a multitude of technical problems.

This acknowledgement will not be complete without mentioning my fellow graduate students, especially David and Karen who had been good friends. I would also like to thank all my other friends in Stony Brook. All those soccer outings, hiking trips and board game nights kept me sane and happy.

Finally, I need to thank my parents for their love and care over the years. They have been the biggest support system in my life and I can never thank them enough.

1 Introduction

The field of particle physics has developed in the last hundred or so years. It is interesting to note that at the onset of the twentieth century the atomic nature of matter was not known. J.C. Maxwell had discovered the classical field theory of electromagnetism, and classical Newtonian mechanics described motion of macroscopic bodies. The experimental observation of the nucleus of an atom came in early twentieth century with the work of E. Rutherford (Rutherford Model of atom, 1911). This marked the beginning of our exploration into the sub-atomic world. With contributions from theory stalwarts Bohr, Heisenberg, Schrodinger, Dirac and many others, the understanding of this world steadily grew. In the 1960s the first quark models were proposed by Gell-Mann and Zweig which postulated that protons, neutrons and other mesons were not fundamental particles, but were composed of quarks. As scientists probed deeper and deeper into the atom, they had to build bigger and bigger experimental machines. With the discovery of a fundamental scalar at the Large Hadron Collider (LHC) in 2012, the last piece of the puzzle called the Standard Model, the most successful theory in High Energy Physics, has apparently been found [1] [2].

This thesis describes the study of vector boson scattering process, a purely electroweak (explained shortly) process which is an important probe of the validity of the Standard Model, in the semi-leptonic final state using data collected by the ATLAS detector in 2012. The introductory chapter presents an overview of the Standard Model of particle physics and then proceeds to describe the motivation and direction of the particular search we have pursued.

1.1 Introduction to the Standard Model

The Standard Model (SM) of particle physics is a quantum field theory. It describes three of the four fundamental forces of nature, electromagnetic, weak nuclear and strong nuclear force, in terms of spin-1 force mediating particles [1]. It also contains three generations of leptons and quarks (both fermions, spin-$\frac{1}{2}$ particles). The quarks interact via all three forces in SM, whereas the leptons only participate in the electromagnetic and weak interactions. The force mediators, vector bosons (spin 1 particles), are $W^{\pm}$

[1] Standard Model leaves out gravity, the fourth fundamental force. A quantum field theory of gravity is still elusive as of the time of this document

	Leptons				Quarks			
	Particle		mass [MeV]	Q	Particle		mass [MeV]	Q
I	electron	e^-	$0.51 \pm 0.11 \times 10^{-7}$	-1	up	u	$2.3^{0.7}_{0.5}$	$+\frac{2}{3}$
	electron neutrino	ν_e	$< 2 \times 10^{-6}$	0	down	d	$4.8^{0.7}_{0.3}$	$-\frac{1}{3}$
II	muon	μ^-	$105.66 \pm 35 \times 10^{-7}$	-1	charm	c	$(1.275 \pm 0.025) \times 10^3$	$+\frac{2}{3}$
	muon neutrino	ν_μ	$< 0.19 \times 10^{-6}$	0	strange	s	95 ± 5	$-\frac{1}{3}$
III	tau	τ^-	1776.82 ± 0.16	-1	top	t	$(173.21 \pm 0.51 \pm 0.71) \times 10^3$	$+\frac{2}{3}$
	tau neutrino	ν_τ	$< 18.2 \times 10^{-6}$	0	bottom	b	$(4.18 \pm 0.03) \times 10^3$	$-\frac{1}{3}$

Table 1: Standard Model fermions.

Particle		Q	mass [GeV]
photon	γ	0	0
W boson	$W^\pm$	± 1	80.385 ± 0.015
Z boson	Z	0	91.188 ± 0.002
gluon	g	0	0
Higgs	H	0	125.7 ± 0.4

Table 2: Standard Model bosons.

and Z bosons (weak force), the gluon (strong force), and the photon (electromagnetic force). Finally, there is the Higgs boson, a fundamental scalar (spin zero) particle. It gives mass to the fundamental particles through the Brout-Englert-Higgs (BEH) mechanism. Tables 1 and 2 list the fundamental particles of SM and some of their properties. The numbers have been taken from Ref. [3].

SM has been hugely successful in explaining a vast range of particle phenomena, although it is not yet a complete theory. In the following sections the theoretical foundation of Standard Model will be described in more detail.

1.2 Electroweak Force and spontaneous symmetry breaking

In the 1960s S. Glashow, A. Salam and S. Weinberg [4, 5] developed the Electroweak theory of particle physics which unified the two fundamental forces - electromagnetism, already described very successfully by Quantum Electrodynamics (QED), and weak nuclear force. Two examples of electroweak

interaction is shown in Fig 1. The first diagram shows electron-photon vertex, the fundamental vertex of QED, and the second one shows an analogous diagram involving quark-W^+ vertex.

Here for simplicity just the first generation of quarks and leptons will be considered. In the Electroweak Lagrangian the left-handed fermions ψ_L appear as doublets

$$q_L = \begin{pmatrix} u \\ d \end{pmatrix}_L , \qquad l_L = \begin{pmatrix} \nu_e \\ e^- \end{pmatrix}_L , \tag{1}$$

and right-handed fermions ψ_R appear as singlets

$$u_R, \qquad d_R, \qquad \nu_R^e, \qquad e_R^- \qquad .$$

Only left-handed fermions participate in weak interaction. Requiring the Lagrangian to be invariant under $SU(2)_L \times U(1)_Y$ gauge transformation, the free fermion Lagrangian can be written as

$$\mathcal{L}_0 = i\bar{\psi}_L(x)\gamma^\mu D_\mu \psi_L(x) + i\bar{\psi}_R(x)\gamma^\mu D_\mu \psi_R(x) \tag{2}$$

where D_μ is the covariant derivative ,

$$D_\mu = \partial_\mu - \frac{ig'Y_R}{2}B_\mu \qquad \text{(right-handed)}, \tag{3}$$

$$D_\mu = \partial_\mu - \frac{ig'Y_L}{2}B_\mu - \frac{ig\tau_i W_\mu^i}{2} \qquad \text{(left-handed)} \tag{4}$$

where g, g' are the coupling constants and B_μ,W_μ^is are vector gauge fields, and τ_i are Pauli matrices for SU(2). The gauge-invariant kinetic terms for the gauge fields are given by

$$\mathcal{L}_{kin} = -\frac{1}{4}B_{\mu\nu}B_{\mu\nu} - \frac{1}{4}W_{\mu\nu}^i W_i^{\mu\nu}. \tag{5}$$

Gauge invariance gives rise to four spin-1 particles, W_μ^1, W_μ^2, W_μ^3 and B_μ^1. These vector bosons are, however, massless as mass terms for these boson fields do not respect gauge symmetry. Therefore, the unbroken $SU(2)_L \times U(1)_Y$ gauge theory fails to generate the particles observed in nature.

In 1960s Englert, Brout, Higgs, Guralnik, Hagen and Kibble devised a mechanism [7] [8] [9] that spontaneously breaks the Electroweak symmetry

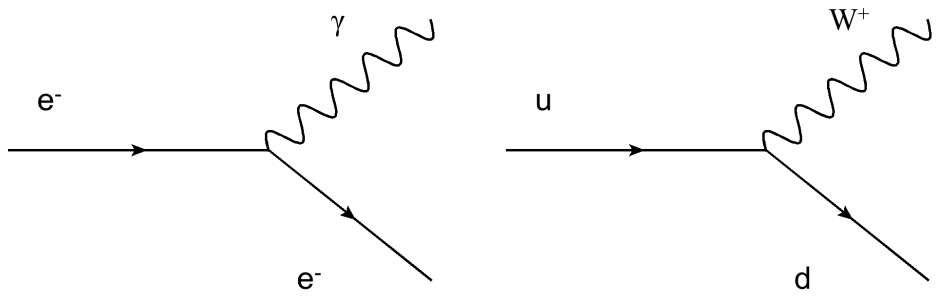

(a) (b)

Figure 1: Example of fundamental Electroweak interactions. (a) electron-photon vertex, (b) quark-boson interaction vertex. These and other Feynman diagrams in this document are made using the JaxoDraw [6] program.

and generates mass for the boson fields. The phenomenon is known as Electroweak Symmetry Breaking (EWSB) and the mechanism came to be known as the Brout-Englert-Higgs (BEH) mechanism, or more popularly the Higgs mechanism. A scalar field doublet was introduced to the Lagrangian

$$\phi(x) \equiv \begin{pmatrix} \phi^{(+)}(x) \\ \phi^{(0)}(x) \end{pmatrix} \qquad . \tag{6}$$

The ϕ field has four degrees of freedom. The Lagrangian for the scalar field ϕ is given by,

$$\begin{aligned} \mathcal{L}_\phi &= D_\mu \phi^\dagger D_\mu \phi - V(\phi) \\ &= D_\mu \phi^\dagger D_\mu \phi - \mu^2 \phi^\dagger \phi - \lambda(\phi^\dagger \phi)^2 \qquad . \end{aligned} \tag{7}$$

If μ^2 is negative and λ is positive, it leads to a degenerate vacuum, the vacuum expectation value being,

$$\langle 0|\phi^{(0)}|0\rangle = \sqrt{\frac{-\mu^2}{2\lambda}} \qquad . \tag{8}$$

The scalar field can be parametrized in terms of polar variables,

$$\phi = e^{\frac{-i\zeta_i(x)\tau^i}{v}} \begin{pmatrix} 0 \\ \frac{v+h(x)}{\sqrt{2}} \end{pmatrix}, \qquad v = \sqrt{\frac{-\mu^2}{\lambda}} \qquad . \tag{9}$$

In this notation the original two complex fields $\phi^+(x)$ and $\phi^0(x)$ have been re-written in terms of four real fields ζ_is (i=1,2,3) and h (Goldstone and Higgs bosons). In the unitary gauge (ζ_i =0) the potential term in scalar field becomes,

$$V(\phi) = -\mu^2 h^2 + \lambda v h^3 + \frac{\lambda}{4} h^4 \qquad . \tag{10}$$

Note, as μ^2 <0, the mass is real now. This equation gives the mass of the physical scalar particle (the Higgs boson), and the triple and quartic scalar vertices. The other three degrees of freedom of the complex scalar doublet gives mass to three of the vector bosons. The mass eigenstates of vector bosons can be written in terms of $W_\mu^{1,2}$ and B_μ in the following way,

$$W_\mu^\pm = \frac{1}{\sqrt{2}}(W_\mu^1 \mp W_\mu^2) \tag{11}$$

$$Z_\mu = \frac{g W_\mu^3 - g' B_\mu}{\sqrt{g^2 + g'^2}} \tag{12}$$

$$A_\mu = \frac{g' W_\mu^3 + g B_\mu}{\sqrt{g^2 + g'^2}}. \tag{13}$$

The mass of the vector bosons can be read off from the Lagrangian.

$$M_W^2 = g^2 v^2/4 \tag{14}$$

$$M_Z^2 = (g^2 + g'^2) v^2/4 \tag{15}$$

$$M_A^2 = 0. \tag{16}$$

The Higgs boson also gives mass to the fermions through Yukawa coupling. Considering the first generation leptons and quarks the Yukawa Lagrangian is,

$$\mathcal{L}_{Yuk} = f_e \bar{l}_L \phi e_R + f_u \bar{q}_L \tilde{\phi} u_R + f_d \bar{l}_L \phi d_R + h.c. \qquad , \tag{17}$$

where

$$\tilde{\phi} = i\tau_2 \phi^* \tag{18}$$

and f_f are $\phi f \bar{f}$ coupling strengths. In the unitary gauge, $\phi = \frac{1}{\sqrt{2}} \begin{pmatrix} 0 \\ v \end{pmatrix}$ the Lagrangian becomes,

$$\mathcal{L}_{Yuk} = \frac{f_e v}{\sqrt{2}}(\bar{e}_L e_R + \bar{e}_R e_L) + \frac{f_u v}{\sqrt{2}}(\bar{u}_L u_R + \bar{u}_R u_L) + \frac{f_d v}{\sqrt{2}}(\bar{d}_L d_R + \bar{d}_R d_L) \quad . \tag{19}$$

From this equation the masses of the fermions are read off as,

$$m_f = \frac{-f_i v}{\sqrt{2}}, \qquad f = e, u, d \qquad . \tag{20}$$

1.3 Strong force: Quantum Chromodynamics

Quantum Chromodynamics (QCD) is the quantum field theory of strong force. The matter content in this theory is spin $\frac{1}{2}$ quarks. Like the electroweak theory, QCD is also a gauge theory. The Lagrangian is invariant under an SU(3) gauge transformation. The SU(3) symmetry leads to eight gauge fields of strong force, called gluons. Both quarks and gluons have a new quantum number called color. Quarks (anti-quarks) come in three colors (anti-colors) conventionally called R, G, B ($\bar{R}$, $\bar{G}$,$\bar{B}$). There are six flavors of quarks (and anti-quarks) (see Table 1). Gluons carry color charge between quarks and each gluon carries one color and one anti-color. Gluons take part in self-interaction. Fig. 2 shows the fundamental QCD vertices.

The free Lagrangian for the quark color fields is given by the Dirac equation, where j = 1, 2, 3 denotes the three color fields.

$$\mathcal{L}_0 = \bar{q}_j(i\gamma^\mu \partial_\mu - m)q_j \tag{21}$$

To impose the SU(3) local gauge invariance, ∂_μ needs to be replaced with the covariant derivative,

$$D_\mu = \partial_\mu + igT_a G^a_\mu \tag{22}$$

where g is the coupling strength, T_a are the SU(3) generators and G^a_μ are gluon fields.

The gauge invariant QCD Lagrangian is given by (ignoring color indices for brevity),

$$\mathcal{L}_{QCD} = \bar{q}(i\gamma^\mu \partial_\mu - m)q - g(\bar{q}\gamma^\mu T_a q)G^a_\mu - \frac{1}{4}G^a_{\mu\nu}G^{\mu\nu}_a \tag{23}$$

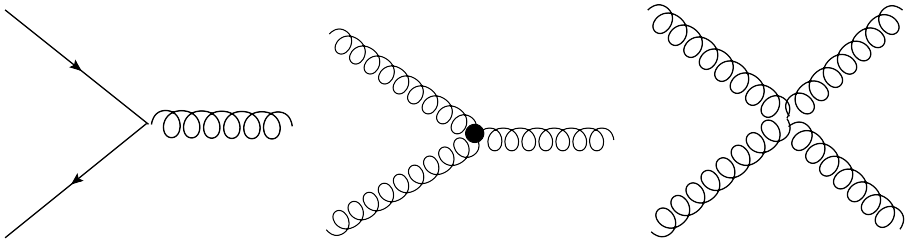

Figure 2: Quantum Chromodynamics interactions. (a) Quark-gluon vertex, (b) triple Gluon self-interaction vertex and (c) quartic Gluon self-interaction vertex.

where $G^a_{\mu\nu}$ are the gluon field strength tensors given by the equation,

$$G^a_{\mu\nu} = \partial_\mu G^a_\nu - \partial_\nu G^a_\mu - g f_{a,b,c} G^b_\mu G^c_\nu \tag{24}$$

where $f_{a,b,c}$ are structure constants. Expanding these two equations we get free propagation of quarks (terms involving $q\bar{q}$), of gluons (terms involving G^2), quark-gluon interaction ($q\bar{q}G$) and three and four gluon vertices (terms with cubic and quartic powers of G).

Quantum Chromodynamics has two features that distinguishes it from Quantum Electrodynamics (QED), namely asymptotic freedom and color confinement. The strong force is vanishingly small at small distance (high energy) but its strength increases with increasing distance between the interacting particles. This is in contrast to the case of electrodynamics where the strength of the force falls off as inverse square of the distance. As a result inside the nucleus the quarks are asymptotically free i.e. the coupling strength of strong force is weak and perturbative calculation is possible. On the other hand, because the force increases without bound as the separation increases, it is energetically impossible to free up a quark from the nucleus, so they are always found in colorless bound states. This phenomenon is called color confinement. Three quarks constitute a barion and a quark-antiquark pair makes up a meson. In baryons all three quarks will have different color, R,G and B so that the bound state itself is colorless (in analogy with three primary colors red, green and blue making up white light). For mesons the color and anti-color of quark-antiquark pair will cancel each other.

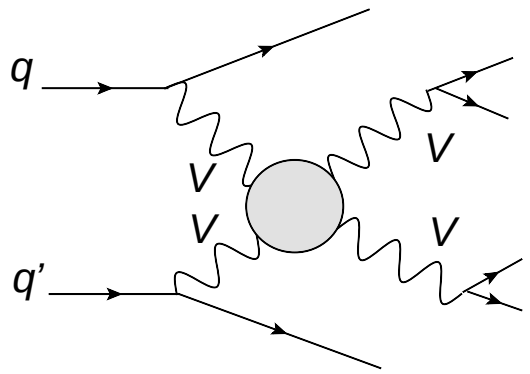

(a)

Figure 3: Vector boson scattering Feynman diagrams.

1.4 VBS process

The vector boson scattering diagram is shown in Fig. 3 with a blob that may contain Feynman diagrams presented in Fig. 4. Massless gauge boson fields have only two degrees of freedom which are expressed as plane waves with two constant polarizations. These are the transverse polarizations $\boldsymbol{\epsilon}$ which is defined by the equation $\mathbf{k}.\ \boldsymbol{\epsilon} = 0$ where $\mathbf{k}$ is the wave propagation vector. There is no distinction between the two transverse polarizations. For massive gauge boson, however, there are three degrees of freedom and the third degree, called the longitudinal polarization, dominates over the transverse modes at E $\gg$ m limit.

The scattering amplitude of longitudinal vector boson $W_L^+W_L^-$ can be approximated as

$$\mathcal{M}_{Gauge}(W_L^+W_L^- \to W_L^+W_L^-) = -\frac{g^2 u}{4m^2} + \mathcal{O}(s^0) \tag{25}$$

where s,u are the Mandelstam variables. This amplitude increases without bound with energy. To restore unitarity we need to have a careful cancellation of this energy-dependent term. As the mass of the heavy vector bosons arises due to the Higgs mechanism, the same mechanism should also regulate the longitudinal cross-section to restore unitarity. Vector boson scattering is thus an important probe of EWSB.

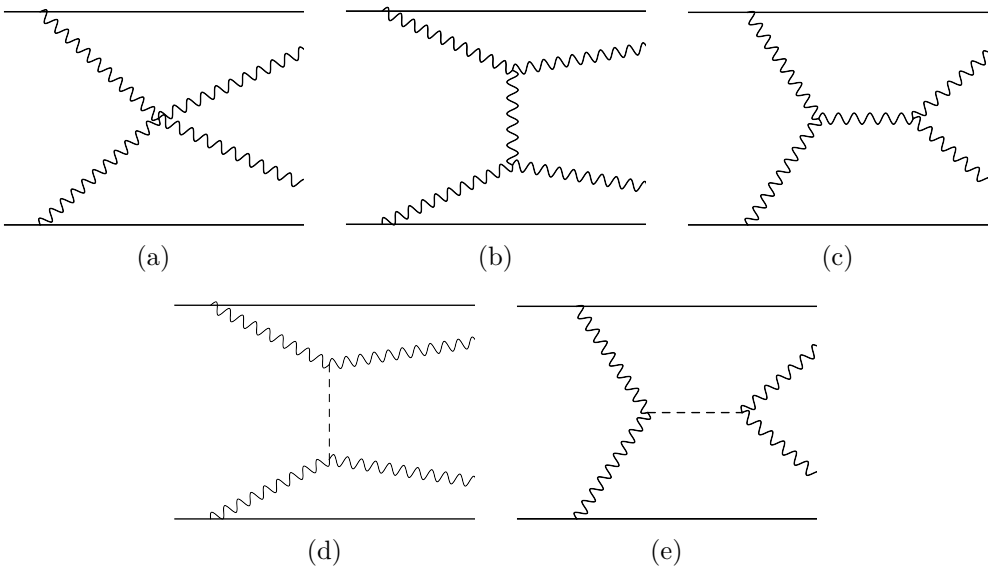

Figure 4: Examples of VBS diagrams. These diagrams are part of EWK production of WV, V=W,Z. The dashed line represents the Higgs boson. The decays of the bosons are not shown.

Adding a Higgs particle in the theory introduces diagrams involving it. The amplitude for those diagrams are

$$\mathcal{M}_{Higgs}(W_L^+W_L^- \to W_L^+W_L^-) = g_{HWW}^2 \frac{u}{m^4} + \mathcal{O}(s^0) \tag{26}$$

With the correct choice of coupling strength this term cancels the energy dependent term in $\mathcal{M}_{Gauge}$ and achieves our goal of restoring unitarity. Similar treatment applies for scattering of all combinations of longitudinal vector bosons.

1.5 Anomalous quartic gauge coupling

Until now we have considered Standard Model processes only. In order to model possible deviations from the SM, we may adopt an effective field theory (EFT) approach. In this approach, it is assumed that there is new physics at some higher energy scale Λ, but that the scale Λ is sufficiently large so that we do not probe it directly (e.g. our energies are too low to directly produce new high-mass resonances). In this case, physics can be described by an EFT, where the SM Lagrangian is supplemented by higher-order suppressed terms:

$$\mathcal{L} = \mathcal{L}_{\text{SM}} + \sum_{k=1} \frac{1}{\Lambda^k} \mathcal{L}_k \,. \tag{27}$$

There are two main approaches that have been adopted to treat VBS in an EFT approach, a linear representation and non-linear representation.

The linear representation uses the SM Higgs picture of EWSB as the starting point, and then adds in higher-order correction terms [10]. In this approach, aQGCs can be produced by both dimension-6 and dimension-8 (non-renormalizable) operators. However, the dimension-6 operators also affect anomalous Triple Gauge Couplings (aTGCs), and are well constrained by aTGC limits. The lowest-dimension operators that are not already highly constrained are dimension-8. Two of these dimension-8 operators are:

$$O_{S,0} = [(D_\mu \Phi)^\dagger D_\nu \Phi] \times [(D^\mu \Phi)^\dagger D^\nu \Phi] \,, \tag{28}$$

$$O_{S,1} = [(D_\mu \Phi)^\dagger D^\mu \Phi] \times [(D_\nu \Phi)^\dagger D^\nu \Phi] \,, \tag{29}$$

and the coefficients of these operators are designated f_{S0}/Λ^4 and f_{S1}/Λ^4, respectively.

The non-linear representation [11] is originally inspired by a strongly-interacting or non-Higgs scenario, where EWSB has a different origin than the SM Higgs. In this case, one imagines an EFT valid up to $4\pi v$ ($v = 246$ GeV), where new physics has to enter in order to solve EWSB. In this case, it is convenient to adopt a chiral Lagrangian written in a non-linear representation, using the matrix $\Sigma = exp[\frac{-i}{v} w^a \tau^a]$ which represents the longitudinal degrees of freedom of the gauge bosons. Although this model doesn't require a SM Higgs boson, it is easy to incorporate a SM Higgs boson into it [12]. In this case, the full Lagrangian of the EFT has the form:

$$\mathcal{L} = \mathcal{L}_{\mathrm{SM}} + \sum_{i=1} \alpha_i \mathcal{L}_i + \frac{1}{\Lambda} \sum_{i=1} \alpha_i^{(5)} \mathcal{L}_i^{(5)} + ... \tag{30}$$

The lowest-order terms which contribute to quartic gauge couplings and which respect custodial SU(2) symmetry and are not already constrained by other measurements (e.g. diboson production) are:

$$\alpha_4 \mathcal{L}_4 = \alpha_4 \, tr[\mathbf{V}_\mu \mathbf{V}_\nu] \, tr[\mathbf{V}^\mu \mathbf{V}^\nu] \,, \tag{31}$$

$$\alpha_5 \mathcal{L}_5 = \alpha_5 \, tr[\mathbf{V}_\mu \mathbf{V}^\mu] \, tr[\mathbf{V}_\nu \mathbf{V}^\nu] \,, \tag{32}$$

where $V_\mu = \Sigma (D_\mu \Sigma)^\dagger$. Thus, there are only two independent parameters, α_4 and α_5, describing anomalous quartic gauge couplings.

Although the formalisms look fairly different between the linear and non-linear approaches, and the operators are not the same in the two approaches, it is nevertheless possible to make a direct relation between the α_4 and α_5 and f_{S0}/f_{S1} parameters [10], although the relation can only be done on a vertex-by-vertex basis (i.e. it differs for the WWWW and WWZZ vertices).

In our analysis, we adopted the non-linear realization, since this was also used by the $W^\pm W^\pm jj$ analysis previously done in ATLAS.

It is well-known that the aQGCs severely violate unitarity at LHC energies, and thus it is crucial to specify a unitarization scheme. In the presence of aQGCs, VBS cross-sections and kinematics are greatly affected by unitarization, so the particular unitarization scheme used makes a large difference. Essentially, the choice of unitarization scheme becomes part of the model. Various schemes have been proposed for unitarizing VBS, including form-factors and sharp cut-offs above a certain energy. In this analysis, we choose the K-matrix unitarization method [11] which has been implemented in the Whizard event generator [13, 14]. In this method, the scattering amplitude

is projected onto the Argand circle, forcing unitarity. This method gives the maximum amplitude possible while still preserving unitarity.

The K-matrix method has been adopted by ATLAS in the $W^{\pm}W^{\pm}jj$ [15] and WZ [16] 8 TeV analyses, and so the aQGC limits obtained in this analysis can be directly compared with those two analyses.

1.6 Cross-section dependence on aQGCs

As mentioned in Sec. 3, the signal samples (with aQGCs) are modeled with Whizard+Pythia8. The Whizard generator supports the aQGC parameters α_4 and α_5 with K-matrix unitarization. In order to model the dependence of the signal on the aQGCs, signal samples were generated at 45 different points in (α_4, α_5) space. The generated samples are summarized in Appendix A, in Tables 33-34.

In Fig. 5, we plot the signal cross-section as a function of (α_4, α_5). The cross-section is calculated for each of the aQGC points for which samples exist, and then interpolated between these aQGC points using a bi-linear interpolation.

1.7 Previous measurements

Electroweak production of WW/WZ processes have been investigated in some previous analyses in both ATLAS and CMS. Because of the small cross-section, it has only recently been feasible to directly investigate these processes.

1.7.1 ATLAS $W^{\pm}W^{\pm}jj$ electroweak production

Using 2012 data ($\sqrt{s} = 8$ TeV), this analysis measured fiducial cross-sections for two phase space regions [15]. The inclusive region where a combined strong and electroweak production of $W^{\pm}W^{\pm}jj$ is measured, the fiducial cross section was found to be $\sigma_{fid} = 2.1 \pm 0.5$ (stat) $\pm$ 0.3 (syst) fb. The measured fiducial cross section for VBS region, where electroweak $W^{\pm}W^{\pm}jj$ production is enhanced, is $\sigma_{fid} = 1.3 \pm 0.4$ (stat) $\pm$ 0.2 (syst) fb. The measured cross sections are in agreement with the respective SM expectations of 1.52 ± 0.11 fb and 0.95 ± 0.06 fb. First evidence for $W^{\pm}W^{\pm}jj$ production and electroweak-only $W^{\pm}W^{\pm}jj$ production is observed with a significance of

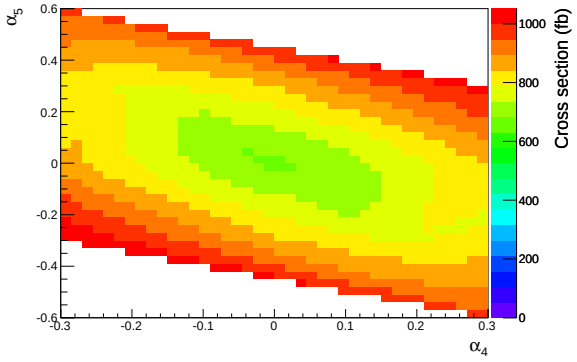

(a)

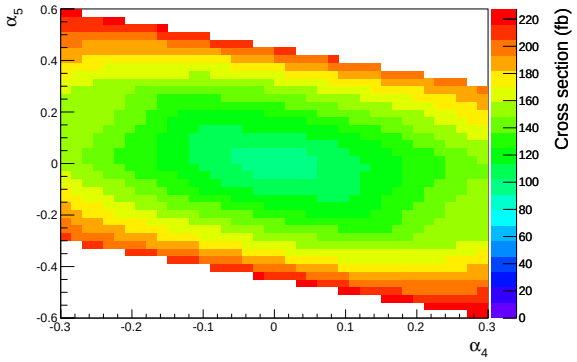

(b)

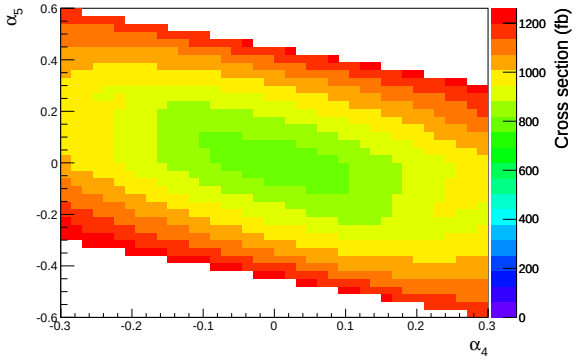

(c)

Figure 5: The cross-section for the WV and ZV processes, as a function of α_4 and α_5. Bi-linear interpolation is done between the aQGC points for which MC samples were generated. The plots show (a) the WV cross-section, (b) the ZV cross-section, and (c) the total WV+ZV cross-section.

4.5σ and 3.6σ respectively. Expected significance is 3.4σ in the inclusive region and 2.8σ in the VBS region.

The analysis also set limits on the aQGC parameters α_4 and α_5. The expected and observed one-dimensional limit at 95% confidence intervals derived are -0.14 $< \alpha_4 <$ 0.16 and -0.23 $< \alpha_5 <$ 0.24. Expected limits were -0.10 $< \alpha_4 <$ 0.12 and -0.18 $< \alpha_5 <$ 0.20.

1.7.2 ATLAS WZ electroweak production

The observed cross section for WZjj Electroweak production was found to be $0.29^{+0.14}_{-0.12}(stat.)^{+0.09}_{-0.1}(syst)$ fb, consistent with the SM expectation of 0.13 $\pm$ 0.01 fb from VBFNLO generator [17].

1.7.3 CMS $W^{\pm}W^{\pm}jj$ electroweak production

The inclusive QCD+EW $W^{\pm}W^{\pm}jj$ fiducial cross section was found to be $\sigma_{fid}(W^{\pm}W^{\pm}jj) = 4.0^{+2.4}_{-2.0}(stat)^{+1.1}_{-1.0}(syst)$ fb with an expectation of 5.8 $\pm$ 1.2 fb. Fiducial cross section of the WZjj process is $\sigma_{fid}(WZjj) = 10.8$ $\pm$ 4.0(stat) $\pm$ 1.3(syst) fb with an expectation of 14.4 $\pm$ 4.0 fb [18]. The observed (expected) significance for the $W^{\pm}W^{\pm}jj$ process is 2.0σ (3.1σ). Considering the QCD component of the $W^{\pm}W^{\pm}jj$ events as background and the EW component together with the EW-QCD interference as signal, the observed (expected) signal significance reduces to 1.9σ (2.9σ).

1.8 Analysis overview

The goal of our analysis was to study vector boson scattering, and by extension the electroweak symmetry breaking mechanism, in the semi-leptonic final state. We endeavored to answer question like whether the electroweak production of WW/WZ in association with the forward jets is consistent with Standard Model prediction. All previous measurements of vector boson scattering focused on the full-leptonic channel where both vector bosons decayed into leptons; W into an electron or a muon and a neutrino and Z into two electrons or two muons. The semi-leptonic channel benefits from a larger cross-section compared to the fully leptonic channel. The big disadvantage, however, is that the final state involves four jets which means there are large backgrounds like W+jets and $t\bar{t}$. This fact alone makes a SM measurement impossible with the current data **(see Appendix B)**. However, the limits

on aQGCs are expected to be competitive with the current best limits from the $W^{\pm}W^{\pm}$ di-lepton final state analysis[15]. The aQGCs cause a large enhancement in the signal in regions of phase-space where the W + jets and $t\bar{t}$ backgrounds play much smaller role. The semi-leptonic channel also has better kinematic measurement of di-boson decay products than the same-sign lepton channel because of only one neutrino in the final state. Vector boson scattering topology is, however, not as sensitive to aTGC parameters. A study, described in Appendix C, was done to evaluate aTGC sensitivity for this analysis with some available set of MC samples.

2 Experimental apparatus

Modern high energy experiments are done in accelerator facilities. These facilities are mainly of two types. First, a fixed target setup where a focused beam of high energy particles is impinged on a fixed target, and second, a collider facility where two beams are made to collide each other. The data used in our analysis was collected at the largest collider facility in the world, the Large Hadron Collider (LHC). This section describes the complex experimental apparatus used to obtain our data.

2.1 LHC

The Large Hadron Collider (LHC) is situated near Geneva at the border of France and Switzerland. The facility is run by European Organization for Nuclear Research (originally Conseil Européen pour la Recherche Nucléaire (CERN) in French). LHC accelerates beams of protons in a circular tunnel 26.7 km in circumference located 100 meters underground. CERN accelerator complex consists of a number of smaller accelerator machines that ramp the beam up to successively higher energies before injecting it to the main beam pipe (see Fig. 6). Four large experiments, ATLAS, CMS, LHCb and ALICE, are housed at the LHC complex.

2.1.1 Proton proton collision

CERN uses a Duoplasmatron source to prepare proton beams. These protons are fed into the first stage of accelerators, a Linear Accelerator. The beam is brought to an energy of 50 MeV and passed onto the second stage, Proton Synchrotron Booster (PSB). The booster accelerates the protons to 1.4 GeV. The protons then enter the third stage called Proton synchroton (PS) which boosts the protons to an energy of 26 GeV. These protons are injected into the fourth stage called Super Proton Synchroton (SPS). The SPS beam pipe runs through a 7 kilometer long tunnel and brings the proton energy to 450 GeV. Finally SPS feeds protons in the LHC beam pipe. The 26.7 km long LHC tunnel has two beam pipes with two opposite direction beam circulating through them. Each beam pipe holds 2808 bunches of protons and successive bunches are separated by 25ns. Proton bunches are further accelerated and then made to collide inside the detectors installed at a few locations around the beam pipe. The LHC is designed to reach a peak center-of-mass energy

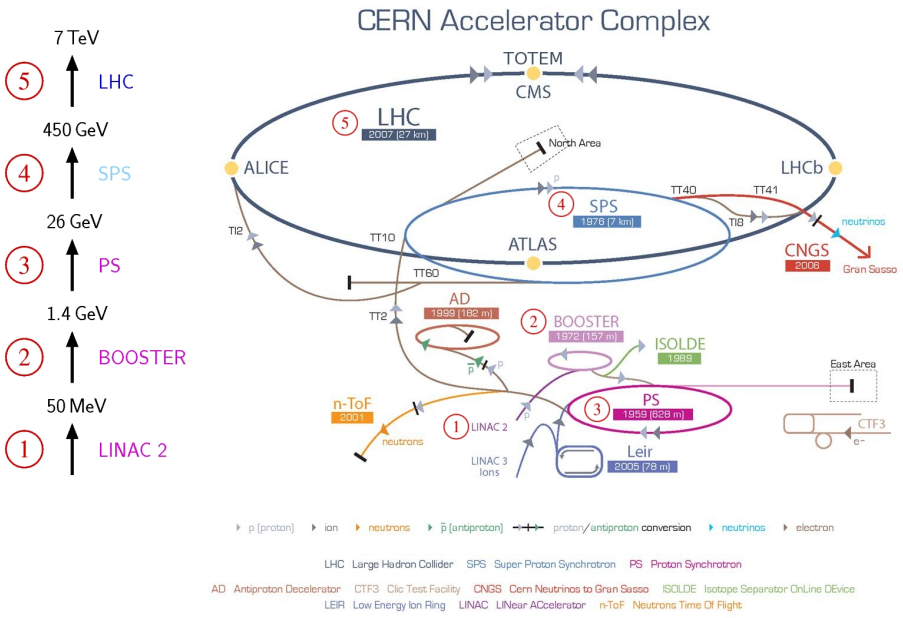

Figure 6: LHC accelerator complex [19]. The proton beam is successively accelerated to an center of mass energy of 7TeV in 2011 (8TeV in 2012).

of 14 TeV and a luminosity of 10^{34} cm^{-2}s^{-1}. The instantaneous luminosity $\mathcal{L}$ of a pp collider is given by [20]

$$\mathcal{L} = \frac{R_{inel}}{\sigma_{inel}} \tag{33}$$

where R_{inel} is the rate of inelastic interaction and σ_{inel} is the cross-section of inelastic interaction. This can also be written as,

$$\mathcal{L} = \frac{\mu_{vis} n_b f_r}{\epsilon \sigma_{inel}} = \frac{\mu_{vis} n_b f_r}{\sigma_{vis}} \tag{34}$$

where f_r is the revolution frequency, n_b is the number of bunch collisions during one revolution and μ_{vis} is the observed number of inelastic interaction per bunch crossing. $\sigma_{vis} = \epsilon \sigma_{inel}$ is the cross-section of the observed inelastic processes which is obtained by multiplying the total cross-section by the efficiency of the detector and algorithm. In terms of accelerator parameters

this can be written as

$$\mathcal{L} = \frac{n_b f_r n_1 n_2}{2\pi \Sigma_x \Sigma_y} \tag{35}$$

where n_1 and n_2 are number of particles in a bunch for beam 1 and beam 2 respectively. Σ_x and Σ_y are the horizontal and vertical convolved beam widths. These parameters are calculated by a van der Meer scan.

2.2 ATLAS

ATLAS is a general purpose particle detector with full 2π coverage in the azimuthal plane [21]. It is a cylindrical detector and employs a right handed coordinate system. A cross-section view of the ATLAS detector and its co-ordinate system is presented in Fig. 7. The x-axis points towards the center of the LHC ring, the y-axis directs upwards, and the z-axis is along the direction of the beam pipe. Location of any point can also be described by the polar co-ordinates (r, θ, ϕ), where r is the radial distance from the interaction point, θ is polar angle measured from the beam-axis (z-axis) and ϕ is the azimuthal angle measured in xy plane. The pseudorapidity angle is often used in physics literature which is defined by

$$\eta = \text{-ln}(\tan(\frac{\theta}{2})) \tag{36}$$

Pseudorapidity is often preferred over θ because for high energy particles it approximates the rapidity angle, which is invariant under boost. Rapidity is defined by

$$y = \frac{1}{2}\ln\frac{E + p_z}{E - p_z} \tag{37}$$

Interaction of particles as the travel through different ATLAS sub-detectors is shown in Fig. 8. Different sub-detectors of ATLAS are described in the following sections.

2.3 Inner detector

Inner detector is the sub-detector closest to the interaction point. It consists of three sub-systems– Pixel detector, the Semiconductor Tracker (SCT) and Transition Radiation Tracker (TRT) arranged radially going out from the interaction point. A cross-section view of the inner detector and its components are shown in Fig. 9.

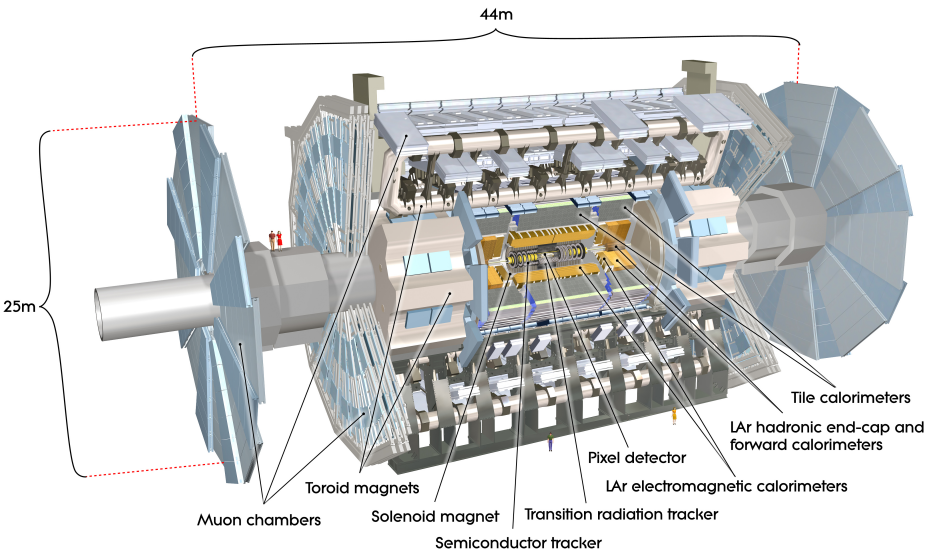

(a)

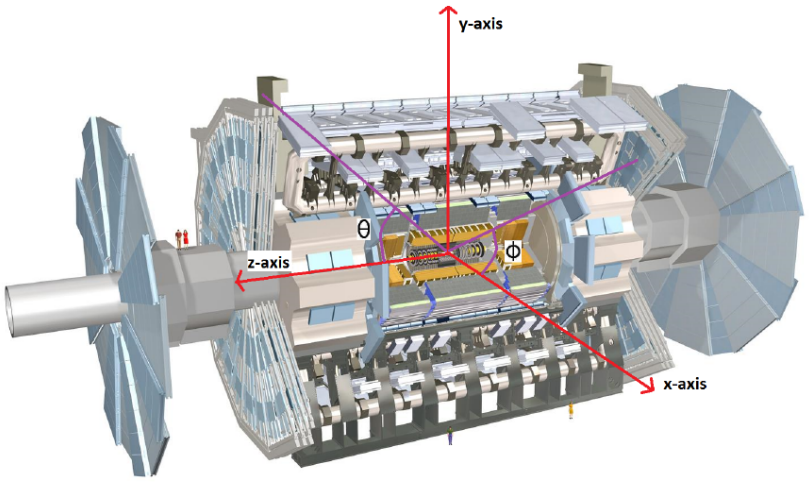

(b)

Figure 7: (a) The whole ATLAS detector [22]. (b) ATLAS detector coordinates. Figure from [23]

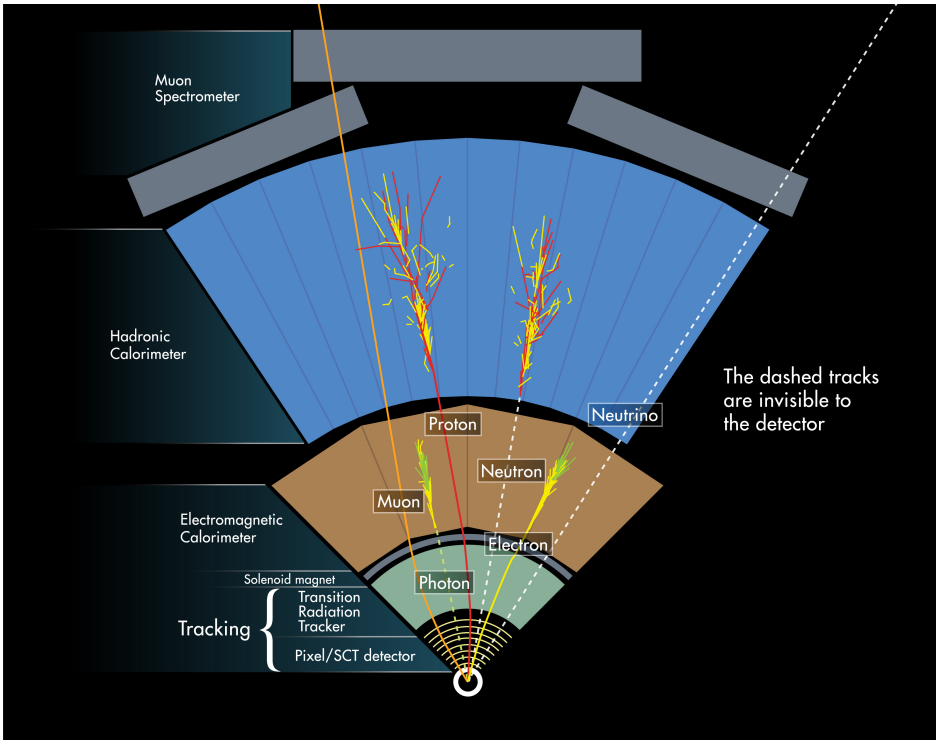

Figure 8: Interaction of particles in the ATLAS detector [24]

2.3.1 Pixel detector

The Pixel Detector is made of very high granularity and radiation hard silicon sensors capable of providing very high resolution reconstruction of interaction vertices [26]. This also plays the vital role in measuring impact parameter of particles from collisions used for distinguishing B-hadrons and τ-leptons. It is cylindrical in shape, 1.4m long and about 0.25m in radius centered on the interaction point (Fig. 10). The original pixel detector consisted of three layers. In 2014 a fourth layer, called the Insertable B-layer (IBL), had been installed closest to the beam pipe at a radius of 31 to 40 mm. It is operational for run 2 data taking. The IBL sensors have 50 $\times$ 250 micron pixels. This layer adds an additional 12 million pixels to the system.

In the original Pixel Detector there are 1744 modules and in total nearly 80 million channels. The barrel part of the pixel detector consists of the 3 cylindrical layers with the radial positions of 50.5 mm, 88.5 mm and 122.5

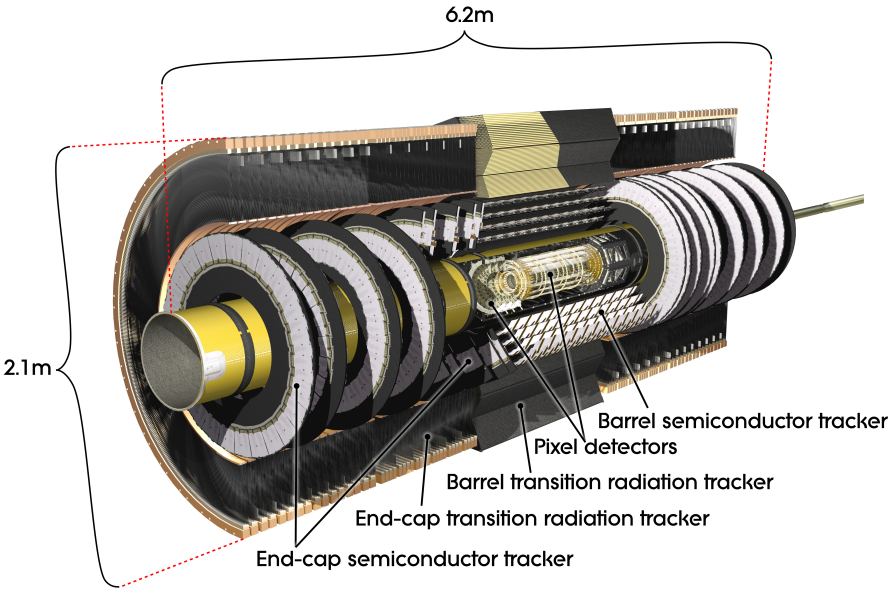

(a)

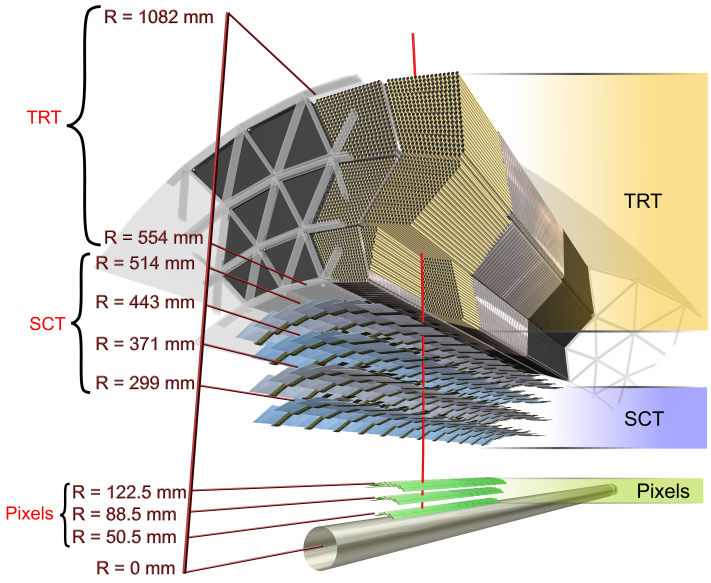

(b)

Figure 9: (a) Inner detector [25], (b) Inner detector, a detailed view showing the sub-detectors [25]

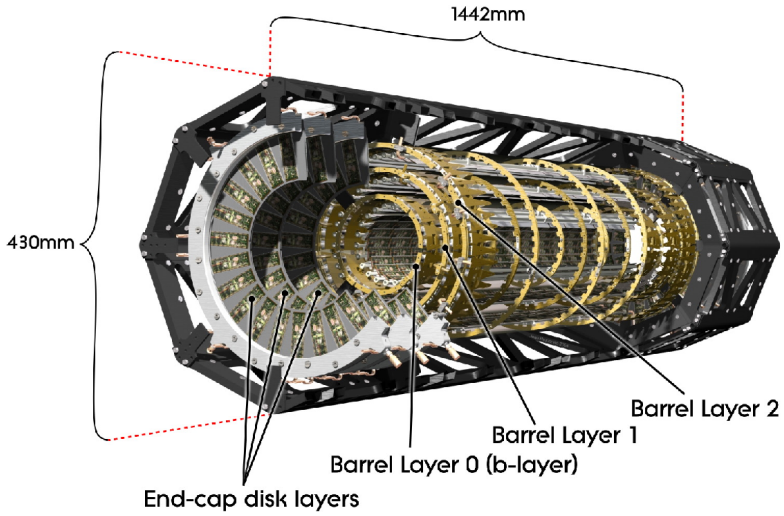

Figure 10: Pixel detector [28]

mm respectively. Barrel layers are made of identical staves inclined with azimuthal angle of 20 degrees. There are 22, 38 and 52 staves in each of these layers respectively. Each stave is composed of 13 pixel modules [27]. There are 16 front-end (FE) chips and one Module Control Chip (MCC) in each module. Apart from the barrel there are three disks on each side to cover the more forward direction. There are 8 sectors in each disk, each sector housing 6 modules. Disk modules are identical to the barrel modules, except for the connecting cables.

A Pixel module consists of 16 front-end chips bump bonded to a sensor substrate. A Pixel sensor is a 16.4 $\times$ 60.8 mm wafer of silicon with 46080 pixels, each pixel measuring around 50 $\times$ 400 microns each. One FE chip contains 160 rows and 18 columns of pixel cells, for a total of 2880 pixels per FE chip. The FE chips are a major heat source (0.8 W/cm^2). It requires integrated cooling channels to dissipate more than 15 kW of heat the Pixel detector generates.

2.3.2 Semiconductor Tracker

The SCT provides high resolution tracking for the measurement of the trajectories of charged particles [29], [30]. It is at a radius of 30 to 52 cm from the interaction point and consists of 4088 silicon modules with 6.2 million readout channels. The SCT has four barrel layers with a total of 2112 modules giving a pseudo-rapidity coverage from $1.1 < |\eta| < 1.4$. There are nine disks on each side, called the end-caps, for forward region coverage ($1.4 < |\eta| < 2.5$). The end-caps contain 1976 modules.

A silicon strip module used in the barrel is built with 2 pairs of identical, single-sided silicon micro-strip sensors each containing 768 AC-coupled, p-strips on n-type silicon, readout strips. The distance between neighboring strips, the pitch, is 80 μm. Each pair of strip sensors is wire bonded together to form 126 mm long sensors and then is glued back to back with another pair at a 40 mrad stereo angle. This geometry allows the sensors to have a position resolution of roughly 580 μm in the z-direction in the barrel , while the resolution in R-ϕ is 16 μm. The modules used in the disk are similar to barrel modules with strip pitches between 57 and 94 μm. For end cap, the pitch increases as we go out radially from the beam axis.

2.3.3 Transition Radiation Tracker

The TRT is a straw (also known as drift tubes) tracker which uses transition radiation to detect charged particle tracks [31]. It provides on average about 35 hits per track in the range $|\eta| <$2.0. TRT has one barrel and two end-cap sections. The barrel has straw tubes arranged parallel to the beamline, while the end-caps have straws arranged radially in layers of constant z. The barrel part provides coverage up to $|\eta| \approx 1.0$, while the end-cap extends the coverage to $|\eta| = 2$.

The straw tubes are made of Kapton (polyimide film), strengthened by thin carbon fibers [32]. The straws are 4 mm in diameter, and 1.44 m (0.37 m) long in the barrel (end-cap). A gold-plated tungsten wire with a diameter of 31 μm runs down the middle of the straw, and acts as the anode. The straws are filled with a gas mixture of 70% Xe, 27% CO_2, and 3% O_2. The straw walls are kept at a potential of -1.5 kV relative to the wire.

There are almost 300,000 straw tubes in the TRT. The barrel part comprises around 53,000 of those. The barrel is split into three concentric layers of 32 trapezoidal modules each. The two end-caps house around 246,000

straws. Each end-cap is composed of stacks of disks called wheels. Each plane has 768 straws, and the planes in all of the wheels are slightly offset from each other in ϕ (with a period of eight planes) to ensure good coverage. TRT is useful for discriminating between electrons and hadrons over a wide energy range (between 0.5 to 100 GeV). In a transition radiation tracker charged particles emits photons as they traverse the detector. In the case of electron, the number of emitted photons is larger than that for a charged hadron at a given fixed momentum. This principle is used for identification of electrons.

2.4 Calorimeter

Calorimeters provide accurate measurements of the energies of electrons, photons, and jets as well as of the missing transverse energy. Calorimetric measurements are also crucial to particle identification, serving to distinguish electrons and photons from jets, and also helping to identify hadronic decays of tau leptons. A cross-section view of the calorimeter system is shown in Fig. 11. The major components are the liquid Argon (LAr) barrel and end-cap electromagnetic (EM) calorimeters [33] covering $|\eta| < 3.2$, the tile scintillator hadronic barrel calorimeter covering $|\eta| < 1.7$, the LAr hadronic end-cap calorimeter covering $1.5 < |\eta| < 3.2$, and the LAr forward calorimeter (FCAL) covering $3.1 < |\eta| < 4.9$.

All these components are sampling calorimeters in nature. They are made of alternating layers of dense absorber and active sensor material. The absorber medium causes the primary particle to shower, producing a number of secondary particles. The secondary particles ionize the active material which is detected as the signal. Signal is proportional to the total charged particle track length in the active medium. In order to accurately measure energy there must be enough layers of absorber and active medium so that the showering of particles is fully contained by the calorimeter. Because energy is being deposited in both the absorber and the active layers but only active layers deposition is measured, a careful calibration is required to infer the total energy deposition from the fraction observed.

Calorimeter systems are different from the tracking detectors in very important ways. The tracking detectors provide little disturbance to the charged particles as they travel through it and cause ionization. Calorimeters, on the other hand, by design absorb and reduce energy of the impinging particle. They are sensitive to both neutral and charged particles.

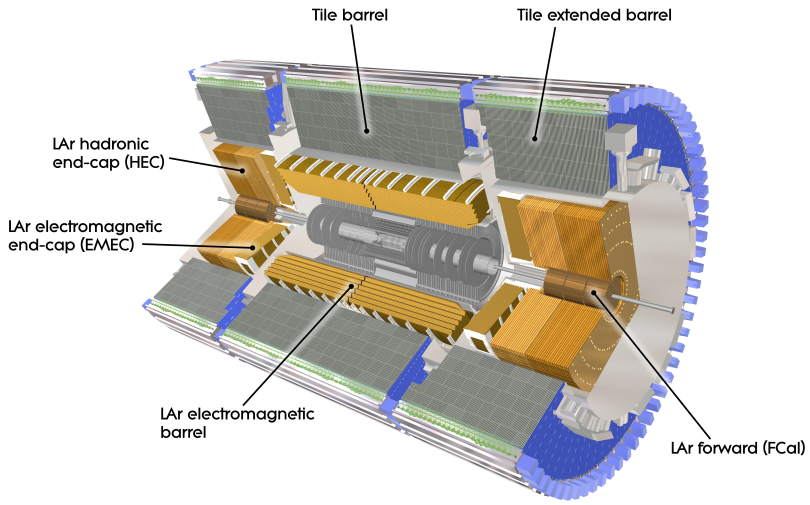

Figure 11: ATLAS calorimeter system [34]

2.4.1 Electromagnetic Calorimeter

The electromagnetic calorimeters use lead absorbers and liquid Argon as the ionization medium, and are contained in three separate cryostats, one for the barrel and two for the end-caps. The calorimeters have an accordion geometry that provides full ϕ symmetry without azimuthal cracks. EM calorimeter has three longitudinal layers in the barrel ($|\eta| < 2.5$) region. Different layers of a barrel module is shown in Fig. 12(a). The first layer is segmented finely with a cell size 0.003$\times$ 0.1 in $\Delta\eta \times \Delta\phi$. The fine granularity helps us to distinguish between π^0 and e/γ. The middle layer contains around 80% of the energy of an electromagnetic shower. The cell size in this layer is 0.025$\times$0.025. The third layer has cell size 0.05$\times$0.025 in $\Delta\eta \times \Delta\phi$. Most EM showers do not extend past the second layer. For $|\eta| > 2.5$, the EM calorimeter is segmented into two longitudinal layers instead of three, with a coarser granularity. This region is intended to help with the reconstruction of jets and $E_T^{missing}$, instead of providing precision measurements for electrons and photons. A presampler (PS) covers the region $|\eta| < 1.8$. Its purpose is to measure energy for particles that start showering before entering the main calorimeter.

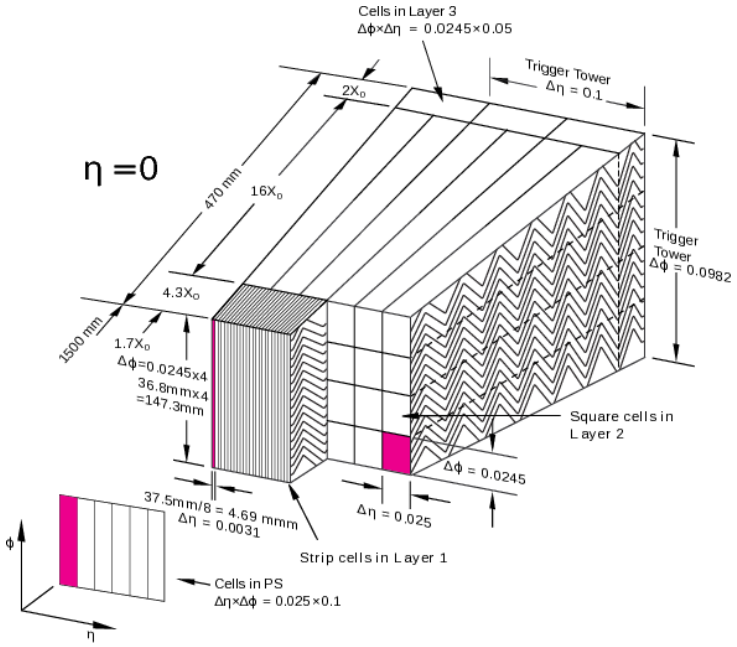

(a)

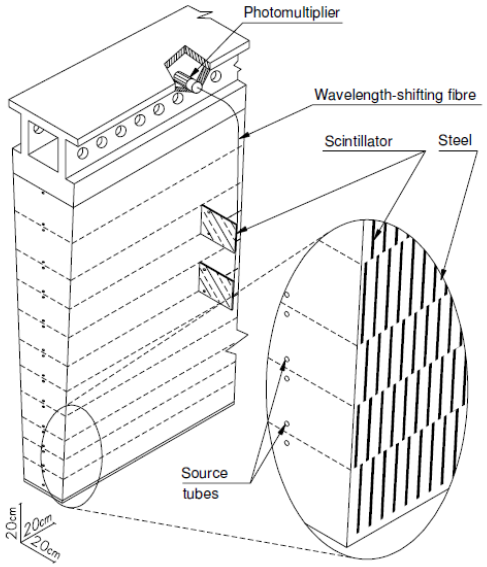

(b)

Figure 12: (a) Sketch of an Barrel module in EM calorimeter where the granularity of the cells in different layers is shown [33], (b) Schematic of the mechanical assembly and the optical readout of the tile calorimeter [21]

2.4.2 Hadronic Calorimeter

The barrel region of hadronic calorimeter uses iron absorbers interleaved with plastic scintillator tiles. It is located behind the EM LAr calorimeter, and is divided into a central barrel and two extended barrels. The central barrel portion covers $|\eta| < 1.0$ while the extended barrels gives coverage in the region $0.8 < |\eta| < 1.7$. The calorimeter is made up of three radial layers. The first two layers have granularity of 0.1×0.1 in $\Delta\eta \times \Delta\phi$, while the third one has twice coarser granularity in η. Fig. 12(b) shows a module in the tile calorimeter. The tiles are coupled with photo-multiplier tubes (PMT), which amplify the photons emitted by the scintillators once a particle passes through it and causes excitation. The end-caps of the hadronic calorimeter use the liquid Argon technology They use copper plates as absorbers. It consists of two wheels which covers the region $1.5 < |\eta| < 3.2$.

2.4.3 Forward Calorimeter

The forward calorimeter (FCAL) covers the forward region, $|\eta| > 3.1$, of the detector. It operates at a very high radiation environment with its front face only 4.7 m away from the interaction point. For that reason it employs very high density material. It consists of three sections as can be seen in Fig. 11. The first section is made of copper and the other two are of tungsten. All three consists of metal matrix with longitudinally oriented rods and tubes (see Fig. 13), with liquid Argon filling the gaps between them. The rods are kept at a positively high voltage relative to the tubes. The liquid Argon filling is the active material in the calorimeter.

2.5 Muon spectrometer

The Muon Spectrometer (MS) is the outermost of the ATLAS sub-detectors. It is designed to detect charged particles in the pseudorapidity region up to $|\eta| = 2.7$, and to provide momentum measurement with a relative resolution better than 3% over a wide p_T range and up to 10% at pT $\approx$ 1 TeV [35]. It is also designed to trigger on muons in the region $|\eta| < 2.4$. Different components of the MS is shown in Fig. 14. The MS consists of one barrel part (for $|\eta| < 1.05$) and two end-cap sections. The chambers in the barrel are arranged in three concentric cylindrical layers around the beam axis at radii of approximately 5 m, 7.5 m, and 10 m. In the end-cap region, chambers

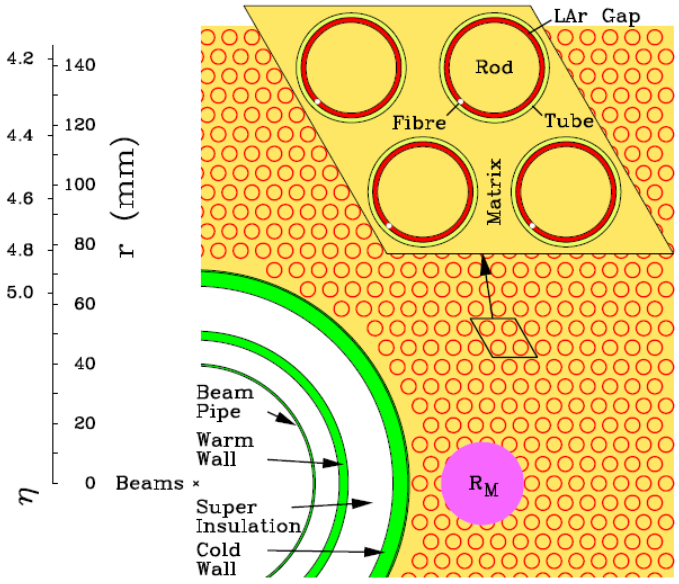

Figure 13: Sketch of Forward calorimeter with matrix and rods [33].

form large wheels, perpendicular to the z-axis. The wheels are located at distances of $|z| \approx 7.4$ m, 10.8 m, 14 m, and 21.5m from the interaction point. A system of three large superconducting air-core toroid magnets, one for barrel and two for end-caps, provides a magnetic field. The MS has four subsystems, namely, Monitored Drift Tube (MDT), Cathode Strip Chambers (CSC), Resistive Plate Chambers (RPC) and Thin Gap Chambers (TGC). The first two are for precision measurements and the other two are for fast (around tens of nanoseconds) trigger decisions on muon tracks.

2.5.1 Monitored Drift Tube (MDT) Chambers

The primary precision measurement is done using MDT chambers. It provides a precise muon momentum measurement up to $|\eta| = 2.7$. It has three layers in the barrel. In the end-cap, there are three layers in the region $|\eta| = 2.0$ and two layers in $2.0 < |\eta| < 2.7$. The drift tubes used in the MDT are made out of 30 mm diameter aluminium tubes with a 400 μm wall thickness and a central Tungsten-Rhenium wire 50 μm in diameter. The tubes are filled with a gas mixture of 93% Argon and 7% CO_2. The chambers consist

of three to eight layers of drift tubes, operated at an absolute pressure of 3 bar. An average resolution of 80 μm per tube, or 35 μm per chamber is achieved in these chambers.

2.5.2 Cathode Strip Chambers (CSC)

In the inner endcap region ($2.0 < |\eta| < 2.7$) counting rate exceeds the safe operating limit of MDT's and they are replaced by the Cathode Strip Chambers for precision measurement. The CSC's are multiwire proportional chambers with the anode wires oriented in the radial direction and cathode plane segmented into strips. The charge induced on segmented cathodes by the avalanche formed on the anode wires provides the measurements. The resolution of a chamber is 40 μm in the bending plane and about 5mm in the transverse plane.

2.5.3 Resistive-Plate Chambers (RPC)

The muon trigger system covering the central region ($|\eta| < 1.05$) consists of RPCs. This is a gaseous parallel plate detector with no wire. Two bakelite plates are kept parallel to each other at a distance of 2mm. The gap is filled by a gas mixture $C_2H_2F_4$, Iso-C_4H_{10} and SF_6 (composition is 94.7,5 and 0.3% respectively). The RPC has a time resolution of 1.5 ns and a spatial resolution of 6 mm. The fine time resolution enables it to easily tag a triggering muon to a particular bunch-crossing.

2.5.4 Thin Gap Chambers (TGC)

In the end-cap region ($1.05 < |\eta| < 2.4$), TGCs provide the trigger. It also provides a second co-ordinate measurement to complement MDT's measurement in the bending plane. TGCs are multi-wire proportional chambers (similar to CSCs). Both trigger chamber types (RPCs and TGCs) deliver signals within 25 ns, thus providing the ability to identify an event with a beam-crossing. The trigger chambers measure both coordinates of the track, one in the bending plane and one in the non-bending plane.

2.6 Trigger system

At the LHC with 25 ns bunch crossing, the bunch collision rate is 40 MHz. It is impractical to read out and store detailed information about all the events

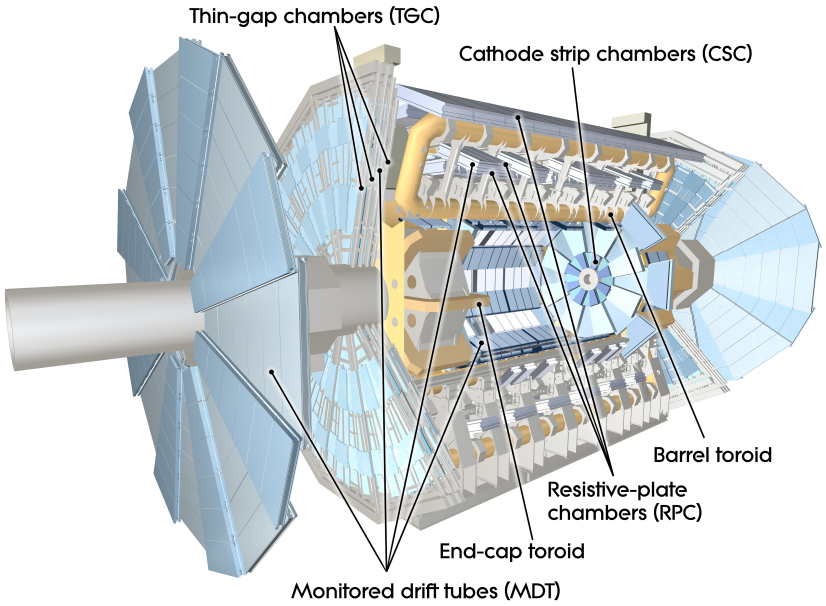

(a)

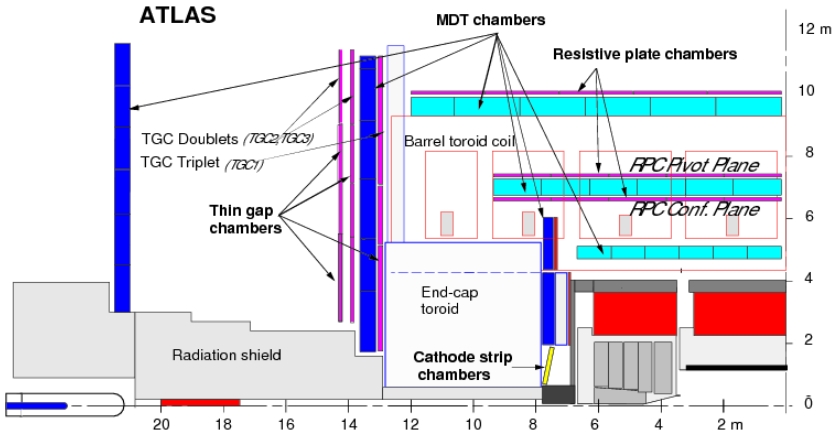

(b)

Figure 14: (a) Muon chambers [36], (b) Cross-section of Muon systems in the x-z plane containing the beam axis [37].

at this rate. Fortunately most of these collisions are uninteresting from a physics perspective. So a trigger system is developed which can filter only interesting events [38].

ATLAS has a three level trigger system. The first level, called L1 is a hardware based trigger. It uses coarse information from calorimeter and muon systems. For muons only RPC and TGC information is considered. For calorimeters, high-p_T objects are searched using a subset of the detectors and using only coarse granularity information. A Central Trigger Processor (CTP) receives information from trigger sub-systems and makes decision on whether to keep the event. When it decides to accept an event the front-end electronic systems are instructed to store detailed information about the event for further investigation. The maximum acceptance rate for L1 is designed to be 75 kHz, hence allowing only one out of every thousand or so events. The second and third tier triggers are collectively called High Level Trigger (HLT) and are software-based. The level-2 trigger, called L2, is seeded by L1 trigger. Although at this stage the trigger considers higher granularity calorimeter objects, it looks at only regions of interest (RoI) identified by L1 instead of the full event. Using a set of offline reconstruction algorithm it is allowed to accept events at the rate of 3.5 kHz with a latency of around 40 ms. The level-3 trigger, called the Event Filter (EF), employ full reconstruction algorithm on events accepted by L2. The final acceptance rate is around 400 Hz and the latency is about 4 seconds. Events passing this level of trigger is written to the mass storage for off-line analysis; at 400Hz acceptance it amounts to about 400 MB/s of stored data.

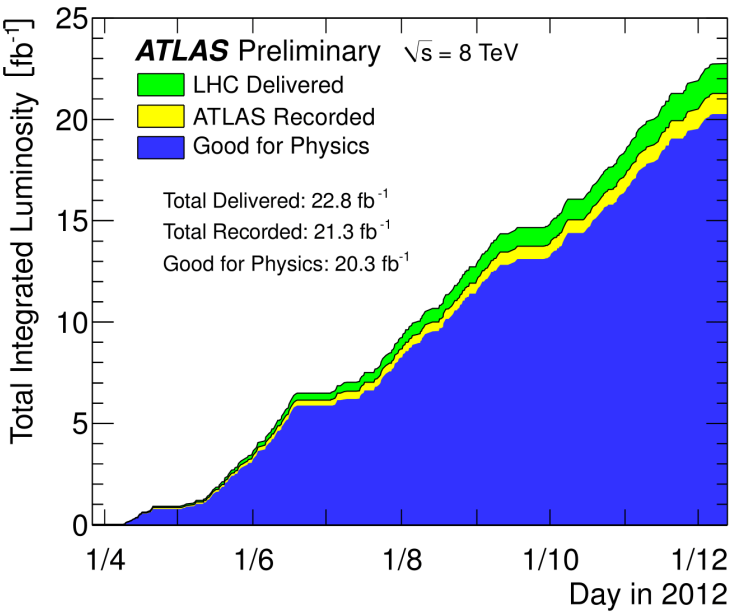

Figure 15: Cumulative luminosity versus time delivered to (green), recorded by ATLAS (yellow), and certified to be good quality data (blue) during stable beams and for pp collisions at 8 TeV centre-of-mass energy in 2012.

3 Collision Data and Simulation

3.1 Data collected in ATLAS detector

The presented analysis is done with the data collected in ATLAS detector with a proton-proton collision energy of 8 TeV in 2012 during Run I of LHC. The integrated luminosity of data is 20.2 ± 0.4 fb^{-1}. To be considered for analysis, data need to pass certain quality requirements, and therefore be part of the Good Runs List (GRL). [2]

3.2 Monte Carlo Simulation

To measure a signal process in the observed data we need good under-

[2]The GRL used for this analysis is *data12_8TeV.periodAllYear_DetStatus-v61-pro14-02_DQDefects-00-01-00_PHYS_StandardGRL_All_Good.xml*.

standing of the composition of the data. Commonly the signal and background contributions are modeled by event generators employing Monte Carlo simulation methods. Simulating high energy particle collisions in a hadron collider like LHC is very challenging. The collision event is factorized into different regimes depending on the momentum transfer involved. At the highest energy level parton interactions are perturbatively computable, but a phenomenological description is necessary for processes involving low energy scale. The simulation of an event goes through several steps before it can be compared to a data event– calculation of the hard (high momentum transfer) sub-processes, showering for the incoming and outgoing partons, hadronization of the partons and eventual decay of the hadrons, and the secondary interactions from beam remnants, known as the underlying event. Fig. 16 shows a typical hadron-hadron collision. These steps are discussed in more detail in the following sections.

3.3 Hard scattering process and Parton Distribution Function

In a proton-proton collider, the hard interaction is dictated by quantum chromodynamics . The first step of simulation involves perturbative quantum chromodynamics (pQCD) and parton distribution functions to model the physics processes.

Although the final state particles observed in the detector are colorless hadrons, the constituents colored quarks and gluons (collectively called partons) are the particles that take part in high momentum transfer or "hard" scale interactions. At hard scale these partons are asymptotically free and the cross-sections of initial partons interacting to give a particular final state can be calculated using pQCD. Because we know about the momenta of initial protons instead of partons, the knowledge of parton distribution function (pdf) i.e., the distribution of momentum fraction x of partons is necessary to calculate the cross-section. The cross-section for the production of N particles in the final state can be written as

$$\sigma_{ab\to N} = \sum_{a,b} \int dx_1 dx_2 f_a(x_1, \mu_F^2) f_b(x_2, \mu_F^2) \hat{\sigma}_{ab\to N} \tag{38}$$

where a, b are partons and f_a and f_b are the corresponding pdfs. μ_F is the factorization scale. The sum is over all the possible parton species that

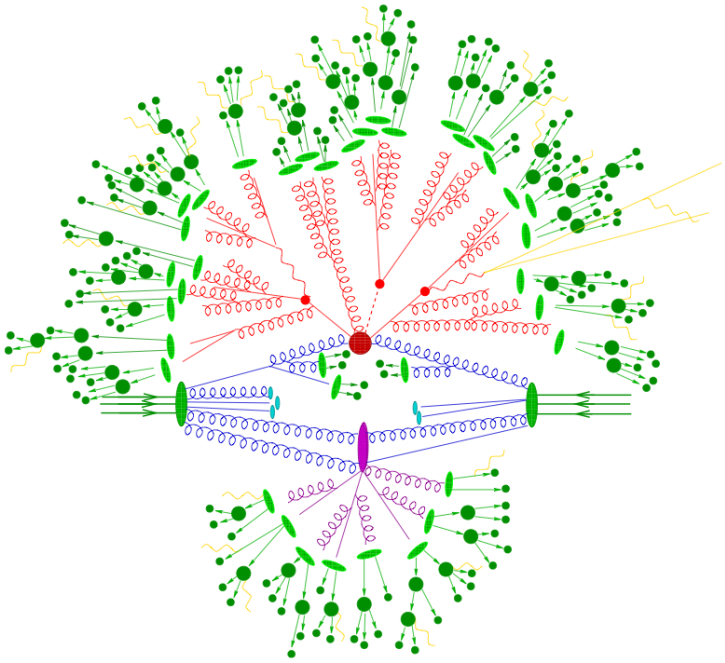

Figure 16: A hadron-hadron collision event: the red blob shows the hard subprocess; the light green blobs represent hadronization and dark green blobs show subsequent decays of the hadrons; underlying event is represented by the purple blob [39].

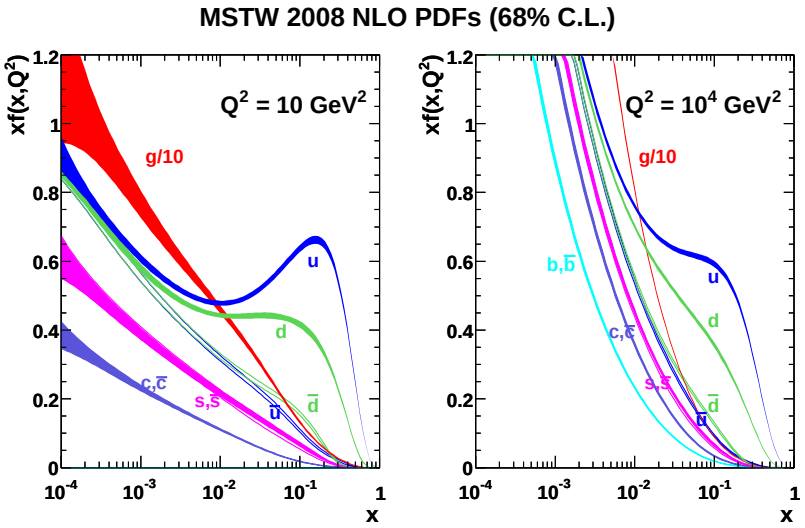

Figure 17: Example parton distribution functions for proton computed to NLO provided by the MSTW group.

can interact to produce the final state. $\hat{\sigma}_{ab\to N}$ is the cross-section of parton a and b interacting to produce N. The parton distribution functions are universal in nature, that is they only depend on the momentum fraction carried by the parton, but not the actual partonic reaction. Pdfs cannot be calculated analytically. They are obtained from global fit to data from various experiments. Three major groups, CTEQ [40] , MSTW [41], and NNPDF [42] are involved with computing and disseminating parton distribution functions.

The partonic cross-section can be written in the following form,

$$\hat{\sigma}_{ab\to N} = \int_{cuts} d\hat{\sigma}_{ab\to N} = \int_{cuts} \left[\prod_{i=1}^{N} \frac{d^3q_i}{(2\pi)^3 2E_i}\right] \delta^4(p_1 + p_2 - \sum_i^N q_i) |\mathcal{M}^{ab}_{p_1p_2\to\{\vec{q}_i\}}|^2 \tag{39}$$

The first part in the square bracket refer to the phase space of final state particles, the Dirac delta function ensures momentum conservation and $\mathcal{M}^{ab}_{p_1p_2\to\{\vec{q}_i\}}$ is the (sum of) probability amplitude of incoming partons with momenta p_1 and p_2 to produce the final state particles. The amplitude is the sum of all possible Feynman diagrams.

The calculation involving QCD Feynaman diagrams are the hardest. They

can be performed perturbatively at hard scale when the strong coupling constant α_s is small. The amplitude can be arranged as a perturbative series in increasing order of α_s. Evaluating the tree-level diagrams produce the leading order calculation which is traditionally been the case for most MC event generators. A next-to-leading order calculation introduces a different kind of difficulty. For one the real emission diagrams in NLO introduces infra-red (IR) divergences which can only be canceled by virtual emission diagrams in all orders. Evaluation of the cross-section to fixed order may lead to remainder terms involving logarithm of ratio of hard scale and hadronization scale. Moreover, the virtual emission diagrams are notoriously difficult to treat and the difficulty increases with additional loops (order). This problem can either be tackled by resumming the large logs (resummation method) or a parton shower method explained later in this section.

The immensely complicated multi-dimensional phase-space integral is evaluated with Monte Carlo methods. The phase-space is sampled with the help of a random number generator and the differential cross-section for a particular point in phase space is calculated using Eq. 39. The events produced in this way are unweighted in an event generator by an acceptance-rejection (also known as Von Neumann) method. The end result of the procedure is a collection of events that will represent the physics process codified in Eq. 39. For a large number of events the numerical integration of this differential cross-section will be approximately equal to the theoretical cross-section.

3.4 Parton shower

The initial partons produced at the hard scale are colored particles which will hadronize into colorless hadrons at the hadronization scale.

Evolution of parton densities in Q^2 from hard scale to hadronization scale can be written in terms of splitting function which is the probability that a parton of type p radiates a quark/gluon and becomes a parton of type p$'$ carrying fraction x/z of the momentum of parton p. The evolution equation is called Dokshitzer-Gribov-Lipatov-Altarelli-Parisi (DGLAP) equation.

$$\frac{dq_i(x,Q^2)}{d\log(Q^2)} = \frac{\alpha_s}{2\pi}\int_x^1 \left(q_i(z,Q^2)P_{qq}(\frac{x}{z}) + g(z,Q^2)P_{qg}(\frac{x}{z})\right)\frac{dz}{z} \qquad (40)$$

$$\frac{dg(x,Q^2)}{d\log(Q^2)} = \frac{\alpha_s}{2\pi}\int_x^1 \left(q_i(z,Q^2)P_{gq}(\frac{x}{z}) + g(z,Q^2)P_{gg}(\frac{x}{z})\right)\frac{dz}{z} \qquad (41)$$

Where q_i and g are quark and gluon density functions respectively and the P functions are Splitting functions which are calculated from pQCD.

Parton shower algorithms recursively add emissions to partons until they reach the hadronization scale. Usually this results in several emissions, or a "shower" of partons, before the scale reaches a cutoff. The parton shower algorithm uses the Sudakov form factor,

$$\Delta_a(q_1^2, q_2^2) = \exp\left[-\int_{q_1^2}^{q_2^2} \frac{dq^2}{q^2}\frac{\alpha_s}{2\pi}\int_{Q_0^2/q^2}^{1-Q_0^2/q^2} P_{ca}(x)dx\right] \tag{42}$$

Where q^2 is the evolution variable and Q_0^2 is the hadronization cutoff scale. The form factor represents the probability of no additional emission from a parton evolving from q_1^2 to q_2^2.

The algorithm starts with partons at hard scale Q^2 and then solves the equation $\Delta_a(Q^2, q^2) = \mathcal{R}$, where $\mathcal{R}$ is a random number between 0 and 1 (denoting a random probability). This goes on recursively for all partons changing Q^2 to parent virtuality and q_1^2 to daughter virtuality q^2 until q^2 goes below the hadronization scale. At the end we are left with a shower of partons which can be matched to a hadronization algorithm.

3.5 Hadronization

Hadronization is a non-perturbative phenomenon which cannot currently be described from first principle. We take resort to phenomenological models to describe it.

3.5.1 String model

The Lund string model is based on the idea that the strong force acting between two colored partons grow with the separation between them. We can visulalize this as two partons connected by a string. As the two partons move apart the potential energy will increase until it is energetically favorable to produce a quark-antiquark pair somewhere along the string. This process goes on until all the partons bind together in pairs to produce bound hadronic states. This model of hadronization is used by Pythia. Fig. 18(a) shows a schematic depiction of the string model.

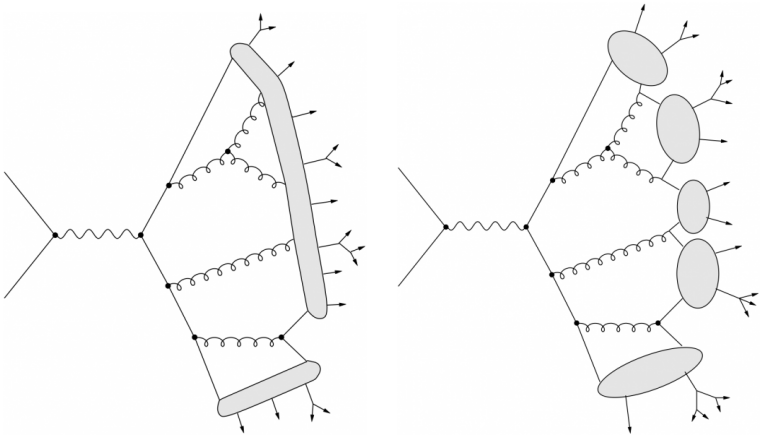

Figure 18: (a) String and (b) Cluster hadronization models.

3.5.2 Cluster model

The cluster hadronization model is based on the "pre-confinement" property of QCD. The basic idea is that the partons in a shower tend to form color-less clusters with invariant mass independent of the hard process, depending only on the evolution scale and the fundamental QCD scale. The model is implemented by forcing gluons to split into quark-antiquark pair near the hadronization scale and these quarks and anti-quarks then form color-less clusters. These clusters are considered to be proto-hadrons which can decay into lighter hadrons to be observed in the detector. Cluster model is used by Herwig and Sherpa. Fig. 18(b) shows a schematic depiction of the cluster model.

3.6 Underlying event

In a hard interaction usually only one of the partons participates from each proton. The remnant of the incoming protons may still interact with each other which is known as the underlying event. These interactions tend to be softer than the hard interaction but more energetic than the non-diffuse interactions from minimum bias events. The biggest source of this kind of events is multiple parton interaction (MPI).

Underlying event contribution are estimated using phenomenological models. A common method to estimate MPI is to parametrize the model in terms of impact parameter, as low impact parameter means a more head-on collision between the proton bunches and a greater probability of multiple interaction [43].

3.7 Event Generators

There is a wide variety of event generators for simulation of high energy particle collision. As described earlier, event simulation involved several steps. Most of the MC programs specialize on one aspect of the simulation procedure and are interfaced to other programs that can do a different part of simulation. There are a few general purpose event generators, e.g. Herwig [44], Sherpa [45], and Pythia [46, 47], which can handle all the aspects of event simulation all by itself. Different event generators used in this analysis have been briefly discussed below.

3.7.1 SHERPA

SHERPA (Simulation for High Energy Reactions of PArticles) is a general-purpose event generator, written in C++. It can simulate the lepton-lepton, lepton-hadron, hadron-hadron collisions, as well as photon induced processes. It provides leading order (LO) matrix-element calculation and phase-space generation for a wide range of physics processes. It covers the SM completely and supports many processes in Beyond Standard Model (BSM) physics, e.g., Two-Higgs-Doublet Model (H2DM) and Minimal Supersymmetric Standard Model (MSSM). Sherpa also simulates parton showering, hadronization and multiple parton interactions (MPI). Hadronization is based on the cluster model. Primary hadron decays are simulated with full spin correlations.

3.7.2 HERWIG

HERWIG [44](Hadron Emission Reactions With Interfering Gluons), like SHERPA, is a general-purpose event generator for the simulation of hard lepton-lepton, lepton-hadron and hadron-hadron collisions. It was originally written in Fortran but since has been improved and replaced by the C++ program HERWIG++ [48, 49]. It contains a large number of $2 \rightarrow$ n subprocesses for both SM and some BSM frameworks, and allows new models to be

added by simply providing the relevant Feynman rules. HERWIG simulates parton showering, hadronization and underlying event. Hadronization uses the cluster model. Hadron decays are simulated using matrix elements, and takes into account spin correlations and off-shell effects.

3.7.3 PYTHIA

PYTHIA is another example of a general-purpose event generator which simulates hadronic events in lepton-lepton, lepton-hadron and hadron-hadron collisions. The older PYTHIA 6 [46] program was written in Fortran and has been succeeded by PYTHIA 8 [47] which is written in C++. The program can handle all stages of event generation. It contains hundreds of hard-coded $2 \rightarrow 1,2,3$ scattering processes at LO, covering SM, SUSY and many other BSM physics processes. Hadronization follows the Lund string model. Multiple parton interactions are used to build up the underlying event.

3.7.4 ALPGEN

ALPGEN [50] is a LO matrix element generator and phase space integrator for multi-parton hard processes in hadronic collisions. It specializes in processes with many jets in the final state. It takes into account Mass effects of heavy quarks, as well as decays of top quarks and vector bosons with full spin correlations. ALPGEN does not perform parton showering or hadronization. It generates parton-level events with full information on their color and flavor structure, the output can then be interfaced to HERWIG or PYTHIA for further simulation.

3.7.5 AcerMC

AcerMC [51] is a specialized LO event generator that is used for simulating a few specific SM processes produced in proton-proton collisions at the LHC. It contains dedicated matrix-element-based generators for the specific processes which provides faster simulation compared to the general-purpose generators. AcerMC is interfaced to PYTHIA or HERWIG for initial- and final-state radiation, hadronization, subsequent decay chains, and the underlying event.

3.7.6 MC@NLO

MC@NLO [52] is a NLO matrix element (ME) event generator which interfaces to parton showering programs. Although most ME event generators produce events at LO, the showering programs need to have an approximate NLO implementation. When events generated at NLO are interfaced to showering programs, it may lead to double counting. MC@NLO introduces negative weight to subtract events to avoid double counting. The program is often interfaced to HERWIG for parton showering and underlying event simulation.

3.7.7 POWHEG

POWHEG [53, 54] (POsitive Weight Hardest Emission Generator) [53] is another program that interfaces NLO calculations from a matrix element generator to parton showering generators. Powheg, unlike MC@NLO, does not introduce negative weights and can interface to any showering program.

3.7.8 WHIZARD

WHIZARD [13] is a LO matrix element generator and phase space integrator used for hadron, lepton, and photon colliders. It has implemented simulations for SM, MSSM, and many other BSM models. Specifically for this analysis, the aQGC samples were produced using WHIZARD. It needs to be interfaced with a parton showering and hadronization program (e.g., PYTHIA) for full simulation.

3.8 Detector Simulation

ATLAS detector's response to particles traversing through it is simulated by the GEANT4 [55]. GEANT4 is a software toolkit used for simulating passage of particles through matter across a wide range of energy. It needs to be interfaced with an event generator that will generate the physics events, including matrix element calculation for hard scattering, parton shower and underlying event. A detailed geometry of the ATLAS detector, including any subsystem misalignment, dead material, electronics and cables, can be implemented in GEANT. Simulation covers a comprehensive range of physics processes including electromagnetic, hadronic and optical processes. Once

the events from the MC generator are fed into GEANT4, it takes into account interaction of particles with the magnetic field, ionization and energy deposition, or hits, in the active materials in the detector. Detector "hits" and energy deposition are digitized and recorded in the same format as would be read out by the detector during data-taking. GEANT4 full simulation is computationally expensive. Physics processes with high cross-section need large Monte Carlo production (so that MC statistics is comparable or larger than data statistics), Atlfast-II simulation package [56] is sometimes used to produce those. Atlfast-II uses the FastCaloSim software package to simulate the calorimeter response of the detector which is the most time-consuming phase of simulation for GEANT4. This cuts down processing time by an order of magnitude, although the fast simulation provides a less accurate representation of the detector. Often the Atlfast simulation is compared against the full simulation or data to correct for disagreements.

3.9 Pileup

There are often more than one interaction during an event. The collisions in addition to the hard scatter is called pileup. If the additional interactions come from the same brunch crossing it is called "in-time" pileup. This is usually the biggest contribution to pileup. Additional proton-proton interaction coming from the bunch crossing just before or after the collision of interest is called "out-of-time" pileup. There are also contributions from cavern background, neutrons and protons from random hits in the muon system; beam halo, originating from proton bunch interacting with an up-stream collimator; and beam gas events, collision of proton bunch with residual gas particles inside the beam pipe. Pileup is a major challenge in high-luminosity environment of LHC. For example, during the data-taking in 2012, the average number of pileup interaction in each bunch crossing was about 20. It is possible to simulate individual components of pileup, but the simulation is highly dependent on detector layout and any change in detector condition needs to be taken into account. Instead, both in-time and out-of-time pile-up can be estimated from data using the so-called minimum bias interactions. Minimum bias interactions are processes that are selected using a loose trigger setup intended to select inelastic collisions with as little bias as possible. A number of minimum bias events are overlaid on top of the hard scatter event at the digitization level before the reconstruction stage. The number is selected randomly from a Poisson distribution with the mean $<\mu>$, the

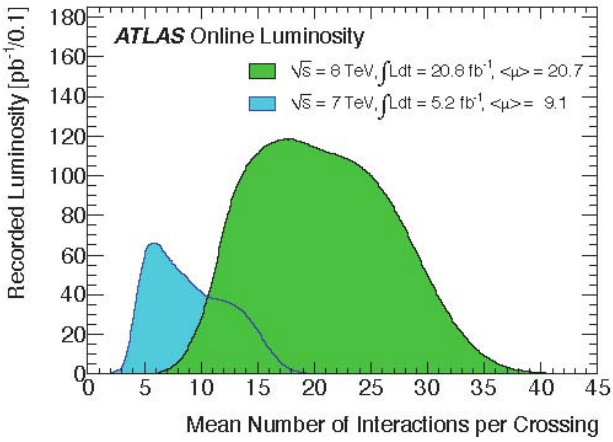

Figure 19: Average number of interaciton per crossing in 2011 and 2012 ATLAS data.

average interaction per bunch crossing.

3.10 Monte Carlo samples

In the following sections different MC samples used in our analysis have been discussed. A detailed list of these samples, their cross-sections and other related information can be found in Appendix A.

3.10.1 Signal Processes

The SM signal is electroweak production of WW/WZ which includes $W^{\pm}W^{\pm}$, $W^{\pm}W^{\mp}$ and WZ. Both SM and aQGC samples are modeled using Whizard v2.1.1 [13, 14], plus PYTHIA8 [47] for fragmentation. The CT10 PDF set [57] is used. The samples are $V(qq)\ell\nu$ +2 partons and $V(qq)\ell^{+}\ell^{-}$+ 2 partons at the matrix-element level, and include all of the purely-electroweak tree-level diagrams (i.e. $\mathcal{O}(\alpha_{EW}^{6})$ diagrams) that contribute to this final state. This includes all of the VBS diagrams, examples of which are shown in Fig. 4, but it also includes non-VBS electroweak diagrams, some examples of which are shown in Fig. 20. The non-VBS diagrams will be greatly suppressed by the event selection in this analysis.

Diagrams that contain a mixture of electroweak and QCD vertices (i.e. $\mathcal{O}(\alpha_{EW}^{4}\alpha_{S}^{2})$ diagrams) are not included in these samples, and are not part of

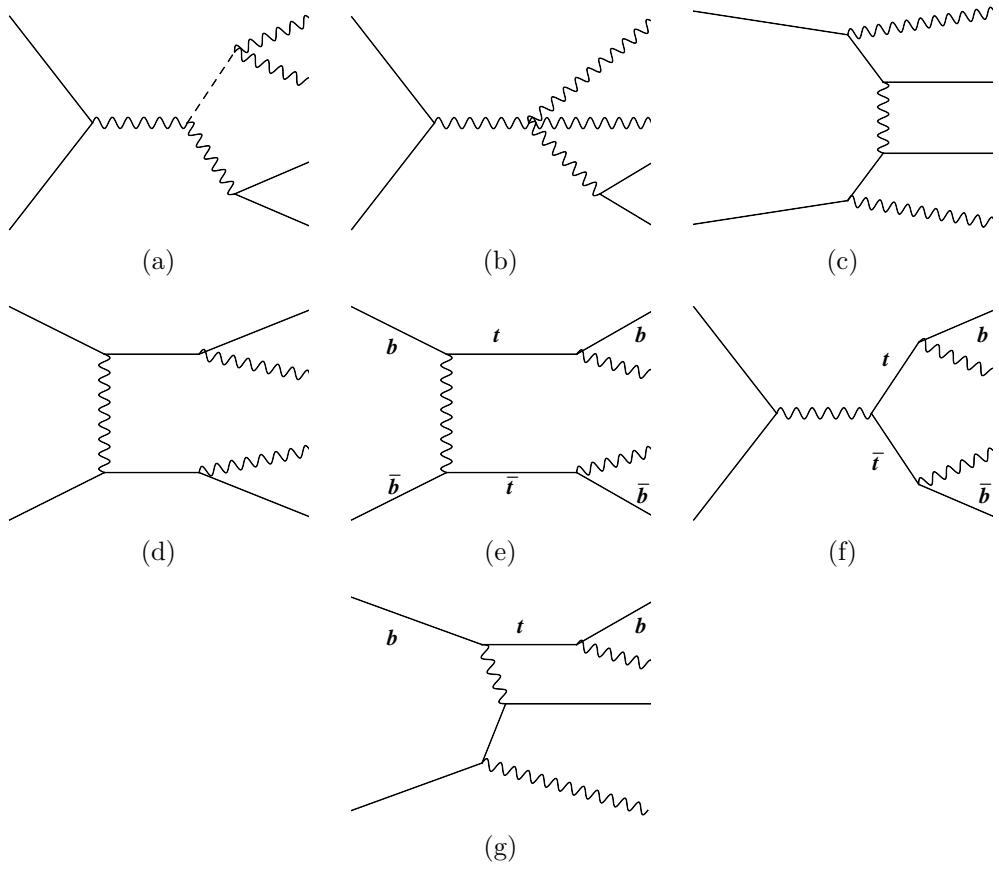

Figure 20: Examples of non-VBS $\mathcal{O}(\alpha_{EW}^6)$ diagrams that contribute to the signal. The decays of the bosons are not explicitly shown, but the counting of powers of α includes the boson decays.

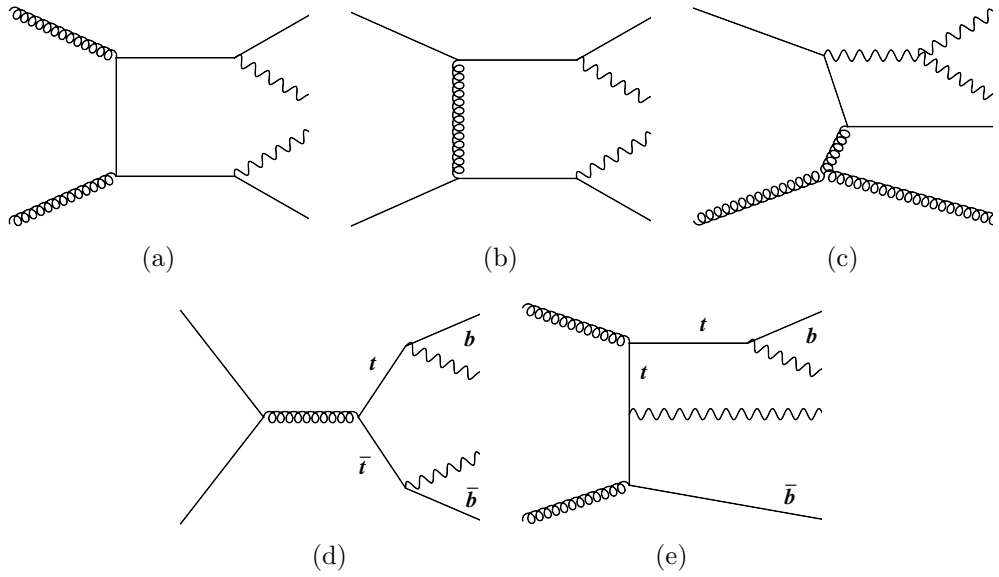

Figure 21: Examples of $\mathcal{O}(\alpha_{EW}^4\alpha_S^2)$ diagrams that lead to the VV+2parton final state. These are not included in the signal definition. The decays of the bosons are not explicitly shown, but the counting of powers of α includes the boson decays.

the signal definition. Examples are shown in Fig. 21. Such processes are not affected by aQGCs, and are accounted for by the background samples ($t\bar{t}$, single-top, and diboson).

Two types of signal samples are generated, referred to as "WV" and "ZV":

- WV samples contain $W(qq)\ell\nu qq$ and $W(qq)\ell\ell qq$ events,
- ZV samples contain $Z(qq)\ell\nu qq$ and $Z(qq)\ell\ell qq$ events,

where $\ell = e, \mu, \tau$. Although the $Z(\ell\ell)V(jj)$ processes have two leptons, and thus do not have the final state we are searching for, some of these events will pass our selection due to a missed lepton. Since the $Z(\ell\ell)V(jj)$ processes are affected by aQGCs, we include these processes in our signal MC samples. Although the cuts in this analysis target $W \to e\nu$ and $W \to \mu\nu$ decays, the $\tau\nu$ decays are also included in the signal samples, since they are equally affected by aQGCs, and some of these events will pass our event selection due to leptonic τ decays.

Process	Generator
W + jets	SHERPA
Z + jets	SHERPA
$t\bar{t}$	POWHEG+PYTHIA
Single top Wt	POWHEG+PYTHIA
Single top s-channel	POWHEG+PYTHIA
Single top t-channel	AcerMC+PYTHIA
WW	SHERPA
WZ	SHERPA
ZZ	SHERPA
$W\gamma$(+jets)	ALPGEN+Herwig
$Z(ee, \mu\mu)\gamma$(+jets)	SHERPA
$W(\ell\nu)W(jj)$+$Z(\ell\ell)W(jj)$	Whizard+PYTHIA8
$W(\ell\nu)Z(jj)$+$Z(\ell\ell)Z(jj)$	Whizard+PYTHIA8

Table 3: Summary of the nominal MC samples used for signal and background processes. Details about the MC samples used are given in Appendix A.

The WV and ZV samples have a small overlap, since both contain $W(\ell\nu)Z(qq)W(qq)$ tri-boson events due to diagrams such as Fig. 20(b). To prevent double-counting, events are removed from the ZV samples if they contain $W(\ell\nu)Z(qq)$+ $2q$ with the invariant mass of the last two quarks within 4GeV of the world-average W mass value.

The WV and ZV samples are generated for a variety of aQGC parameters. As mentioned already, the aQGC parameters to be investigated in this analysis are α_4 and α_5. As a shorthand, the notation "WV(α_4,α_5)" (and analagously for ZV) will be used to refer to signal MC predictions for particular values of the aQGC parameters. For example, "WV(0.1,0)" is shorthand notation for the WV sample with aQGC parameters $\alpha_4 = 0.1$, $\alpha_5 = 0$.

The nominal MC generators used for the various signal and background processes are summarized in Table 3. More details can be found in Appendix A.

3.10.2 V+jets Processes

The W + jets and Z + jets processes are modeled with SHERPA v1.4.1 [45, 58, 59, 60], using the CT10 PDF set. The samples use massive c- and b-quarks, and contain up to 4 final-state partons in the matrix element. The decays $W \to e\nu, \mu\nu, \tau\nu$ and $Z \to ee, \mu\mu, \tau\tau$ are included. The samples are generated in ranges of the true $\mathrm{p_T}(V)$, in order to generate more events at high-p_T. The following p_T-ranges are included:

- $40 < \mathrm{p_T}(V) < 70$GeV, $70 < \mathrm{p_T}(V) < 140$GeV, $140 < \mathrm{p_T}(V) < 280$GeV, $280 < \mathrm{p_T}(V) < 500$GeV, $\mathrm{p_T}(V) > 500$GeV.

To cover the low-p_T region, samples inclusive in $\mathrm{p_T}(V)$ are used, with a $\mathrm{p_T}(V) < 40$GeV cut applied in order to remove overlap with the p_T-slice samples. The W+jets (Z+jets) samples are normalized to W+jets (Z+jets) QCD NNLO inclusive cross-section obtained from FEWZ [61] program with MSTW2008NNLO PDF set and renormalization and factorization scales set equal to the mass of the vector boson, $\mu_F = \mu_R =$ MW (MZ) [62].

In addition to the nominal samples, alternate SHERPA W + jets samples are used with varied factorization and renormalization scales and with different parton shower/matrix element merging scales, in order to assess systematic uncertainties.

The previously-mentioned W + jets and Z + jets samples do not include the vector-boson fusion (VBF) production of W + jets or Z + jets. The VBF process is a much smaller background for our analysis, the cross-section being $< 5\%$ of that of QCD production. We model VBF W + jets using additional samples generated with SHERPA v1.4.3 using the CT10 PDF set. These samples include up to 3 final-state partons in the matrix element. The VBF Z + jets process is considered negligible.

3.10.3 $t\bar{t}$ and Single t Processes

The $t\bar{t}$, single-top Wt, and single-top s-channel backgrounds are modeled with POWHEG [53, 54] plus PYTHIA v6.426 [46] for fragmentation with the P2011C tune [63]. The CTEQ6L1 PDF set [40] is used.

The single-top t-channel process is modeled with AcerMC [51] plus PYTHIA v6.426 with the P2011C tune and the CTEQ6L1 PDF set.

The $t\bar{t}$ samples are normalized to cross section for pp collisions at a centre-of-mass energy of $\sqrt{s} = 8TeV$, $\sigma_{t\bar{t}} = 253^{+13}_{-15}$ pb. This cross-section has

been calculated at next-to-next-to leading order (NNLO) in QCD including resummation of next-to-next-to-leading logarithmic (NNLL) soft gluon terms with top++2.0 [64, 65, 66, 67, 68, 69, 70]. The PDF and α_S uncertainties were calculated using the PDF4LHC prescription [71] with the MSTW2008 68% CL NNLO [41, 72], CT10 NNLO [57, 73] and NNPDF2.3 5f fixed flavor number (FFN) [42] PDF sets, added in quadrature to the scale uncertainty. The single top samples are normalized to NLO+NNLL calculations [74, 75, 76].

3.10.4 Other Backgrounds

Diboson backgrounds from the WW, WZ, and ZZ processes are modeled with SHERPA 1.4.3 with the CT10 PDF set. Up to 3 additional final-state partons are modeled in the matrix element. Massive c- and b-quarks are used. The semileptonic decays ($\ell\nu qq$ and $\ell\ell qq$) are included, as well as the decay modes $W(\ell\nu)W(\ell\nu)$, $W(\ell\nu)Z(\ell\ell)$, and $W(\ell\nu)Z(\nu\nu)$, where $\ell = (e, \mu, \tau)$. These samples were normalized to NLO cross-section calculated using MCFM [77] program with MSTW2008NLO PDF set [62]. These diboson processes only include non-electroweak diboson production (i.e. $\alpha_s^2\alpha_{\rm EW}^4$ diagrams), and so do not overlap with the signal.

The $W\gamma$ process, with up to 5 additional final-state partons, is modeled with ALPGEN [50] plus HERWIG v6.520.2 [44] plus JIMMY [78]. The AUET2 tune [79] and CTEQ6L1 PDF set are used.

The $Z\gamma$ process with $Z \to (ee, \mu\mu)$, with up to 3 additional final-state partons, is modeled with SHERPA 1.4.1 using the CT10 PDF set.

3.11 MC correction

3.11.1 Pileup re-weighting

In a hadron collider event topology can be extremely complex. To simulate pileup in Monte Carlo, we generate minimum bias events and overlay on top of the hard interaction events. The minimum bias events are dependent on the rate of interaction per bunch crossing, $\langle\mu\rangle$. This pileup profile may not agree with the data, as in the case of 2012 data, so re-weighting is done to reproduce $\langle\mu\rangle$ observed in data.

4 Object reconstruction

The raw output of the detector comes in the form of hits, energy deposition, times etc. These outputs are stored in Raw Data Object files (RDO). The ATLAS detector produces a huge amount of raw data. The sheer size of data means it is impractical to distribute them widely within the collaboration. Instead, datasets go through additional stages of processing before it is made available to the physics analyzers. Unlike RDO these datasets contain objects that we are more familiar with, like vertices, tracks, electrons, muons, jets etc. The Event Summary Data (ESD) is produced from running pattern recognition algorithm on raw data and contains detailed output of detector reconstruction. The Analysis Object Data (AOD) contains summary of the reconstructed event which is sufficient for most analyses. An additional level of compression is achieved when Derived Physics Data (DPD) datasets are created from AOD for different groups of physics analysis.

4.1 Track reconstruction

The track and vertex reconstructions are inter-dependent. In ATLAS charged particle tracks are reconstructed in the Inner Detector (ID). The tracking mainly follows two sequences or sets of algorithms; first the "inside-out" algorithm and a subsequent "outside-in" algorithm [80]. Inside-out is the primary pattern recognition sequence for track finding. The first step is to create three-dimensional representations of two-dimensional hits in Pixel and SCT detectors, called the SpacePoint objects. The second step involves searching for track seeds and the creation of track candidates. Valid combinations of the SpacePoint objects are to be used as seeds for track search in the ID. Proceeding inside-out from the interaction point additional hits are added to the track candidate if they are found to be compatible with the track as determined by a combinatorial Kalman filter [81]. Each time a new hit is added the track fit is updated. The third step is to resolve ambiguity arising due to the large track multiplicity close to interaction point. The tracks are ranked on the basis of their likelihood to describe real particle trajectories. The scoring process involves a detail material description of the detectors. On top of a simple χ^2 track fit it also puts different weights on measurements from different sub-detectors (for example, preferring tracks with overlap hit in Pixel and SCT and penalizing tracks that had holes in Pixel detector). The forth step is to extend the tracks to the TRT. Compatible TRT measurements are

added to the silicon-only tracks without modification of the original track information. The association of the TRT hits are purely extensions and no refit is done at this stage.

The inside-out sequence is dependent on finding a track in the silicon detector. During the reconstruction process, some of these initial tracks may not be found or ambiguous hits can prevent the real track to be chosen. Therefore a second sequence in track reconstruction has been developed following an outside-in approach. This sequence starts with a dedicated segment finding algorithm and then traces the segments back into the silicon detector. Like the inside-out algorithm, ambiguity is resolved and a global track fit is performed. TRT segments without associated track in the silicon detector is saved as TRT-standalone tracks.

4.2 Vertex reconstruction

Accurate identification of interaction point or vertices is of vital importance for proper reconstruction of event kinematics and measurement of impact parameter. The hard interaction vertex is called the primary vertex . There may be secondary vertices in an event arising from decays of heavy particles and interactions of particles produced in the primary vertex. As mentioned earlier, the reconstruction of vertices is dependent on reconstruction of charged particle tracks. The vertex reconstruction proceeds in two stages, i) primary vertex finding (algorithm deals with associating the tracks to a primary vertex candidate) and ii) vertex fitting (algorithm reconstructs the vertex position and calculates the covariance matrix) [82], [80]. First, the reconstructed tracks with origins compatible with the interaction region are pre-selected. From the distribution of z co-ordinates of tracks at the point of closest approach with respect to the nominal beam spot, a global maxima is found and used as a seed for the vertex. Taking this seed and its surrounding tracks as inputs, an adaptive χ^2-based vertex fitting algorithm is run to determine the vertex position. Each track is assigned a weight based on its compatibility with the fitted vertex position and outliers are down-weighted. Tracks that are incompatible with the vertex position by more than 7σ are used for fitting another vertex. This procedure is continued until the list of tracks is exhausted. Secondary vertices are reconstructed using kinematic properties of the interaction likely to happen in that vertex. The displaced tracks are fitted with the secondary vertex candidate with the kinematic constraints set by, for example, the parent particle mass or the

angular distribution of the daughter particles.

4.3 Electron reconstruction

In ATLAS the inner detector tracks are matched to the energy deposits in the EM calorimeter to reconstruct electron objects. In addition, the Transition Radiation Tracker (TRT) is used for electron identification. In ATLAS there are three algorithms for electron reconstruction.

The main algorithm is called the sliding window algorithm [83] which reconstructs electron clusters in the central region ($|\eta|$ <2.47). In the first step, EM calorimeter is divided into towers of dimension $\Delta\eta \times \Delta\phi = 0.025 \times 0.025$. This is based on the middle EM calorimeter layer's granularity but the towers extend to all the layers in the EM calorimeter. The energy of all cells inside each of these towers is summed to get the tower energy. A cluster is seeded by towers with total transverse energy above 2.5 GeV. The sliding-window algorithm is then employed to form a cluster using a window size of 3×5 (0.075×0.125 in $\eta\phi$ space). Clusters matched to a well-reconstructed ID track are classified as electrons. Finally, the electron cluster is rebuilt using 3×7 towers in the Electromagnetic Barrel (EMB), and 5×5 towers in Electromagnetic EndCap (EMEC). Using MC samples of W and Z leptonic decays, the efficiency of the initial cluster reconstruction was derived. It is expected to be approximately 97% at $E_T = 7$ GeV and almost 100% for electrons with $E_T > 20$ GeV [84].

The track-based algorithm is used to find low p_T electrons and is seeded by tracks in the inner detector instead of calorimeter clusters. The tracks must satisfy several quality requirements and have hits in all three layers of the ID. Tracks are then matched to 3×7 clusters in the middle EM layer and an overlap removal between these clusters is performed. If an electron is reconstructed by both cluster-based and track-based algorithms, the cluster-based algorithm is used by default.

A forward calorimeter based reconstruction algorithm is used to find forward electrons. The discussion of that is outside the scope of this document.

4.4 Muon reconstruction

Muon objects are reconstructed using available information from the ID, the MS, and the calorimeter sub-detector systems [85]. There are a few different

types of muons in ATLAS depending on the reconstruction criteria [86]. They are:

- Stand-alone muons: only the MS is used to reconstruct the trajectory of muons. The muon track parameters at the interaction point are determined by extrapolating the track back to the point of closest approach to the beam line, taking into account the estimated energy loss of the muon in the calorimeters. The muon has to travel through at least two layers of MS chambers to provide a track measurement. Standalone muons are mainly used to extend the acceptance to the range $2.5 < |\eta| < 2.7$ which is not covered by the ID.

- Combined muons: track reconstruction is preformed independently for ID and MS and a combination is done to reconstruct a combined track. This is the main reconstructed muon type.

- Segment-tagged (ST) muons: a track in the ID is classified as a muon if the extrapolated trajectory can be matched to at least one local track segment in the Monitored Drift Tube Chambers (MDT) or Cathode Strip Chambers (CSC). Segment-tagged muons can be used to increase the acceptance for muons which crossed only one layer of MS chambers.

- Calorimeter-tagged (CaloTag) muons: a track in the ID is identified as a muon if it could be matched to an energy deposit in the calorimeter compatible with a minimum ionizing particle. This type of muons has the lowest purity of all the muon types but it recovers acceptance in the regions not covered by the MS.

In ATLAS, the reconstruction of the Stand-alone, Combined and Segment-tagged muons has been performed using two independent reconstruction software packages, implementing different strategies (called "chains") both for the reconstruction of muon objects in the spectrometer and for the ID-MS combination. The first chain (called STACO) does a statistical combination of the track parameters of the Stand-alone muon and ID muon tracks. The second (called MUID) performs a global refit of the muon track using the hit information from the ID and MS. A new unified chain (called "MUONS") has been developed to incorporate the best features of the two original chains. In our analysis the STACO muons have been used uniformly. The ID tracks used for Combined or Segment-tagged muons need to satisfy the following quality requirements:

- at least 1 Pixel hit;
- at least 5 SCT hits;
- at most 2 active Pixel or SCT sensors traversed by the track but without hits;
- in the region of full TRT acceptance, $0.1 < |\eta| < 1.9$, at least 6 TRT hits.

The number of hits required in the first two points is reduced by one if the track traverses a sensor known to be inefficient according to a time-dependent database.

4.5 Jet reconstruction

Jets are collimated shower of hadrons, resulting from hadronization of quarks and gluons, produced in great quantity in a hadron collider. ATLAS hadronic calorimeter is specially suited to detect these hadrons. The calorimeter cells also record random noise from readout electronics and pileup interaction. The noise in individual cells is the quadratic sum of readout noise and pileup noise evaluated from MC simulation. To construct the jets we need to consider cells that have large signal over noise ratio (S/N). As a first step cells with S/N greater than 4 is used as seed for a proto-cluster [87]. All neighboring cells with S/N > 2 are iteratively added to it. If a cell is in the boundary of more than one proto-cluster, the proto-clusters are merged. Finally, all neighboring cells is added to it irrespective of its S/N ratio.

At this stage, the proto-clusters are split around the local maxima, a cell with energy E> 0.5 GeV greater than any of its neighboring cell. These local maxima cells are used to seed exactly one "topological" cluster consisting of only those cells that were part of the initial cluster. Cells that are shared by two topological clusters contribute to each according to the cluster energies and distance of the cell from the cluster cell containing the local maximum. The resulting new clusters and any original proto-clusters lacking local maxima are sorted in order of E_T. These topological clusters are defined to have zero mass and their direction is calculated on the basis of weighted average of η and ϕ of the constituent cells.

The topological clusters [83] then are fed to the one of the sequential recombination jet-finding algorithms. Jet algorithms are defined by two distances,

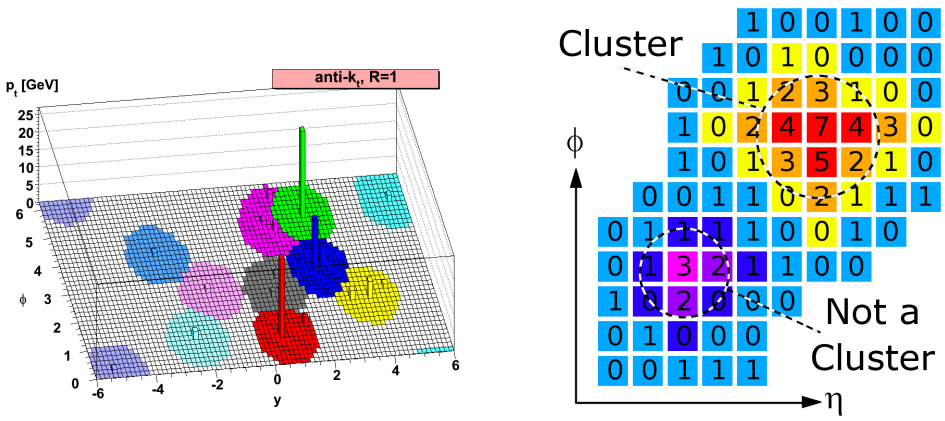

(a) (b)

Figure 22: (a) Jet reconstruction using the anti-k_T jet algorithm with R=1.0. Anti-k_T jets generally are centered around an energy peak and are conical in shape. Figure taken from [88]. (b) A topological cluster. The cells with S/N > 4 are used to seed the clusters. Neighboring cells with S/N > 2 are added. Finally all neighbors are added to form the cluster. Figure from [89]

distance between two clusters,

$$d_{ij} = min(k_{Ti}^{2p}, k_{Tj}^{2p}) \frac{(\Delta R)_{ij}^2}{R_c^2} \tag{43}$$

and distance between a cluster and beam,

$$d_{ib} = k_{Ti}^{2p} \tag{44}$$

where

$$(\Delta R)_{ij}^2 = (y_i - y_j)^2 + (\phi_i - \phi_j)^2$$

and k_{Ti}, y_i, ϕ_i are the transverse momentum, rapidity and azimuthal angle of the i-th cluster. R_c is called the characteristic radius parameter which decides the size of the eventual radius of the jet. The variable p takes different values for different algorithms, e.g. for k_T, anti-k_T [88] and Cambridge-Aachen algorithms [90] the value of p is 1,-1 and zero respectively. The current ATLAS recommendation has been to use the anti-k_T jet algorithm with R_c=0.4 for standard jet clustering. For some analysis large-R jets are necessary. Anti-k_T and Cambridge-Aachen jets have been considered for this with $R_c \approx 1$.

At first, the highest p_T cluster i is considered and the distances between it and other clusters (d_{ij}) and distance from the beam (d_{ib}) are calculated. If d_{ij} is smaller than d_{ib}, the j-th cluster is added to the i-th cluster. This goes on till there are no cluster with distance smaller than d_{ib} is left. The jet i is then considered to be complete and removed from further consideration. The same procedure is then continued for the remaining clusters until there is none remaining. The p=-1 value for anti-k_T algorithm means the low p_T clusters have larger weight in d_{ij} and merge with the large p_T jets before harder jets at the same distance from the i-th cluster. This ensures that the algorithm produces roughly conical-shaped jets with a soft-resilient boundary which are infra-red safe. Also Eqn. 43 and Eqn. 44 ensure that any cluster j with $(\Delta R)_{ij} < R_c$ is merged with cluster i, which makes the algorithm collinear-safe.

The energy measurement of these topological clusters underestimate jet energy because jets have a lower detector response than electromagnetic shower objects, due mainly to the non-compensating nature of the ATLAS calorimeter. To correctly measure the jet response, cluster energies need to go through a Jet Energy Scale (JES) calibration [91]. The local cell signal

weighting (LCW) method of calibrating the topological cluster jet has been used in this analysis. The LCW method classifies the topo-clusters as either electromagnetic or hadronic, based on the measured energy density and the longitudinal shower depth. Corrections are applied for calorimeter non-compensation, signal losses due to noise threshold effects, and energy losses in the non-instrumented regions close to the clusters. The LC-jet calibration is carried out in a four-step procedure in the following way.

Pileup subtraction: Energy deposit due to pileup contribution is subtracted using MC simulation. The corrected p_T of jet is given by

$$p_T^{corr} = p_T^{jet} - \rho A_T - \alpha(N_{PV} - 1) - \beta(\langle\mu\rangle) \tag{45}$$

where the first term on the right hand side of the equation is the uncorrected transverse momentum; in the second term ρ is the estimated pileup p_T density and A_T is the jet area in the transverse plane; the third term captures the in-time pileup contribution which is parametrized by the number of reconstructed primary vertex, N_{PV}; forth term captures out-of-time pileup contribution parametrized by the average number of interaction per branch crossing $\langle\mu\rangle$. The pileup p_T density is calculated on a even-by-event basis. It is defined as the median of the distribution of the p_T density of k_T jets in the event [92]. The third and forth terms are called the residual corrections; α and β are calculated after the ρ-term has already been subtracted.

Origin correction: Keeping the jet energy unchanged the direction of jet momentum is corrected so that it points towards the primary vertex of the event instead of the center of the detector. This improves the η resolution of the jets tremendously.

Jet calibration based on MC simulation: Jet energy is calibrated by applying Jet Energy Scale (JES) derived from MC. These calibration factors are determined by spatially matching calorimeter jets to particle-level jets and then taking the ratio of the measured and true jet energies.

Residual in situ correction: Finally, a global sequential calibration scheme is employed. This leaves the mean jet energy unchanged but improves the jet energy resolution and reduce the sensitivity of the response to jet flavor.

After the full calibration, the scale of the calorimeter jets built from LCW-scale topo-clusters is referred to as LCW+JES.

4.6 MET reconstruction

In hadron collider the momentum carried by partons moving along the beam-pipe can not be measured. But the total momentum in the plane transverse to the beam-axis is still expected to be zero before and after the proton-proton collision. The unbalanced "Missing" Transverse Energy in the detector arises from particles that leave the detector without being detected e.g. neutrinos or weakly interacting exotic particles evading detection. This is pertinent to our analysis because of the neutrino from the decay of W-boson. The $E_T^{missing}$ is calculated using all the objects detected within the calorimeter system and also the muons detected using the inner detector and muon spectrometer. The $E^{missing,calo}$ term is calculated as negative vector sum of calorimeter objects such as electron, photon, jet, tauon and soft energy contributions. The topo-cluster energies are replaced by the calibrated object energies. Muon energy deposited in the calorimeter is subtracted to avoid double counting. The muon term is calculated as the negative sum of muon track momenta. Combined muon tracks are used for $|\eta| < 2.5$. For $2.5 < |\eta| < 2.7$ region, outside the inner detector acceptance, stand alone muons are used. The missing transverse energy has x- and y-components, which can be written down in the form of

$$E_{x(y)}^{missing} = E_{x(y)}^{missing,calo} + E_{x(y)}^{missing,\mu} \tag{46}$$

The total magnitude and azimuthal angle of the vector $E_T^{missing}$ are calculated as,

$$E_T^{missing} = \sqrt{(E_x^{missing})^2 + (E_y^{missing})^2} \tag{47}$$

$$\phi^{missing} = arctan(\frac{E_y^{missing}}{E_x^{missing}}) \tag{48}$$

4.7 b-tagging

Hadrons containing b-quarks have a relatively long life-time. A b hadron with a transverse momentum of 50 GeV will travel on average 3 mm before decaying which leads to a displaced secondary vertex (see Fig. 23). This property can be used to identify jets containing b hadrons, known as b jets, and distinguish them from jets containing only "light-flavor" (u,d and s quark

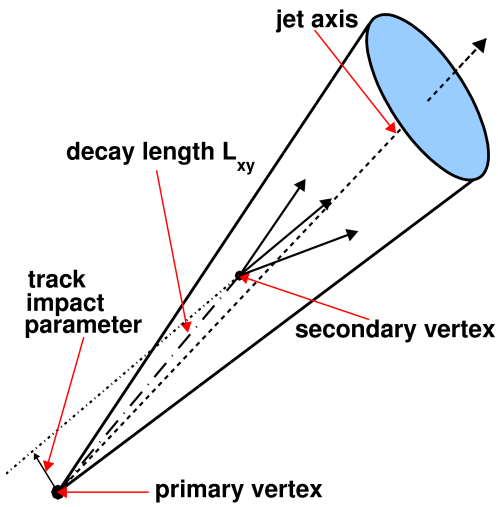

Figure 23: Schematic view of a b-hadron decay inside a jet resulting in a displaced secondary vertex. The track impact parameter, defined as the distance of closest approach between the extrapolation of the track and the primary vertex, is also shown. Figure from [93]

or gluon) hadrons or c hadrons. Identification of b jets, or b-tagging, is important for the current analysis because of the $t\bar{t}$ and single top backgrounds. These backgrounds can be suppressed by rejecting events with b jets in the final state.

ATLAS has developed several algorithms for identifying b jets. The b-tagging algorithms can be categorized into two groups. One group exploits the large impact parameter of tracks with respect to the primary vertex. The other group reconstructs the displaced vertices characteristic of b hadron decay. A good algorithm needs to have large efficiency of selecting the b jets and low rate of mis-tagging light-quark jets as b jets. The vertex-based algorithms exhibit much lower mis-tag rates than the impact parameter-based ones, but their b-tagging efficiency is relatively small. The two approaches are therefore combined to define more powerful tagging algorithms. The current analysis uses the MV1 algorithm which is widely used in ATLAS for 2011 and 2012 data [94]. It is an artificial neural network algorithm

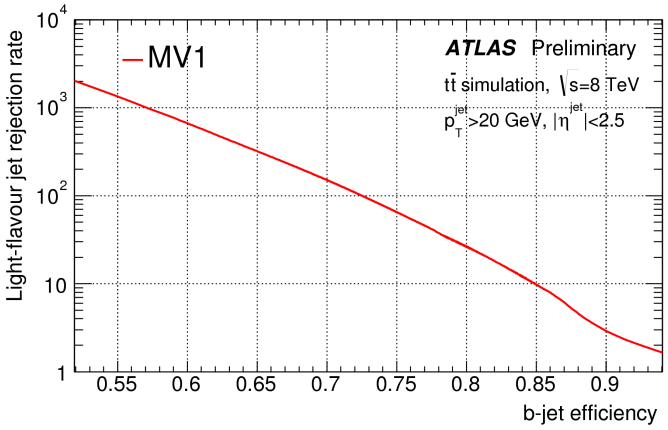

Figure 24: Light-flavor jet rejection versus b jet tagging efficiency.

which combines the discriminating power of both impact-parameter and secondary vertex based algorithms. The inputs come from the IP3D, SV1 and IP3D+JetFitter algorithms. The impact parameter based IP3D algorithm uses both transverse and longitudinal impact parameter significance variables, d_0/σ_{d_0} and z_0/σ_{z_0}, in a log likelihood ratio (LLR) formalism. The vertex based SV1 algorithm uses the flight length significance L/σ_L , i.e., the distance between the primary vertex and the secondary vertex divided by the measurement uncertainty, to distinguish between b jets, c jets and light-flavor jets. SV1 is also based on a LLR formalism. The JetFitter is also a vertex-based algorithm. It uses topological features of b and c hadron decays inside a jet. In JetFitter several variables describing the primary and secondary vertices are used as input nodes in an artificial neural network. The IP3D algorithm can be combined with JetFitter by using the output weight from IP3D as an additional input node.

The performance of the tagging algorithms is estimated using large $t\bar{t}$ Monte Carlo samples [95]. Fig. 24 shows the light-flavor jet rejection as a function of b jet tagging efficiency.

5 Object Selection

Object reconstruction algorithms have relatively large efficiency and allow for fake or misidentified objects. At the analysis level, stricter requirements are imposed on different objects to enhance purity of the true objects. In the present analysis, the final state has one W decaying leptonically and the other boson decaying hadronically, in association with two forward jets, therefore we select events containing an isolated electron or muon, missing transverse momentum and multiple jets. We follow recommendations provided by the ATLAS combined performance groups when defining the object selection criteria and use the corresponding analysis tools developed by corresponding groups. The complete list of ATLAS tools used in the analysis is shown in Table 4.

5.1 Electron

5.1.1 "Loose" electron

For electrons to be selected, the reconstruction algorithm, called author, needs to be equal to 1 or 3 which means electron candidates are reconstructed as clusters of energy deposited in the electromagnetic calorimeter associated to a track reconstructed in the Inner Detector. Candidate transverse energy, E_T needs to be greater than 15 GeV. The absolute value of pseudorapidity, η needs to be less than 2.47 and not in the region between barrel and end-cap EM calorimeters ($1.37<|\eta|<1.52$). Candidates are excluded if they are reconstructed using EM calorimeter clusters known to have dead or poorly functioning detector hardware. They are required to satisfy the ATLAS "medium++" [96] identification criteria. The identification criteria are based on information from shower shape, track quality, transition radiation identification and matching of the track to calorimeter cluster. Requirements on impact parameter variables are imposed to ensure electron candidate originates from the primary vertex. The transverse impact parameter significance, $|d_0/\sigma_{d_0}|$, needs to be less than 5 and longitudinal impact parameter projection along the z-axis, $\mid z_0 sin\theta \mid$ needs to be less than 0.5 mm. The electron is rejected if it is within ΔR =0.1 of a "good" muon (defined below).

5.1.2 "Good" electron

A tighter electron definition is also used, which we call "good" electrons. "Good" electrons satisfy the loose electron criteria, and in addition satisfy the following criteria:

- Pass the ATLAS "Tight++" [96] ID criteria.
- Calorimeter isolation $\Sigma E_T\text{Cone30}/E_T<0.14$
- Track isolation $\Sigma p_T\text{Cone30}/E_T<0.07$

All corrections to electrons, such as energy scale and resolution, trigger efficiency and isolation are done using the *egammaAnalysisUtils* package listed in Table 4. Data-MC scale factors for the isolation and impact-parameter selections were centrally produced by the EGamma group. These scale factors are produced for several p_T and η bins and account for disagreement seen in selection efficiency for data and MC.

5.2 Muon

5.2.1 "Loose" muon

Muons are reconstructed using the STACO combined muon reconstruction algorithm. In the algorithm, a muon trajectory is reconstructed in the Inner Detector and the muon spectrometer separately at first, then combined by a statistical combination approach into a combined track [85]. Muons are selected with the following further criteria:

- Transverse momentum, $p_T > 15$ GeV
- Absolute pseudorapidity, $|\eta|< 2.4$
- Number of pixel hits + number of dead pixel sensors hits > 0
- Number of SCT hits + number of dead SCT sensors hits > 4
- Number of pixel holes + number of SCT holes < 3.
- For $0.1< |\eta|<1.9$, $n_{TRT}^{hits} + n_{TRT}^{outliers} > 5$ and $n_{TRT}^{outliers}/(n_{TRT}^{hits} + n_{TRT}^{outliers}) < 0.9$
- longitudinal impact parameter projection along the z-axis, $\mid z_0 sin\theta \mid <$ 0.5 mm.

5.2.2 "Good" muon

A tighter muon definition is also used, which we call "good" muons. "Good" muon criteria are chosen that are designed to reject multijet background or muons that do not originate from the hard process. "Good" muons satisfy the loose muon criteria, and in addition satisfy the following criteria:

- Transverse impact parameter significance, $|d_0/\sigma_{d_0}| < 3$
- Calorimeter isolation, $\Sigma E_T\text{Cone30}/p_T{<}0.07$
- Track isolation, $\Sigma p_T\text{Cone30}/p_T{<}0.07$

All corrections to muons, such as transverse momentum and resolution scale factors, trigger matching and efficiency scale factors and isolation are done using the *MuonTool* package listed in Table 4.

5.3 Jets

Jets are reconstructed from topological clusters using the anti-k_{T} algorithm [88] with radius parameter $R = 0.4$ ("antiKt4 jets") and full four-momenta recombination. The baseline calibration of the topological clusters is the Local Cluster Weighting (LCW). The calibration applied is an average shift (to correct for pile-up) and multiplicative correction factor, obtained from the Monte Carlo simulation in bins of η and p_{T} [97]. As a last step, the calibration is refined by using in-situ measurements [98] that improve the energy estimate and lead to a reduction in the uncertainty on the jet energy scale. AntiKt4 jets are selected with the following criteria.

- Transverse momentum, $p_T > 30$ GeV.
- Absolute pseudorapidity, $|\eta|< 4.5$
- The jet vertex fraction, defined as the fraction of summed track p_T for all tracks matched to a given jet and associated with the primary vertex, relative to the total summed p_T for all tracks matched to the jet, $|\text{JVF}| > 0.5$ for jets with $p_T < 50$ GeV and $|\eta| < 2.4$.
- Overlap removal: Remove jets if $\Delta\text{R}(\text{lepton, jet}) < 0.3$.

Apart from the jets standard in many ATLAS analysis, we also consider large-R jets. We have used the Cambridge-Aachen algorithm [90] to cluster the jet constituents with radius parameter R set to 1.2. We apply mass-drop filtering [99] to the large-R jets with filtering parameters: $\mu_{\text{frac}} < 0.67$ and $y_f > 0.09$. Additional requirements are,

- $p_T > 200$ GeV.
- $|\eta| < 1.2$
- Overlap removal: Remove jets if ΔR(lepton, jet) < 1.2.
- groomed-mass of jet: m(J)>40 GeV.

5.4 Missing Transverse Momentum

Large unbalanced "missing" momentum, $E_T^{missing}$, is expected in the transverse plane because of the neutrino in the final state. The "RefFinal" definition [100] of $E_T^{missing}$ is used in this analysis, with cluster-based soft terms (the so-called "CST" version [101] of "MET_RefFinal"). This definition uses the sum of calorimeter energy deposits and of the p_T of muons reconstructed in the inner detector or muon spectrometer. The estimate of the energy deposited in the calorimeter is refined by associating calorimeter energy deposits with reconstructed objects (electrons, photons, jets, etc.) and replacing the calorimeter energy estimate by the calibrated object p_T. For the $E_T^{missing}$ calculation the MissingETUtility package has been used. The smearing, energy correction, and calibration applied to the objects are propagated to the $E_T^{missing}$ calculation.

6 Event Selection

The signal events will contain a charged lepton (electron or muon), $E_T^{missing}$, a hadronically-decaying W/Z candidate (consisting of either two small-R jets or one large-R jet), and two additional small-R jets. Since one of the largest backgrounds (W+jets) and the signal , both same-sign WW production and WZ production have more ℓ^+ than ℓ^-, are charge asymmetric, this analysis separates events containing positively- and negatively-charged leptons.

6.1 Trigger selection

The unprescaled [3] single lepton triggers with the lowest p_T threshold are used in this analysis. For the electron channel, events are required to pass `EF_e24vhi_medium1` OR `EF_e60_medium1`. For the muon channel, events are required to pass `EF_mu24i_tight` OR `EF_mu36_tight`. The electron and muon trigger efficiencies are measured using a Z$\rightarrow$ ee and Z $\rightarrow$ $\mu\mu$ tag-and-probe method respectively. Depending on the p_T of the electron candidate and the trigger used the electron trigger efficiencies are found to be approximately 90-98% [102]. The muon trigger efficiencies are equal to approximately 70% in the barrel and 85% in the endcaps [103]. Discrepancy between data and MC efficiency is corrected by using trigger efficiency scale factors employing ATLAS approved tools.

6.2 Event Cleaning

A number of event-cleaning cuts standard to ATLAS analyses are applied to remove bad events.

- Veto events with Liquid Argon noise burst and data corruption
- Veto Tile calorimeter corrupted events
- Remove a small number of events in data that had Tile Calorimeter data corruption in one specific channel.
- Veto incomplete events (events where a timing, trigger and control (TTC) system restart happened).

[3] Due to high event rate sometimes a trigger prescale is used which randomly rejects events which would otherwise pass to the next level of triggering. An un-prescaled trigger passes all events with accept signal.

- Veto events where a small-R jet points to a specific noisy Tile Calorimeter cell during some data periods.
- $E_T^{missing}$ cleaning: remove events that have a so-called 'IsBadLooser' jet with $p_T \geq 20$GeV.
- Remove events in which small-R jets are flagged as being on the edge of a masked Tile region known to be inadequately modeled in MC.

6.3 Basic selection

Both data and MC are processed using official ATLAS tools. The package versions that are used are listed in Table 4. The selection starts by requiring exactly one "good" electron or muon as defined in Section 5. In addition, any events with additional "loose" electrons or muons are vetoed. The selected lepton must furthermore have $p_T > 30$ GeV. Events are required to have $E_T^{missing} > 30$ GeV to account for the presence of the unobserved neutrino from the $W \to l\nu$ decay. The lepton and $E_T^{missing}$ are combined to form a leptonically-decaying W candidate, W_{lep}.

The reconstruction of the hadronic portion of the event is more complex. The goal is to reconstruct both the hadronically-decaying W/Z candidate (V_{had}) and the two additional forward jets which characterize the VBS process, which may be called as the "VBS tagging" jets. The reconstruction of the V_{had} candidate is complicated by the fact that if the V_{had} is highly boosted, the product decays become tightly collimated and thus the two jets begin to merge, resulting in $V \to$ jj reconstruction inefficiency at high $p_T(V_{\text{had}})$, above 300 GeV or so. In order to recover these V_{had} at high p_T, we also attempt to reconstruct the V_{had} as a single large-radius jet. The advantage of the large-radius jet reconstruction at high $p_T(V_{\text{had}})$ is shown in Appendix D. As a result, this analysis has two different event selections, a *resolved* event selection, where the V_{had} candidate is reconstructed as two small-R jets, and a *merged* event selection, where the V_{had} candidate is reconstructed as a single large-R jet. In addition, for both the resolved and merged event selection, two levels of cuts are defined: a looser set of cuts, called the "loose VBS region", and a tighter set of cuts which defines the "optimized signal region." The various sets of cuts are summarized in Table 5, and are described in more detail in the following sections.

6.4 Resolved jet selection

We require at least four AntiKt4 jets in the event. The strategy for reconstructing the event is to first determine which jets came from V_{had}, and then to choose the tagging jets from the remaining jets.

All jet-pair combinations are looked at, and the jet-pair with m_{jj} closest to the W-mass is chosen to form the V_{had}-candidate. The exception is if two or more jet-pairs have m_{jj} within 15 GeV of the W-mass; in this case, whichever one of these jet pairs has the highest-p_T jets is chosen. Then, once the V_{had}-jets have been chosen, the remaining jets are looked at, and the pair with the largest m_{jj} is chosen as the tagging jets [4].

After this jet-selection procedure has been applied, an additional cut is made: the two jets selected to form the V_{had} candidate must have $64 < m_{\text{jj}} < 96\text{GeV}$; if not, the event is rejected.

A study was done to see how often this procedure assigns the correct jets to the V_{had} candidate. Signal MC WV events (with $\alpha_4 = 0.3$, $\alpha_5 = 0$) were studied, requiring that the truth-level quarks be within the detector acceptance, and that the "tagging" quarks have $m(qq) > 500\text{GeV}$. Truth-level cuts of $p_T(\ell) > 30\text{GeV}$ and $E_T^{missing} > 30\text{GeV}$ were also applied. The results of this study are shown in Tables 6 and 7. The correct jets are assigned to the V_{had} candidate in 75-90% of cases, depending on how exactly this percentage is defined; different definitions of this percentage are explained in the captions of Tables 6 and 7. For signal events with correctly-assigned jets, the $64 < m_{\text{jj}} < 96\text{GeV}$ requirement removes about 5-7% of events.

6.5 Merged (Large-R jet) selection

For the large-R jets we are using the Cambridge-Aachen split-filtered jets defined in Section 5.3. In case there are multiple large-R jets satisfying these criteria, the one with $m(\text{J})$ closest to the PDG value of the W mass is chosen as the V_{had}-jet candidate. We require at least two AntiKt4 jets and at least one large-R jet. We will denote a large-R jet with an uppercase J. The two tagging jets are chosen from among the AntiKt4 jets that are well separated from the V_{had}-jet candidate: $\Delta R(\text{j}, \text{J}) \geq 1.2$. If there are more than two

[4] The possibility of choosing the tagging jets based on highest $|\Delta\eta(\text{j}, \text{j})|$ was also investigated, both for the resolved jet selection and for the merged jet selection. Both methods of selecting the tagging jets (largest m_{jj}, largest $|\Delta\eta(\text{j}, \text{j})|$) gave nearly identical expected performance in terms of aQGC sensitivity.

AntiKt4 jets satisfying this criterion, then the pair with the maximum m_{jj} are chosen as the tagging jets.

After this jet-selection procedure has been applied, an additional cut is made: the groomed mass of the large-R jet must be in the range $64 < m(\mathrm{J}) < 96$ GeV; if not, the event is rejected.

6.6 *b*-tag veto

One of the largest backgrounds in this analysis is $t\bar{t}$. Top-quark (anti-top quark) decays into a W^+ (W^-) and a b-quark (anti-b quark) before hadronization. A b-jet coming from the hadronization of the b-quark is characterized by a displaced vertex due to comparatively longer life-time of b-quarks. In order to remove most of the $t\bar{t}$ events, we apply a *b*-tag veto. We use the MV1 *b*-tagging algorithm, with a working point designed to be 85% efficient for *b*-jets. This working point gives a light-jet rejection factor of about 10. Any AntiKt4 jet that has $|\eta| < 2.5$ and is *b*-tagged using this MV1 working point is referred to as a "b-tagged" jet.

For the resolved selection, if any AntiKt4 jets (other than the V_{had}-jets) are b-tagged jets, then the event is rejected. In addition, if *both* of the V_{had}-jets are b-tagged jets, then the event is rejected. The reason that the event is not rejected if only a single V_{had}-jet is b-tagged, is so that $W \to cs$ signal events are not rejected when a *c*-jet is misidentified as a *b*-jet.

For the merged selection, if any AntiKt4 jet satisifying $\Delta R(\mathrm{j}, V_{\mathrm{had}}) > 0.4$ is a b-tagged jet, then the event is rejected.

6.7 Loose VBS region

We define a "loose" VBS selection, which includes all the already-mentioned cuts, plus the invariant mass of the tagging jets must satisfy $m_{\mathrm{jj,tag}} > 500$GeV. This selection gives a VBS-like phasespace, but still contains a large number of events, which is useful for data-MC comparisons. However, the final selection used for placing aQGC limits uses a tighter set of cuts, which will be discussed next.

6.8 Kinematic variable definitions and optimized signal regions

This analysis involves $E_T^{missing}$ from W-boson decaying into neutrino. Because there is only one neutrino in the final state, the z-component of the neutrino momentum may be computed by constraining the invariant mass of the $(\ell\nu)$ candidate to be equal to the true (PDG) W-mass. If the resulting quadratic equation has two real solutions, the solution with the smaller absolute value is chosen. If the quadratic equation has complex solutions (i.e., the discriminant is negative), the discriminant is set to zero. Once all four components of neutrino 4-momenta is known, variables like mass of the di-boson system, $m(WV)$, where W is the leptonically decaying boson and V is the hadronically decaying boson, can be easily computed. Another variable of interest is the transverse mass of the di-boson system defined as,

$$m_{\mathrm{T}}(WV) = \sqrt{(E_T(W_{\mathrm{lep}}) + E_T(V_{\mathrm{had}}))^2 - (p_x(W_{\mathrm{lep}}) + p_x(V_{\mathrm{had}}))^2 - (p_y(W_{\mathrm{lep}}) + p_y(V_{\mathrm{had}}))^2} \tag{49}$$

where E_T are the transverse energies of the reconstructed vector bosons, and p_x, p_y are the x and y-components of their momentum.

The *boson centrality*, ζ_V, is defined as

$$\zeta_V = min\{\Delta\eta_-, \Delta\eta_+\}\,, \tag{50}$$

where

$$\Delta\eta_- = min\{\eta(V_{\mathrm{had}}), \eta(W_{\mathrm{lep}})\} - min\{\eta_{\mathrm{j}_{t1}}, \eta_{\mathrm{j}_{t2}}\}\,, \tag{51}$$

$$\Delta\eta_+ = max\{\eta_{\mathrm{j}_{t1}}, \eta_{\mathrm{j}_{t2}}\} - max\{\eta(V_{\mathrm{had}}), \eta(W_{\mathrm{lep}})\}\,. \tag{52}$$

Here, j_{t1} and j_{t2} are the two tagging jets. The variable ζ_V is a topological variable that tends toward large positive values when the tagging jets have large separation in η and both boson candidates are in the pseudo-rapidity gap between the two tagging jets.

The variable $\cos\left(\theta^*_{\mathrm{j}}\right)$ is only used in the resolved channel, and is defined as $\cos(\Delta\theta(\mathrm{j}, V_{\mathrm{had}}))$, where j is one of the jets from the V_{had} candidate, and the j direction is measured in the rest frame of the V_{had} and the V_{had} direction is measured in the WV rest frame. The V_{had}-jet used in this calculation is chosen to be whichever jet has a smaller $\Delta\theta(\mathrm{j}, V_{\mathrm{had}})$, so that $\cos\left(\theta^*_{\mathrm{j}}\right) >= 0$ by definition. This variable is correlated with the polarization of the vector

boson. At high $p_T(V_{\text{had}})$, where the aQGC sensitivity is best, background events tend to have larger values of $\cos\left(\theta^*_{\text{j}}\right)$ than for aQGC-signal events.

The p_T-balance for the event, A_{full}, is defined as:

$$A_{\text{full}} = \frac{|\vec{p_T}(V_{\text{had}}) + \vec{p_T}(W_{\text{lep}}) + \vec{p_T}(\text{j}_{t1}) + \vec{p_T}(\text{j}_{t2})|}{|p_T(V_{\text{had}})| + |p_T(W_{\text{lep}})| + |p_T(\text{j}_{t1})| + |p_T(\text{j}_{t2})|}\,. \tag{53}$$

The p_T-balance for the diboson system, A_{WV}, is defined as:

$$A_{WV} = \frac{|\vec{p_T}(V_{\text{had}}) + \vec{p_T}(W_{\text{lep}})|}{|p_T(V_{\text{had}})| + |p_T(W_{\text{lep}})|}\,. \tag{54}$$

This variable is closer to zero for aQGC signal events than for the background.

In order to obtain the final aQGC limits, a tighter event selection is used, which was optimized for the best aQGC limits (see Sec. 9.2). These cuts are summarized in Table 5. This will be referred to as the "optimized signal" selection. In this document, we will refer to the loose VBS regions and optimized signal regions collectively as "signal regions" and will abbreviate them "loose VBS SR" and "optimized SR" when referring to the resolved selection, and "loose VBS SR_fatOnly" and "optimized SR_fatOnly" when referring to the merged selection.

The optimized signal selection includes a cut on the p_T of W_{lep}: $\text{p}_\text{T}(W_{\text{lep}}) >$ 150GeV. In addition to increasing aQGC sensitivity, this cut is useful because ATLAS does not have Sherpa W + jets modeling systematics MC samples for low $\text{p}_\text{T}(W_{\text{lep}})$ values.

In addition to the $\text{p}_\text{T}(W_{\text{lep}})$ cut, a cut optimization study was done to maximize aQGC sensitivity; this study is described later in Sec. 9.2. Based on that study, additional cuts on the *boson centrality*, $m_{\text{jj,tag}}$, $\cos\left(\theta^*_{\text{j}}\right)$, and A_{WV} are applied.

6.9 Sample yields due to event selection

The analysis starts with a set of loose event selections. Different selection criteria are imposed to improve signal over background ratio. In this section the yields of different samples are presented as the previously-mentioned event selection criteria, also known as "cuts", are imposed. This way of presenting yields is known as a cutflow. Details on how the various backgrounds are estimated and validated are given in Sections 3 and 7 respectively.

The cutflows for the optimized selection are given in Tables 8-15 for the electron and muon channels, separated by charge. The tables are shown separately for the resolved and merged selections. The initial cuts are common between the resolved and merged selections and the resolved and merged cutflows share some events. It's only at the very end (during the selection labeled "!(resolved)") that events are removed from the merged selection if they also passed the resolved selection so that the final yields for the two selections are devoid of any overlap. At the "Preselection" stage events are selected with exactly 1 lepton and at least two small-R jets. At the "resolved jet select." stage, events require at least 4 small-R jets, and for the "merged jet select.", events require at least two small-R jets and at least 1 large-R jet. The "loose $m_{\mathrm{jj,tag}}$ cut" applies a selection of $m_{\mathrm{jj,tag}} > 500\mathrm{GeV}$, and this point in the cutflow corresponds to the "loose VBS selection" except that it doesn't contain a b-jet veto or requirement on the $m(V_{\mathrm{had}})$ mass yet. The "tight $m_{\mathrm{jj,tag}}$ cut" applies the optimized $m_{\mathrm{jj,tag}}$ selection mentioned in Section 9.4.

Table 4: List of ATLAS packages used in this analysis, and the version numbers used.

Package Name	Version
MissingETUtility	01-03-03
METAnalysisCommon	00-00-03
METSystematics	00-00-04
JetUncertainties	00-08-25
ApplyJetCalibration	00-03-40
JetResolution	02-00-02
ApplyJetResolutionSmearing	00-01-02
JetSelectorTools	00-01-01
MuonSelectorTools	00-01-13
MuonEfficiencyCorrections	02-01-20
MuonMomentumCorrections	00-09-29
TrigMuonEfficiency	00-02-54
MuonIsolationCorrection	01-01
egammaAnalysisUtils	00-04-56
ElectronEfficiencyCorrection	00-00-50
PATCore	00-00-12
ElectronPhotonSelectorTools	00-00-56
egammaEvent	04-00-07
PileupReweighting	00-02-12
TileTripReader	00-00-19-01
BCHCleaningTool	00-00-10
GoodRunsLists	00-01-09
ObjectSelectorCore	00-00-17
CalibrationDataInterface	00-03-06

	Resolved		*Merged*	
Name of cut	*Loose VBS*	*Optimized Signal*	*Loose VBS*	*Optimized Signal*
lepton p_T	$p_T(\ell)$>30 GeV			
jet select.	$\geq$ 4 small-R jets, p_T(j) > 30GeV		$\geq$ 2 small-R jets, p_T(j) > 30GeV $\geq$ 1 large-R jet, p_T(J) > 200GeV	
$E_T^{missing}$	$E_T^{missing}$ > 30 GeV			
Loose $m_{\text{jj,tag}}$ cut	$m_{\text{jj,tag}}$> 500 GeV			
$p_T Wlep$	—	$p_T Wlep$ > 150GeV	—	$p_T Wlep$ > 150GeV
Boson centrality	—	$\zeta_V > 0.9$	—	$\zeta_V > 0.9$
p_T balance	—			$A_{WV} < 0.30$
$\cos\left(\theta^*_{\text{j}}\right)$	—	$\cos\left(\theta^*_{\text{j}}\right) < 0.50$	—	
Tight $m_{\text{jj,tag}}$ cut	—	$m_{\text{jj,tag}}$ > 900GeV	—	$m_{\text{jj,tag}}$ > 900GeV
b-tag veto	b-jet veto applied (see text)		b-jet veto applied (see text)	
$m(V_{\text{had}})$ window	$64 < m_{\text{jj}} < 96$GeV		$64 < m$(J) < 96GeV	
!(resolved)	—		!(loose VBS resolved)	!(optimized signal resolved)

Table 5: Summary of selection criteria for signal regions and loose VBS regions. Variables are defined in the text.

	Correct V_{had}-jet assigment?		
Truth-level Cuts	Yes	No	N.A.
Base cuts	0.76	0.16	0.08
Base cuts and $p_T(V \to qq') > 200$GeV	0.83	0.14	0.03

Table 6: The fraction of the time that the correct jets are assigned to the V_{had}-candidate (i.e. both of the jets assigned to the V_{had}-candidate are within $\Delta R = 0.4$ of a truth-quark from the $V \to qq'$ decay). The "N.A." column refers to events where at least one of the quarks from the $V \to qq'$ decay does not have a reconstructed jet matched to it, and so by definition it is impossible to assign the correct jets in these cases.

Truth-level Cuts	Correct V_{had}-jet assigment? Yes	No	Fraction of correctly-assigned events in m_{jj} window
Base cuts	0.85	0.15	0.93
Base cuts and $p_T(V \to qq') > 200$GeV	0.89	0.11	0.95

Table 7: The fraction of the time that the correct jets are assigned to the V_{had}-candidate (i.e. both of the jets assigned to the V_{had}-candidate are within $\Delta R = 0.4$ of a truth-quark from the $V \to qq'$ decay). Unlike Table 6, in this table, we are only considering events where each of the matrix-element-level quarks (the $V \to qq'$ quarks and the "tagging" quarks) has a reconstructed jet matched to it (within $\Delta R = 0.4$). The last column lists the fraction of the events with a correct V_{had}-jet assignment that have a reconstructed m_{jj} in the range $64 < m_{\text{jj}} < 96$GeV.

Table 8: Cutflow for the μ^+ channel , for the resolved selection. Values are expected number of events for $20.3 \pm 0.6 fb^{-1}$. Uncertainties are statistical only. Data-driven SF is used to scale W + jets on all the cutflows.

Selection	WV(0,0)	WV(0.1,0)	ZV(0,0)	ZV(0.1,0)	Ttbar	SingleTop	Diboson	Z+jets	W+jets	BG	Data
Preselection	797 ± 6	874 ± 7	133 ± 2	154 ± 3	145 140 ± 79	24 476 ± 25	19 816 ± 58	35 484 ± 310	400 080 ± 638	624 995 ± 717	763878
$p_T(\ell) > 30$GeV	706 ± 6	784 ± 6	118 ± 2	139 ± 3	130 546 ± 75	21 673 ± 24	17 613 ± 55	31 078 ± 275	351 969 ± 585	552 879 ± 653	624917
Res. jet select.	431 ± 5	486 ± 5	79 ± 2	94 ± 2	74 926 ± 56	8344 ± 15	4805 ± 30	6281 ± 103	75 822 ± 241	170 178 ± 270	179836
$E_T^{missing} > 30$GeV	333 ± 4	383 ± 4	62 ± 2	77 ± 2	58 943 ± 50	6474 ± 13	3627 ± 26	3428 ± 72	57 323 ± 205	129 794 ± 225	134875
loose $m_{\mathrm{jj,tag}}$	78 ± 2	116 ± 2	22 ± 1	30 ± 1	6768 ± 16	1305 ± 6	594 ± 11	567 ± 30	9558 ± 80	18 792 ± 88	18938
b-tag veto	41 ± 1	72 ± 2	10 ± 1	14 ± 1	1423 ± 8	395 ± 3	429 ± 9	404 ± 27	7051 ± 70	9701 ± 76	10097
$m(V_{\mathrm{had}})$ window	30 ± 1	56 ± 2	7 ± 1	9 ± 1	935 ± 6	196 ± 2	232 ± 7	200 ± 18	3657 ± 52	5220 ± 56	5193
Optimized SR:											
$p_T(W_{\mathrm{lep}})$	9.7 ± 0.7	31.5 ± 1.3	2.1 ± 0.3	4.7 ± 0.5	244.1 ± 3.0	36.5 ± 1.0	74.6 ± 3.7	32.3 ± 1.9	853.1 ± 11.7	1240.7 ± 12.8	1190
Centrality	3.9 ± 0.4	18.8 ± 1.0	0.5 ± 0.1	2.6 ± 0.3	96.1 ± 1.9	15.5 ± 0.6	15.9 ± 1.7	6.9 ± 0.9	177.9 ± 5.5	312.4 ± 6.1	282
$\cos(\theta_{\mathrm{j}}^*)$	2.7 ± 0.4	12.5 ± 0.8	0.3 ± 0.1	1.8 ± 0.3	66.0 ± 1.6	9.5 ± 0.5	10.2 ± 1.3	4.5 ± 0.7	107.9 ± 4.3	198.1 ± 4.8	188
tight $m_{\mathrm{jj,tag}}$	1.5 ± 0.3	8.1 ± 0.6	0.2 ± 0.1	1.1 ± 0.2	27.0 ± 1.0	4.5 ± 0.3	3.7 ± 0.8	2.1 ± 0.5	45.5 ± 2.8	82.9 ± 3.2	73

Table 9: Cutflow for the μ^+ channel, for the merged selection. Values are expected number of events for $20.3 \pm 0.6 fb^{-1}$. Uncertainties are statistical only.

Selection	WV(0,0)	WV(0.1,0)	ZV(0,0)	ZV(0.1,0)	Ttbar	SingleTop	Diboson	Z+jets	W+jets	BG	Data
Preselection	797 ± 6	874 ± 7	133 ± 2	154 ± 3	145 140 ± 79	24 476 ± 25	19 816 ± 58	35 484 ± 310	400 080 ± 638	624 995 ± 717	763878
$p_T(\ell) > 30$GeV	706 ± 6	784 ± 6	118 ± 2	139 ± 3	130 546 ± 75	21 673 ± 24	17 613 ± 55	31 078 ± 275	351 969 ± 585	552 879 ± 653	624917
Merged jet select.	46 ± 1	81 ± 2	10 ± 1	20 ± 1	6159 ± 15	554 ± 4	605 ± 11	427 ± 14	6899 ± 54	14 643 ± 59	13816
$E_T^{missing} > 30$GeV	39 ± 1	73 ± 2	9 ± 1	18 ± 1	5283 ± 14	479 ± 4	503 ± 10	279 ± 10	5813 ± 48	12 359 ± 52	11678
loose $m_{\mathrm{jj,tag}}$	13 ± 1	38 ± 1	4 ± 0	9 ± 1	876 ± 6	94 ± 2	85 ± 4	50 ± 4	1068 ± 21	2173 ± 22	2133
b-tag veto	7 ± 1	27 ± 1	1 ± 0	5 ± 0	112 ± 2	18 ± 1	54 ± 3	31 ± 3	680 ± 17	895 ± 18	851
$m(V_{\mathrm{had}})$ window	4 ± 0	20 ± 1	1 ± 0	4 ± 0	50 ± 1	8 ± 0	22 ± 2	11 ± 2	238 ± 10	329 ± 11	326
!(loose VBS res.) $\star$	0.7 ± 0.2	4.9 ± 0.5	0.4 ± 0.1	1.9 ± 0.3	12.3 ± 0.7	3.1 ± 0.3	8.2 ± 1.1	5.2 ± 1.6	87.5 ± 5.7	116.2 ± 6.1	142
Optimized SR:											
$p_T(W_{\mathrm{lep}})$	1.9 ± 0.3	17.2 ± 0.9	0.5 ± 0.1	2.9 ± 0.4	23.2 ± 0.9	4.1 ± 0.3	11.4 ± 1.4	3.2 ± 0.5	97.1 ± 3.6	138.9 ± 4.0	171
Centrality	1.1 ± 0.2	13.6 ± 0.8	0.1 ± 0.1	2.2 ± 0.3	13.1 ± 0.7	2.6 ± 0.2	3.4 ± 0.7	1.1 ± 0.3	32.4 ± 2.2	52.7 ± 2.4	66
p_T balance	0.6 ± 0.2	11.7 ± 0.8	0.1 ± 0.1	1.6 ± 0.3	8.9 ± 0.6	2.0 ± 0.2	2.0 ± 0.5	0.7 ± 0.3	19.7 ± 1.6	33.3 ± 1.8	43
tight $m_{\mathrm{jj,tag}}$	0.3 ± 0.1	7.7 ± 0.6	0.1 ± 0.1	1.0 ± 0.2	3.6 ± 0.4	1.0 ± 0.1	0.6 ± 0.3	0.1 ± 0.1	7.7 ± 0.9	13.0 ± 1.0	12
!(optim. SR resolved)	0.2 ± 0.1	3.4 ± 0.4	0.1 ± 0.1	0.6 ± 0.2	1.8 ± 0.3	0.7 ± 0.1	0.3 ± 0.2	0.0 ± 0.0	6.0 ± 0.8	8.8 ± 0.9	6

Table 10: Cutflow for the μ^- channel, for the resolved selection. Values are expected number of events for $20.3 \pm 0.6 fb^{-1}$. Uncertainties are statistical only.

Selection	WV(0,0)	WV(0.1,0)	ZV(0,0)	ZV(0.1,0)	Ttbar	SingleTop	Diboson	Z+jets	W+jets	BG	Data
Preselection	761 ± 6	802 ± 6	72 ± 2	83 ± 2	145 234 ± 79	16 915 ± 22	17 171 ± 54	34 606 ± 318	283 096 ± 531	497 021 ± 626	615283
$p_T(\ell) > 30$GeV	682 ± 6	724 ± 6	64 ± 2	75 ± 2	130 646 ± 75	15 129 ± 21	15 689 ± 52	30 242 ± 283	258 392 ± 497	450 097 ± 579	517159
Res. jet select.	417 ± 4	440 ± 5	42 ± 1	50 ± 2	74 984 ± 56	5835 ± 13	4217 ± 28	6193 ± 111	52 270 ± 200	143 500 ± 238	153964
$E_T^{missing} > 30$GeV	311 ± 4	335 ± 4	31 ± 1	39 ± 1	59 039 ± 50	4524 ± 12	2988 ± 24	3377 ± 74	37 265 ± 167	107 193 ± 191	112517
loose $m_{\mathrm{jj,tag}}$	66 ± 2	83 ± 2	11 ± 1	15 ± 1	6735 ± 16	733 ± 4	455 ± 9	501 ± 23	5694 ± 67	14 118 ± 74	14585
b-tag veto	32 ± 1	44 ± 1	5 ± 0	7 ± 1	1428 ± 8	217 ± 2	331 ± 8	378 ± 22	4247 ± 62	6601 ± 67	6815
$m(V_{\mathrm{had}})$ window	24 ± 1	34 ± 1	3 ± 0	5 ± 0	934 ± 6	114 ± 2	192 ± 6	187 ± 14	2119 ± 39	3546 ± 43	3627
Optimized SR:											
$p_T(W_{\mathrm{lep}})$	8.0 ± 0.6	16.1 ± 0.9	1.1 ± 0.2	2.4 ± 0.3	248.6 ± 3.1	24.0 ± 0.8	64.0 ± 3.4	33.8 ± 2.1	466.6 ± 8.9	837.0 ± 10.2	830
Centrality	2.6 ± 0.3	8.1 ± 0.6	0.3 ± 0.1	1.0 ± 0.2	99.4 ± 2.0	9.7 ± 0.5	14.2 ± 1.6	6.3 ± 0.8	103.9 ± 4.4	233.4 ± 5.2	215
$\cos(\theta_{\mathrm{j}}^*)$	1.5 ± 0.3	6.3 ± 0.6	0.2 ± 0.1	0.7 ± 0.2	67.1 ± 1.6	6.5 ± 0.4	9.9 ± 1.4	3.5 ± 0.6	66.8 ± 3.8	153.7 ± 4.4	132
tight $m_{\mathrm{jj,tag}}$	0.9 ± 0.2	3.9 ± 0.4	0.2 ± 0.1	0.5 ± 0.1	27.6 ± 1.0	2.6 ± 0.3	5.3 ± 1.0	1.2 ± 0.3	23.0 ± 2.0	59.7 ± 2.5	57

Table 11: Cutflow for the μ^- channel, for the merged selection. Values are expected number of events for $20.3 \pm 0.6 fb^{-1}$. Uncertainties are statistical only.

Selection	WV(0,0)	WV(0.1,0)	ZV(0,0)	ZV(0.1,0)	Ttbar	SingleTop	Diboson	Z+jets	W+jets	BG	Data
Preselection	761 ± 6	802 ± 6	72 ± 2	83 ± 2	145 234 ± 79	16 915 ± 22	17 171 ± 54	34 606 ± 318	283 096 ± 531	497 021 ± 626	615283
$p_T(\ell) > 30$GeV	682 ± 6	724 ± 6	64 ± 2	75 ± 2	130 646 ± 75	15 129 ± 21	15 689 ± 52	30 242 ± 283	258 392 ± 497	450 097 ± 579	517159
Merged jet select.	43 ± 1	58 ± 2	5 ± 0	10 ± 1	6034 ± 15	457 ± 4	506 ± 10	417 ± 12	4477 ± 44	11 891 ± 49	11598
$E_T^{missing} > 30$GeV	34 ± 1	50 ± 2	4 ± 0	8 ± 1	5196 ± 14	397 ± 4	397 ± 9	277 ± 11	3557 ± 37	9824 ± 42	9511
loose $m_{\mathrm{jj,tag}}$	9 ± 1	21 ± 1	1 ± 0	4 ± 0	854 ± 5	71 ± 1	60 ± 3	54 ± 4	615 ± 16	1655 ± 18	1619
b-tag veto	3 ± 0	13 ± 1	1 ± 0	2 ± 0	109 ± 2	11 ± 1	37 ± 3	32 ± 3	382 ± 13	571 ± 13	557
$m(V_{\mathrm{had}})$ window	2 ± 0	9 ± 1	0 ± 0	2 ± 0	48 ± 1	5 ± 0	16 ± 2	15 ± 3	136 ± 7	220 ± 8	215
!(loose VBS res.) $\star$	0.6 ± 0.2	2.8 ± 0.4	0.2 ± 0.1	0.6 ± 0.2	12.0 ± 0.6	1.7 ± 0.2	5.2 ± 0.9	5.3 ± 1.6	50.6 ± 4.2	74.8 ± 4.7	81
Optimized SR:											
$p_T(W_{\mathrm{lep}})$	0.8 ± 0.2	6.8 ± 0.6	0.1 ± 0.1	1.0 ± 0.2	23.2 ± 0.9	2.5 ± 0.3	8.0 ± 1.2	3.7 ± 0.6	59.9 ± 2.9	97.3 ± 3.4	95
Centrality	0.3 ± 0.1	5.0 ± 0.5	0.1 ± 0.1	0.9 ± 0.2	12.7 ± 0.7	1.5 ± 0.2	3.2 ± 0.8	2.1 ± 0.4	22.9 ± 2.0	42.4 ± 2.3	37
p_T balance	0.2 ± 0.1	4.0 ± 0.4	0.0 ± 0.0	0.8 ± 0.2	9.1 ± 0.6	1.1 ± 0.2	2.4 ± 0.6	1.3 ± 0.3	17.5 ± 1.8	31.3 ± 2.0	21
tight $m_{\mathrm{jj,tag}}$	0.2 ± 0.1	2.1 ± 0.3	0.0 ± 0.0	0.4 ± 0.1	3.4 ± 0.4	0.4 ± 0.1	0.4 ± 0.3	0.3 ± 0.2	4.9 ± 0.7	9.4 ± 0.9	7
!(optim. SR resolved)	0.0 ± 0.0	1.4 ± 0.3	0.0 ± 0.0	0.2 ± 0.1	1.5 ± 0.2	0.2 ± 0.1	0.4 ± 0.3	0.1 ± 0.1	3.9 ± 0.6	6.0 ± 0.8	5

Table 12: Cutflow for the e^+ channel, for the resolved selection. Values are expected number of events for $20.3 \pm 0.6 fb^{-1}$. Uncertainties are statistical only.

Selection	WV(0,0)	WV(0.1,0)	ZV(0,0)	ZV(0.1,0)	Ttbar	SingleTop	Diboson	Z+jets	W+jets	BG	Data
Preselection	830 ± 6	978 ± 7	137 ± 2	161 ± 3	152 572 ± 81	26 158 ± 26	23 305 ± 61	97 866 ± 577	404 987 ± 618	704 888 ± 852	1018218
$p_T(\ell) > 30$GeV	753 ± 6	896 ± 7	125 ± 2	149 ± 3	139 635 ± 77	23 624 ± 25	21 248 ± 58	88 625 ± 533	366 037 ± 573	639 168 ± 790	891965
Res. jet select.	457 ± 5	550 ± 5	84 ± 2	102 ± 2	78 016 ± 57	8590 ± 15	5362 ± 30	19 352 ± 219	71 325 ± 230	182 645 ± 325	225851
$E_T^{missing} > 30$GeV	347 ± 4	427 ± 5	66 ± 2	81 ± 2	61 146 ± 51	6643 ± 13	3751 ± 26	7532 ± 135	53 317 ± 194	132 388 ± 243	150654
loose $m_{\mathrm{jj,tag}}$	81 ± 2	133 ± 3	25 ± 1	33 ± 1	7097 ± 17	1360 ± 6	660 ± 11	1338 ± 66	9019 ± 78	19 474 ± 104	21246
b-tag veto	45 ± 1	82 ± 2	11 ± 1	17 ± 1	1476 ± 8	405 ± 3	476 ± 9	1013 ± 56	6657 ± 70	10 028 ± 90	11545
$m(V_{\mathrm{had}})$ window	32 ± 1	64 ± 2	7 ± 1	11 ± 1	967 ± 6	198 ± 2	269 ± 7	521 ± 43	3347 ± 49	5303 ± 66	5919
Optimized SR:											
$p_T(W_{\mathrm{lep}})$	12.1 ± 0.8	38.2 ± 1.4	2.5 ± 0.3	6.9 ± 0.6	279.3 ± 3.2	41.1 ± 1.0	99.4 ± 4.3	44.6 ± 2.1	873.8 ± 11.4	1338.2 ± 12.8	1336
Centrality	4.1 ± 0.4	22.8 ± 1.1	0.5 ± 0.2	3.4 ± 0.4	112.6 ± 2.1	16.9 ± 0.6	22.1 ± 2.0	9.3 ± 1.0	191.2 ± 5.4	352.1 ± 6.2	362
$\cos(\theta^*_{\mathrm{j}})$	2.6 ± 0.3	14.9 ± 0.9	0.3 ± 0.1	2.3 ± 0.3	76.1 ± 1.7	10.8 ± 0.5	12.6 ± 1.5	4.9 ± 0.7	115.6 ± 4.2	220.1 ± 4.9	214
tight $m_{\mathrm{jj,tag}}$	1.7 ± 0.3	10.4 ± 0.7	0.2 ± 0.1	1.4 ± 0.3	31.7 ± 1.1	5.6 ± 0.4	4.9 ± 1.0	2.4 ± 0.5	46.7 ± 2.8	91.2 ± 3.2	100

Table 13: Cutflow for the e^+ channel, for the merged selection. Values are expected number of events for $20.3 \pm 0.6 fb^{-1}$. Uncertainties are statistical only.

Selection	WV(0,0)	WV(0.1,0)	ZV(0,0)	ZV(0.1,0)	Ttbar	SingleTop	Diboson	Z+jets	W+jets	BG	Data
Preselection	830 ± 6	978 ± 7	137 ± 2	161 ± 3	152 572 ± 81	26 158 ± 26	23 305 ± 61	97 866 ± 577	404 987 ± 618	704 888 ± 852	1018218
$p_T(\ell) > 30$GeV	753 ± 6	896 ± 7	125 ± 2	149 ± 3	139 635 ± 77	23 624 ± 25	21 248 ± 58	88 625 ± 533	366 037 ± 573	639 168 ± 790	891965
Merged jet select.	50 ± 2	97 ± 2	11 ± 1	22 ± 1	6796 ± 16	619 ± 4	685 ± 11	954 ± 27	6797 ± 52	15 851 ± 61	17042
$E_T^{missing} > 30$GeV	43 ± 1	86 ± 2	10 ± 1	20 ± 1	5825 ± 15	538 ± 4	566 ± 10	501 ± 19	5720 ± 45	13 150 ± 52	13536
loose $m_{\mathrm{jj,tag}}$	13 ± 1	45 ± 2	4 ± 0	10 ± 1	956 ± 6	106 ± 2	103 ± 4	93 ± 7	1044 ± 20	2303 ± 23	2349
b-tag veto	7 ± 1	30 ± 1	2 ± 0	7 ± 1	123 ± 2	21 ± 1	65 ± 3	55 ± 7	655 ± 16	919 ± 18	980
$m(V_{\mathrm{had}})$ window	5 ± 0	23 ± 1	1 ± 0	5 ± 0	56 ± 1	9 ± 0	26 ± 2	16 ± 2	220 ± 9	326 ± 9	351
!(loose VBS res.) $\star$	1.0 ± 0.2	7.3 ± 0.6	0.4 ± 0.1	2.4 ± 0.3	13.3 ± 0.7	3.4 ± 0.3	9.6 ± 1.3	6.1 ± 1.0	81.6 ± 5.0	114.2 ± 5.4	140
Optimized SR:											
$p_T(W_{\mathrm{lep}})$	2.5 ± 0.3	20.7 ± 1.0	0.3 ± 0.1	4.5 ± 0.5	28.2 ± 1.0	5.3 ± 0.4	15.0 ± 1.7	4.5 ± 0.6	99.7 ± 3.5	152.7 ± 4.1	177
Centrality	1.1 ± 0.2	16.9 ± 0.9	0.1 ± 0.1	3.5 ± 0.4	16.8 ± 0.8	3.6 ± 0.3	6.6 ± 1.1	1.5 ± 0.4	34.6 ± 1.8	63.1 ± 2.3	80
p_T balance	0.6 ± 0.2	13.8 ± 0.8	0.0 ± 0.0	2.8 ± 0.4	11.3 ± 0.7	2.7 ± 0.3	3.6 ± 0.8	1.5 ± 0.4	23.7 ± 1.6	42.8 ± 1.9	50
tight $m_{\mathrm{jj,tag}}$	0.4 ± 0.1	9.7 ± 0.7	0.0 ± 0.0	1.8 ± 0.3	4.3 ± 0.4	1.2 ± 0.2	0.8 ± 0.4	0.5 ± 0.2	8.6 ± 0.9	15.4 ± 1.1	16
!(optim. SR resolved)	0.1 ± 0.1	5.6 ± 0.5	0.0 ± 0.0	1.2 ± 0.2	2.1 ± 0.3	0.8 ± 0.1	0.6 ± 0.3	0.3 ± 0.2	6.6 ± 0.9	10.4 ± 1.0	15

Table 14: Cutflow for the e^- channel, for the resolved selection. Values are expected number of events for $20.3 \pm 0.6 fb^{-1}$. Uncertainties are statistical only.

Selection	WV(0,0)	WV(0.1,0)	ZV(0,0)	ZV(0.1,0)	Ttbar	SingleTop	Diboson	Z+jets	W+jets	BG	Data
Preselection	840 ± 6	883 ± 7	82 ± 2	94 ± 2	153 003 ± 81	18 381 ± 23	20 892 ± 58	96 131 ± 581	300 347 ± 526	588 753 ± 790	882755
$p_T(\ell) > 30$GeV	765 ± 6	809 ± 6	76 ± 2	87 ± 2	140 036 ± 77	16 750 ± 22	19 398 ± 56	87 530 ± 542	278 964 ± 497	542 679 ± 742	781075
Res. jet select.	461 ± 5	494 ± 5	50 ± 1	57 ± 2	78 231 ± 57	6138 ± 14	4914 ± 29	18 557 ± 200	51 309 ± 194	159 149 ± 286	201073
$E_T^{missing} > 30$GeV	342 ± 4	371 ± 4	36 ± 1	43 ± 1	61 350 ± 51	4742 ± 12	3236 ± 24	7134 ± 116	36 333 ± 162	112 795 ± 207	130500
loose $m_{\mathrm{jj,tag}}$	73 ± 2	93 ± 2	11 ± 1	17 ± 1	7109 ± 17	779 ± 5	507 ± 9	1235 ± 50	5541 ± 64	15 170 ± 83	17346
b-tag veto	35 ± 1	50 ± 2	5 ± 0	9 ± 1	1489 ± 8	223 ± 2	365 ± 8	909 ± 43	4129 ± 57	7115 ± 73	8768
$m(V_{\mathrm{had}})$ window	25 ± 1	39 ± 1	4 ± 0	6 ± 1	974 ± 6	118 ± 2	214 ± 6	493 ± 35	2100 ± 43	3900 ± 56	4701
Optimized SR:											
$p_T(W_{\mathrm{lep}})$	8.4 ± 0.6	19.3 ± 1.0	1.3 ± 0.2	3.4 ± 0.4	289.9 ± 3.3	26.4 ± 0.9	70.0 ± 3.5	52.1 ± 4.2	520.3 ± 9.3	958.7 ± 11.3	1067
Centrality	2.9 ± 0.4	10.8 ± 0.7	0.4 ± 0.1	2.0 ± 0.3	117.6 ± 2.1	11.0 ± 0.6	14.6 ± 1.6	10.2 ± 1.2	115.0 ± 4.3	268.5 ± 5.2	324
$\cos(\theta_{\mathrm{j}}^*)$	1.9 ± 0.3	7.2 ± 0.6	0.3 ± 0.1	1.3 ± 0.2	80.7 ± 1.8	6.9 ± 0.4	10.2 ± 1.4	6.4 ± 1.0	70.3 ± 3.4	174.6 ± 4.2	218
tight $m_{\mathrm{jj,tag}}$	1.1 ± 0.2	3.9 ± 0.4	0.2 ± 0.1	0.9 ± 0.2	35.1 ± 1.2	2.9 ± 0.3	5.5 ± 1.0	2.2 ± 0.5	27.6 ± 1.9	73.3 ± 2.5	74

Table 15: Cutflow for e^- channel, for the merged selection. Values are expected number of events for $20.3 \pm 0.6 fb^{-1}$. Uncertainties are statistical only.

Selection	WV(0,0)	WV(0.1,0)	ZV(0,0)	ZV(0.1,0)	Ttbar	SingleTop	Diboson	Z+jets	W+jets	BG	Data
Preselection	840 ± 6	883 ± 7	82 ± 2	94 ± 2	153 003 ± 81	18 381 ± 23	20 892 ± 58	96 131 ± 581	300 347 ± 526	588 753 ± 790	882755
$p_T(\ell) > 30$GeV	765 ± 6	809 ± 6	76 ± 2	87 ± 2	140 036 ± 77	16 750 ± 22	19 398 ± 56	87 530 ± 542	278 964 ± 497	542 679 ± 742	781075
Merged jet select.	51 ± 2	69 ± 2	7 ± 1	11 ± 1	6683 ± 16	522 ± 4	590 ± 10	917 ± 24	4589 ± 43	13 300 ± 53	14775
$E_T^{missing} > 30$GeV	42 ± 1	60 ± 2	6 ± 0	9 ± 1	5751 ± 15	453 ± 4	454 ± 9	471 ± 15	3626 ± 37	10 755 ± 43	11402
loose $m_{\mathrm{jj,tag}}$	11 ± 1	24 ± 1	2 ± 0	6 ± 1	934 ± 6	80 ± 2	81 ± 4	84 ± 4	596 ± 15	1775 ± 17	1867
b-tag veto	5 ± 0	15 ± 1	1 ± 0	3 ± 0	119 ± 2	14 ± 1	51 ± 3	50 ± 3	382 ± 12	616 ± 13	655
$m(V_{\mathrm{had}})$ window	3 ± 0	11 ± 1	0 ± 0	2 ± 0	52 ± 1	6 ± 0	24 ± 2	18 ± 2	131 ± 7	232 ± 8	267
!(loose VBS res.) $\star$	0.6 ± 0.2	3.2 ± 0.4	0.2 ± 0.1	0.8 ± 0.2	12.0 ± 0.6	2.5 ± 0.3	9.2 ± 1.3	8.0 ± 1.7	55.2 ± 5.2	86.9 ± 5.6	111
Optimized SR:											
$p_T(W_{\mathrm{lep}})$	1.7 ± 0.3	8.9 ± 0.7	0.2 ± 0.1	1.9 ± 0.3	27.1 ± 1.0	3.9 ± 0.3	12.2 ± 1.5	5.7 ± 0.7	58.1 ± 3.1	107.1 ± 3.7	112
Centrality	0.7 ± 0.2	7.6 ± 0.6	0.1 ± 0.1	1.5 ± 0.3	15.8 ± 0.8	2.4 ± 0.3	4.0 ± 0.8	1.3 ± 0.4	20.4 ± 1.6	43.9 ± 2.0	43
p_T balance	0.5 ± 0.1	6.6 ± 0.6	0.1 ± 0.1	1.1 ± 0.2	10.2 ± 0.6	1.9 ± 0.2	1.7 ± 0.5	1.0 ± 0.3	13.8 ± 1.3	28.7 ± 1.6	28
tight $m_{\mathrm{jj,tag}}$	0.1 ± 0.1	3.8 ± 0.4	0.1 ± 0.1	0.7 ± 0.2	3.4 ± 0.4	0.8 ± 0.2	0.4 ± 0.2	0.2 ± 0.1	5.1 ± 0.9	9.9 ± 1.0	7
!(optim. SR resolved)	0.1 ± 0.1	2.3 ± 0.3	0.0 ± 0.0	0.4 ± 0.1	1.4 ± 0.2	0.5 ± 0.1	0.1 ± 0.1	0.2 ± 0.1	3.1 ± 0.6	5.3 ± 0.6	6

7 Signal and Background Modeling

7.1 Control regions

In addition to defining loose VBS and optimized signal regions (Sec. 6), we also define control regions to validate the modeling of various backgrounds. Control regions are defined for top-quark backgrounds (the control regions for the resolved and merged selections are called CR_Top and CR_TopFat, respectively) and for W + jets (CR_Wjet and CR_WjetFat).

Just as there are loose VBS regions and optimized signal regions, different versions of the background control regions can be defined, either by slightly modifying the loose VBS cuts (to create loose control regions), or by slightly modifying the optimized signal cuts (to create optimized control regions).

The definitions of these control regions are discussed below.

7.1.1 W+jets control regions

The W + jets control regions are defined exactly the same way as the signal regions, except the V_{had} candidates are selected from jets that *fail* the m_{jj} requirement of the signal region. Therefore, these are events that are in the m_{jj} sidebands outside of the W and Z masses.

For CR_Wjet, the V_{had} jets are chosen to be the pair of jets with m_{jj} closest to the W-mass, but with $[36 < m_{jj} < 64\text{GeV}]$ or $[m_{jj} > 96\text{GeV}]$.

For CR_WjetFat, the large-R jet representing the V_{had} candidate must have a groomed mass outside of the [64–96 GeV] window. If more than one large-R jet satisfy this requirement, then the one with a groomed mass closest to the world-average W-mass is chosen.

By these definitions, there is no overlap between the SR and CR_Wjet, or between SR_fatOnly and CR_WjetFat.

7.1.2 Top-quark control regions

The top-quark control regions are defined exactly the same way as the signal regions, except that the event selection requires the presence of b-jets, instead of vetoing on b-jets like in the signal regions.

In the resolved CR_Top, at least one of the following must be true:

- At least one of the non-V_{had}-jets must have $|\eta| < 2.5$ and be b-tagged using the 60% efficiency working point.

- Both of the V_{had}-jets must have $|\eta| < 2.5$ and be b-tagged using the 60% efficiency working point. This criterion could be satisfied by top-events that are incorrectly reconstructed (wrong jets assigned to V_{had}).

In the CR_TopFat, there must be at least one AntiKt4 jet with $|\eta| < 2.5$ that has $\Delta R(\text{j}, V_{\text{had}}) > 0.4$ and which is b-tagged using the 60% efficiency MV1 working point.

By these definitions, there is no overlap between the SR and CR_Top, or between SR_fatOnly and CR_TopFat.

7.2 V+jets Modeling

The $W+$jets process is the biggest background for this analysis. $Z+$jets has a much smaller contribution in the final selection as we require exactly one lepton. The Sherpa LO generator was used for both $W+$jets and $Z+$jets.

The modeling has been checked by looking at the data-MC agreement in the $W+$jets control regions. A mild deficit in the data is observed. This can be seen in Figure 25, which shows data-MC comparisons of the $m(V_{\text{had}})$, E_T^{miss} and m_T distributions for the loose VBS $W+$jets control regions, without applying any scale factors to the $W+$jets estimates.

Since $W+$jets has the largest contribution in these control regions (and another one of the largest contributions comes from $t\bar{t}$, which looks well modeled based on Sec. 7.3), it is assumed that the data-MC disagreement is due to an overestimate of $W+$jets. To account for this discrepancy, a $W+$jets scale factor, $f_{W+\text{jets}}$, is calculated:

$$f_{W+\text{jets}} = \frac{N_{\text{data}} - N_{\text{non}-W+\text{jets}}}{N_{W+\text{jets},MC}} \,. \tag{55}$$

No striking differences in the scale factor are seen between the various lepton channels e^+, e^-, μ^+, μ^-, or between the resolved/merged jet selections, so a single scale factor is calculated, summing together all the lepton channels and summing together the resolved and merged channels. A scale factor of 0.82 is found. This scale factor will be applied to the $W+$jets MC estimate, and the full difference (i.e. 0.82 ± 0.18) will be taken as a systematic uncertainty.

Data-MC comparisons for several important distributions, the di-jet invariant mass of the VBS tagging jets, di-jet invariant mass of W-jet candidates, boson centrality, $\cos\left(\theta^*_{\text{j}}\right)$, $m_{\text{T}}(WV)$, and $\text{p}_{\text{T}}(W_{\text{lep}})$, are shown in Figures 26-33, for the $W+$jets control regions for the loose VBS cuts. The

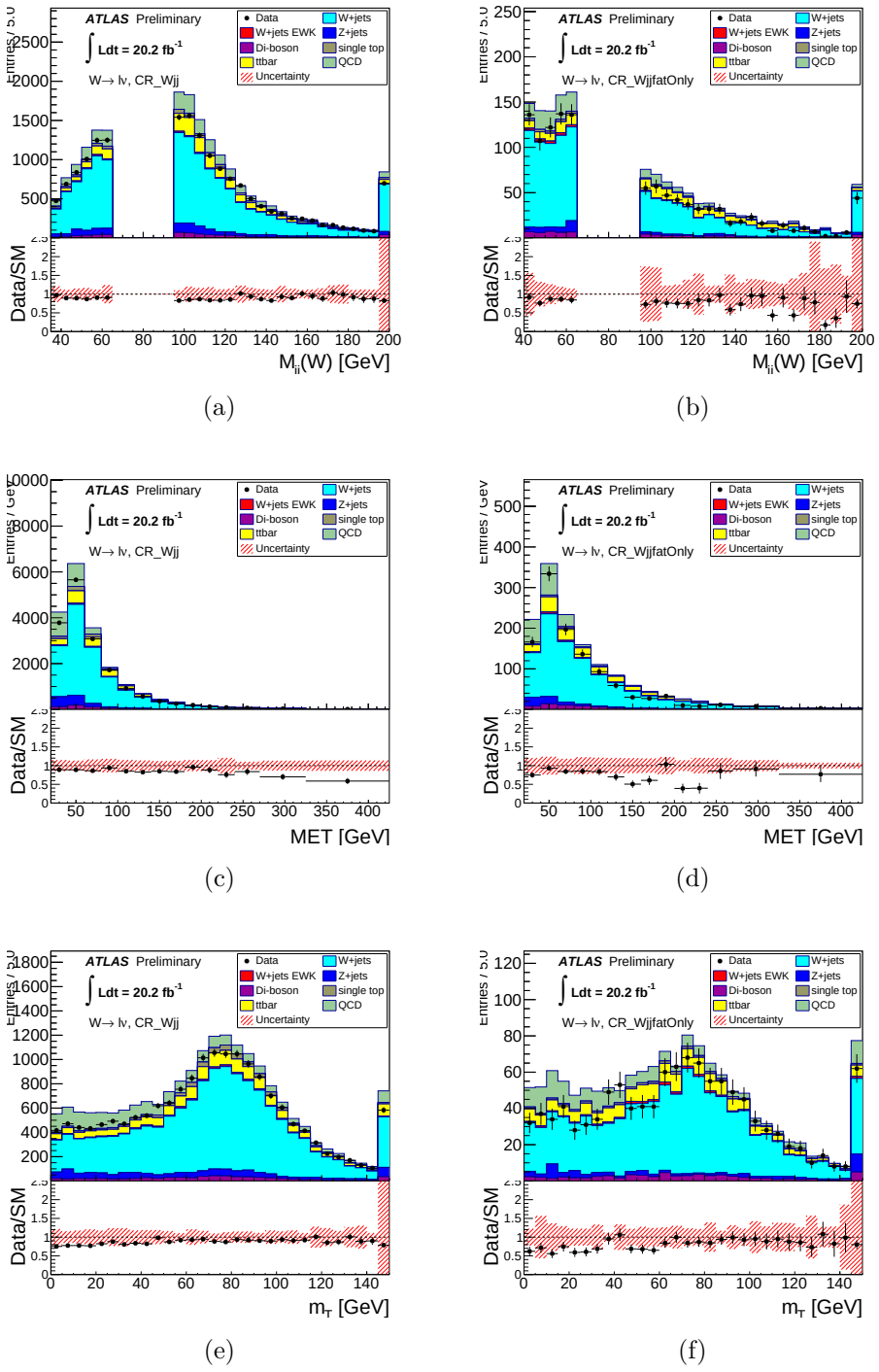

Figure 25: Plots of the mass of the hadronic-V candidate, $m(V_{\text{had}})$ ((a) resolved selection and (b) merged selection) , E_T^{miss} ((c) resolved selection and (d) merged selection) and m_T ((e) resolved selection and (f) merged selection) in the loose VBS $W+$jets CR. No scaling has been applied to the W+jets sample. As can be seen, $W+$jets seems to be over-estimated by the MC.

Table 16: Observed purity in Top-quark and W+jets control regions for loose VBS cut

Region	signal(0,0)	signal(0,0.1)	$t\bar{t}$	W+jets	total bkg	$t\bar{t}$/bkg	W+jets/bkg
CR_Top	65	70	11000	860	13000	0.84	0.07
CR_TopFat	1.2	3.4	147	40	219	0.67	0.18
CR_Wjet	52	73	2000	13000	17000	0.12	0.75
CR_WjetFat	6.8	15	180	910	1240	0.15	0.73

signal contamination in these control regions is small, and is not shown in the plots. The SM signal contribution is less than 1%. For the resolved selection, a signal with $\alpha_5 = 0.3$ would still contribute less than 1% of the total events, whereas for the merged-jet selection, a signal with $\alpha_5 = 0.3$ would have a roughly 1% contribution.

7.3 $t\bar{t}$ Modeling

The $t\bar{t}$ is one of the largest backgrounds. It has been modeled by the Powheg generator which calculates the matrix element at next to leading order (NLO). The fragmentation has been calculated with Pythia.

Previous ATLAS analyses have shown that Powheg-Pythia samples do not model experimental data perfectly, as evidenced by the unfolded differential top quark pair cross-section measurement [104]. Following the conclusions of the study, two reweighting functions were derived so that the MC sample agrees with unfolded data for the p_T of the parton-level $t\bar{t}$ and the p_T of the top-quark (not anti-top). These weights are applied as additional event weights. weights and more details can be found in [105] and in Appendix G.

The modeling has been checked by looking at the data-MC agreement in the top-quark control regions. Data-MC comparisons for several important distributions, the di-jet invariant mass of the VBS tagging jets, di-jet invariant mass of W-jet candidates, boson centrality, $\cos\left(\theta^*_{\mathrm{j}}\right)$, $m_{\mathrm{T}}(WV)$, and $\mathrm{p_T}(W_{\mathrm{lep}})$, are shown in Figures 34-41, for the top-quark control regions for the loose VBS cuts. All data-MC comparison plots use a data-driven scale factor, as explained in section 7.2, to scale the W+jets contribution unless otherwise stated. The multjet in these plots is estimated using the data-driven method described in Section 7.5. The signal contamination in these control regions is small, and is not shown in the plots. The SM signal con-

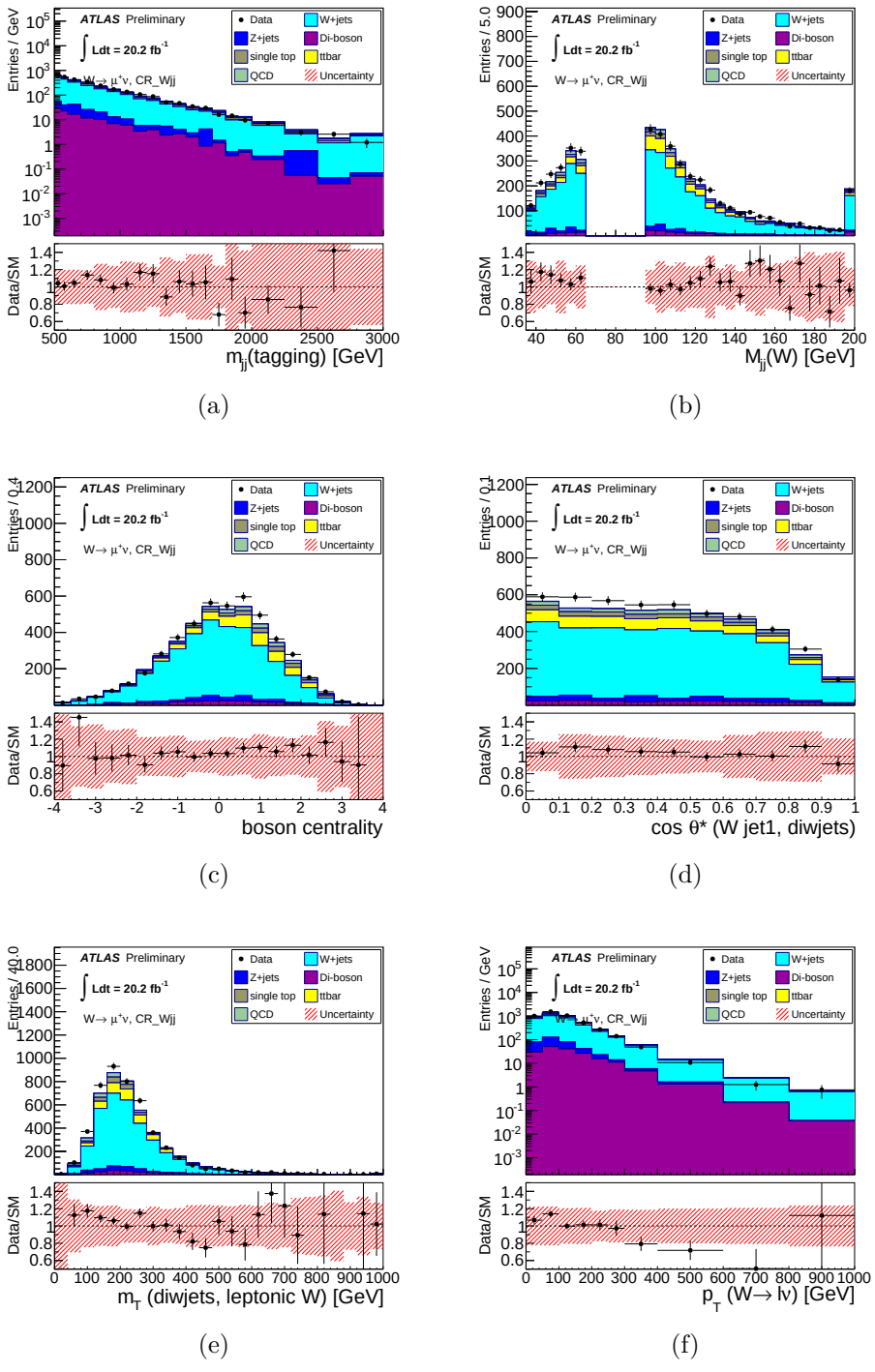

Figure 26: Data-MC comparison for the loose VBS W + jets CR for the resolved selection in the μ^+ channel. (a) Tag jet di-jet mass, (b) W-jet di-jet mass, (c) boson centrality, (d) cos θ^* , (e) $m_{\mathrm{T}}(WV)$, (f) $p_T(W_{lep})$. W + jets samples have been scaled by the data-driven SF.

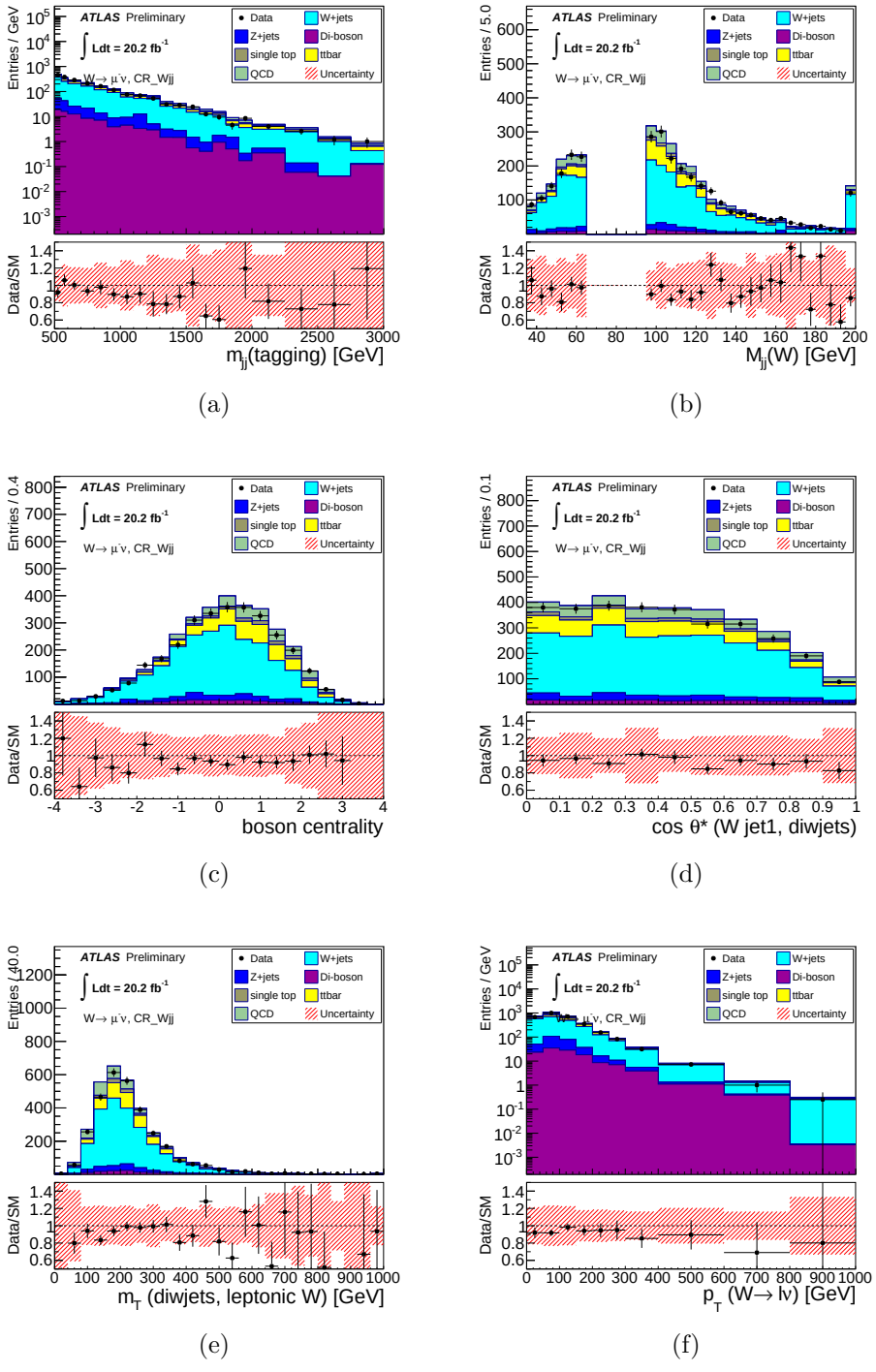

Figure 27: Data-MC comparison for the loose VBS W + jets CR for the resolved selection in the μ^- channel. (a) Tag jet di-jet mass, (b) W-jet di-jet mass, (c) boson centrality, (d) cos θ^* , (e) $m_{\mathrm{T}}(WV)$, (f) $p_T(W_{lep})$. W + jets samples have been scaled by the data-driven SF.

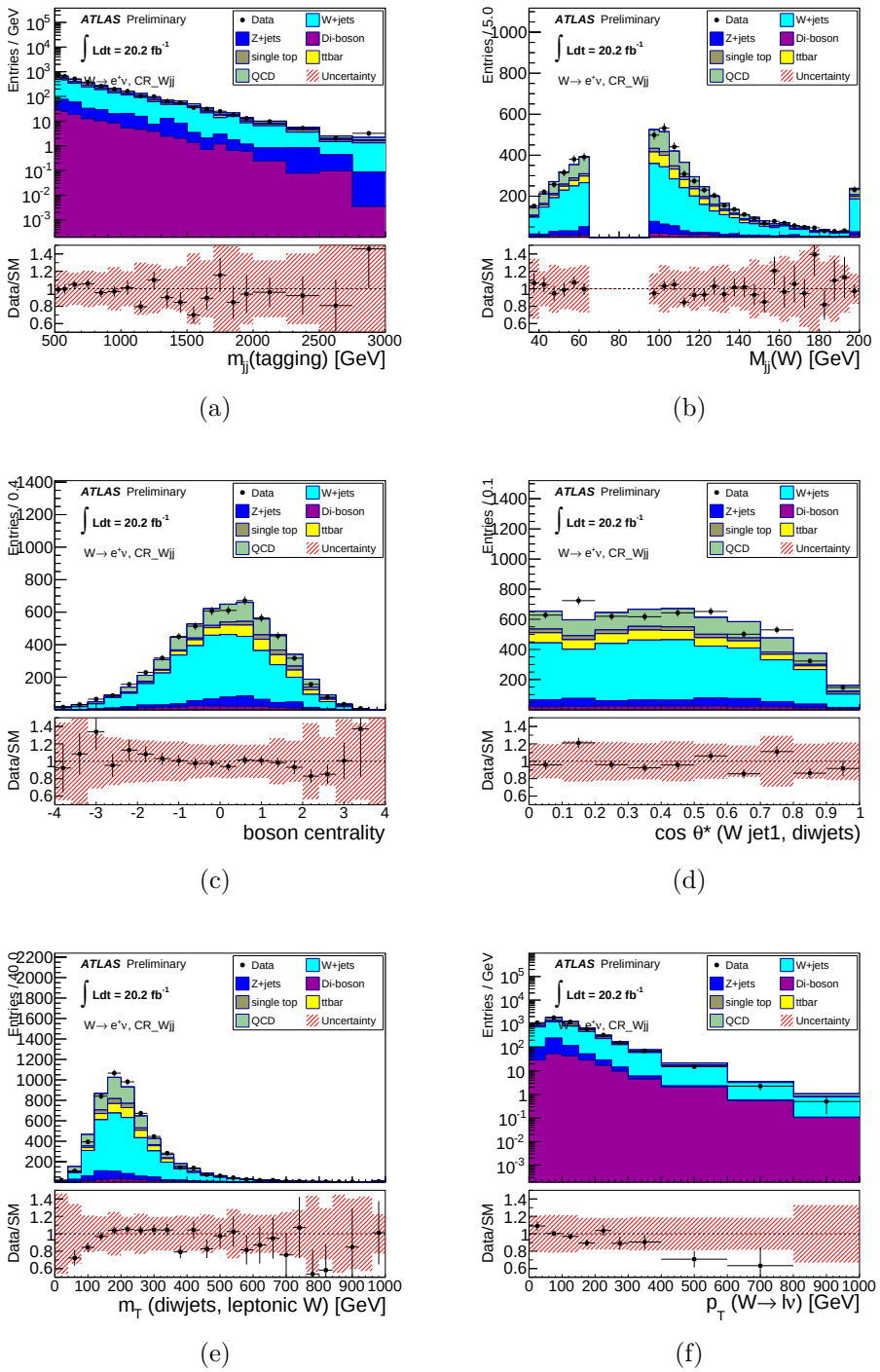

Figure 28: Data-MC comparison for the loose VBS W + jets CR for the resolved selection in the e^+ channel. (a) Tag jet di-jet mass, (b) W-jet di-jet mass, (c) boson centrality, (d) cos θ^* , (e) $m_{\mathrm{T}}(WV)$, (f) $p_T(W_{lep})$. W + jets samples have been scaled by the data-driven SF.

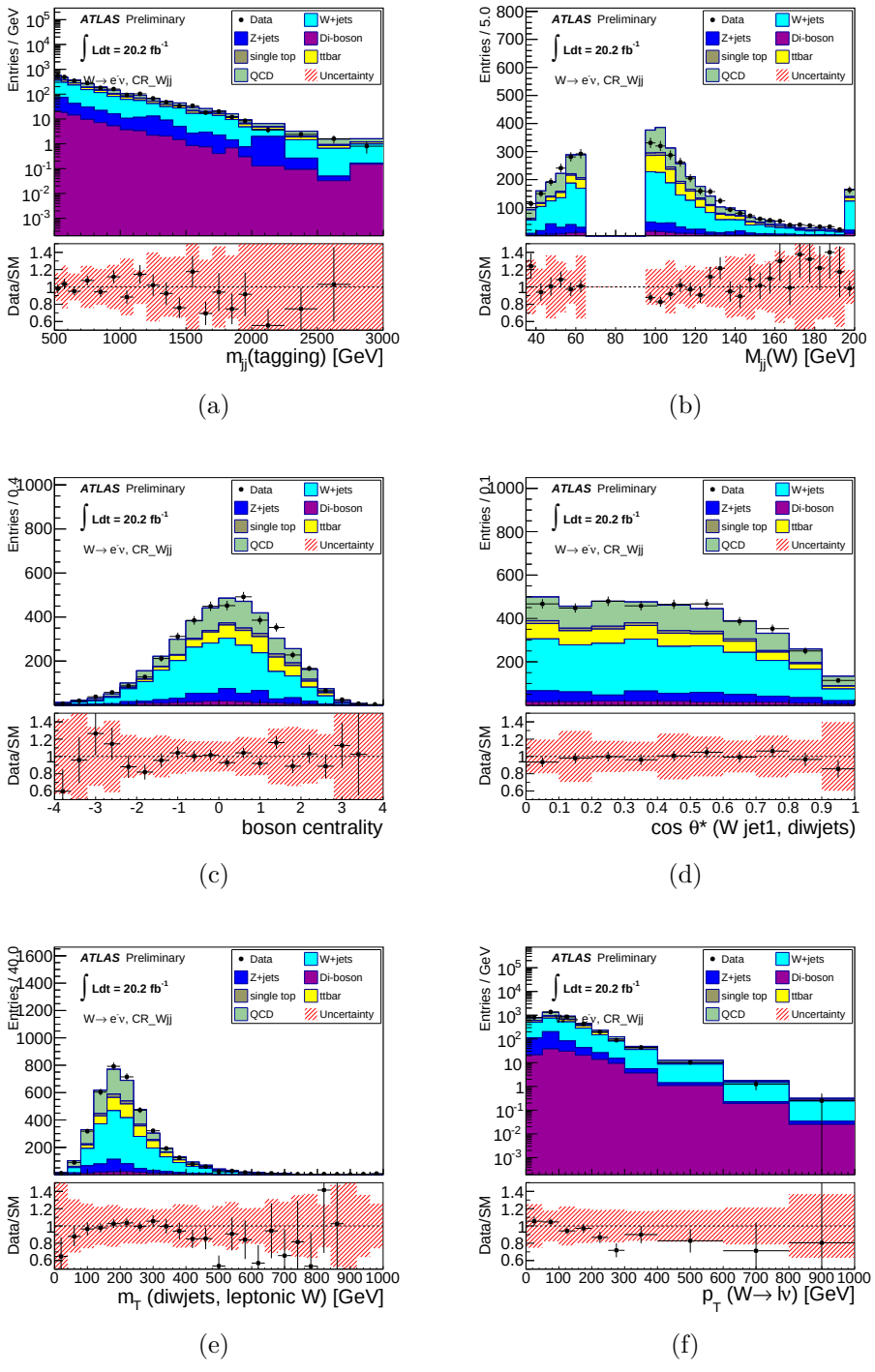

Figure 29: Data-MC comparison for the loose VBS W + jets CR for the resolved selection in the e^- channel. (a) Tag jet di-jet mass, (b) W-jet di-jet mass, (c) boson centrality, (d) cos θ^* , (e) $m_{\mathrm{T}}(WV)$, (f) $p_T(W_{lep})$. W + jets samples have been scaled by the data-driven SF.

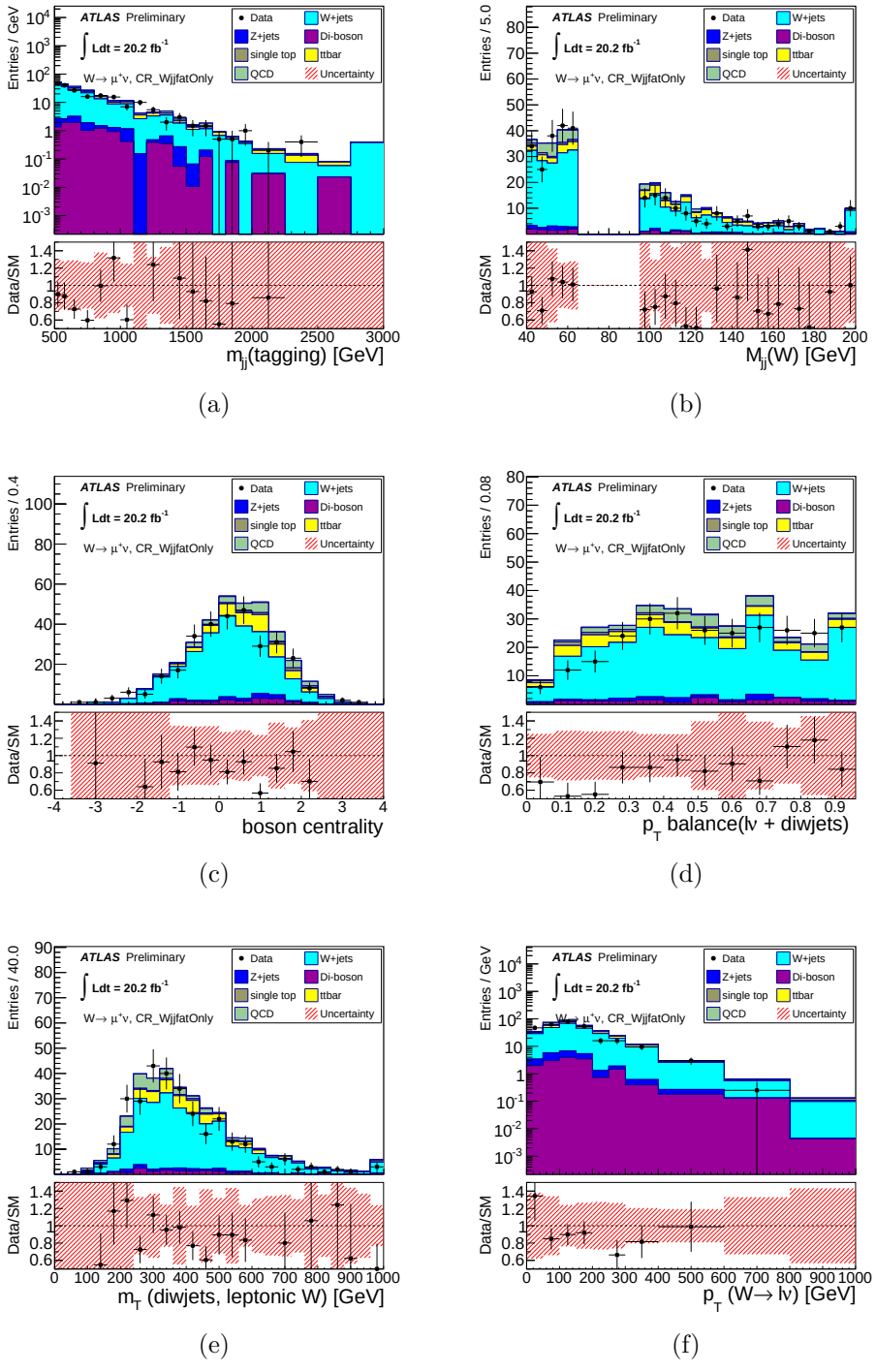

Figure 30: Data-MC comparison for the loose VBS W + jets CR for the merged selection in the μ^+ channel. (a) Tag jet di-jet mass, (b) W-jet di-jet mass, (c) boson centrality, (d) cos θ^* , (e) $m_{\mathrm{T}}(WV)$, (f) $p_T(W_{lep})$. W + jets samples have been scaled by the data-driven SF.

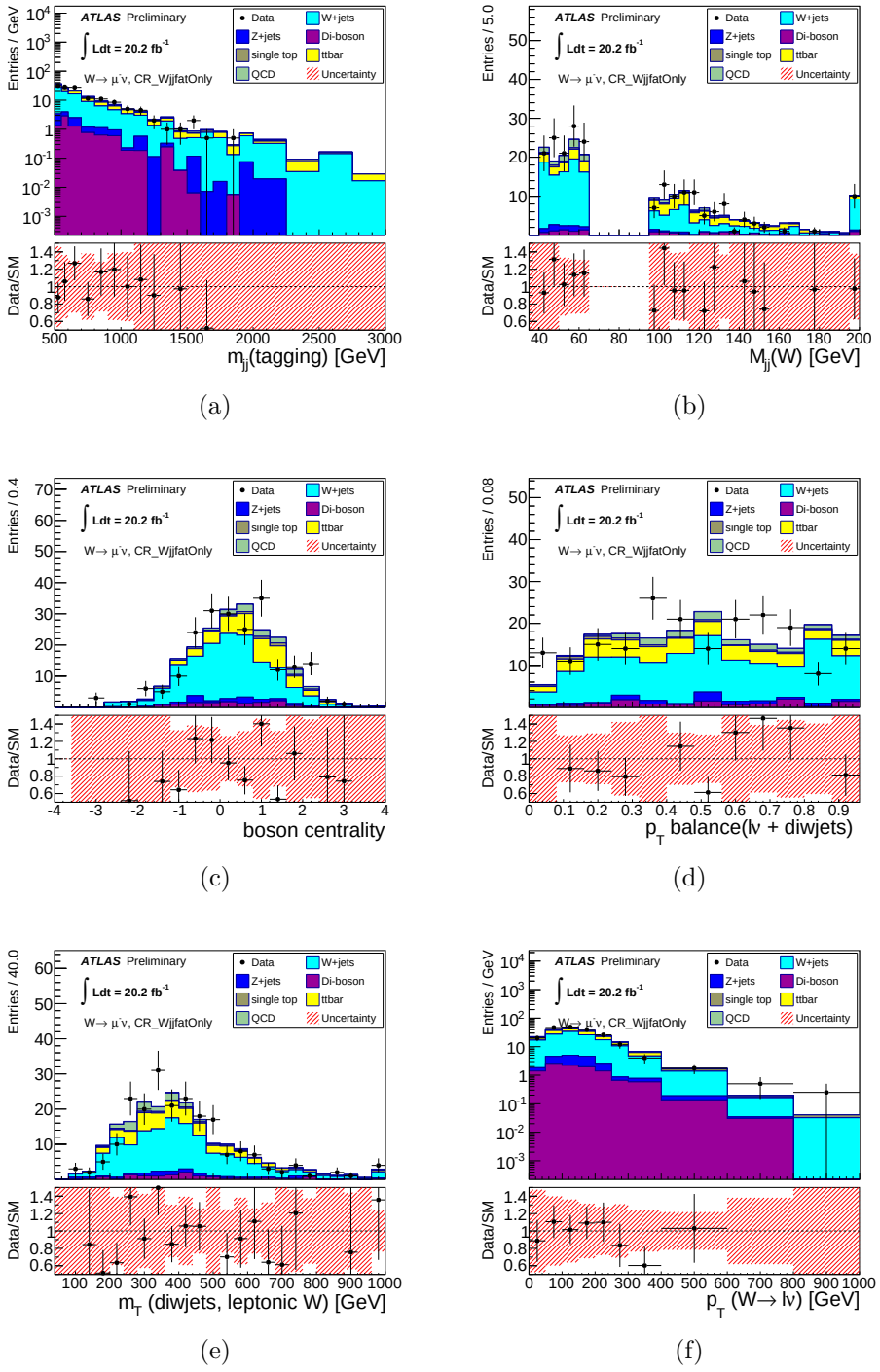

Figure 31: Data-MC comparison for the loose VBS W + jets CR for the merged selection in the μ^- channel. (a) Tag jet di-jet mass, (b) W-jet di-jet mass, (c) boson centrality, (d) cos θ^* , (e) $m_{\mathrm{T}}(WV)$, (f) $p_T(W_{lep})$. W + jets samples have been scaled by the data-driven SF.

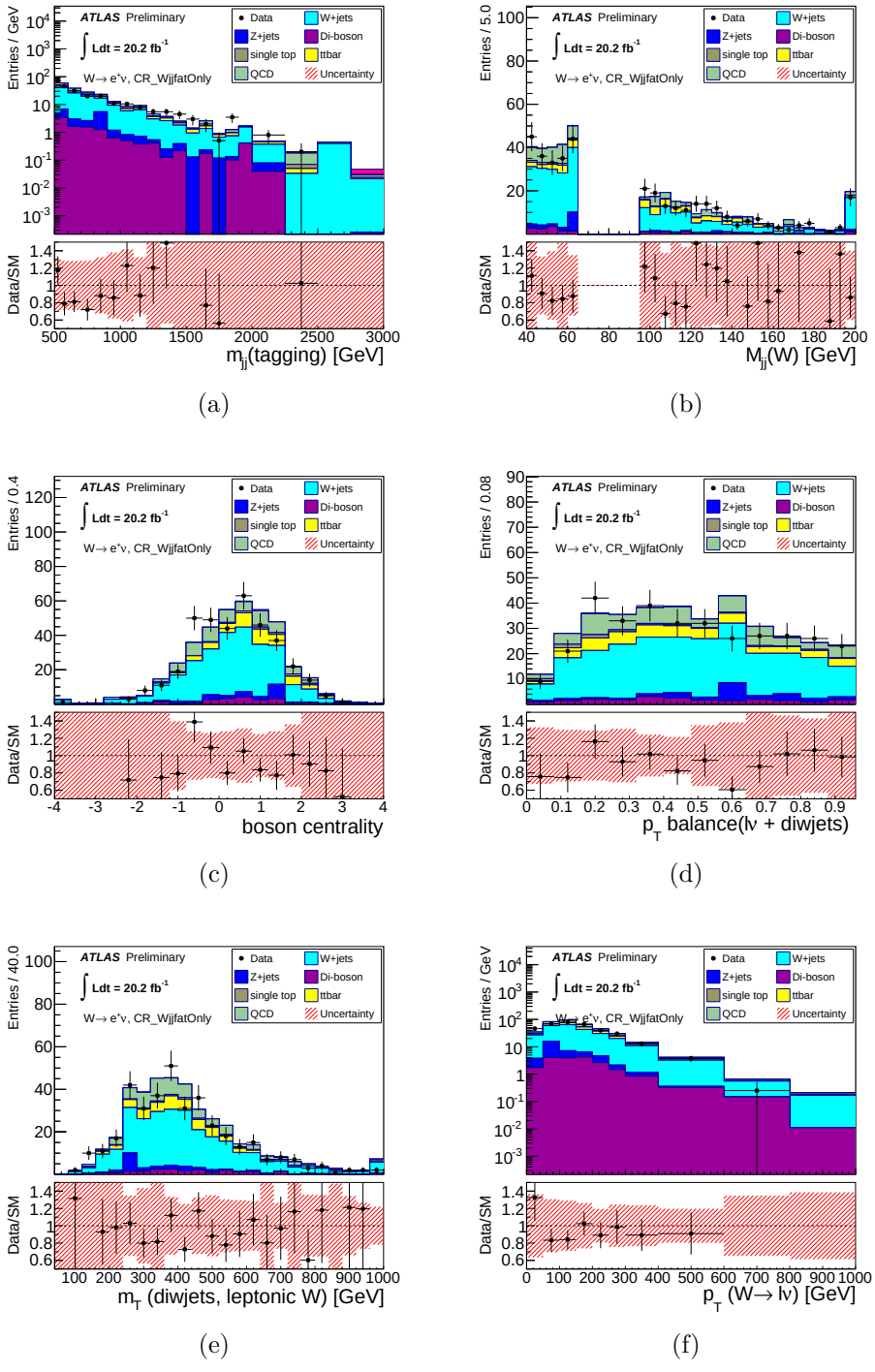

Figure 32: Data-MC comparison for the loose VBS W + jets CR for the merged selection in the e^+ channel. (a) Tag jet di-jet mass, (b) W-jet di-jet mass, (c) boson centrality, (d) cos θ^* , (e) $m_{\mathrm{T}}(WV)$, (f) $p_T(W_{lep})$. W + jets samples have been scaled by the data-driven SF.

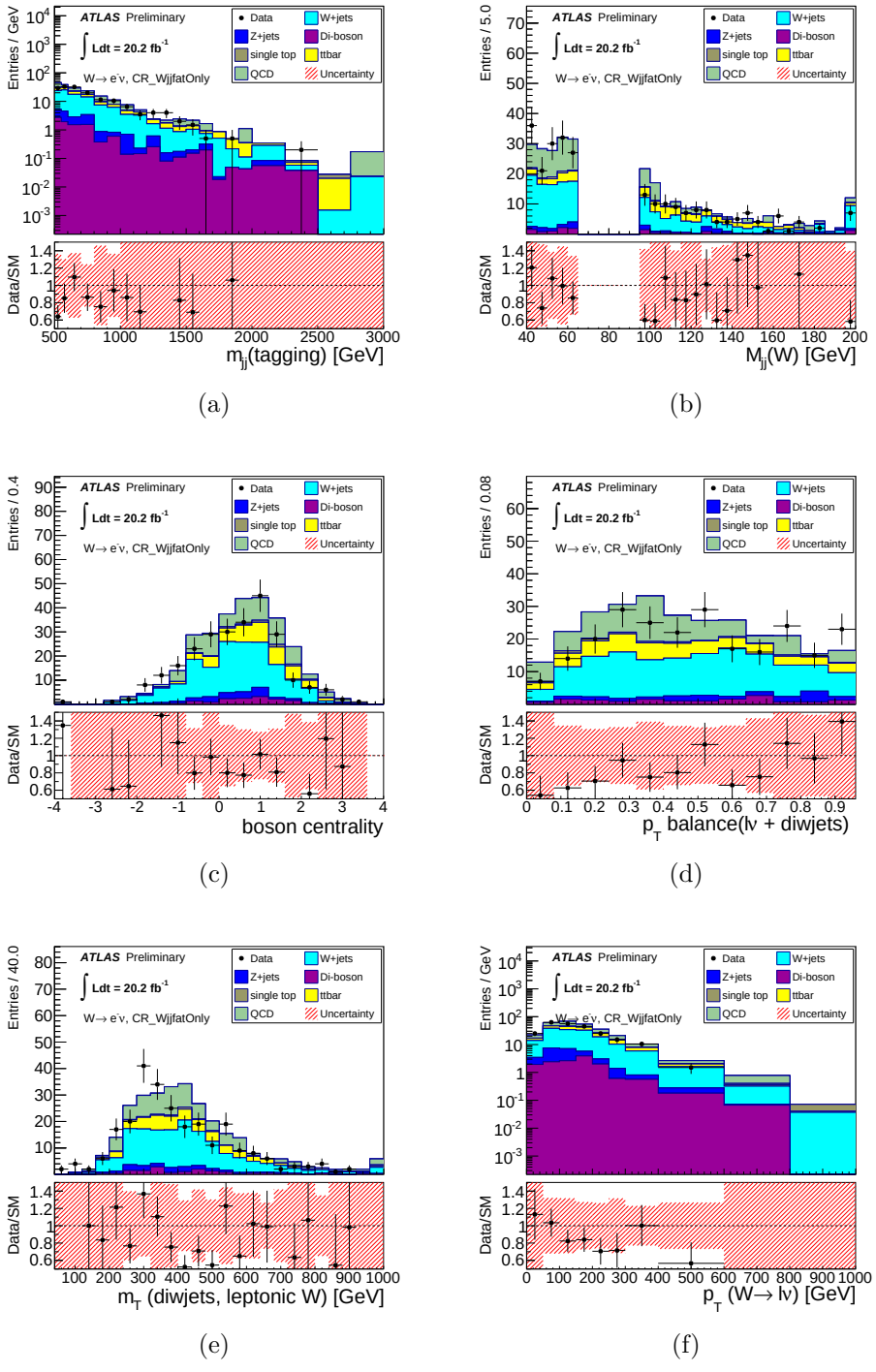

Figure 33: Data-MC comparison for the loose VBS W + jets CR for the merged selection in the e^- channel. (a) Tag jet di-jet mass, (b) W-jet di-jet mass, (c) boson centrality, (d) cos θ^* , (e) $m_{\mathrm{T}}(WV)$, (f) $p_T(W_{lep})$. W + jets samples have been scaled by the data-driven SF.

tribution is less than 1%, for both the resolved and merged-jet selections. For the resolved selection, a signal with $\alpha_5 = 0.3$ would contribute less than 1% of the total events, whereas for the merged-jet selection, a signal with $\alpha_5 = 0.3$ would have a roughly 3% contribution.

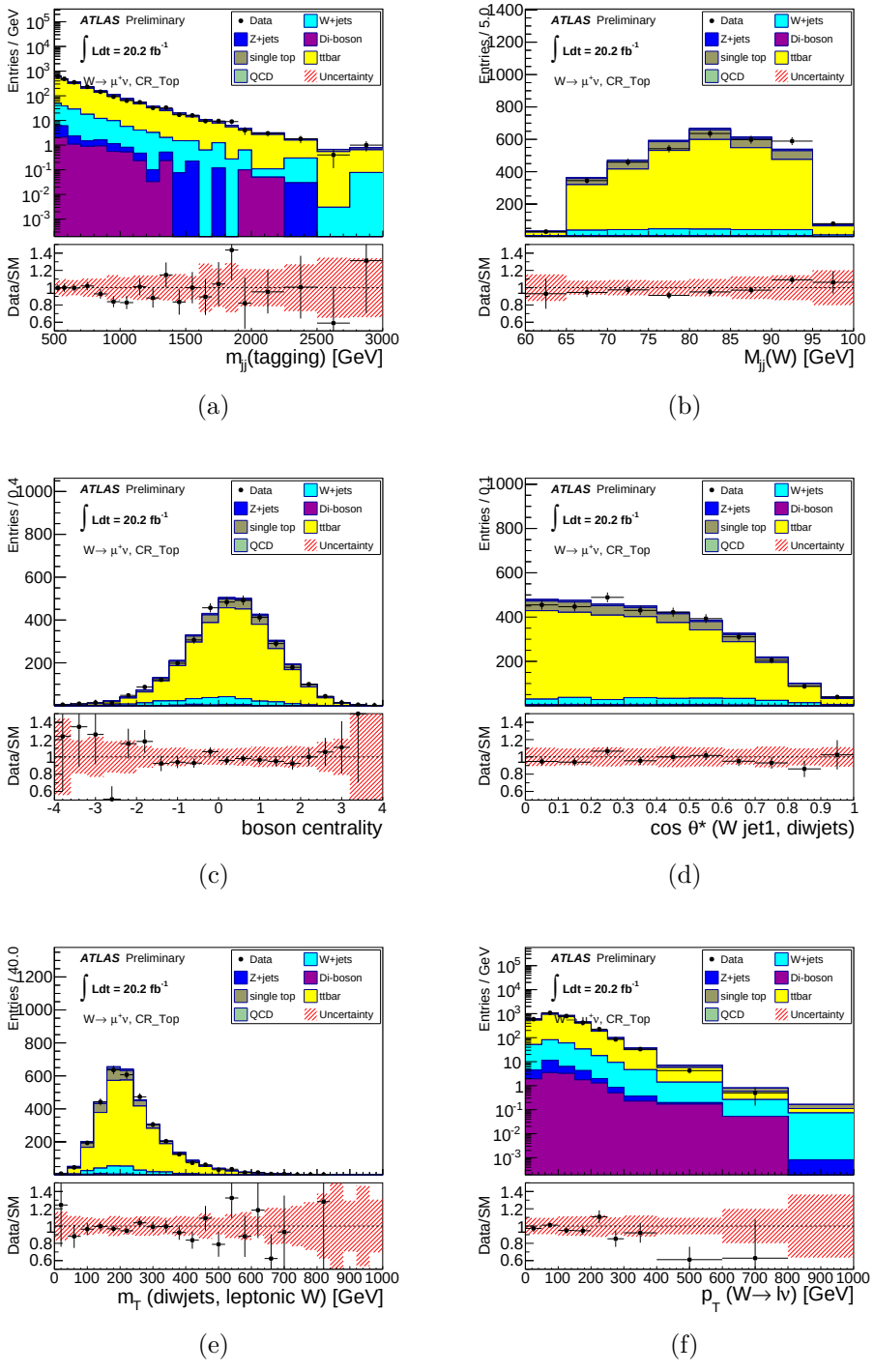

Figure 34: Data-MC comparison for the loose VBS Top CR for the resolved selection in the μ^+ channel. Here MV1 cut with 60% b-tag efficiency has been used. W + jets samples have been scaled by the data-driven SF. (a) Tag jet di-jet mass, (b) W-jet di-jet mass, (c) boson centrality, (d) cos θ^* , (e) $m_{\mathrm{T}}(WV)$, (f) $p_T(W_{lep})$.

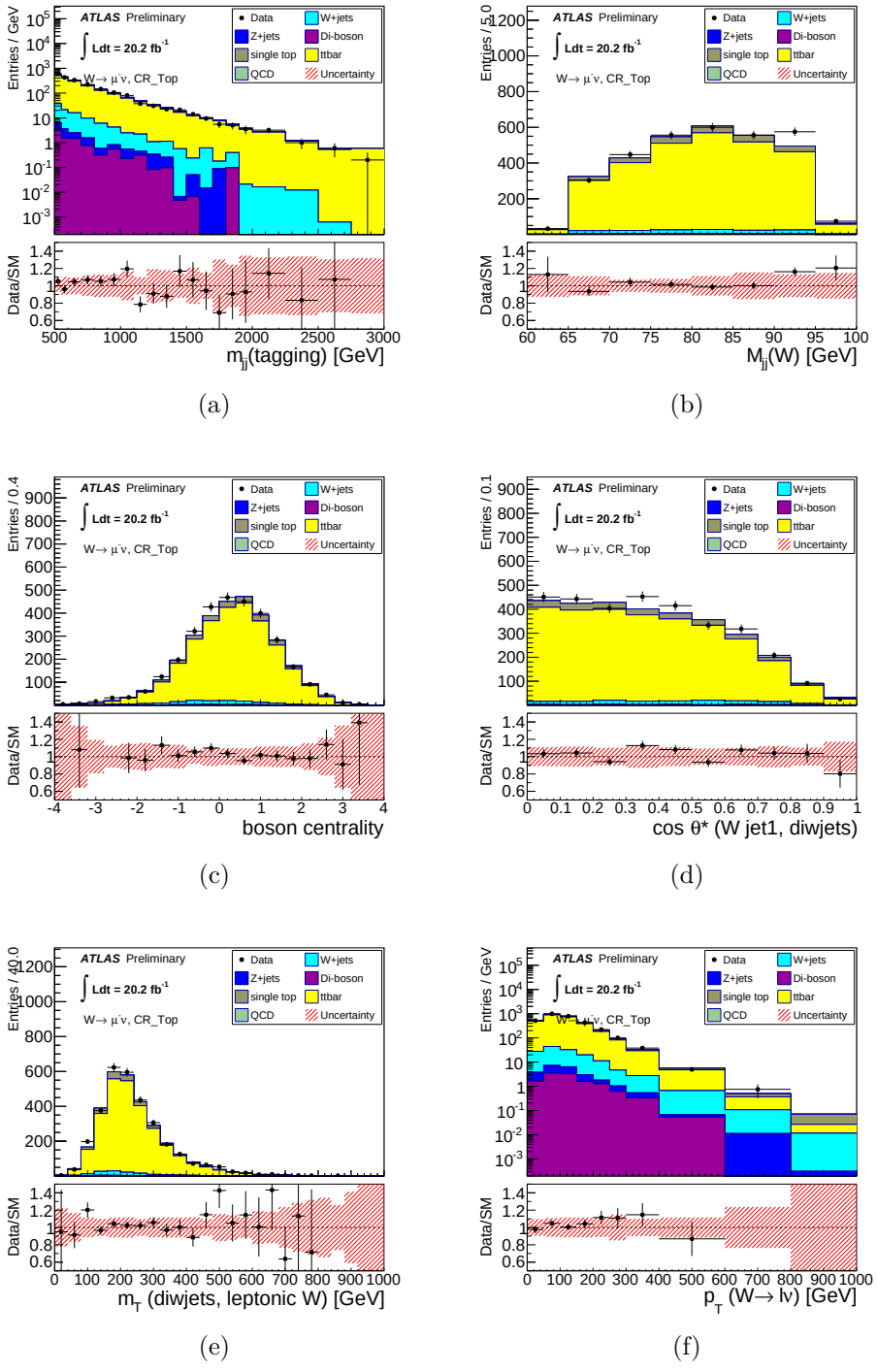

Figure 35: Data-MC comparison for the loose VBS Top CR for the resolved selection in the μ^- channel. Here MV1 cut with 60% b-tag efficiency has been used. W + jets samples have been scaled by the data-driven SF. (a) Tag jet di-jet mass, (b) W-jet di-jet mass, (c) boson centrality, (d) cos θ^* , (e) $m_{\mathrm{T}}(WV)$, (f) $p_T(W_{lep})$.

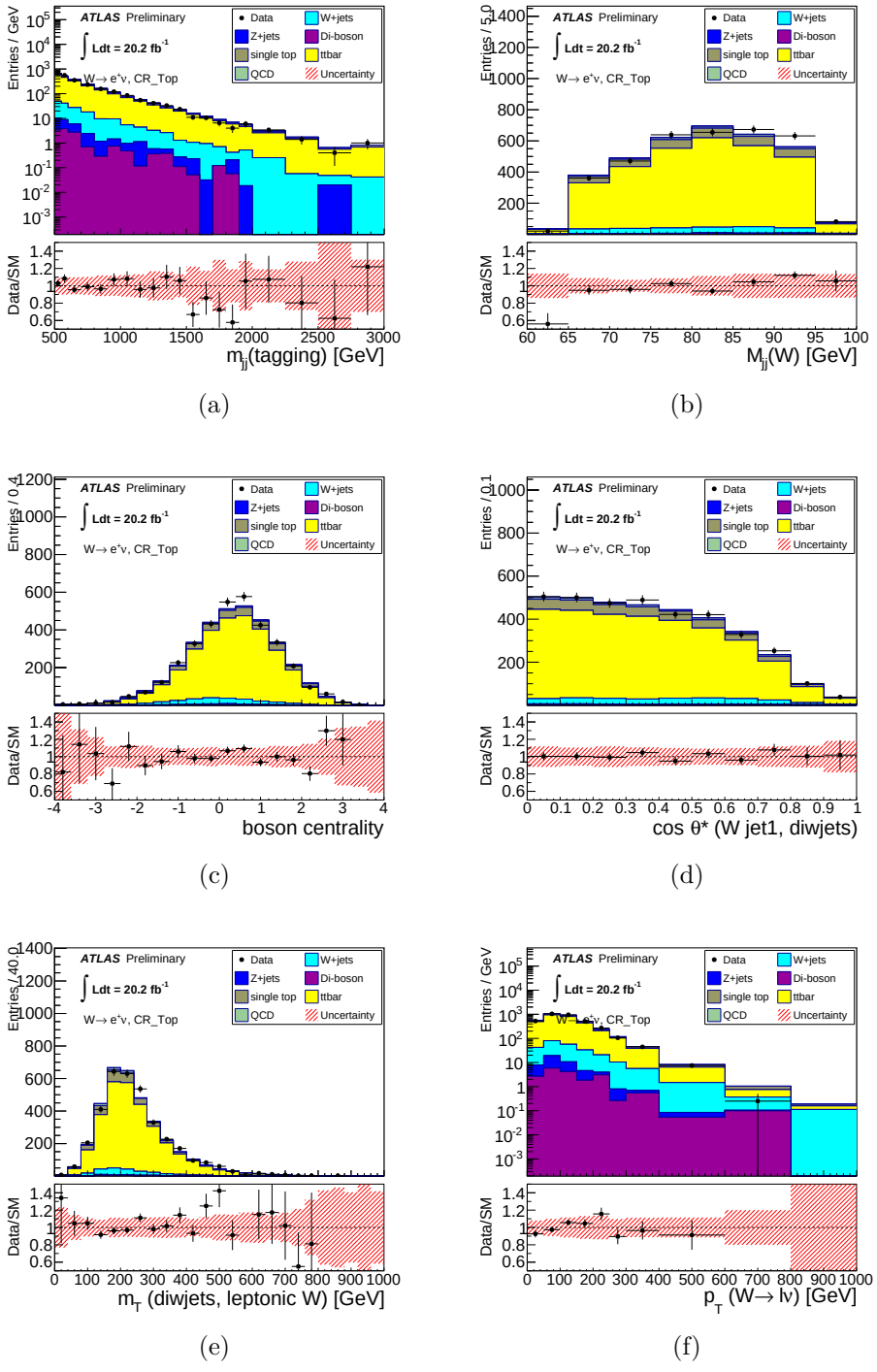

Figure 36: Data-MC comparison for the loose VBS Top CR for the resolved selection in the e^+ channel. Here MV1 cut with 60% b-tag efficiency has been used. W + jets samples have been scaled by the data-driven SF. (a) Tag jet di-jet mass, (b) W-jet di-jet mass, (c) boson centrality, (d) cos θ^* , (e) $m_{\mathrm{T}}(WV)$, (f) $p_T(W_{lep})$.

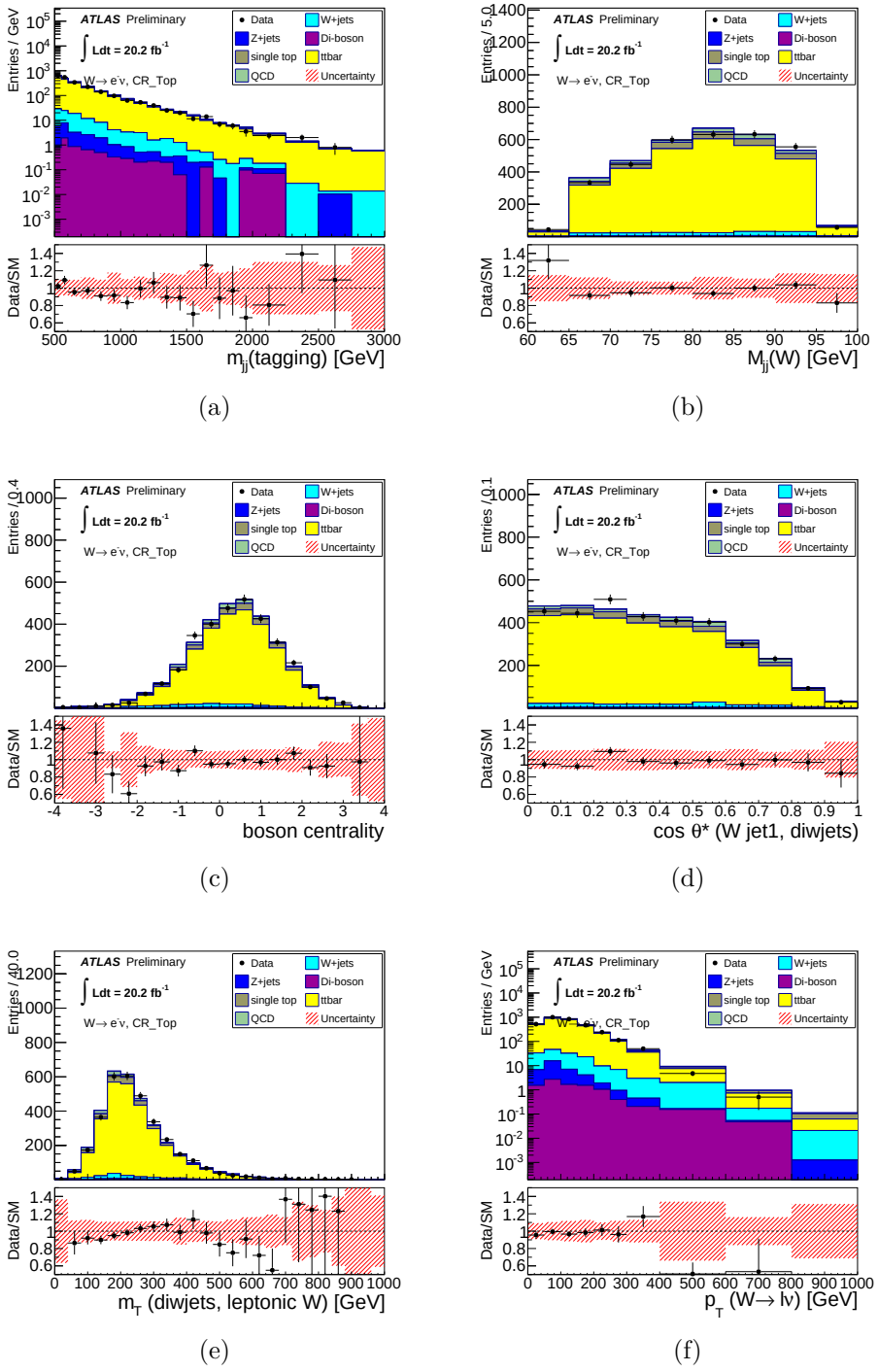

(a) (b) (c) (d) (e) (f)

Figure 37: Data-MC comparison for the loose VBS Top CR for the resolved selection in the e^- channel. Here MV1 cut with 60% b-tag efficiency has been used. W + jets samples have been scaled by the data-driven SF. (a) Tag jet di-jet mass, (b) W-jet di-jet mass, (c) boson centrality, (d) cos θ^* , (e) $m_{\mathrm{T}}(WV)$, (f) $p_T(W_{lep})$.

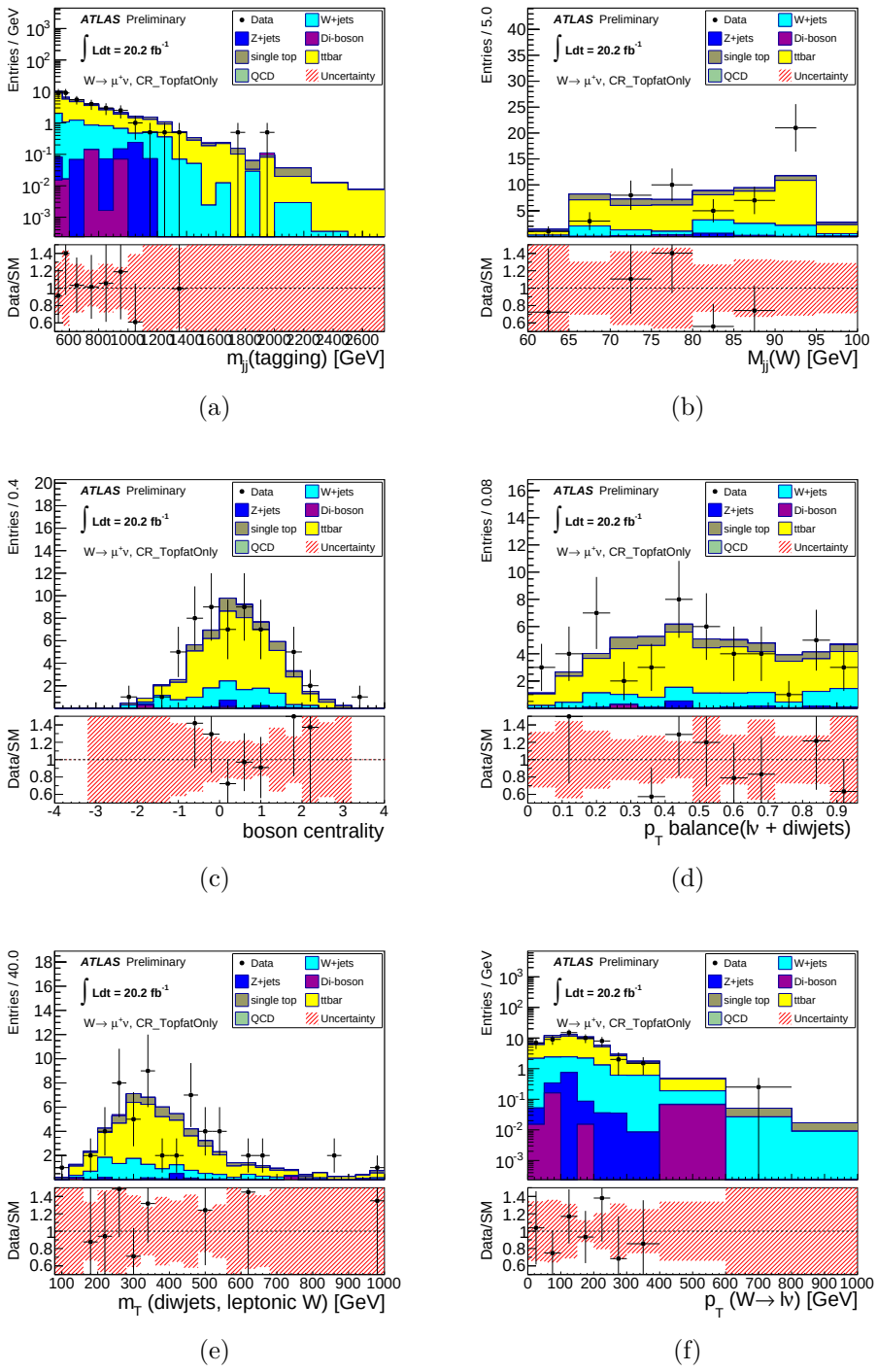

Figure 38: Data-MC comparison for the loose VBS Top CR for the merged selection in the μ^+ channel. Here MV1 cut with 60% b-tag efficiency has been used. W + jets samples have been scaled by the data-driven SF. (a) Tag jet di-jet mass, (b) W-jet di-jet mass, (c) boson centrality, (d) cos θ^* , (e) $m_{\mathrm{T}}(WV)$, (f) $p_T(W_{lep})$.

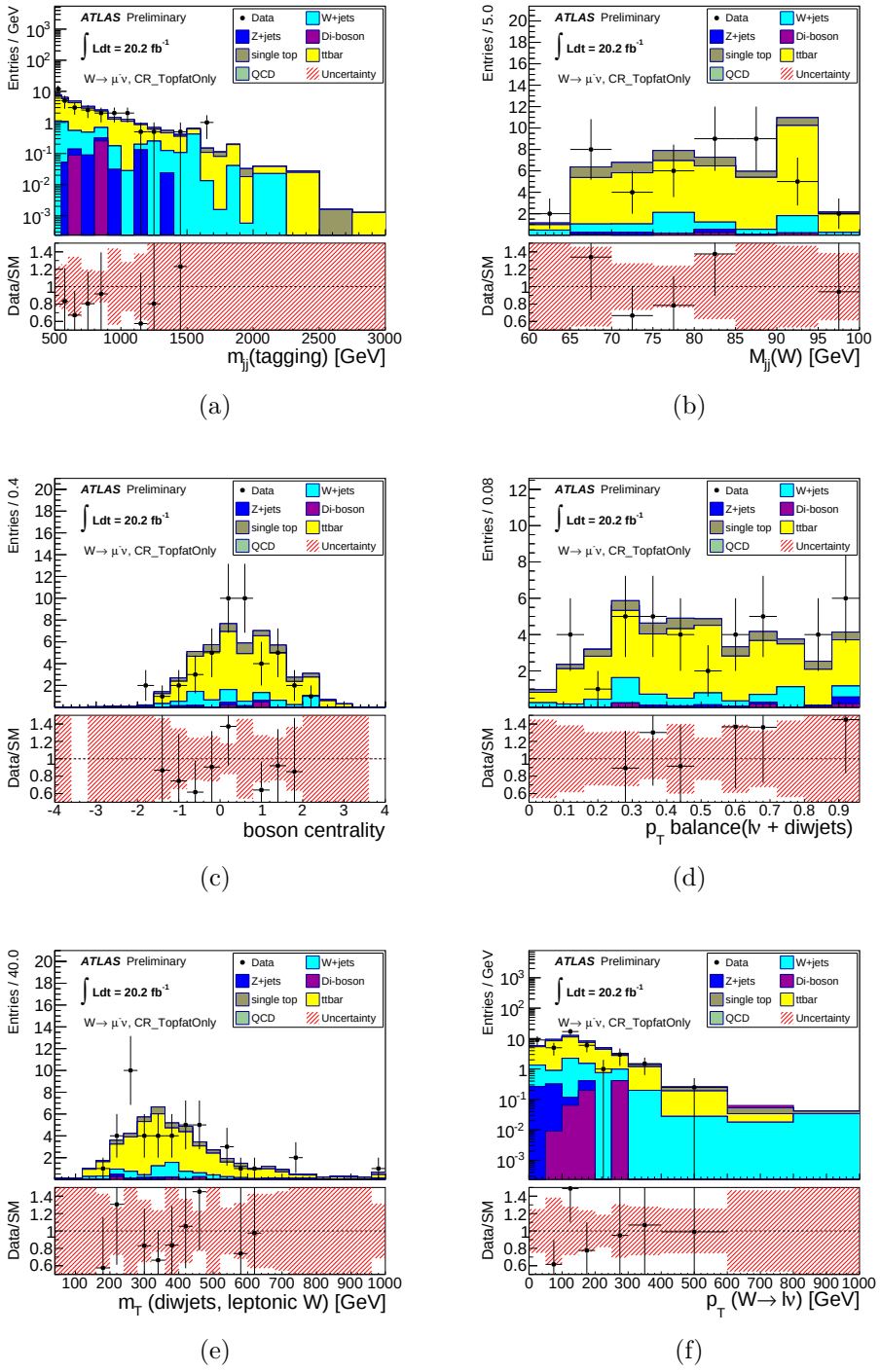

Figure 39: Data-MC comparison for the loose VBS Top CR for the merged selection in the μ^- channel. Here MV1 cut with 60% b-tag efficiency has been used. W + jets samples have been scaled by the data-driven SF. (a) Tag jet di-jet mass, (b) W-jet di-jet mass, (c) boson centrality, (d) cos θ^* , (e) $m_{\mathrm{T}}(WV)$, (f) $p_T(W_{lep})$.

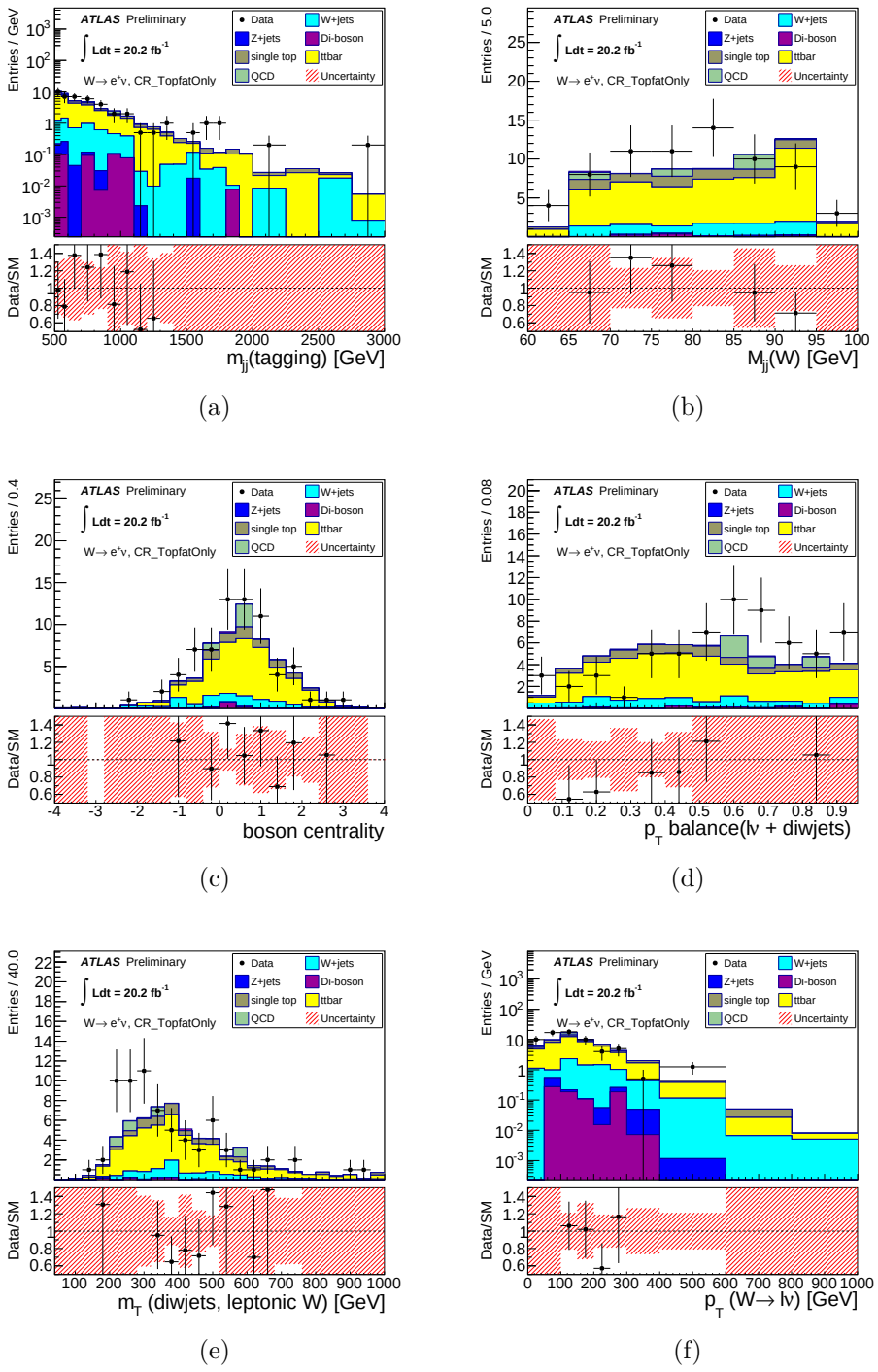

Figure 40: Data-MC comparison for the loose VBS Top CR for the merged selection in the e^+ channel. Here MV1 cut with 60% b-tag efficiency has been used. W + jets samples have been scaled by the data-driven SF. (a) Tag jet di-jet mass, (b) W-jet di-jet mass, (c) boson centrality, (d) cos θ^* , (e) $m_{\mathrm{T}}(WV)$, (f) $p_T(W_{lep})$.

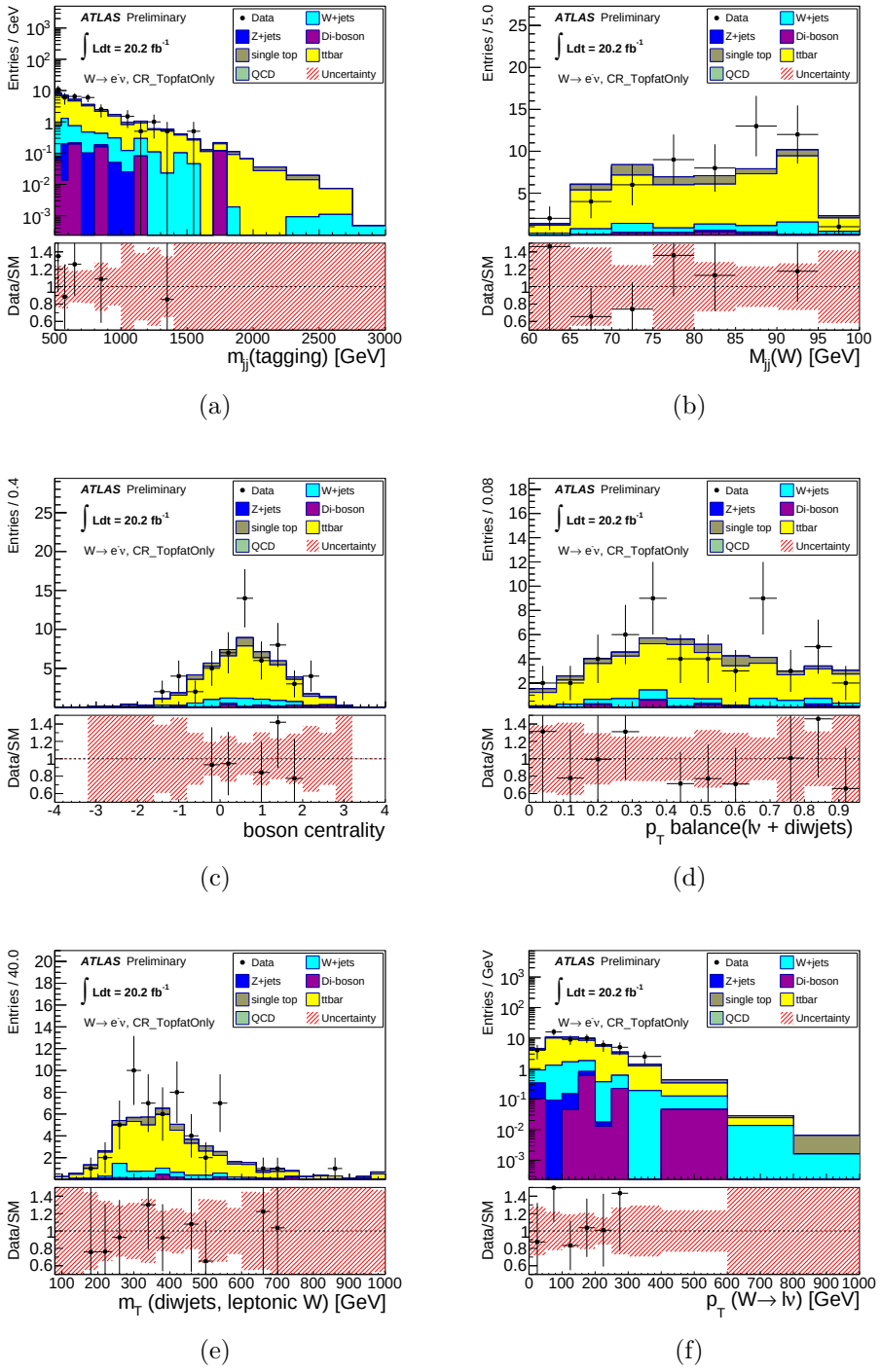

Figure 41: Data-MC comparison for the loose VBS Top CR for the merged selection in the e^- channel. Here MV1 cut with 60% b-tag efficiency has been used. W + jets samples have been scaled by the data-driven SF. (a) Tag jet di-jet mass, (b) W-jet di-jet mass, (c) boson centrality, (d) cos θ^* , (e) $m_{\mathrm{T}}(WV)$, (f) $p_T(W_{lep})$.

7.4 Signal Region Modeling

Data-MC comparisons for several important distributions, the di-jet invariant mass of the VBS tagging jets, di-jet invariant mass of W-jet candidates, boson centrality, $\cos\left(\theta^*_{\mathrm{j}}\right)$, $m_{\mathrm{T}}(WV)$, and $\mathrm{p_T}(W_{\mathrm{lep}})$, are shown in Figures 42-49, for the signal regions (SR and SRfatOnly) for loose VBS cuts. Signal Monte Carlo samples are absent in these plots.

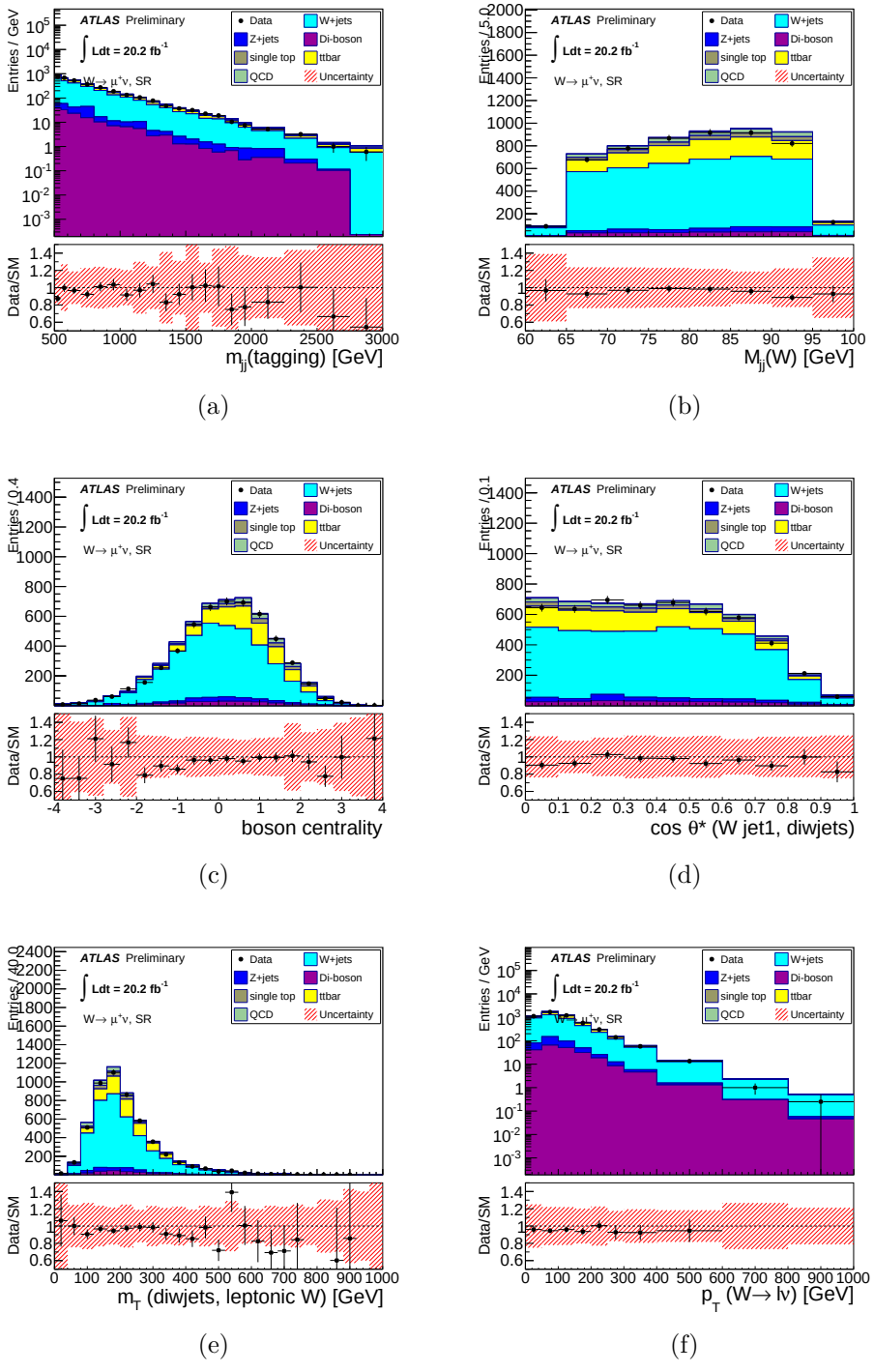

(a) (b)

(c) (d)

(e) (f)

Figure 42: Data-MC comparison for the loose VBS SR for the resolved selection in the μ^+ channel. $W+$jets samples have been scaled by the data-driven SF. (a) Tag jet di-jet mass, (b) W-jet di-jet mass, (c) boson centrality, (d) cos θ^* , (e) $m_{\mathrm{T}}(WV)$, (f) $p_T(W_{lep})$.

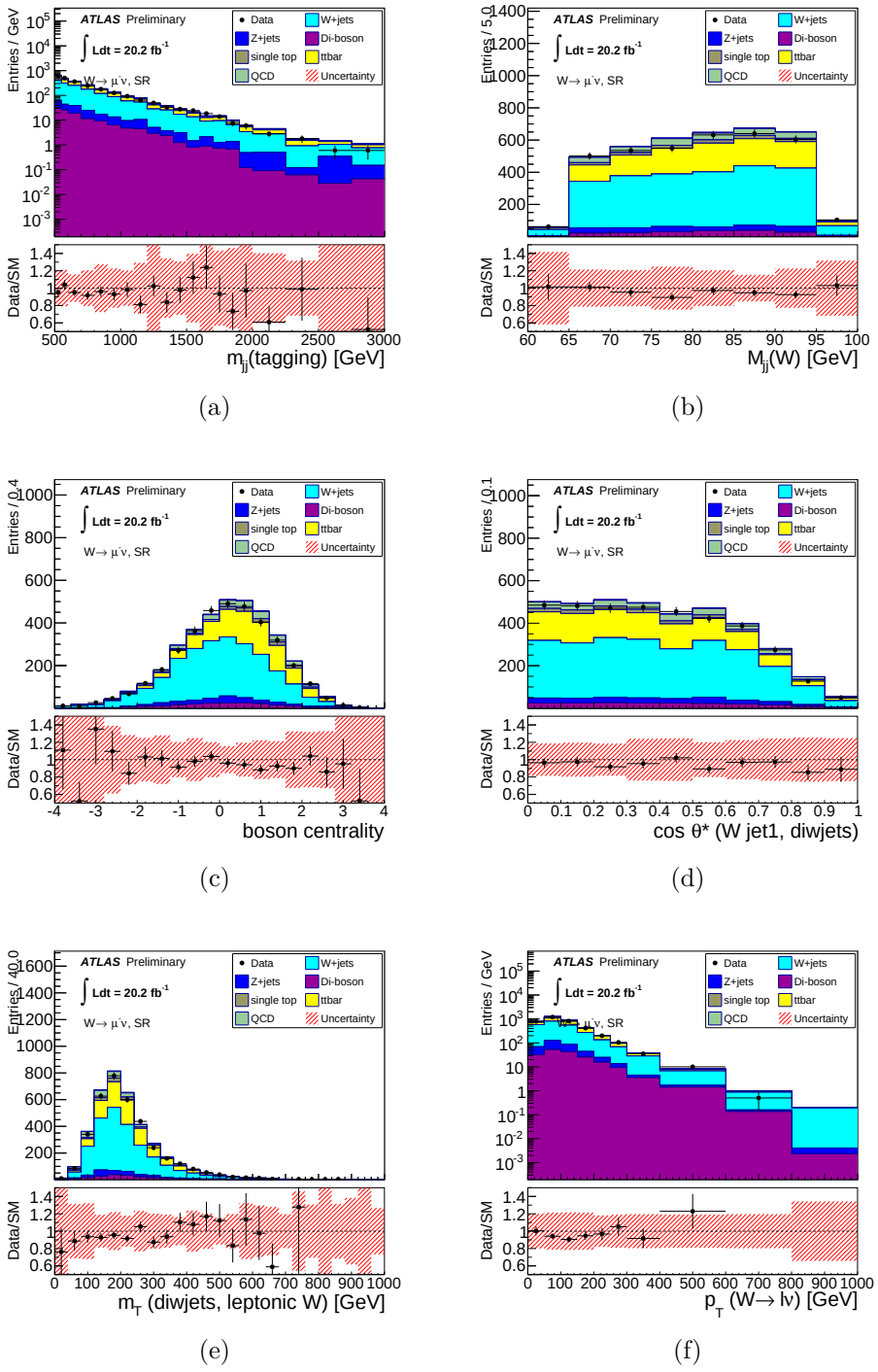

Figure 43: Data-MC comparison for the loose VBS SR for the resolved selection in the μ^- channel. $W+$jets samples have been scaled by the data-driven SF. (a) Tag jet di-jet mass, (b) W-jet di-jet mass, (c) boson centrality, (d) cos θ^* , (e) $m_{\mathrm{T}}(WV)$, (f) $p_T(W_{lep})$.

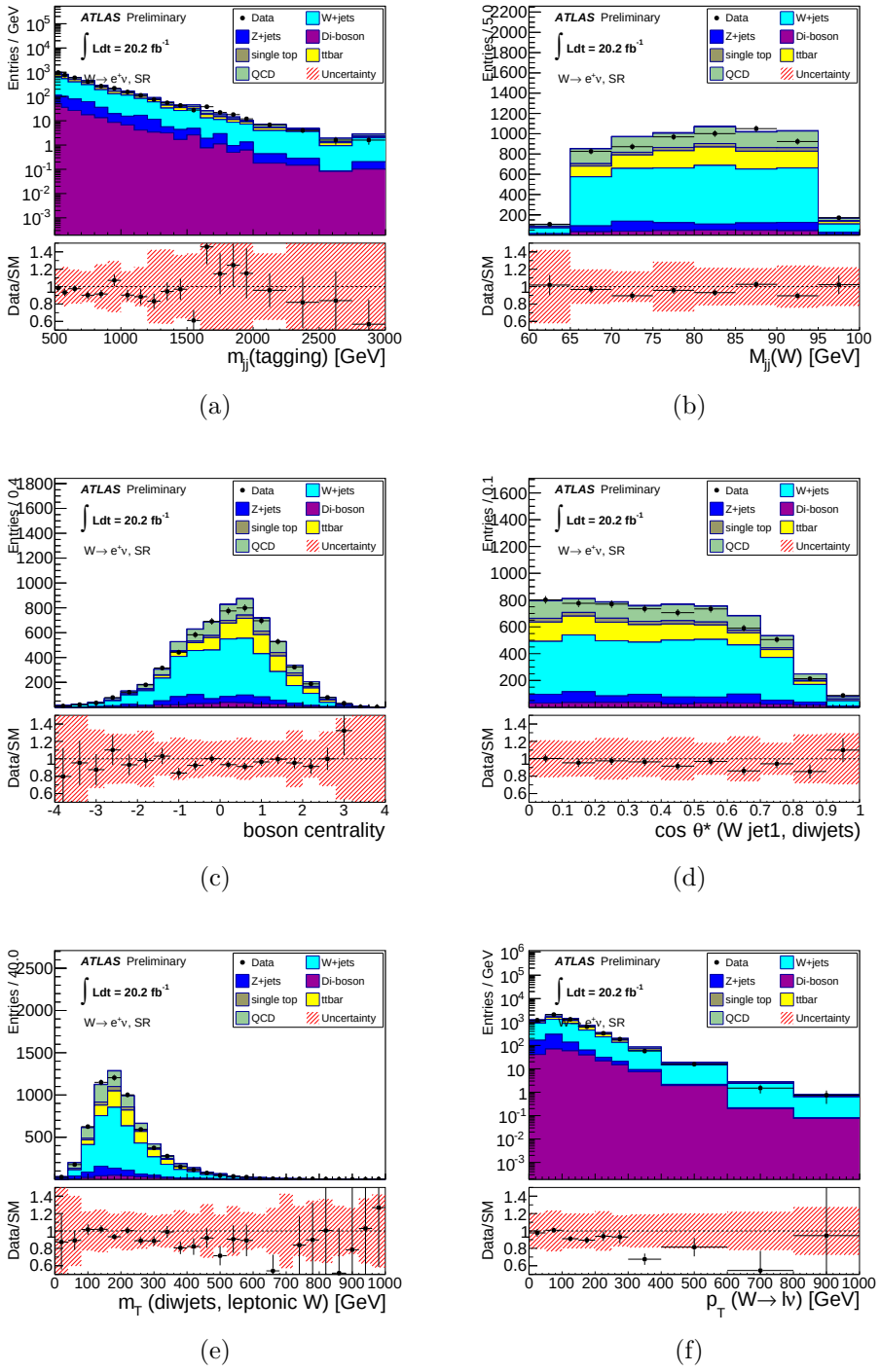

Figure 44: Data-MC comparison for the loose VBS SR for the resolved selection in the e^+ channel. $W+$jets samples have been scaled by the data-driven SF. (a) Tag jet di-jet mass, (b) W-jet di-jet mass, (c) boson centrality, (d) cos θ^* , (e) $m_{\mathrm{T}}(WV)$, (f) $p_T(W_{lep})$.

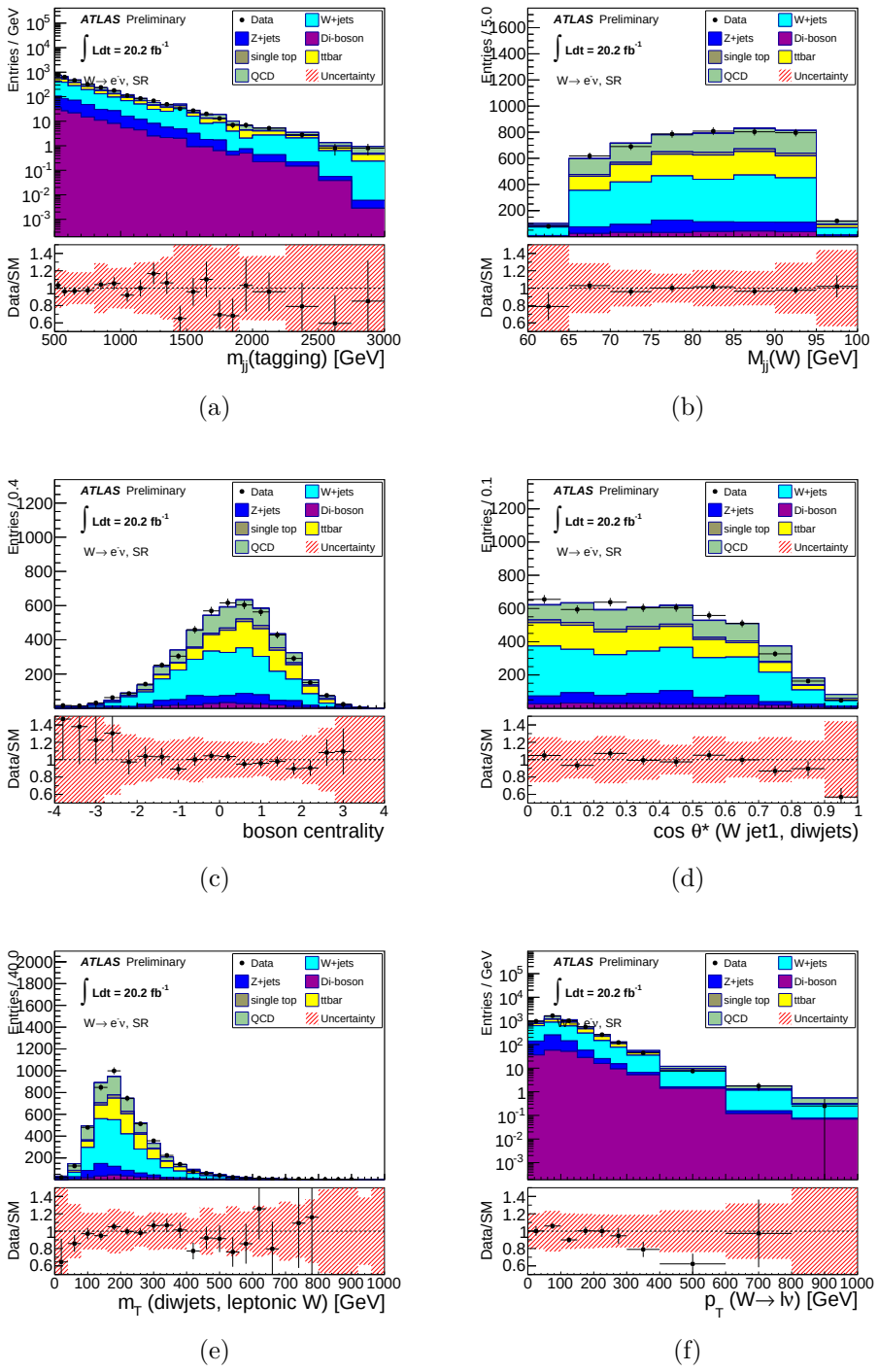

(a) (b) (c) (d) (e) (f)

Figure 45: Data-MC comparison for the loose VBS SR for the resolved selection in the e^- channel. $W+$jets samples have been scaled by the data-driven SF. (a) Tag jet di-jet mass, (b) W-jet di-jet mass, (c) boson centrality, (d) cos θ^* , (e) $m_{\mathrm{T}}(WV)$, (f) $p_T(W_{lep})$.

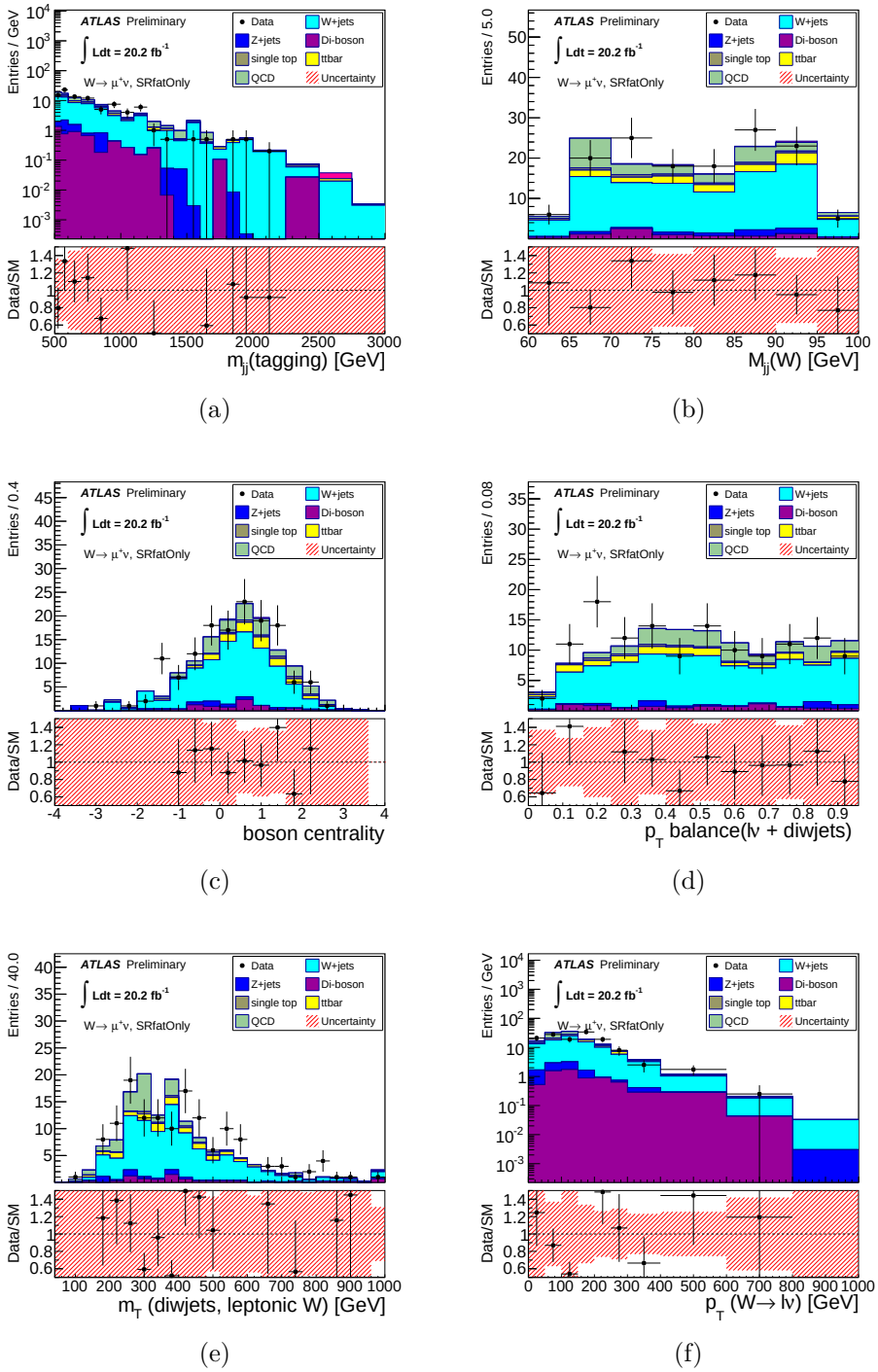

Figure 46: Data-MC comparison for the loose VBS SR for the merged selection in the μ^+ channel. $W+$jets samples have been scaled by the data-driven SF. (a) Tag jet di-jet mass, (b) W-jet di-jet mass, (c) boson centrality, (d) $\cos\theta^*$, (e) $m_{\mathrm{T}}(WV)$, (f) $p_T(W_{lep})$.

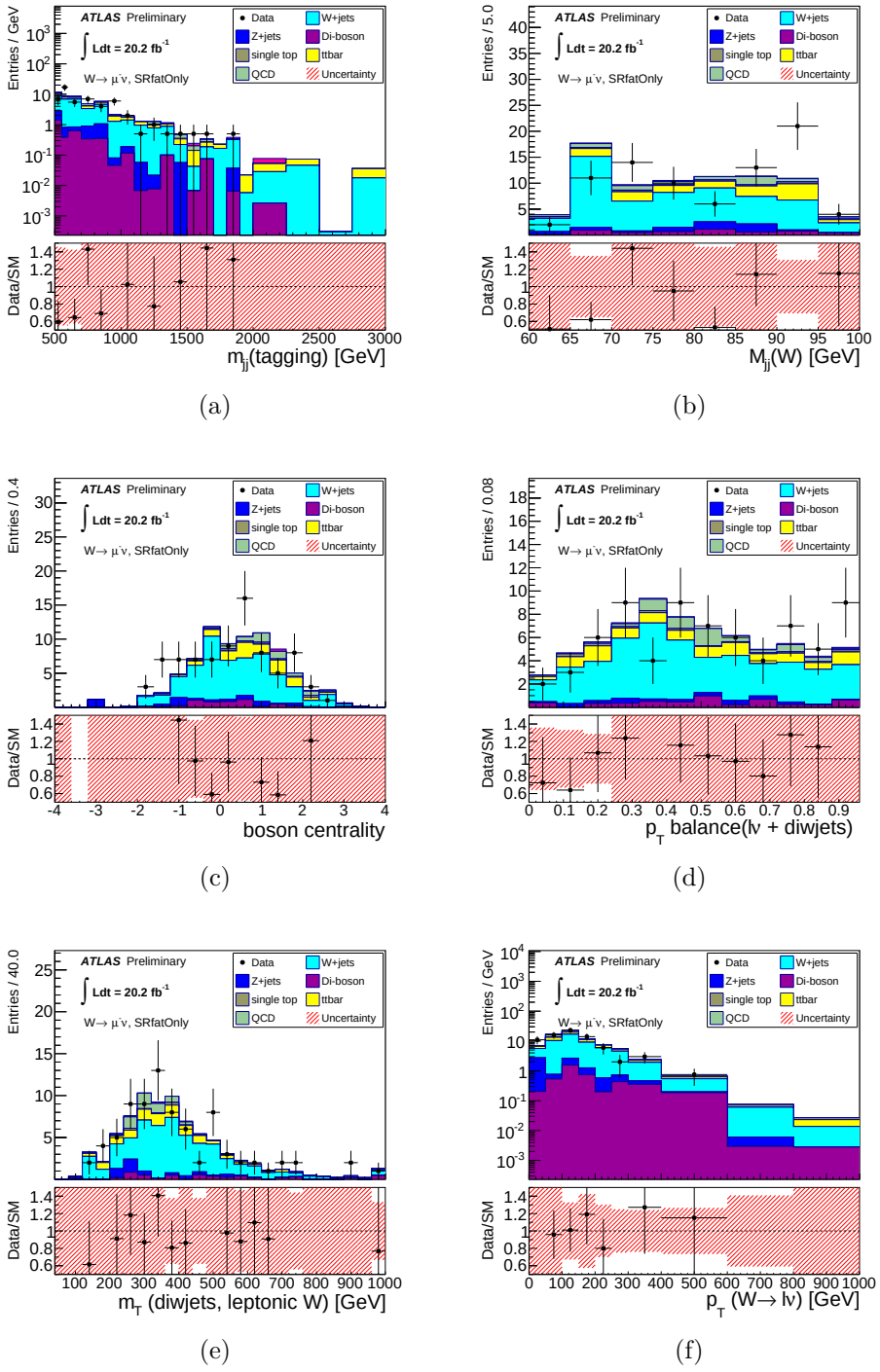

Figure 47: Data-MC comparison for the loose VBS SR for the merged selection in the μ^- channel. $W+$jets samples have been scaled by the data-driven SF. (a) Tag jet di-jet mass, (b) W-jet di-jet mass, (c) boson centrality, (d) cos θ^* , (e) $m_{\mathrm{T}}(WV)$, (f) $p_T(W_{lep})$.

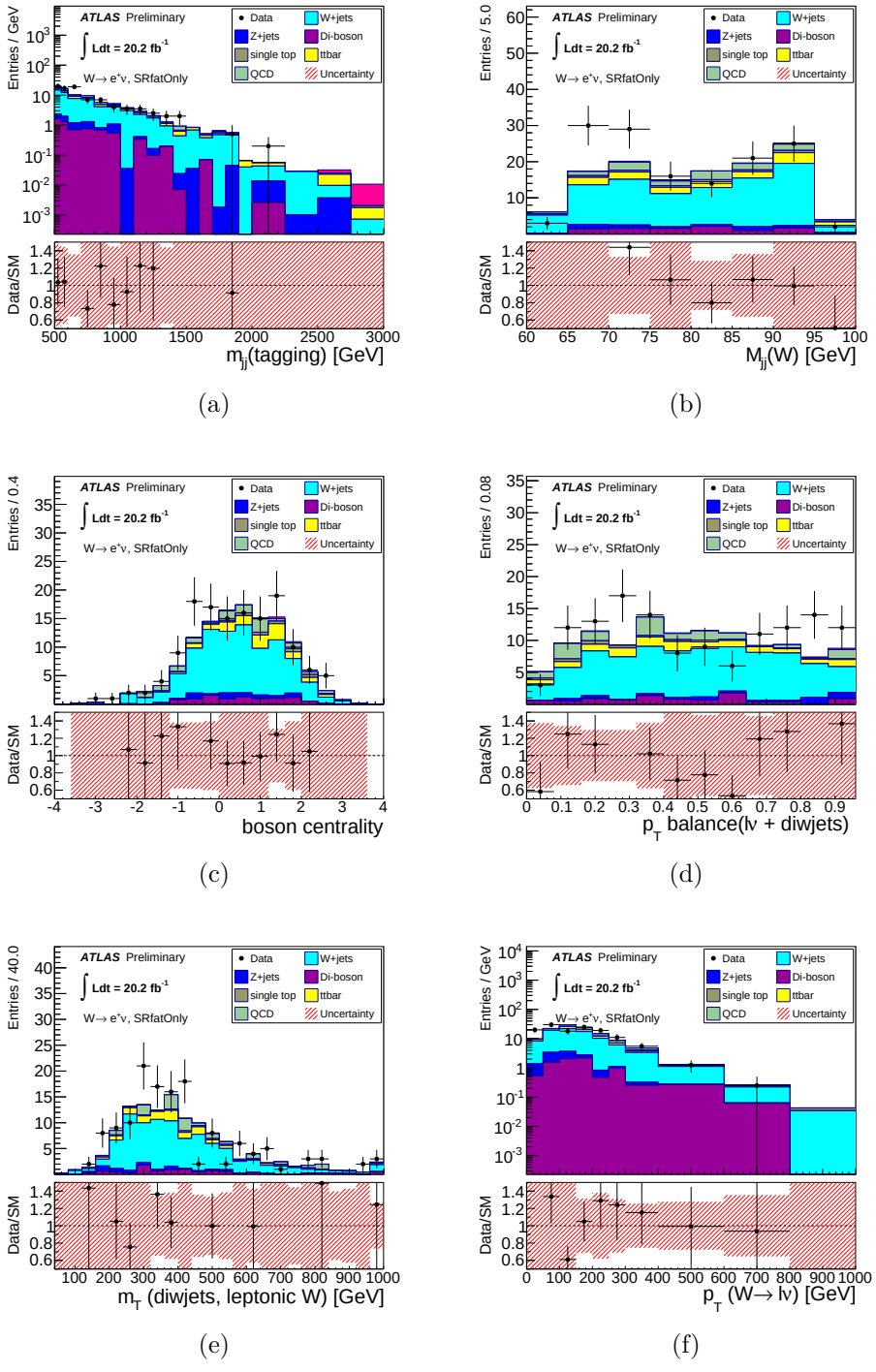

Figure 48: Data-MC comparison for the loose VBS SR for the merged selection in the e^+ channel. $W+$jets samples have been scaled by the data-driven SF. (a) Tag jet di-jet mass, (b) W-jet di-jet mass, (c) boson centrality, (d) cos θ^* , (e) $m_{\mathrm{T}}(WV)$, (f) $p_T(W_{lep})$.

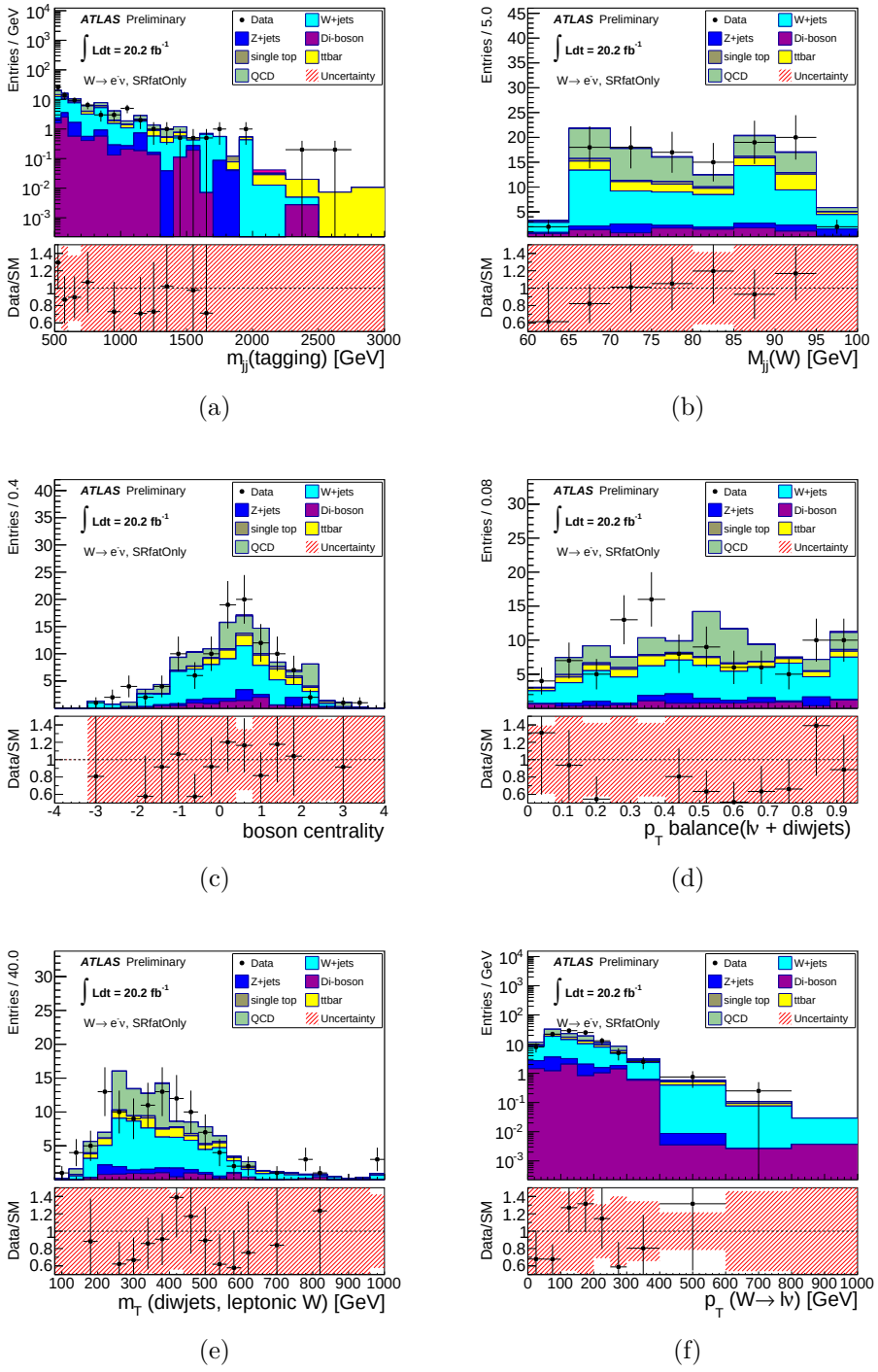

Figure 49: Data-MC comparison for the loose VBS SR for the merged selection in the e^- channel. $W+$jets samples have been scaled by the data-driven SF. (a) Tag jet di-jet mass, (b) W-jet di-jet mass, (c) boson centrality, (d) cos θ^* , (e) $m_{\mathrm{T}}(WV)$, (f) $p_T(W_{lep})$.

7.5 QCD multijet control region

There is a small background contribution from QCD multijet processes. This background comes primarily from jets misreconstructed as electrons, or from leptons originating from heavy-flavor decays inside jets. For simplicity all of these sources will be referred to as "fake" leptons. Because of the very high cross-section and low fake rate of these processes, and because of the difficulty in modeling the fake-rate, this background is difficult to estimate with MC. Therefore, a data-driven method has been used for multijet background estimation.

A fake-lepton-enriched region can be constructed by modifying the identification criteria of the leptons, to create "bad" lepton candidates. Bad electrons are required to pass the medium++ requirement but fail the tight++ one. For bad muons, the cut on the significance of the transverse component of the impact parameter, $|d_0/\sigma_{d_0}|$, is inverted with respect to the good muon definition, i.e. bad muons must satisify $|d_0/\sigma_{d_0}| > 3$. In order to improve the statistics and purity of the fake-enriched region, the isolation requirements on the bad lepton are also modified with respect to the good lepton definition. We require bad leptons to have $\Sigma E_T\text{Cone30}/p_T > 0.04$ and $\Sigma p_T\text{Cone30}/p_T$ <0.5.

The multijet background shape and yield are estimated in two separate steps.

The $m_{\text{T}}(WV)$ shape for the multi-jet background is taken from data, applying the optimized signal region cuts, except requiring a bad lepton instead of a good lepton. The data in this region are shown in Fig. 50, overlaid with the MC prediction for non-multijet events. We subtract off the non-multijet MC contributions from the data to obtain the multijet $m_{\text{T}}(WV)$ shape estimate. (However, as can be seen from the plots and from the yields in table 17 , the bad-lepton region has essentially no contamination from non-multijet events, so in this case the subtraction doesn't have an effect.)

To check how much the bad lepton isolation-requirement affects the kinematics, we create an alternative bad lepton definition, in which the isolation requirements are dropped entirely (the medium++ and d_0/σ_{d_0} selection are kept the same as for the nominal bad lepton definition). The data-MC comparison for the bad-lepton region (with optimized signal region cuts) using this modified bad-lepton definition, is shown in Fig. 51. This is an important cross-check, given that some of the single-lepton trigger objects used in the analysis already have cuts on a track isolation variable, $\Sigma p_T\text{Cone20}/p_T$ <0.1,

so we want to check for possible biases.

In order to estimate the multijet background yield in the signal region, we do a fit to the $E_T^{missing}$ data distribution, since this variable provides good separation between multijet backgrounds and the other main backgrounds. This technique has been used in several other ATLAS analyses involving $\ell + E_T^{missing}$+jets [106]. This analysis has a particular complication, though, caused by the $p_T(W_{lep} > 150GeV$ cut which is part of the optimized signal cuts. As can be seen in Fig. 53, the $p_T(W_{lep})$ cut removes almost all of the multijet background. This means that after the $p_T(W_{lep})$ cut has been applied, the data statistics are so small that any data-driven estimate is difficult. Furthermore, $(p_T(W_{lep}))$ is found to be positively correlated with the $E_T^{missing}$ in the muon channel. Therefore, after the $p_T(W_{lep})$ cut is applied, the $E_T^{missing}$ shape of the multijet background starts to closely resemble the other backgrounds, making an extraction of the multijet background yield even more difficult.

As a solution, the multijet yield is estimated in two steps. First, the yield is estimated with all cuts except for the $p_T(W_{lep})$ cut applied. To do this, the $E_T^{missing}$ cut is also removed, and the multijet $E_T^{missing}$ shape is estimated from the bad-lepton region, as illustrated in Fig. 54. This $E_T^{missing}$ shape is then used to perform an extended maximum likelihood fit to $E_T^{missing}$ in the good-lepton region, with no $E_T^{missing}$ or $p_T(W_{lep})$ cut. The $E_T^{missing}$ shapes for the multijet background, compared to the other background $E_T^{missing}$ shapes in the good-lepton region, are shown in Figures 55 and 56. The results of the fits to $E_T^{missing}$ are shown in Figures 57 and 58. The fitted multijet yields are then extrapolated to the $E_T^{missing} > 30$ GeV region. This gives a multijet yield estimate for the set of all cuts except for the $p_T(W_{lep})$ cut.

Finally, to estimate the final multijet yield for the full signal region cuts, the yield estimate from the previous step is extrapolated to the $p_T(W_{lep}) > 150GeV$ region. For this purpose, the $p_T(W_{lep})$ shape for the multijet background is estimated from the bad-lepton region, after applying all cuts except for the $p_T(W_{lep})$ cut. The final multijet yield estimates are shown in Table 18.

For muons, even in the fake-enriched region the data are consistent with zero for the merged selection. So for both the muon and anti-muon channels, template fitting becomes impossible. Because the yield is already zero in the fake region, our estimate for QCD in those two channels in the signal region is zero.

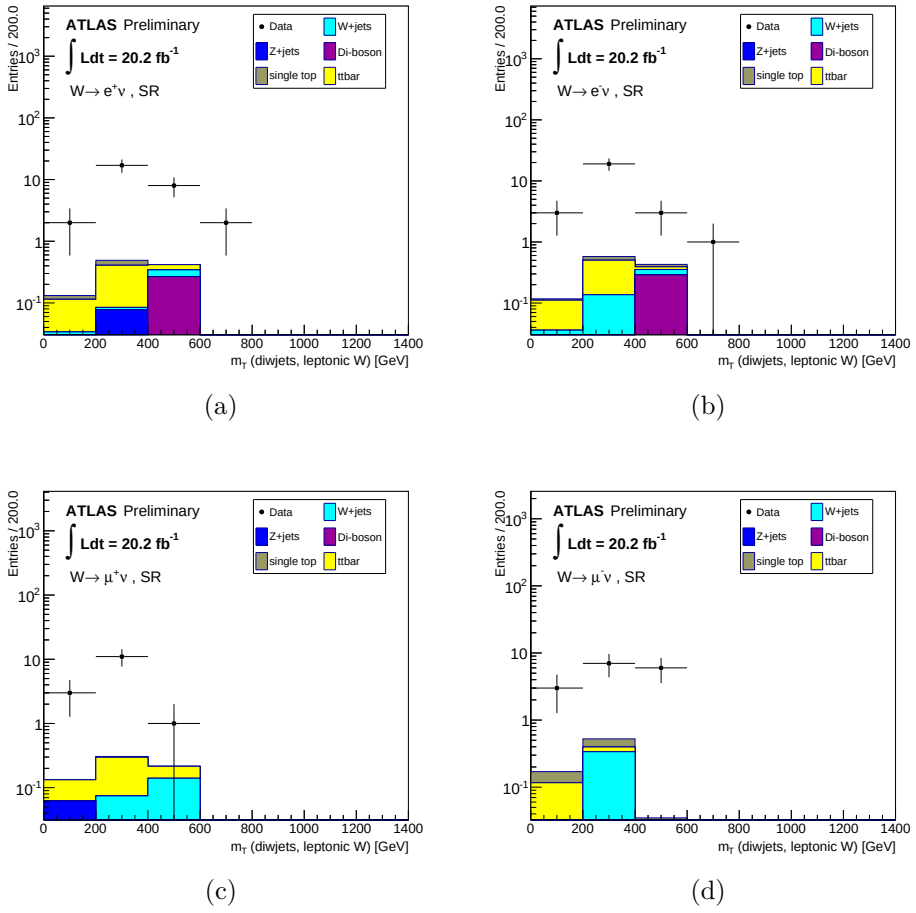

Figure 50: $m_{\mathrm{T}}(WV)$ plots for bad-lepton region, for resolved-jet selection with optimized cuts. Bad lepton definition includes $\Sigma E_T\mathrm{Cone30}/p_T$ >0.04 and $\Sigma p_T\mathrm{Cone30}/p_T$ <0.5. (a) e^+ channel, (b) e^- channel, (c) μ^+ channel, (d) μ^- channel.

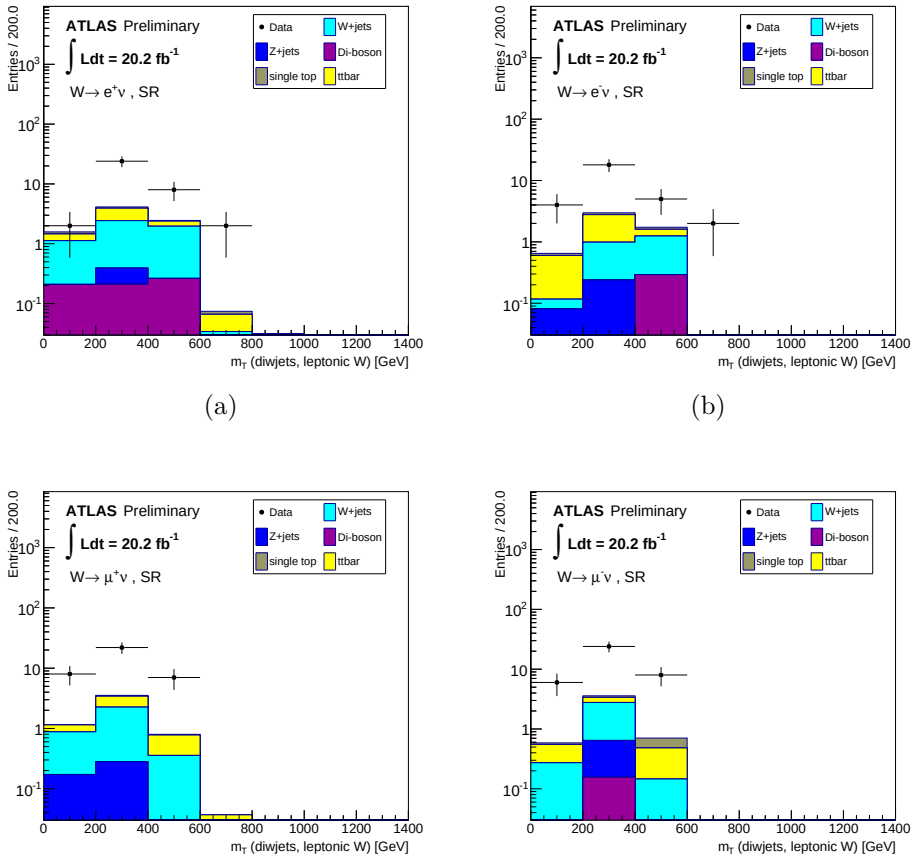

Figure 51: $m_{\mathrm{T}}(WV)$ plots for bad-lepton region, for resolved-jet selection with optimized cuts. Bad lepton definition does not have any isolation requirement. (a) e^+ channel, (b) e^- channel, (c) μ^+ channel, (d) μ^- channel.

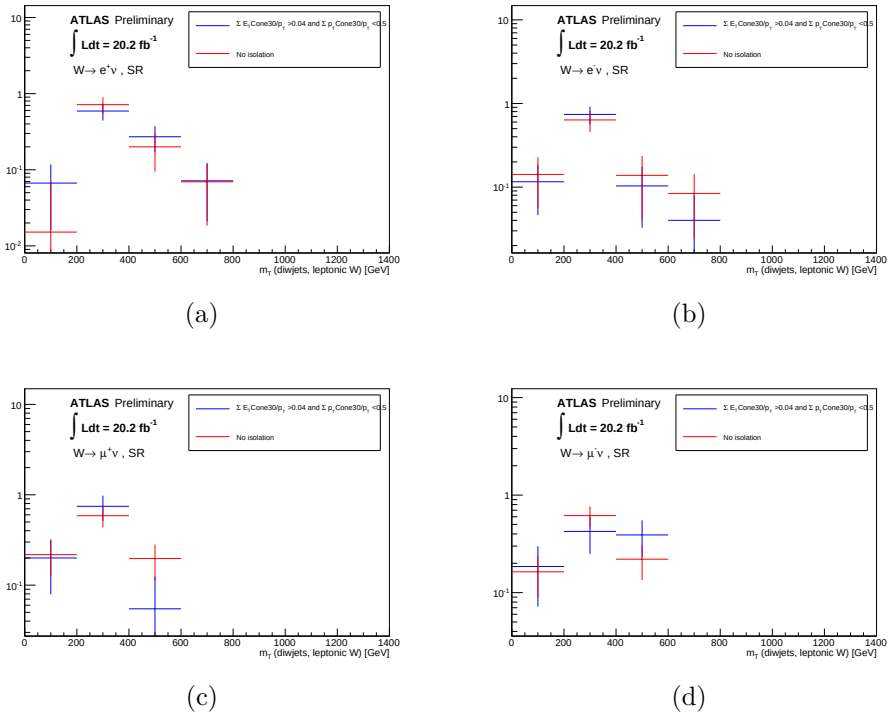

(a) (b)

(c) (d)

Figure 52: Comparison of $m_{\mathrm{T}}(WV)$ plots for the two bad-lepton definitions, for resolved-jet selection with optimized cuts. (a) e^+ channel, (b) e^- channel, (c) μ^+ channel, (d) μ^- channel.

Table 17: Observed and expected number of events in the bad lepton enriched region with otherwise optimized cuts , for the resolved and merged selections. $\Sigma E_T\mathrm{Cone30}/p_T > 0.04$ and $\Sigma p_T\mathrm{Cone30}/p_T < 0.5$ fake-lepton definition.

	multijet CR resolved				multijet CR merged			
	e^+	e^-	μ^+	μ^-	e^+	e^-	μ^+	μ^-
Data	29	26	15	16	13	4	4	4
W+jets	0.12±0.05	0.24±0.14	0.21±0.12	0.34±0.24	0.14±0.07	0.24±0.13	0.13±0.08	0.0±0.0
$t\bar{t}$	0.48±0.15	0.48±0.15	0.37±0.12	0.20±0.08	0.10±0.06	0.0±0.0	0.07±0.05	0.06±0.05
Total bkg	1.04±0.31	1.13±0.36	0.65±0.18	0.73±0.27	0.47±0.24	0.24±0.13	0.19±0.09	0.07±0.05
signal SM	0.0±0.0	0.0±0.0	0.05±0.05	0.0 ±0.0	0.0 ±0.0	0.0 ±0.0	0.0 ±0.0	0.0 ±0.0
signal (α_5=0.3)	0.28±0.13	0.22±0.1	0.07±0.07	0.0± 0.0	0.0±0.0	0.0±0.0	0.07±0.07	0.0±0.0
Bkg/Data	0.04±0.01	0.04±0.02	0.04±0.02	0.04±0.02	0.04±0.02	0.06±0.04	0.05±0.03	0.02±0.01
signal (α_5=0.3)/Data	0.01±0.005	0.01±0.005	0.005±0.005	0.0±0.0	0.0±0.0	0.0±0.0	0.01±0.01	0.0±0.0

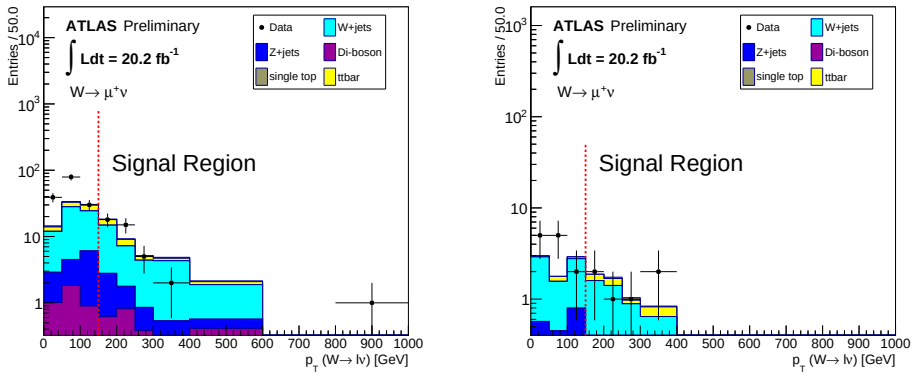

(a) (b)

Figure 53: $p_T(W_{lep})$ distribution from fake-enriched region for the μ^+ channel with loose VBS but without the $E_T^{missing}$ cut. (a) SR, (b) SRfatOnly.

Table 18: Observed and expected number of events in the optimized signal regions, for the resolved and merged selections. $\Sigma E_T\text{Cone30}/p_T > 0.04$ and $\Sigma p_T\text{Cone30}/p_T < 0.5$ fake-lepton definition.

	SR resolved				SR merged			
	e^+	e^-	μ^+	μ^-	e^+	e^-	μ^+	μ^-
Data	94	66	67	54	15	6	4	5
W+jets	51.6±3.3	30.5±2.2	48.6±3.0	25.9±2.4	7.7±1.0	3.7±0.7	6.4±0.9	4.2±0.7
$t\bar{t}$	29.6±1.1	32.6±1.1	25.4±1.0	25.6±1.0	2.1±0.3	1.5±0.2	1.8±0.3	1.5±0.2
Z+jets	1.8±0.4	1.8±0.5	1.8±0.5	1.2±0.3	0.3±0.2	0.1±0.1	0.0±0.0	0.1±0.1
single top	5.2±0.4	2.8±0.3	4.2±0.3	2.5±0.3	0.7±0.1	0.5±0.1	0.7±0.1	0.2±0.1
Diboson	4.3±0.9	4.7±0.9	3.1±0.7	4.3±0.9	0.6±0.3	0.1±0.1	0.3±0.2	0.2±0.2
QCD	12.6±2.2	10.7±2.3	1.2±0.7	0.2±0.8	0.3±0.2	2.1±1.7	0.0	0.0

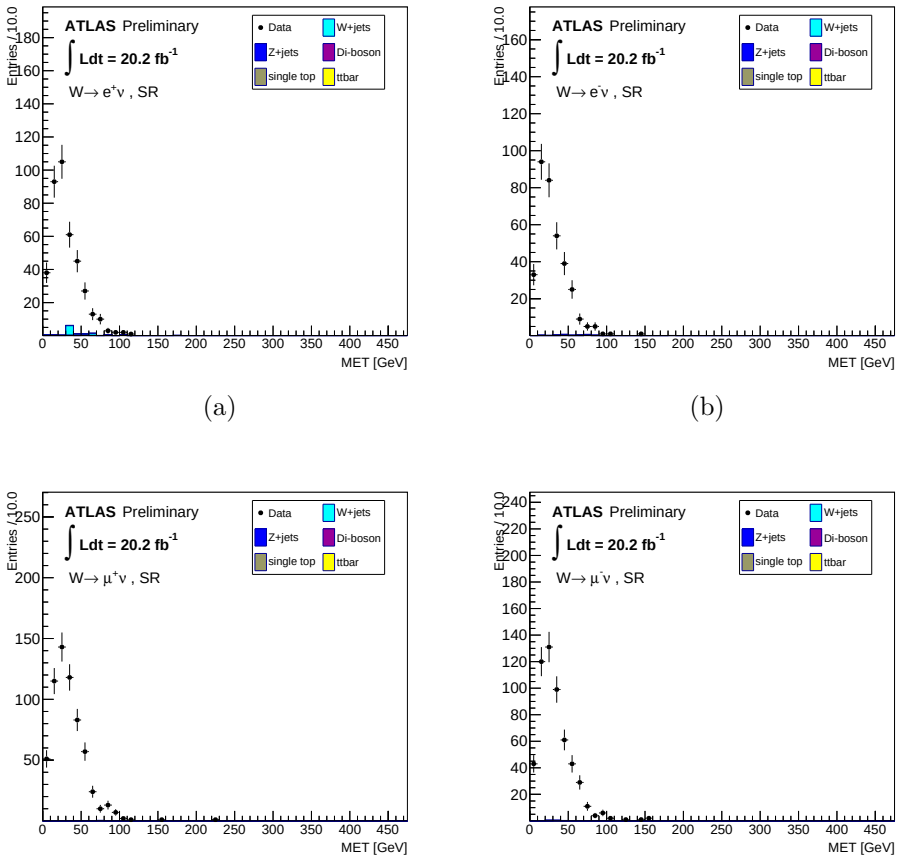

Figure 54: $E_T^{missing}$ plots for resolved jet fake region with optimized cuts but without the $p_T(W_{lep}) > 150GeV$ cut. For fakes $\Sigma E_T\text{Cone30}/p_T$ >0.04 and $\Sigma p_T\text{Cone30}/p_T$ <0.5. (a) e^+ channel, (b) e^- channel, (c) μ^+ channel, (d) μ^- channel.

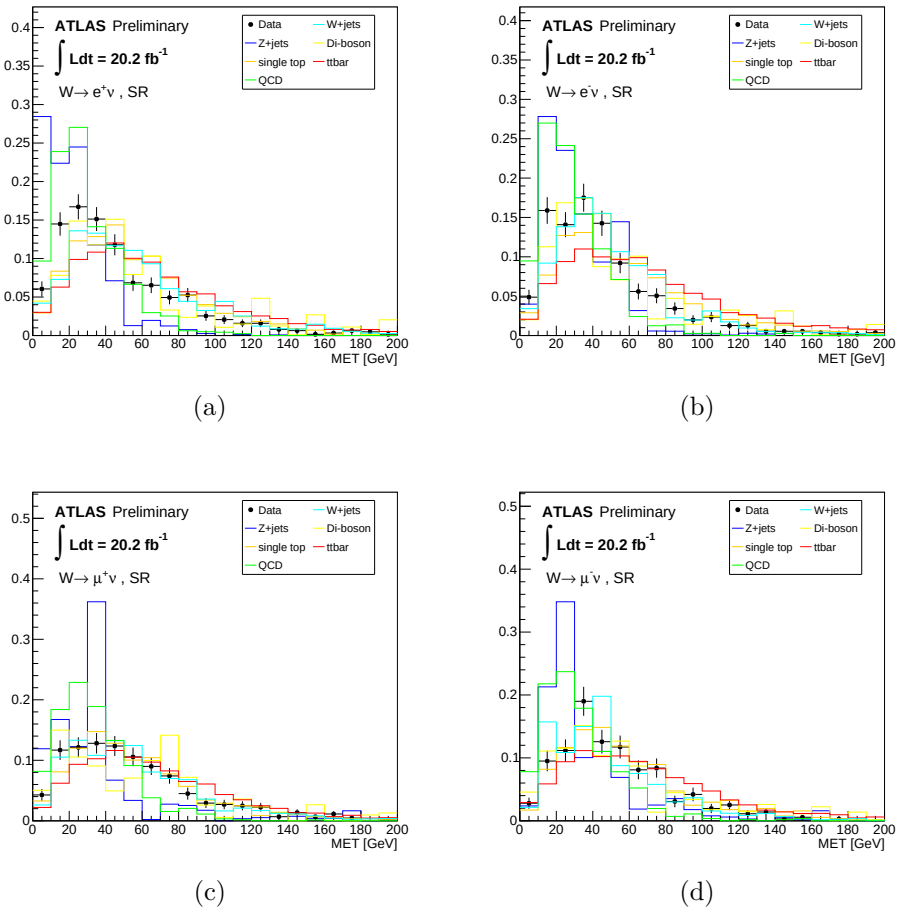

Figure 55: Comparison of $E_T^{missing}$ shapes between multijet, data, and other backgrounds for the resolved jet selection with optimized cuts but without the $p_T(W_{lep}) > 150$ GeV cut. Each histogram is normalized to 1. (a) e^+ channel, (b) e^- channel, (c) μ^+ channel, (d) μ^- channel.

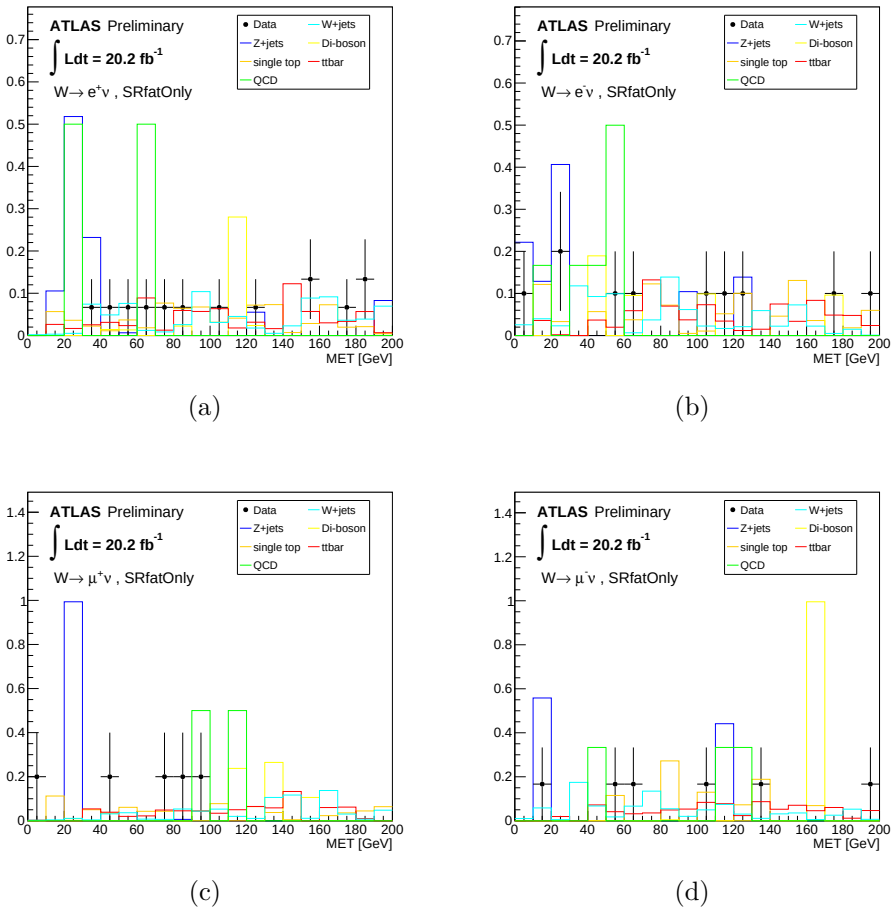

Figure 56: Comparison of $E_T^{missing}$ shapes between multijet, data, and other backgrounds for boosted jet selection for optimized cuts but without the $p_T(W_{lep}) > 150GeV$ cut. Each histogram is normalized to 1. (a) e^+ channel, (b) e^- channel, (c) μ^+ channel, (d) μ^- channel.

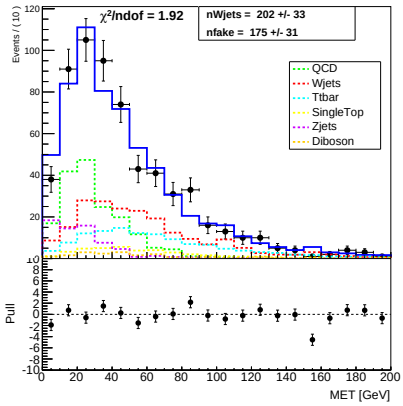

(a)

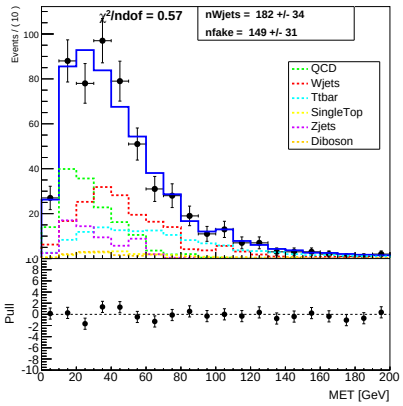

(b)

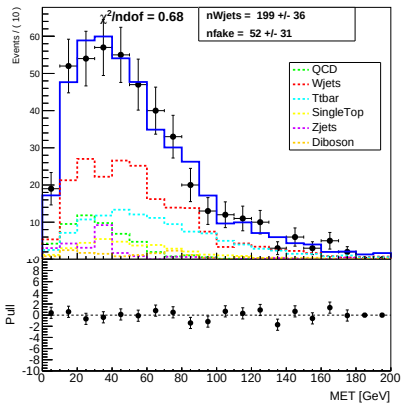

(c)

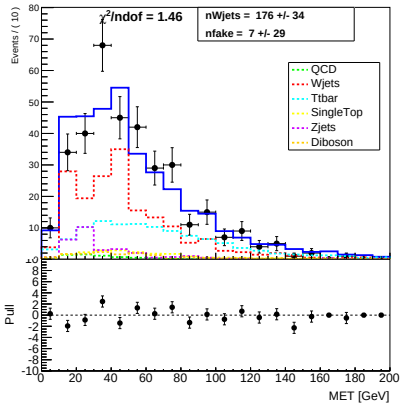

(d)

Figure 57: QCD fit plots for resolved jet selection with optimized cuts but without the $p_T(W_{lep}) > 150GeV$ cut. The blue line indicates the sum of all the fit components. (a) e^+ channel, (b) e^- channel, (c) μ^+ channel, (d) μ^- channel.

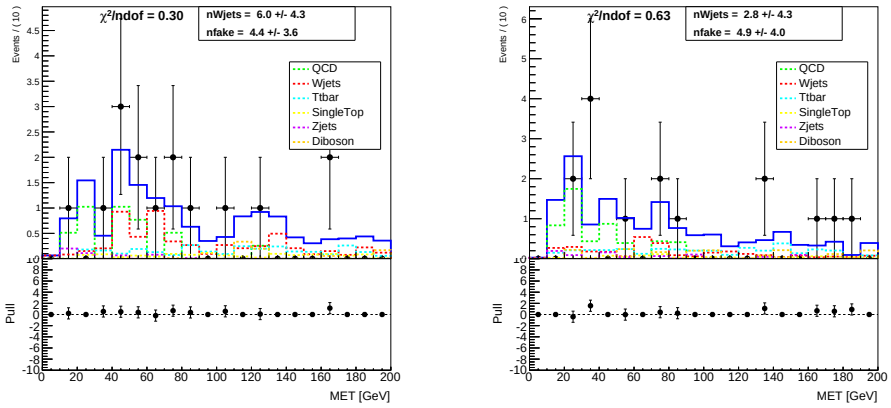

(a) (b)

Figure 58: QCD fit plots for boosted jet selection with optimized cuts but without the $p_T(W_{lep}) > 150GeV$ cut. The blue line indicates the sum of all the fit components. (a) e^+ channel, (b) e^- channel.

7.6 Cross-check of $p_T(W_{lep})$ extrapolation

As explained previously, the multijet yield is estimated by first performing an $E_T^{missing}$-fit to data without a $p_T(W_{lep})$ cut, and then using extrapolation to estimate the number of multijet events surviving the $p_T(W_{lep})$ cut. The validity of this extrapolation technique is checked by comparing this method to a simpler method, where the multijet yield is estimated directly from an $E_T^{missing}$-fit to data after applying the $p_T(W_{lep})$ cut. For this validation test, only the loose VBS cuts are used, rather than the optimized cuts, in order to have sufficient statistics.

The comparison of these two methods is shown in Fig. 59, for the resolved selection only. For electron channels the two methods give consistent results. For the muon channels the two methods are also consistent, although with large fit uncertainties. This behavior is expected because, as pointed out earlier, in the μ channels, the high $p_T(W_{lep})$ cut distorts the $E_T^{missing}$ distribution of fakes to make it look more like other backgrounds, thus degrading the fit quality.

The extrapolation method gives a multijet yield that is consistent with the alternative method, but with considerably smaller uncertainty. The uncertainty on the extrapolation method is calculated by quadratically adding the fit uncertainty on the multijet yield (without a $p_T(W_{lep})$ cut) and the uncertainty on the $p_T(W_{lep})$ cut efficiency (assuming binomial statistics).

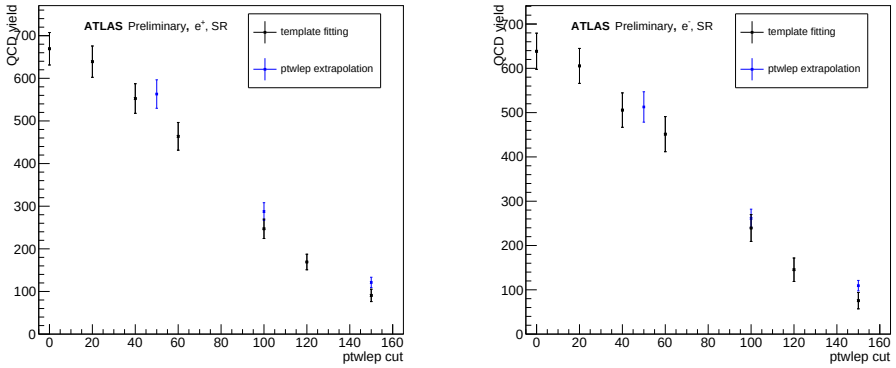

(a)

(b)

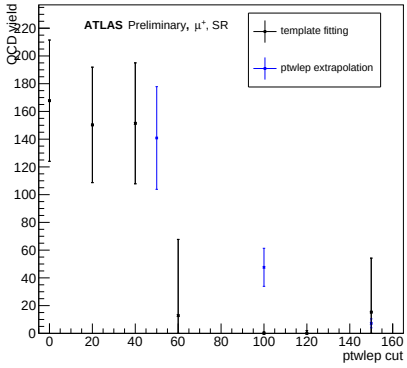

(c)

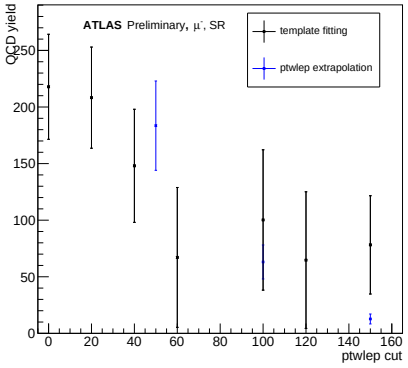

(d)

Figure 59: QCD yield against the $p_T(W_{lep})$ cut for resolved jet selection with loose VBS cuts. Yield denoted by black points are obtained by $E_T^{missing}$ template fitting with the $p_T(W_{lep})$ cut in place, the blue points were obtained by first removing the $p_T(W_{lep})$ cut and then using the $p_T(W_{lep})$ distribution to extrapolate the yield. (a) e^+ channel, (b) e^- channel, (c) μ^+ channel, (d) μ^- channel.

Table 19: Summary of the fractional uncertainty on the signal and total background yields, broken down into different categories of systematic uncertainties. The systematic uncertainties are given in three different signal regions: the merged signal region and the resolved signal regions (separated into positive and negative lepton charges). The three regions correspond to the regions used for the final limit setting, as explained in Section 9.4.

	Signal			Background		
Systematic	*merged*	*resolved,* ℓ^+	*resolved,* ℓ^-	*merged*	*resolved,* ℓ^+	*resolved,* ℓ^-
multijet yield	0	0	0	0.05	0.10	0.08
$t\bar{t}$ modeling	0	0	0	0.06	0.08	0.21
W/Z + jets modeling	0	0	0	0.25	0.12	0.13
W + jets scale factor	0	0	0	0.11	0.10	0.07
minor bkg yields	0	0	0	0.05	0.04	0.04
signal modeling	0.25	0.17	0.13	0	0	0
JES and JER	0.13	0.08	0.15	0.22	0.19	0.23
other detector/lumi	0.03	0.03	0.03	0.03	0.04	0.04
limited stats in MC or CR	0.06	0.05	0.08	0.07	0.03	0.03
Total	0.29	0.20	0.21	0.38	0.28	0.36

8 Systematic Uncertainties

As described in Section 9, the aQGC limits are extracted from a fit to $m_{\mathrm{T}}(WV)$. Systematic uncertainties are evaluated both for the normalizations of the background and signal, but also on the $m_{\mathrm{T}}(WV)$ shapes of the background and signal. Source of systematic uncertainties can be categorized into mainly two groups, one the theoretical uncertainty in modeling the signal and background Monte Carlo, and the other experimental uncertainty in detection, reconstruction and identification of physics objects. Different sources of systematic uncertainties and their estimation are described in this section.

The normalization effect of the various systematic uncertainties on the signal and background is summarized in Table 19. The effect on the background in the control regions is summarized in Table 20. More details on the sizes of the uncertainties as a function of $m_{\mathrm{T}}(WV)$ and correlations between $m_{\mathrm{T}}(WV)$ bins are given in Appendix I.

The rest of this section explains these various systematic uncertainties and how they are calculated.

Table 20: Summary of the fractional uncertainty on the total background yields in the top quark and W+jets control regions, broken down into different categories of systematic uncertainties. The systematic uncertainties are given in three different regions: the merged region and the resolved regions (separated into positive and negative lepton charges). The three regions correspond to the regions used for the final limit setting, as explained in Section 9.4.

	CR_Top			CR_Wjj		
Systematic	*merged*	*resolved,* ℓ^+	*resolved,* ℓ^-	*merged*	*resolved,* ℓ^+	*resolved,* ℓ^-
$t\bar{t}$ modeling	0.28	0.23	0.22	0.07	0.12	0.13
W/Z + jets modeling	0.05	0.01	0.01	0.39	0.20	0.21
W + jets scale factor	0.01	0.01	0.0	0.10	0.11	0.09
JES and JER	0.17	0.16	0.16	0.19	0.16	0.18
other detector/lumi	0.03	0.02	0.01	0.02	0.04	0.01
limited stats in MC or CR	0.08	0.02	0.02	0.06	0.04	0.05
Total	0.34	0.28	0.27	0.45	0.32	0.33

8.1 Jet systematics

As this analysis has several jets in the final state, understanding the systematic uncertainty that arises from measurement of jet energy is of utmost importance. The largest experimental source of systematic uncertainty in this analysis comes from jet energy scale and resolution uncertainties. Jet uncertainties are considered both for small-R and large-R jets.

For small-R jets, the uncertainties due to the jet energy scale (JES) and the jet energy resolution (JER) are considered.

In order to evaluate the jet uncertainties the ATLAS recommendations have been followed. The JES uncertainties are broken down into 18 different components, following an official ATLAS recipe [107]. The components are:

- Six nuisance parameters summarizing various in-situ measurements used for jet calibration [98]. The in-situ measurements exploit the transverse momentum balance between a jet and a reference object. For central jets ($|\eta| < 1.2$), the reference object is a photon or a Z-boson. For forward jets, a dijet p_T balance measurement was used.

- Two from η intercalibration due to modeling and statistics. η intercalibration is performed using a dijet tranverse momentum balance

method.

- One for the behavior of high-p_T jets. High-p_T jets were calibrated using the multijet balance method. The transverse momentum of high-p_T jet was calculated from the momentum of the properly calibrated sub-leading jet system at a lower p_T scale.

- One for Monte Carlo (MC) non-closure relative to MC12a, a particular Monte Carlo production for 2012 data which was the baseline sample with which the calibrations were derived. This term is applied if the MC sample is not MC12a.

- Four components to describe pileup-related uncertainties. They are uncertainties on N_{PV}, μ, $\mathrm{p_T}$ and ρ terms of pileup offset (see Eq. 45).

- Two components from flavor composition and flavor response uncertainty. Jet energy scale is sensitive to the flavor of the originating parton. These components take into account the difference in fragmentation and showering properties of, and calorimeter response to light quark induced and gluon induced jets.

- Uncertainty due to punch-through jets.

- b-jet energy scale.

Each of these systematics can be varied up and down. The effect of these systematic uncertainties being varied "up" is shown in Fig. 60 and Fig. 62.

For large-R jets, four uncertainties are considered, following the recipe in Ref. [108]:

- The uncertainty on the jet momentum scale (JPTS).

- The uncertainty on the jet momentum resolution (JPTR).

- The uncertainty on the jet mass scale (JMS).

- The uncertainty on the jet mass resolution (JMR).

The uncertainties due to transverse momenta and mass scale and resolution have been presented in Fig. 62. The scale uncertainties are among the largest sources of uncertainties in the merged jet selection cases.

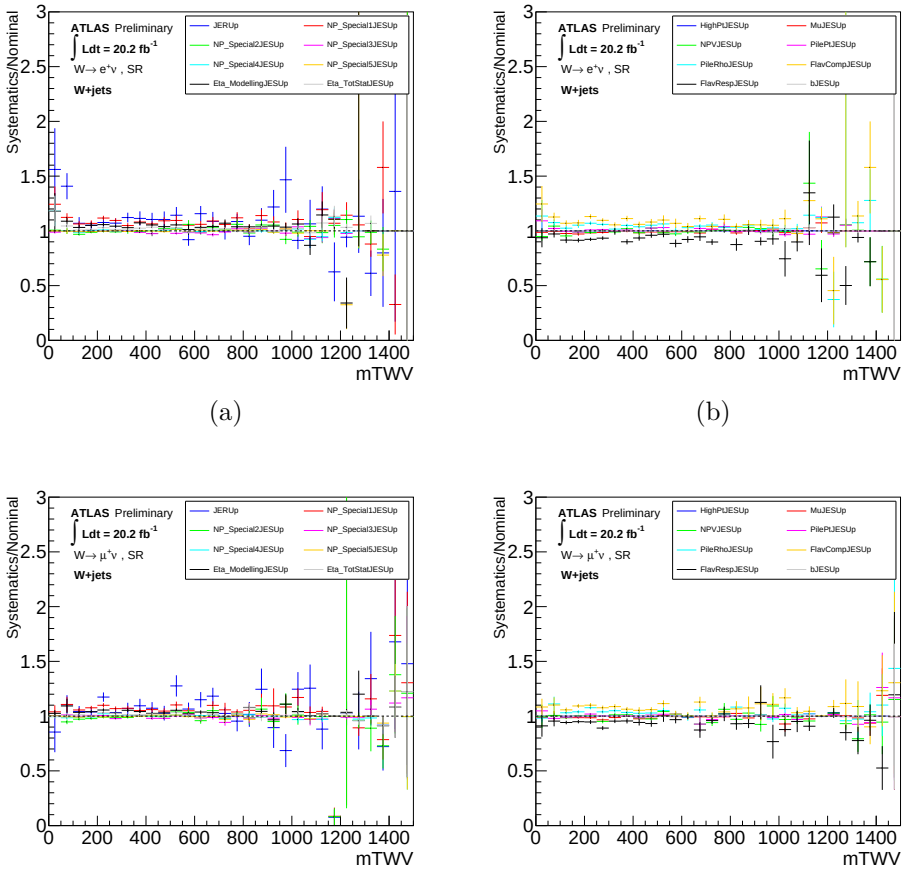

Figure 60: Effect of JER and JES sytematics on the $m_{\mathrm{T}}(WV)$ distributions. Loose VBS cuts are in place. The JER and fifteen components of JES systematics have been split into two groups. (a) and (b) show these systematics for the positron channel in the resolved selection case. (c) and (d) show the same for μ^{+}.

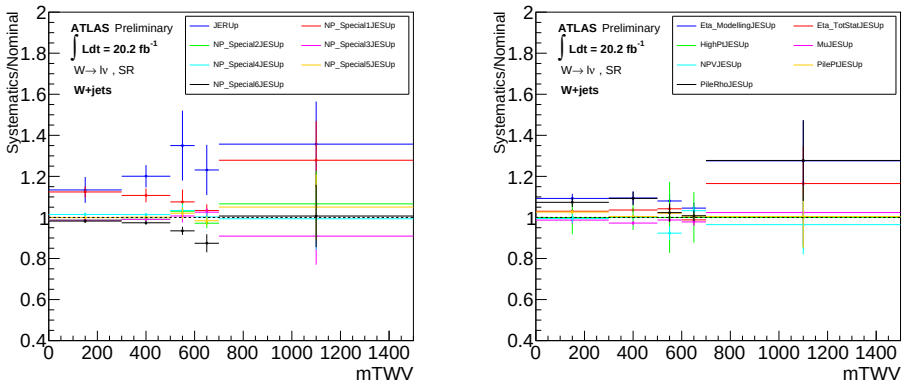

Figure 61: Effect of various sytematics on the $m_{\mathrm{T}}(WV)$ distributions. These plots are for resolved selection with optimized SR cuts in place. The components of systematics have been split into several groups. All lepton flavors added together.

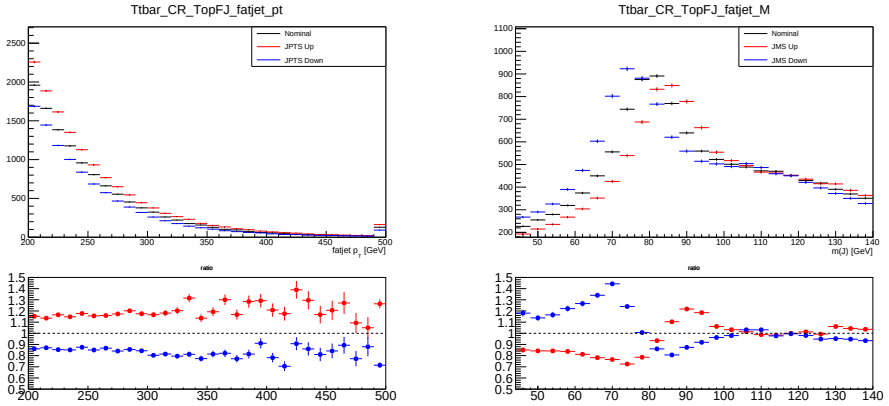

(a)

(b)

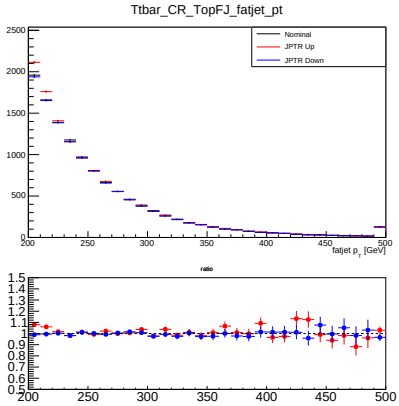

(c)

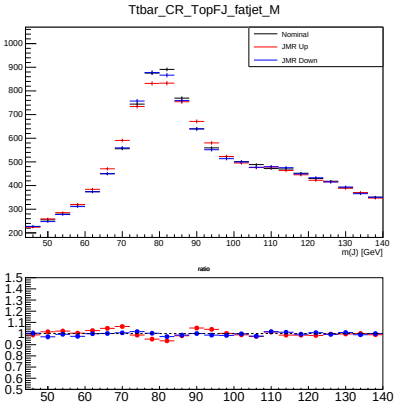

(d)

Figure 62: Comparison of Nominal against large-R jet systematics. (a) p_T scale, (b) mass scale, (c) p_T resolution and (d) mass resolution.

8.2 Lepton systematics

Sources for lepton uncertainties include energy scale and resolution uncertainties. There were also uncertainties related to the scale factors used to correct mismodelling of trigger, identification and reconstruction efficiency and isolation in the MC. The official *egammaAnalysisUtils* and *MuonMomentumCorrections* tools as mentioned in Table 4 are used for this.

8.3 $E_T^{missing}$ systematics

The uncertainties on the energy and momentum measurement of different calibrated objects (electron, muon, jets etc.) are propagated to the calculation of $E_T^{missing}$. There is also a contribution from clusters and tracks that are not associated with the above mentioned objects, called the soft terms. The energy scale and resolution uncertainties from soft terms are considered as additional uncertainties. The tools *MissingETUtility* and *METSystematics* as menitioned in Table 4 are used for this purpose.

8.4 W/Z + jets modeling

To account for systematic uncertainties in the W/Z + jets model (not including VBF W + jets), we compare the nominal W + jets Sherpa sample to alternative W + jets Sherpa samples generated with varied parameters. The nominal factorization and renormalization scale for the W/Z + jets production is the mass of the vector boson: $\mu_F = \mu_R$ =M(V). The following Sherpa parameters are varied:

- Factorization scale: varied to 2.0 × (*nominal*) and 0.5 × (*nominal*)
- Renormalization scale: varied to 2.0 × (*nominal*) and 0.5 × (*nominal*)
- Merging scale for the parton shower and matrix element, in the CKKW scheme. Merging scales of $Q_{\text{cut}} = 15$ GeV and $Q_{\text{cut}} = 30$ GeV are tried (instead of the default scale of 20 GeV).

The effect of these parameter variations on the W + jets background in the resolved and merged signal regions is shown in Fig. 63, for the loose VBS cuts plus the $pT(W_{lep}) > 150GeV$ cut. Both the systematic effect on the W + jets normalization and the effect on the $m_{\text{T}}(WV)$ shape are considered.

The largest effect is caused by the renormalization scale variation. The uncertainty on the W + jets normalization in the signal region due to the model variation is about 30-40%.

The modeling uncertainty is also investigated by looking into W + jets samples produced by the Alpgen generator. Sherpa and Alpgen agree in their modeling within the theoretical systematic uncertainty for loose VBS cut as can be seen in Fig. 64. We further investigated the modeling by adding $p_T(W_{lep})$ cut as shown in Fig. 65 and Fig. 66. Good agreement is seen in all cases and therefore no additional systematic uncertainty is assigned due to generator modeling.

8.5 $t\bar{t}$ systematics

Systematic uncertainties on the $t\bar{t}$ model from the following sources were evaluated:

- Generator. Take the difference between Powheg+fHerwig and MC@NLO+fHerwig.
- Parton shower/fragmentation model. Take the difference between Powheg+Pythia6 and Powheg+fHerwig.
- Initial State Radiation (ISR)/Final State Radiation (FSR) uncertainty. Take half of the difference between AcerMC samples generated with ISR "up" and ISR "down."

8.6 Other background systematics

Contributions from VBF W+jets, diboson (WW, WZ, $W\gamma$, ZZ) and single-top are small. A 50% normalization uncertainty is included on each of them to account for possible mismodeling of their contributions to this analysis's phasespace. These systematics don't have a large effect on the expected limits; if the diboson and single-top normalization uncertainties are increased to 100%, this only makes the expected limits 2% worse than when using the default choice of 50%.

8.7 Signal systematics

To account for uncertainties in the signal modeling, the following systematics are considered: scale variations, parton shower/hadronization model, and PDF variations.

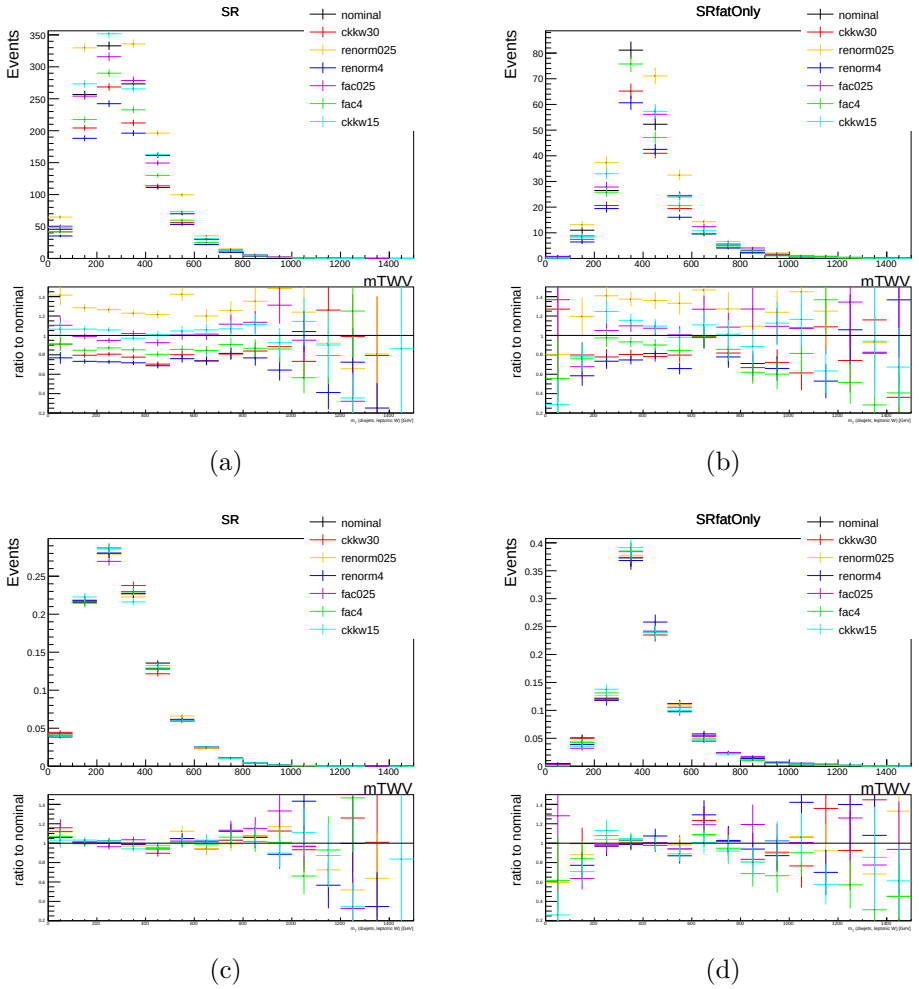

Figure 63: Sherpa W + jets modeling systematics for $m_{\mathrm{T}}(WV)$. The plots give the ratio of the systematic Sherpa sample to the nominal Sherpa sample. Plots (a) and (b) show the resolved and merged signal regions, respectively, showing the effect of the systematic on the normalization and $m_{\mathrm{T}}(WV)$ shape. Plots (c) and (d) are identical to (a) and (b), except that all samples are normalized to the same area, so that only the effect of the systematics on the $m_{\mathrm{T}}(WV)$ shape is shown, not the normalization effect. The plots are made for the loose VBS selection plus the $p_T(W_{lep}) > 150GeV$ cut.

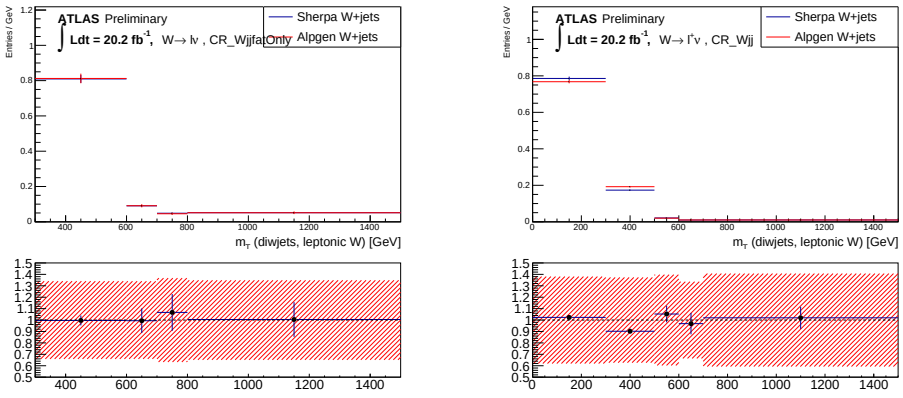

(a)

(b)

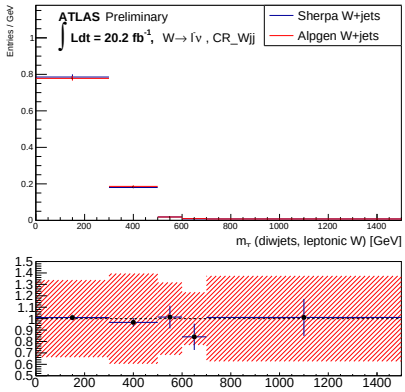

(c)

Figure 64: Comparison of $W+$jets modeling with Sherpa and Alpgen generators. The plots are made for the loose VBS selection. They show $m_{\mathrm{T}}(WV)$ distribution normalized to unity for Sherpa and Alpgen for (a) the W+jets merged control region, $e+$, $e-$, $\mu+$, and $\mu-$ combined; (b) the W+jets resolved control region, $e+$ and $\mu+$ combined; and (c) the resolved region, $e-$ and $\mu-$ combined. The systematic uncertainty due to renormalization, factorization and CKKW merging scale variation in Sherpa has been shown in the ratio plot as the systematics band in the bottom panel.

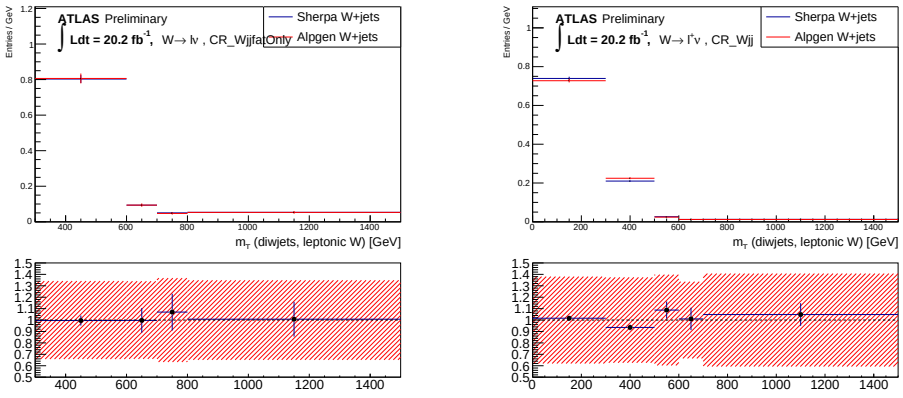

(a)

(b)

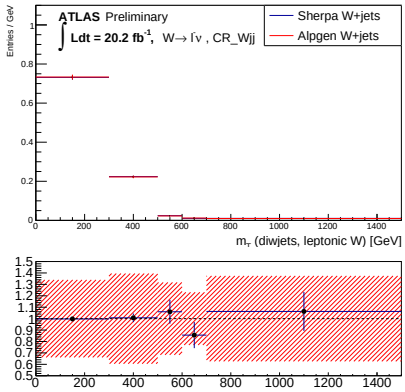

(c)

Figure 65: Comparison of W + jets modeling with Sherpa and Alpgen generators. The plots are made for the loose VBS selection plus the $p_T(W_{lep}) > 50GeV$ cut. They show $m_{\mathrm{T}}(WV)$ distribution normalized to unity for Sherpa and Alpgen for (a) the W+jets merged control region, $e+$, $e-$, $\mu+$, and $\mu-$ combined; (b) the W+jets resolved control region, $e+$ and $\mu+$ combined; and (c) the resolved region, $e-$ and $\mu-$ combined. The systematic uncertainty band shown in the bottom panel is due to renormalization, factorization and CKKW merging scale variation in Sherpa.

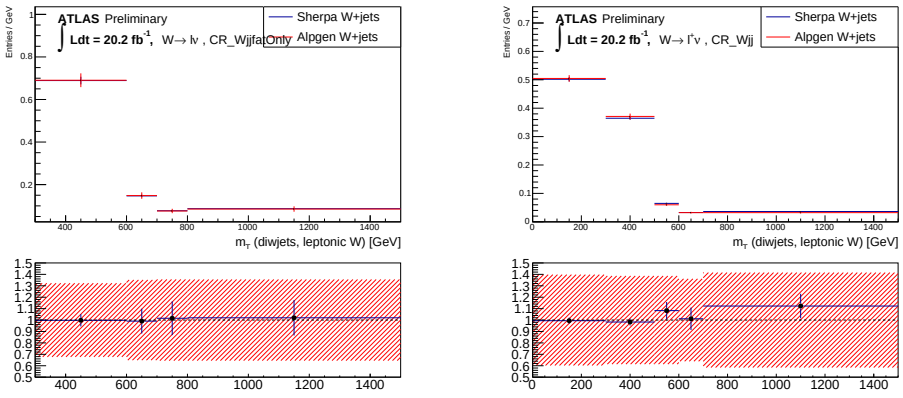

(a)

(b)

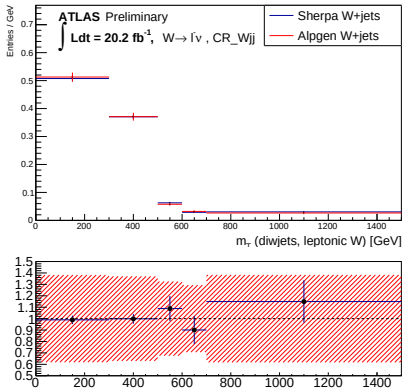

(c)

Figure 66: Comparison of $W+$jets modeling with Sherpa and Alpgen generators. The plots show $m_{\mathrm{T}}(WV)$ distribution normalized to unity for Sherpa and Alpgen for (a) the W+jets merged control region, $e+$, $e-$, $\mu+$, and $\mu-$ combined; (b) the W+jets resolved control region, $e+$ and $\mu+$ combined; and (c) the resolved region, $e-$ and $\mu-$ combined. The plots are made for the loose VBS selection plus the $p_T(W_{lep}) > 150GeV$ cut. The systematic uncertainty band shown in the bottom panel is due to renormalization, factorization and CKKW merging scale variation in Sherpa.

The default factorization and renormalization scale for the signal generation is the invariant mass of the di-boson system: $\mu_F = \mu_R = m(WV)$. In order to look at systematic variations, the scales μ_F and μ_R were independently varied up and down by a factor of two: $(0.5\mu_F, 0.5\mu_R)$, $(0.5\mu_F, \mu_R)$, $(0.5\mu_F, 2\mu_R)$, $(\mu_F, 0.5\mu_R)$, $(\mu_F, 2\mu_R)$, $(2\mu_F, 0.5\mu_R)$, $(2\mu_F, \mu_R)$, $(2\mu_F, 2\mu_R)$. We take the $(2\mu_F, 2\mu_R)$ and $(0.5\mu_F, 0.5\mu_R)$ variations as the "up" and "down" systematics, which was found to reasonably cover the variation of the 8 samples. The uncertainty on the signal normalization in the signal region due to the scale variations is about 10%.

The parton shower and hadronization model systematic is done by comparing signal samples showered with Pythia8 to samples showered with Herwig++. The PDF systematic is calculated by changing the PDF set from CT10 to CTEQ6.

8.8 Smoothing and symmetrization

Most of the systematics mentioned in this section can affect both the $m_{\mathrm{T}}(WV)$ shape and the event yields of background/signal components. However, due to limited MC statistics, the effect on the $m_{\mathrm{T}}(WV)$ shape is subject to large statistical fluctuations. Smoothing out these fluctuations is necessary; otherwise, the systematics would be severely overestimated. For the nominal analysis, we use a simple linear-approximation of the systematics, i.e., we assume the ratio $N_{\mathrm{syst}}/N_{\mathrm{nom}}$ can be modeled by a first-order polynomial in $m_{\mathrm{T}}(WV)$. This seems to be a reasonable approximation, given the limited statistics available. Also, as shown in Sec. 9.4, in the final analysis, we only use 4 or 5 bins in $m_{\mathrm{T}}(WV)$, so a detailed knowledge of the $m_{\mathrm{T}}(WV)$ dependence is not so important. An example of the smoothing technique is shown in Fig. 67.

To cross-check the smoothing method, we tried an alternative smoothing technique which just consisted of coarsely binning the systematics in $m_{\mathrm{T}}(WV)$ (no linear approximation). This technique gave slightly better limits (about 5% better expected aQGC limits than using the linear-approximation smoothing), so we decided to use the linear-approximation smoothing in order to be conservative.

In addition to smoothing, we also need to symmetrize the upward and downward variation of the systematics. We take whichever variation is larger and symmetrize the systematic uncertainty with it. For systematic sources that only have a single variation (like JER, signal parton shower model, $t\bar{t}$

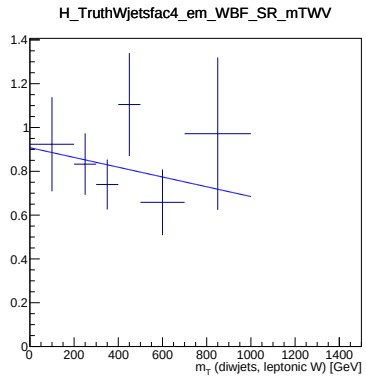

(a)

Figure 67: Illustration of the smoothing of one of the W + jets generator systematics, where the Sherpa factorization scale is multiplied by 2.0. The points with error bars give the ratio of the systematic sample to the nominal sample, as a function of $m_{\mathrm{T}}(WV)$, and the line shows the linear approximation to this ratio. The linear approximation represents the "smoothed" systematic. The plot is made for the resolved e^{-} signal region, after applying the full optimized cuts.

generator, etc.), we take the one-sided systematic variation and symmetrize it.

The formalism of how the systematics enter into the aQGC limit calculation is given in Section 9.3, in particular Eq. 61.

9 Anomalous Quartic Gauge Boson Couplings

9.1 Effect of aQGCs on Kinematics

Not only do aQGCs affect the cross-section of the signal, they also affect the kinematic distributions of the signal events. Extensive studies were done of the kinematic effects of the aQGCs. The effects can be broken down into four main categories:

1. Modified diboson kinematics. The aQGCs increase the p_T of the two bosons, and cause the two bosons to be more back-to-back, and to have p_T's that balance each other out more. This is reflected by the following variables: $\mathrm{p_T}(V_{\mathrm{had}})$, $\mathrm{p_T}(W_{\mathrm{lep}})$, $m(WV)$, $m_{\mathrm{T}}(WV)$, A_{full}, A_{WV}

2. Tagging-jets kinematics. The aQGCs increase the signal in the VBS-like area of phasespace where $m_{\mathrm{jj,tag}}$ and $\Delta\eta(jj)$ are large.

3. VBS topology. The aQGCs tend to increase the likelihood of the two bosons being produced centrally between the two tagging jets. This is reflected in increased values for the centrality variables, ζ_ℓ and ζ_V.

4. Boson polarization. At high $p_T(V)$, the aQGCs cause the bosons to be more longitudinally polarized. This is reflected in the variables $\cos\left(\theta^*_{\mathrm{j}}\right)$ and $\cos(\theta^*_\ell)$.

In Figs. 68-71, distributions of many of the aforementioned variables are shown, for background, SM signal, and signal generated with a non-zero aQGC. The plots show that aQGCs can have large effects on the kinematics, and allow the signal to stand out more against the backgrounds. Additional plots of the shape of $m_{\mathrm{T}}(WV)$ of signal events for a variety of aQGC values are given in Appendix H.

9.2 Optimization of Event Selection

Since the signal kinematics are greatly altered by the aQGCs, the analysis strategy will be to place limits on the aQGCs by fitting a kinematic distribution that is particularly sensitive to the aQGCs. In order to further improve the sensitivity to aQGCs, cuts will be placed on other variables; these cuts will be optimized to achieve the best expected limits.

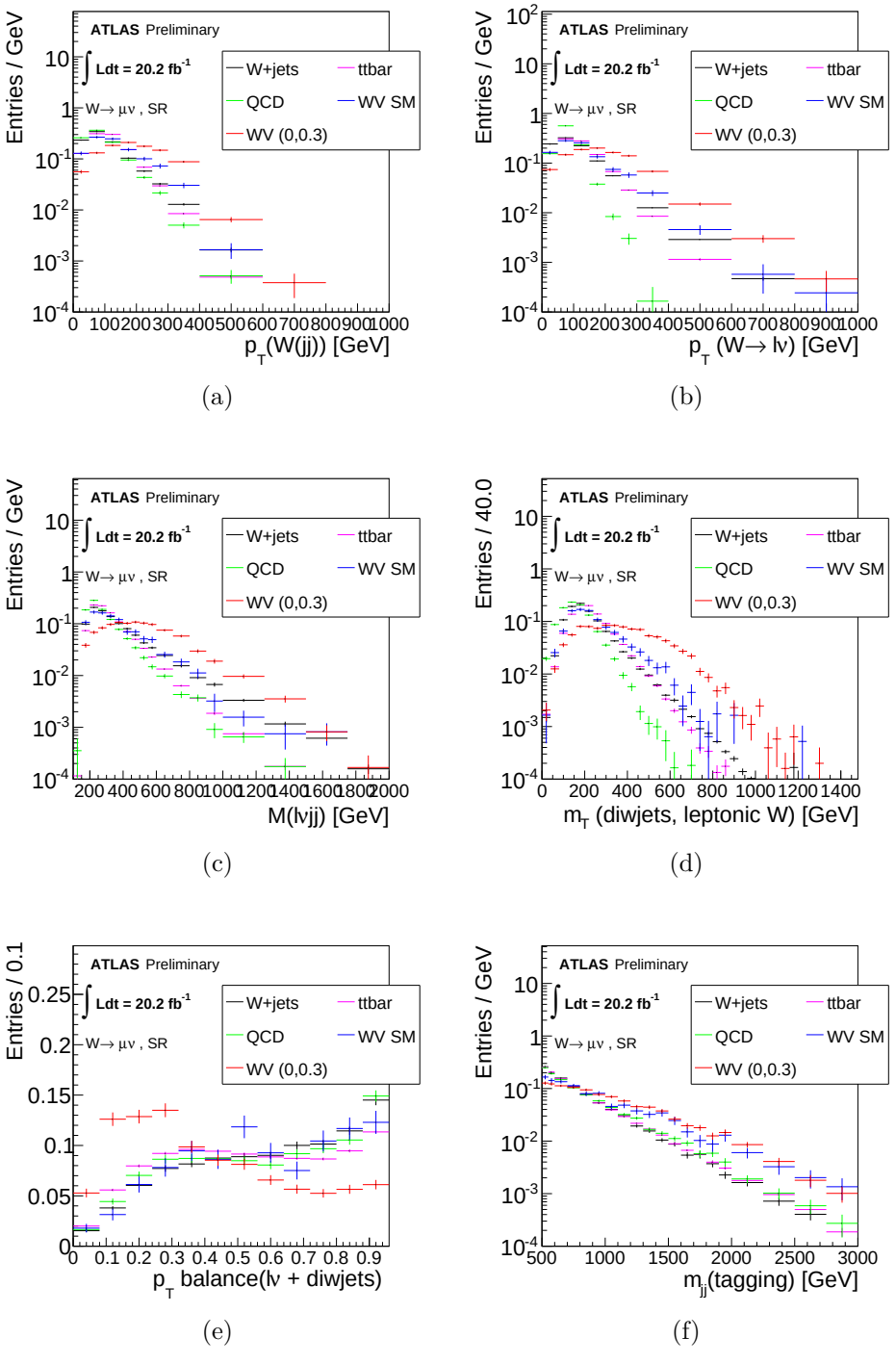

(a) (b) (c) (d) (e) (f)

Figure 68: Shape comparisons between different samples for the resolved jet selection in the Signal Region in the muon channel. Loose VBS cuts. (a) $p_T(V_{had})$, (b)$p_T(W_{lep})$, (c)$m(WV)$, (d)$m_T(WV)$, (e) A_{WV}, (f)$m_{jj,tag}$.

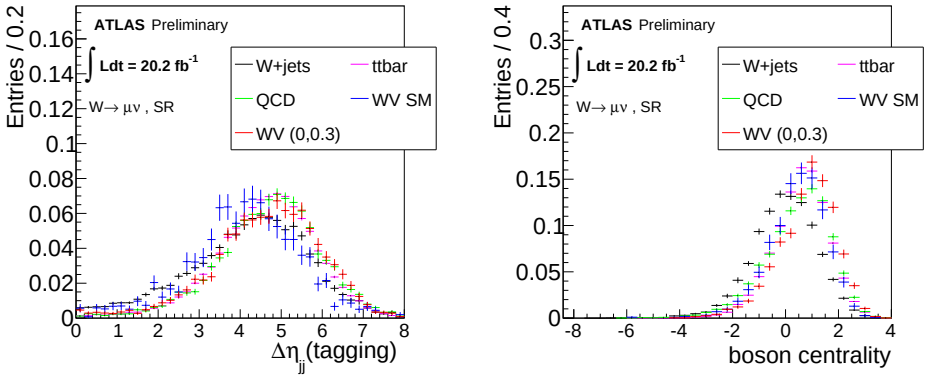

(a)

(b)

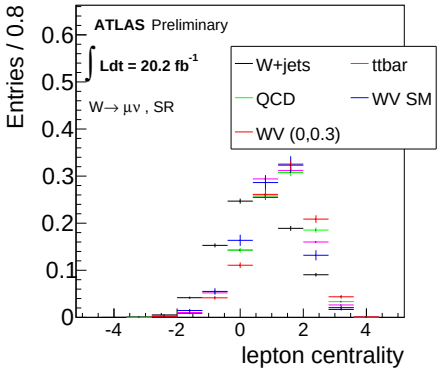

(c)

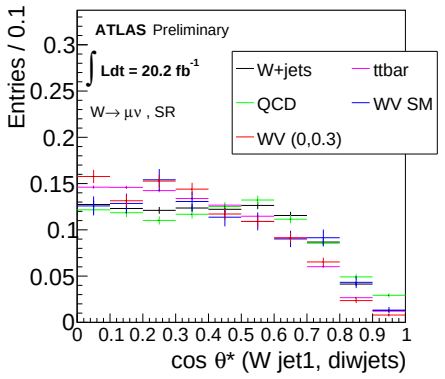

(d)

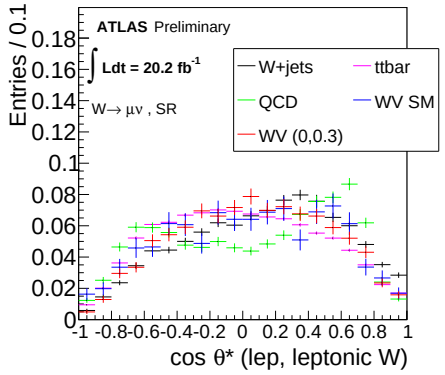

(e)

Figure 69: Shape comparisons between different samples for the resolved jet selection in the Signal Region in the muon channel. Loose VBS cuts. (a) $\Delta\eta(\mathrm{j},\mathrm{j})$, (b) boson centrality ζ_V, (c) lepton centrality, (d) $\cos\left(\theta^*_{\mathrm{j}}\right)$, (e) $\cos(\theta^*_\ell)$.

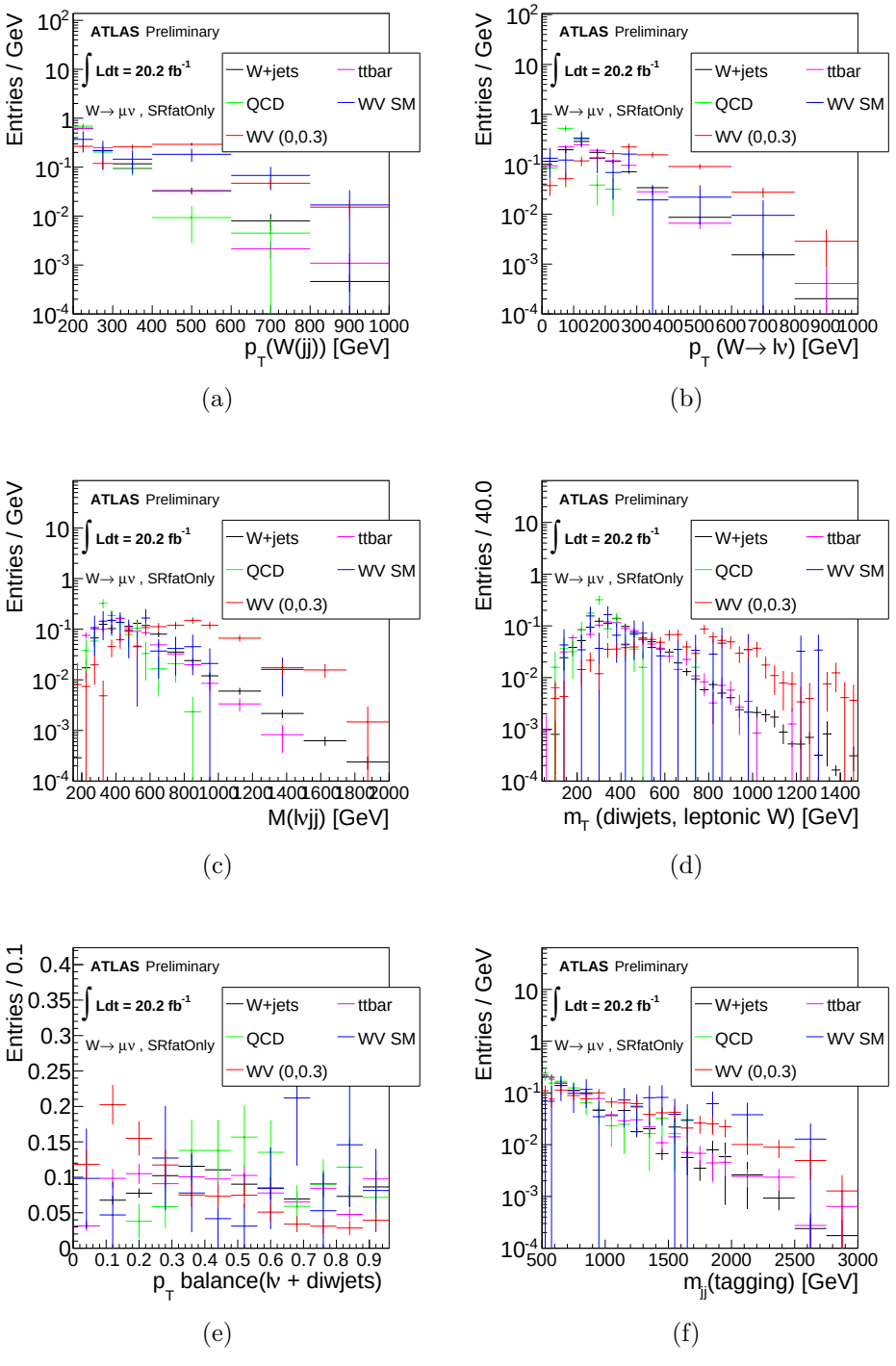

Figure 70: Shape comparisons between different samples for the merged jet selection in the Signal Region in the muon channel. Loose VBS cuts. (a) $\mathrm{p_T}(V_{\mathrm{had}})$, (b)$\mathrm{p_T}(W_{\mathrm{lep}})$, (c)$m(WV)$, (d)$m_{\mathrm{T}}(WV)$, (e) A_{WV}, (f)$m_{\mathrm{jj,tag}}$.

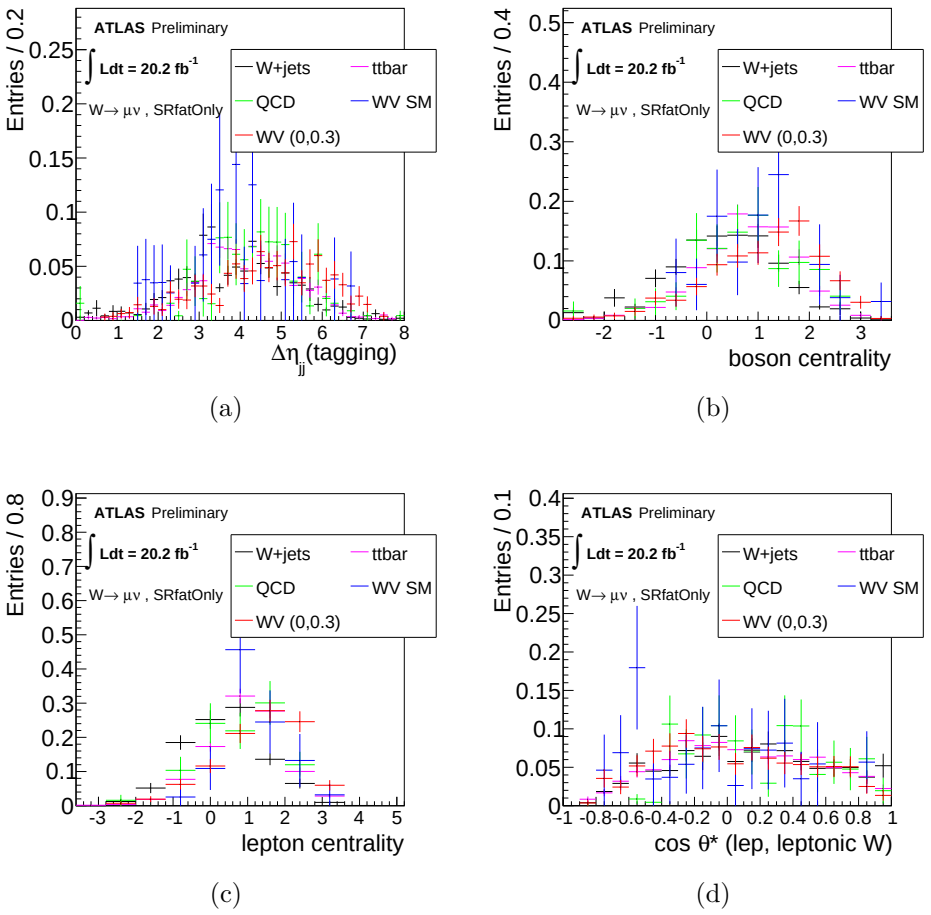

Figure 71: Shape comparisons between different samples for the merged jet selection in the Signal Region in the muon channel. Loose VBS cuts. (a) $\Delta\eta(\mathrm{j},\mathrm{j})$, (b) boson centrality ζ_V, (c) lepton centrality, (d) $\cos(\theta^*_\ell)$.

Variables that were investigated include: $\mathrm{p_T}(V_{\mathrm{had}})$, $\mathrm{p_T}(W_{\mathrm{lep}})$, $m(WV)$, $m_{\mathrm{T}}(WV)$, ζ_V, ζ_ℓ, $m_{\mathrm{jj,tag}}$, A_{full}, A_{WV}, $\cos\left(\theta^*_{\mathrm{j}}\right)$, $\cos(\theta^*_\ell)$, $\Delta\eta(\mathrm{j},\mathrm{j})$ of the tagging jets, $\Delta R(\mathrm{j},\mathrm{j})$ for the V_{had}-jets, $|\mathrm{p_T}(\mathrm{j}_1) - \mathrm{p_T}(\mathrm{j}_2)|$ for the V_{had}-jets, $\mathrm{p_T}(WV)$, and the $\mathrm{p_T}$ of the tagging-jet system.

After extensive studies of the sensitivities of the variables to aQGCs, and of the correlations between the different variables, the following variables were chosen for cut optimization:

1. For the resolved selection: $m_{\mathrm{T}}(WV)$, ζ_V, $m_{\mathrm{jj,tag}}$, and $\cos\left(\theta^*_{\mathrm{j}}\right)$.

2. For the merged selection: $m_{\mathrm{T}}(WV)$, ζ_V, $m_{\mathrm{jj,tag}}$, and A_{WV}.

It should be noted that there are many other variables that are sensitive to aQGCs, but which are highly correlated with the variables just listed, and so cutting on additional variables would not considerably improve the sensitivity to aQGCs. For example, in Appendix E, it is shown that $m_{\mathrm{jj,tag}}$ is highly correlated with the η of the tagging jets, so no cut on the η of the tagging jets is applied.

As explained in Sec. 9.4, for the final limit setting, a fit will be done to $m_{\mathrm{T}}(WV)$, so no cuts will actually be placed on $m_{\mathrm{T}}(WV)$. However, the cut optimization study estimates the aQGC sensitivity using a single-bin cut-and-count approximation, instead of a fit to the $m_{\mathrm{T}}(WV)$ distribution, because the latter method would be too computationally intensive. So, for the cut optimization study, $m_{\mathrm{T}}(WV)$ is included in the set of variables to optimize.

The optimal cuts are searched for in the multi-dimensional space, and the best cuts are chosen to be those that give the smallest expected aQGC limits (calculated using the formalism in Sec 9.3, for a 1-bin fit). The multi-dimensional search method first scans the space using a random-grid-search method [23], in order to obtain a rough location of the optimal point. Then, an iterative procedure with additional grid searches is performed to narrow in better on the optimal point in the multi-dimensional space.

The optimal cuts are determined in this fashion both for the α_4 and α_5 limits. However, for the final analysis, the same cuts will be used for both α_4 and α_5; the final cuts are chosen such that they do a nearly-optimal job for both aQGC parameters.

The location of the optimized cuts depends on the size of the systematic uncertainties. The cut optimization was performed using various assumptions about the size of the systematics. The optimal cuts for various

Systematics	Cuts				
Bkg Syst	$m_{\mathrm{T}}(WV) > X$	$\zeta_V > X$	$m_{\mathrm{jj,tag}} > X$	$\cos\left(\theta^*_{\mathrm{j}}\right) < X$	α_5 95% CL width
10%	$575GeV$	0.9	$900GeV$	0.75	0.183
20%	$575GeV$	0.9	$900GeV$	0.50	0.209
40%	$575GeV$	1.0	$1000GeV$	0.50	0.244
60%	$625GeV$	0.9	$1000GeV$	0.50	0.275

Table 21: The optimal cuts for the SR region that are found for 4 different assumptions about the background systematics. The expected width of the 95% CL interval for α_5 is also given for each value of the background systematics.

Systematics	Cuts				
Bkg Syst	$m_{\mathrm{T}}(WV) > X$	$\zeta_V > X$	$m_{\mathrm{jj,tag}} > X$	$A_{WV} < X$	α_5 95% CL width
10%	$675GeV$	0.9	$700GeV$	0.25	0.146
20%	$700GeV$	0.9	$900GeV$	0.30	0.168
40%	$800GeV$	1.0	$900GeV$	0.25	0.188
60%	$800GeV$	1.4	$850GeV$	0.25	0.211

Table 22: The optimal cuts for the SRfatOnly region that are found for 4 different assumptions about the background systematics. The expected width of the 95% CL interval for α_5 is also given for each value of the background systematics.

systematics scenarios are shown in Tables 21 and 22 for the SR and SRfatOnly regions, respectively. Generally, tighter cuts tend to be favored if the systematics are larger, although the optimal cut values don't change that dramatically. The modeling of the backgrounds can be checked by looking at the so called "n-1" plots in Appendix F. In Section 9.4, we will revisit these cuts using the full fit machinery, and at that time we will decide which of these sets of cuts to use for the final analysis.

We also investigate how stable the expected limits are when the cut values are modified slightly. To do this, we look at sets of cuts that are similar to the set of cuts optimized for a 40% background systematic uncertainty, but where the cut on one of the variables is modified. In Figs. 72-73, the expected limits

(using the 1-bin approximation) are shown as a function of the cut values on one of the variables, with the cuts on the other variables held fixed. For small perturbations in the cut values, the expected limits do not change radically.

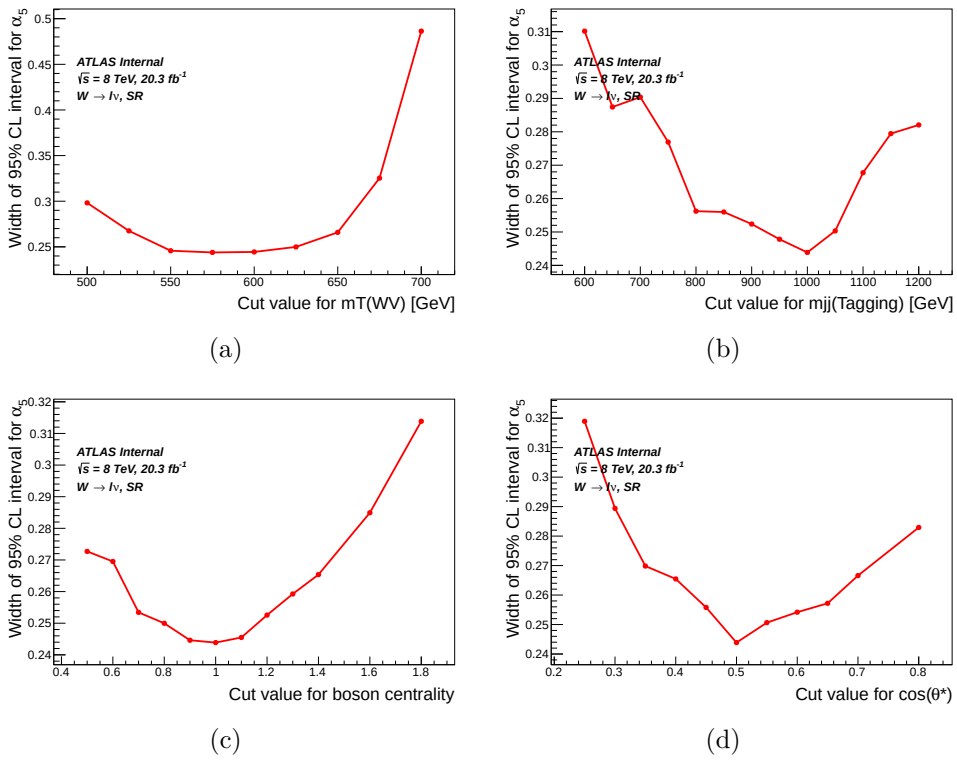

Figure 72: The expected width of the 95% CL interval of α_5, as a function of the cuts applied on different variables. This is for the resolved jet selection. In each plot, the cut on one variable is varied, while the cuts on the other three variables are held fixed to their optimized cut values.

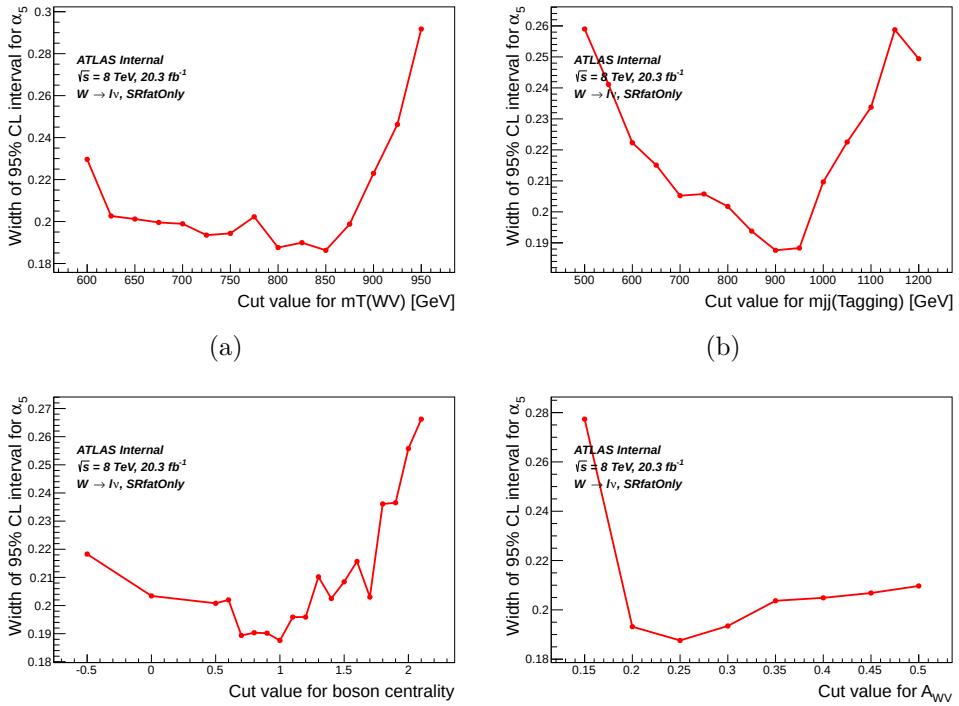

Figure 73: The expected width of the 95% CL interval of α_5, as a function of the cuts applied on different variables. This is for the merged jet selection. In each plot, the cut on one variable is varied, while the cuts on the other three variables are held fixed to their optimized cut values.

9.3 aQGC Fit Formalism

The aQGC limit-setting is performed using the TGClim [5] package. The limits are calculated by doing a 1-D binned maximum-likelihood fit to a certain variable, which we will call x for sake of generality. For example, x could be $m_{\mathrm{T}}(WV)$ or $\mathrm{p_T}(W_{\mathrm{lep}})$.

Systematics are included in the fit through nuisance parameters. Each nuisance parameter represents the systematic uncertainty on one particular x bin. Let $\vec{\alpha} = \{\alpha_4, \alpha_5\}$ be the vector of aQGC parameters and $\vec{\beta}$ be a vector of nuisance parameters which will be described later. The likelihood function is:

$$\mathcal{L}(\vec{\alpha}, \vec{\beta}) = \prod_{i=1}^{m} Poisson(N^i_{\mathrm{data}}, \mu^i(\vec{\alpha}, \vec{\beta})) \times \frac{1}{(2\pi)^m} e^{-\frac{1}{2}(\vec{\beta}\cdot C^{-1}\cdot\vec{\beta})}\,, \tag{56}$$

where the product is over the bin number i and μ^i is the expected number of events in bin i:

$$\mu^i(\vec{\alpha}, \vec{\beta}) = N^i_{\mathrm{sig}}(\vec{\alpha})\, h(1+\beta_i) + N^i_{\mathrm{bkg}}\, h(1+\beta_{i+m})\,. \tag{57}$$

The function h describes log-normal uncertainties on the event yields:

$$\begin{aligned} h(1+\beta_i) &= (1+\sigma_i)^{\beta_i/\sigma_i}, \beta_i \geq 0 \\ &= (1-\sigma_i)^{-\beta_i/\sigma_i}, \beta_i < 0\,, \end{aligned} \tag{58}$$

where

$$\sigma_i = \sqrt{C_{i,i}}\,. \tag{59}$$

In Eq. 57, N^i_{sig} and N^i_{bkg} are the predicted number of signal and background events, respectively, in bin i. There are $2m$ nuisance parameters β_i, where m is the number of bins, and they permit the signal and background in each bin to vary within systematic uncertainties. The β parameters are allowed to vary within Gaussian constraints which are defined by the covariance matrix C that appears in Eq. 56. Equations 57-58 thus describe systematic uncertainties on the signal and background subject to log-normal constraints.

The matrix C describes the systematic uncertainties on the signal and background in each bin, and the bin-to-bin correlations between these uncertainties, including correlations between signal and background. Thus, C

[5] `https://svnweb.cern.ch/trac/atlasphys/browser/Physics/StandardModel/ElectroWeak/Common/Software/TGC/TGClim`

describes both normalization and shape systematics. The matrix C is calculated including all the systematics described in Section 8. It is calculated by forming C^s matrices for each independent systematic source s, and then linearly summing together each matrix to get the total matrix C representing all systematics (this is equivalent to adding systematic uncertainties in quadrature):

$$C_{i,j} = \sum_{s=1}^{N_{\text{syst}}} C^s_{i,j} \,. \tag{60}$$

The matrix C^s is formed for each systematic source described in Section 8, and is calculated as:

$$C^s_{i,j} = \frac{(N^s_i - N^0_i)(N^s_j - N^0_j)}{N^0_i N^0_j} \,, \tag{61}$$

where

$$\begin{aligned} N^{s/0}_i &= N^{i,s/0}_{\text{sig}},\ i < m \,, \\ &= N^{i-m,s/0}_{\text{bkg}},\ m <= i < 2m \,, \end{aligned} \tag{62}$$

where $N^{i,0}_{\text{sig}}$ is the "nominal" expected signal yield in bin i and $N^{i,s}_{\text{sig}}$ is the expected signal yield in bin i for the systematic "up" variation. Similarly, $N^{i,0}_{\text{bkg}}$ is the "nominal" expected background yield in bin i and $N^{i,s}_{\text{bkg}}$ is the expected background yield in bin i for the systematic "up" variation. (Eq. 61 could have been defined using the systematic "down" variation instead, but both definitions give exactly the same C matrix, assuming that the systematics are symmetric.)

The observed and expected 95% confidence intervals (CI) are determined using a hybrid Bayesian-frequentist method like that used by ATLAS's $W(\ell\nu)V(\text{jj})$ aTGC analysis [109, 110].

- The profile-likelihood ratio $\lambda(\alpha)$ is used as a test statistic. It is the ratio of the maximum likelihood for a given aQGC value α to the overall maximum likelihood (for any α value):

  $$\lambda(\alpha) = \frac{\mathcal{L}(N_{\text{data}}|\alpha, \hat{\hat{\beta}})}{\mathcal{L}(N_{\text{data}}|\hat{\alpha}, \hat{\beta})} \,, \tag{63}$$

  where $\hat{\hat{\beta}}$ are the values of β that conditionally maximize the likelihood for the given value of α, and $\hat{\alpha}$ and $\hat{\beta}$ are the values of α and β, respectively that simultaneously give the overall maximum likelihood. Note

that β is a vector of nuisance parameters, not just a single parameter. By this definition, profile likelihood ratio is always less than or equal to one.

- The observed value of the test statistics, $\lambda_{\text{obs}}(\alpha)$, is determined at a variety of different values of α by scanning over α.

- The p-value or the probability of obtaining a result at least as unlikely as the observed one has been estimated with the help of toy Monte Carlo. "Toy" datasets for each test-value of α are generated in the following way. First the nuisance parameters β are Gaussian fluctuated around the mean value of $\hat{\hat{\beta}}$. The number of "observed" events N^i_{toy} in each bin is then randomly drawn from a Poisson distribution using a mean calculated from the values of α and β. Many toy datasets for each value of α is generated and the profile likelihood ratio $\lambda_{\text{toy}}(\alpha)$s are calculated for each of them.

- The p-value for each value of α is computed as

$$\text{p-value} = \frac{\text{Number of toys with } \lambda_{\text{toy}} \leq \lambda_{\text{obs}}}{\text{Total number of generated toys}} \tag{64}$$

  This defines the 95% CI for α.

- The 95% CI for α is defined by those values of α for which the p-value is $\leq 5\%$.

The procedure explained above will lead to observed limits when observed data is used to calculate the likelihood function. The expected limits, on the other hand, are calculated by generating a large number of pseudo-datasets, $N^{\text{pseudo}}_{\text{obs}}$, by randomly drawing events from the probability density function. The pseudo-datasets are generated with the SM values of background and signal (i.e. no aQGC's), but with the nuisance parameters β smeared by their uncertainties. For each of these pseudo-datasets, the 95% CI's on α are determined following the procedure already mentioned. The ensemble of CI's is used to determine the expected limits on α.

This pseudo-data-based method is very computationally intensive, so it has been used only to obtain the final expected and observed limits. The final expected limits are given in Section 9.5. For the optimization studies, a much quicker method has been used to estimate the expected aQGC limits.

The Monte Carlo expectation is fit to the "Asimov" dataset [111] and the likelihood function is calculated for different values of α. The Asimov dataset consists of exactly the SM expectation (signal plus background) in each bin. The expected limit is the interval corresponding to $\Delta(\ln\mathcal{L}) = 1.92$.

9.4 Final fit setup

As mentioned in Section 9.2, we optimized cuts for four variables, separately for the resolved and merged selections. The optimal cuts were summarized in Tables 21-22. However, in order to maximize the information available, we fit a distribution rather than do a cut-and-count analysis. So, we decided to remove the cut on one of the four variables, and perform a fit to that variable instead. Since $m_{\mathrm{T}}(WV)$ is by far the most important of the four variables for obtaining good aQGC limits, it was decided to fit $m_{\mathrm{T}}(WV)$ instead of cutting on it.

The aQGC limits are set by fitting $m_{\mathrm{T}}(WV)$ simultaneously for the merged and resolved signal regions. Since the statistics are low and the electron and muon channels do not differ much, the electron and muon channels are merged together for the fit. Some difference between the $\ell+$ and $\ell-$ channels is seen, both for the backgrounds and the signal, so in the resolved signal region, the $\ell+$ and $\ell-$ channels are fitted separately. However, the $\ell+$ and $\ell-$ channels are combined for the large-R jet selection, since the statistics are low and little improvement in the expected limits is obtained by splitting the channels. In summary, the fit is done simultaneously to three channels:

- Channel 0. The merged signal region, $e+$, $e-$, $\mu+$, and $\mu-$ combined.
- Channel 1. The resolved signal region, $e+$ and $\mu+$ combined.
- Channel 2. The resolved signal region, $e-$ and $\mu-$ combined.

These three channels are shown in Fig. 74, overlaid with Asimov data. In this figure, we use the cuts from Tables 21-22 that were optimized for a 20% background systematic uncertainty (except no $m_{\mathrm{T}}(WV)$ cut is applied). The figure shows the sensitivity of each channel to an aQGC of ($\alpha_4 = 0.1$, $\alpha_5 = 0$). The expected aQGC limits for these cuts, and also for the cuts optimized for a 10% and 40% background systematic, are shown in Table 23. The limits calculated in this table include all systematics. As can be seen

Cuts optimized for bkg syst =	Expect. Limit on α_4	Expect. Limit on α_5
10%	$[\ -0.049 < \alpha_4 < 0.060\ ]$	$[\ -0.089 < \alpha_5 < 0.082\ ]$
20%	$[-0.047 < \alpha_4 < 0.057]$	$[-0.081 < \alpha_5 < 0.074]$
40%	$[\ -0.048 < \alpha_4 < 0.058\ ]$	$[\ -0.082 < \alpha_5 < 0.076\ ]$

Table 23: The expected limits on α_4 and α_5 at 95% CL, using a fit to $m_{\mathrm{T}}(WV)$ in 3 channels, as explained in Sec. 9.4. The expected limits are shown for 3 different sets of cuts, which are defined in Tables 21-22. These limits are estimated using the $\Delta(\ln\mathcal{L}) = 1.92$ formula on the Asimov dataset.

from this table, for the most part, the expected limits do not depend much on which of the three sets of cuts are used (only a few percent differences in the expected limits, except for the limit on α_5, which is about 10% worse when using the first set of cuts). For our final analysis cuts, we choose the cuts optimized for a 20% background systematic, namely:

- resolved selection: $\zeta_V > 0.9$, $m_{\mathrm{jj,tag}} > 900GeV$, $\cos\left(\theta^*_{\mathrm{j}}\right) < 0.50$.
- merged selection: $\zeta_V > 0.9$, $m_{\mathrm{jj,tag}} > 900GeV$, $A_{WV} < 0.30$.

9.5 Final Expected aQGC Limits

The expected 1D limits on the aQGC parameters are $[-0.056 < \alpha_4 < 0.058]$ and $[-0.083 < \alpha_5 < 0.078]$ at 95% confidence level

The full systematics are included. The limits are computed using ∼500 pseudo-datasets, and the results are shown in Fig. 75. The expected upper and lower limits are calculated as the means of the limits for the ensemble of pseudo-datasets.

9.6 Sensitivity of aQGC limits to Systematics

To get a feel for how much the aQGC limits are affected by systematics, we check how the expected aQGC limits change when certain sources of systematic uncertainty are included or excluded. Since most of the sensitivity to aQGCs comes from the highest-$m_{\mathrm{T}}(WV)$ bins, we decided to simplify this study by only calculating the expected aQGC limits using 3 bins, namely,

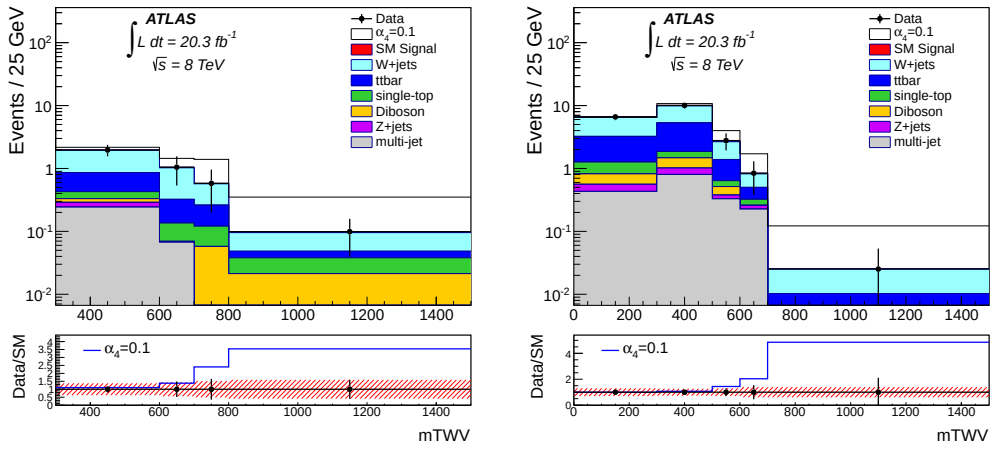

(a) (b)

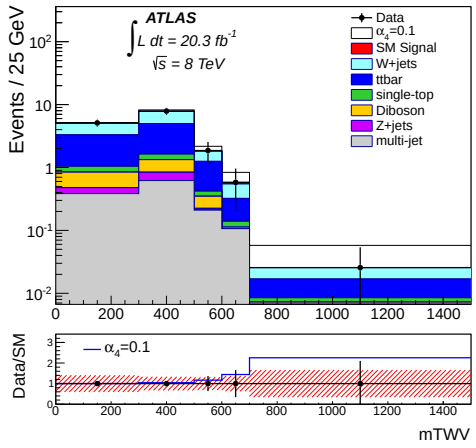

(c)

Figure 74: The expected $m_{\mathrm{T}}(WV)$ distribution, overlaid with **Asimov** data, after applying the final optimized cuts. The expected enhancement due to an aQGC of ($\alpha_4 = 0.1$, $\alpha_5 = 0$) is also shown. The plotted regions are (a) the merged signal region, $e+$, $e-$, $\mu+$, and $\mu-$ combined; (b) the resolved signal region, $e+$ and $\mu+$ combined; and (c) the resolved signal region, $e-$ and $\mu-$ combined.

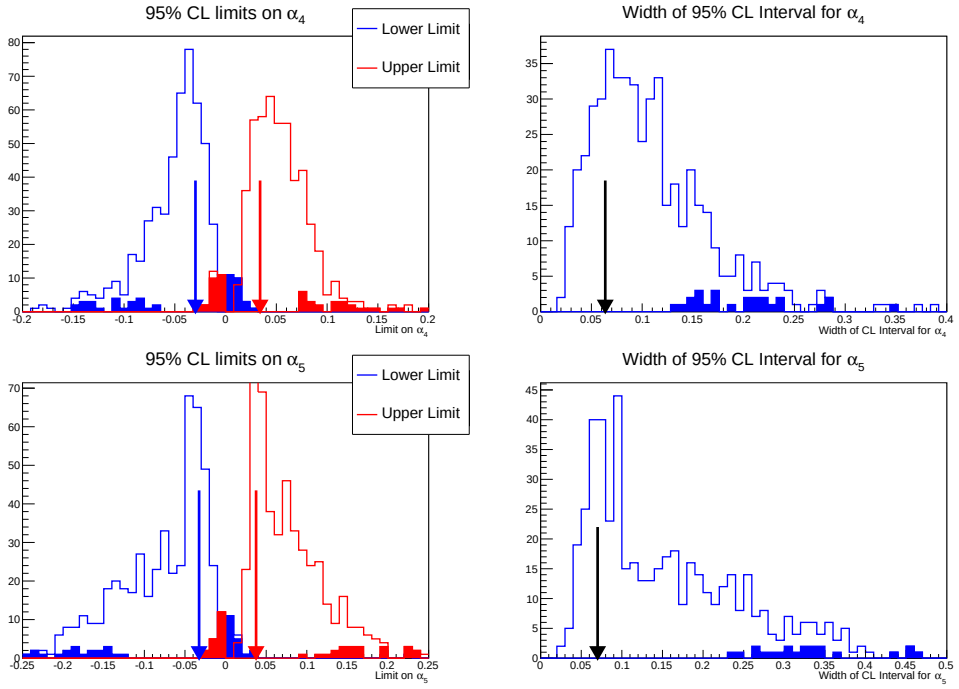

Figure 75: Summary of pseudo-experiments used to calculate the expected 1D aQGC limits. Limits for α_4 and α_5 are shown in the top and bottom plots, respectively. The left plots give the upper (red) and lower (blue) 95% limits calculated for each pseudo-dataset. The right plots show the total width of the 95% confidence interval for each pseudo-dataset. The solid histograms indicate pseudo-datasets for which the 95% confidence region consists of two separate intervals rather than a single interval. The arrows in both the left and right plots indicate the observed limits from the data.

3-bin fit	
	95% CL interval on α_4
all systs	[-0.057, 0.066]
without signal modeling	[-0.049, 0.059]
without JES/JER	[-0.050, 0.060]
without W/Z + jets modeling	[-0.054, 0.064]
without $t\bar{t}$ modeling	[-0.056, 0.065]
without W + jets scale factor	[-0.057, 0.066]
no systs	[-0.040, 0.050]

Table 24: The expected limits on α_4, from a 3-bin fit (fitting only the highest-$m_{\mathrm{T}}(WV)$ bin in each of the 3 fit channels). The expected limits are shown including all systematic uncertainties, no systematic uncertainties, and a subset of systematic uncertainties. The rows labeled "without XX" mean that the XX systematic uncertainties are excluded, but all other systematic uncertainties are included. Expected limits are estimated by applying the delta-log-likelihood formula to the Asimov dataset.

the highest-$m_{\mathrm{T}}(WV)$ bin in each of the three fit channels. This study is summarized in Table 24. As can be seen, the expected limits would be 25–30% better if there were no systematic uncertainties at all. The dominant systematic uncertainties are JES/JER and signal modeling.

10 Summary and Results

10.1 Observed aQGC Limits

The observed $m_{\mathrm{T}}(WV)$ distribution, after the full optimized cuts, is shown in Fig. 76, compared to the expected $m_{\mathrm{T}}(WV)$ distribution. The plots also show the expected contribution from an aQGC of ($\alpha_4 = 0.1$, $\alpha_5 = 0$). The data are consistent with the SM expectation.

The observed limits on α_4 and α_5 are calculated from a fit to $m_{\mathrm{T}}(WV)$ in the three channels, as described in Sec. 9.4.

The observed 1D limits on the aQGC parameters are $[-0.030 < \alpha_4 < 0.034]$ and $[-0.033 < \alpha_5 < 0.038]$ at 95% confidence level. These limits are smaller than the expected limits, but they are compatible with expectation.

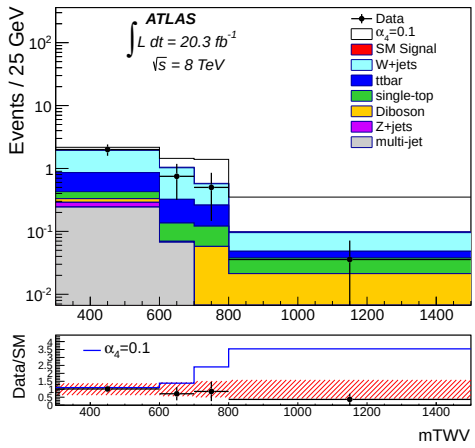

(a)

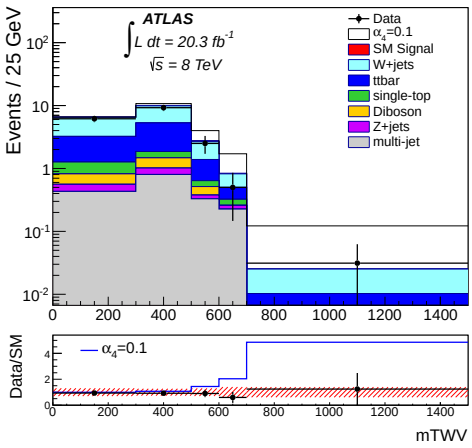

(b)

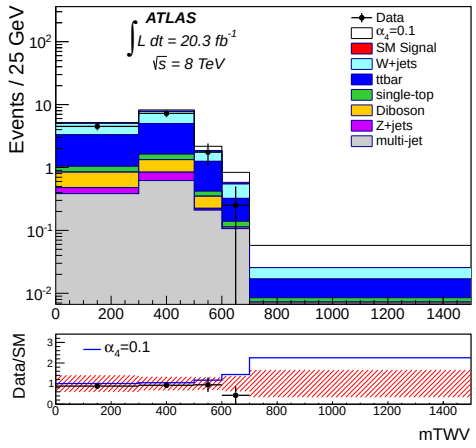

(c)

Figure 76: The expected $m_{\mathrm{T}}(WV)$ distribution, overlaid with data, after applying the final optimized cuts. The expected enhancement due to an aQGC of ($\alpha_4 = 0.1$, $\alpha_5 = 0$) is also shown. The plotted regions are (a) the merged signal region, $e+$, $e-$, $\mu+$, and $\mu-$ combined; (b) the resolved signal region, $e+$ and $\mu+$ combined; and (c) the resolved signal region, $e-$ and $\mu-$ combined.

Based on the pseudo-experiments shown in Fig. 75, there was about a 20% chance of observing aQGC limits this small or smaller. The limits on α_4 and α_5 obtained in this analysis improve the limits set by previous analyses at ATLAS and CMS (see Sec. 1.7). The fitted nuisance parameters are shown in Fig. 77, in the case that α_4 and α_5 are fixed to zero (SM). The background parameters tend to be pushed a bit low, because the prediction tends to be a bit higher than the data. The background parameters are more constrained at low-$m_{\mathrm{T}}(WV)$ than at high-$m_{\mathrm{T}}(WV)$, which is expected given that there are more events and a smaller signal contribution at low-$m_{\mathrm{T}}(WV)$.

The observed 2D 95% CL limits in the (α_4,α_5) plane are shown in Fig. 78, The correlation between α_4 and α_5 is similar to that seen in ATLAS's same-sign WW analysis [15].

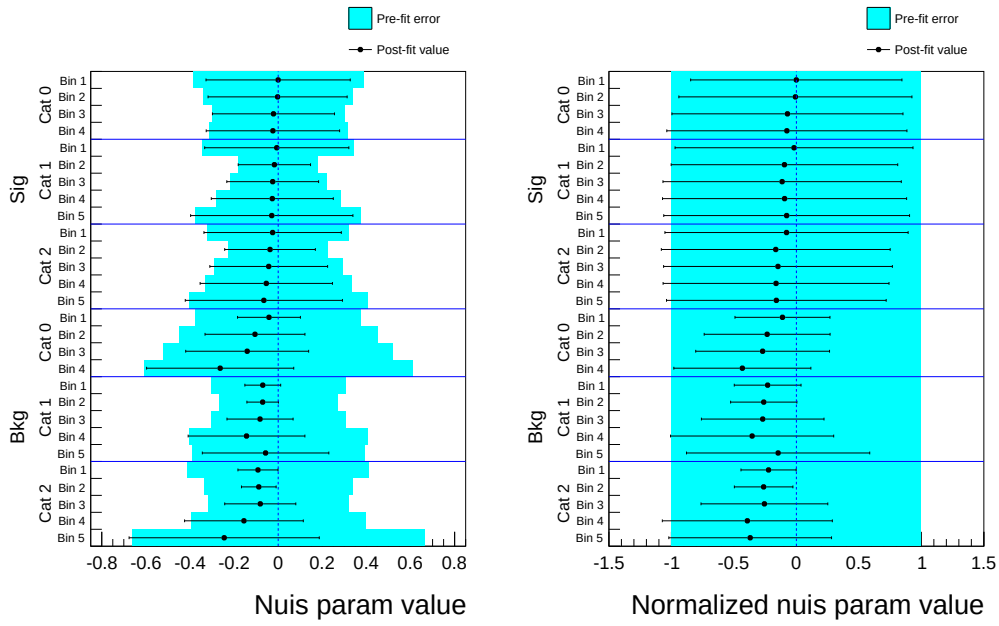

(a) (b)

Figure 77: The fitted values of the nuisance parameters, when fitting the observed data, with α_4 and α_5 are fixed to zero (SM). In the left-hand plot, the points show the post-fit result for each nuisance parameter. Each nuisance parameter represents the fractional deviation of the background yield or signal yield in a particular bin from its pre-fit expectation. For example, if the "Bkg-Cat1-Bin3" nuisance parameter has a value of -0.1, that means the total background in the 3rd $m_{\mathrm{T}}(WV)$ bin of the "Cat1" signal region is shifted by approximately -10% with respect to the nominal background prediction in that bin. (The shift is only *approximately* -10% because the nuisance parameters represent log-normal systematics; the actual formula is given in Eq. 58.) Cat0/Cat1/Cat2 are the three fit channels described in Section 9.4. Within each category, the bin numbering increases as a function of $m_{\mathrm{T}}(WV)$. The colored band shows the pre-fit Gaussian constraint put on the nuisance parameter. The right-hand plot is the same as the left-hand plot, except normalized so that the pre-fit uncertainty is 1.

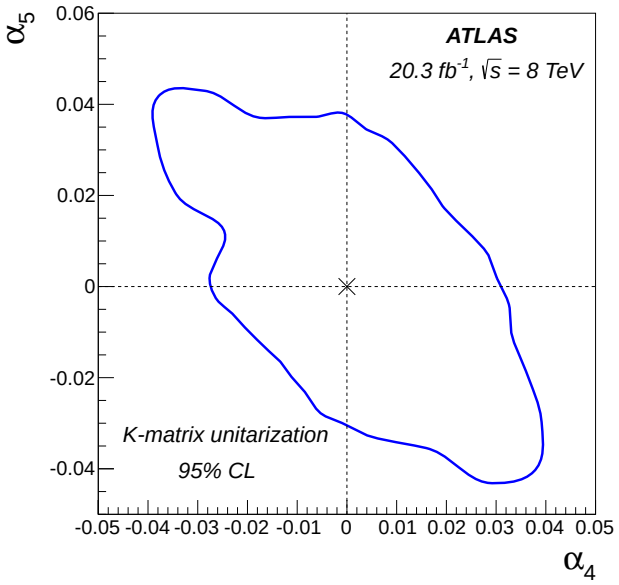

Figure 78: The observed two-dimensional 95% CL limits in the (α_4,α_5) plane.

11 Conclusion

A study on vector boson scattering processes was performed by looking at the electroweak production of $WV + 2\text{j}$, with $W \to \ell\nu$ and $V \to qq'$. Two reconstruction channels were looked at, one in which the $V \to qq'$ candidate was reconstructed as two small-radius jets, and another in which the $V \to qq'$ candidate was reconstructed as a single large-radius jet. An area of phase-space with large di-jet invariant mass, representative of vector boson scattering, was examined. Selection criteria were chosen which were optimized for sensitivity to anomalous quartic gauge couplings. These criteria selected events with a high-p_T W, a longitudinally polarized $V \to qq'$, a large di-jet invariant mass of the forward jets, and a VBS-like topology. Limits on the anomalous quartic gauge coupling parameters α_4 and α_5 were set by fitting the transverse mass of the diboson system. Using a profile likelihood ratio test statistic the observed 95% CL limits are $[-0.030 < \alpha_4 < 0.034]$ and $[-0.033 < \alpha_5 < 0.038]$. These limits, when published, will be the most stringent on the aforementioned parameters of anomalous Quartic Gauge Couplings.

References

[1] ATLAS Collaboration. "Observation of a new particle in the search for the Standard Model Higgs boson with the ATLAS detector at the LHC". In: *Phys. Lett. B* 716 (2012), p. 1. DOI: 10.1016/j.physletb.2012.08.020. arXiv: 1207.7214 [hep-ex].

[2] CMS Collaboration. "Observation of a new boson at a mass of 125 GeV with the CMS experiment at the LHC". In: *Phys. Lett. B* 716 (2012), p. 30. DOI: 10.1016/j.physletb.2012.08.021. arXiv: 1207.7235 [hep-ex].

[3] K. A. Olive et al. "Review of Particle Physics". In: *Chin. Phys.* C38 (2014), p. 090001. DOI: 10.1088/1674-1137/38/9/090001.

[4] Steven Weinberg. "A Model of Leptons". In: *Phys. Rev. Lett.* 19 (21 1967), pp. 1264–1266. DOI: 10.1103/PhysRevLett.19.1264. URL: http://link.aps.org/doi/10.1103/PhysRevLett.19.1264.

[5] Abdus Salam. "Weak and Electromagnetic Interactions". In: *Elementary particle theory. Relativistic groups and analyticity.* Proceedings of the Eighth Nobel Symposium. (Aspenäsgarden, Lerum, May 19–25, 1968). Ed. by Nils Svartholm. Stockholm: Almquist & Wiksell, 1968, pp. 367–377.

[6] D. Binosi and L. Theussl. "JaxoDraw: A Graphical user interface for drawing Feynman diagrams". In: *Comput. Phys. Commun.* 161 (2004), pp. 76–86. DOI: 10.1016/j.cpc.2004.05.001. arXiv: hep-ph/0309015 [hep-ph].

[7] F. Englert and R. Brout. "Broken Symmetry and the Mass of Gauge Vector Mesons". In: *Phys. Rev. Lett.* 13 (9 1964), pp. 321–323. DOI: 10.1103/PhysRevLett.13.321. URL: http://link.aps.org/doi/10.1103/PhysRevLett.13.321.

[8] Peter W. Higgs. "Broken Symmetries and the Masses of Gauge Bosons". In: *Phys. Rev. Lett.* 13 (16 1964), pp. 508–509. DOI: 10.1103/PhysRevLett.13.508. URL: http://link.aps.org/doi/10.1103/PhysRevLett.13.508.

[9] G. S. Guralnik, C. R. Hagen, and T. W. B. Kibble. "Global Conservation Laws and Massless Particles". In: *Phys. Rev. Lett.* 13 (20 1964), pp. 585–587. DOI: 10.1103/PhysRevLett.13.585. URL: http://link.aps.org/doi/10.1103/PhysRevLett.13.585.

[10] M. Baak et al. "Working Group Report: Precision Study of Electroweak Interactions". In: *Community Summer Study 2013: Snowmass on the Mississippi (CSS2013) Minneapolis, MN, USA, July 29-August 6, 2013*. 2013. arXiv: 1310.6708 [hep-ph].

[11] Ana Alboteanu, Wolfgang Kilian, and Juergen Reuter. "Resonances and Unitarity in Weak Boson Scattering at the LHC". In: *JHEP* 0811 (2008), p. 010. DOI: 10.1088/1126-6708/2008/11/010. arXiv: 0806.4145 [hep-ph].

[12] J. Reuter, Wolfgang Kilian, and Marco Sekulla. "Simplified Models for New Physics in Vector Boson Scattering - Input for Snowmass 2013". In: (2013). arXiv: 1307.8170 [hep-ph].

[13] Wolfgang Kilian, Thorsten Ohl, and Jurgen Reuter. "WHIZARD: Simulating Multi-Particle Processes at LHC and ILC". In: *Eur. Phys. J.* C71 (2011), p. 1742. DOI: 10.1140/epjc/s10052-011-1742-y. arXiv: 0708.4233 [hep-ph].

[14] Mauro Moretti, Thorsten Ohl, and Jurgen Reuter. "O'Mega: An Optimizing matrix element generator". In: (2001). arXiv: hep-ph/0102195 [hep-ph].

[15] ATLAS Collaboration. "Evidence for Electroweak Production of $W^{\pm}W^{\pm}jj$ in pp Collisions at $\sqrt{s} = 8$ TeV with the ATLAS Detector". In: *Phys. Rev. Lett.* 113 (2014), p. 141803. DOI: 10.1103/PhysRevLett.113.141803. arXiv: 1405.6241 [hep-ex].

[16] P Anger et al. *A Measurement of WZ Production in Proton-Proton Collisions at $\sqrt{\mathbf{s}} = \mathbf{8}$ TeV with the ATLAS Detector*. ATL-COM-PHYS-2014-144 (support note). URL: https://cds.cern.ch/record/1663539.

[17] Georges Aad et al. "Measurements of $W^{\pm}Z$ production cross sections in pp collisions at $\sqrt{s} = 8$ TeV with the ATLAS detector and limits on anomalous gauge boson self-couplings". In: *Phys. Rev.* D93.9 (2016), p. 092004. DOI: 10.1103/PhysRevD.93.092004. arXiv: 1603.02151 [hep-ex].

[18] Vardan Khachatryan et al. "Study of vector boson scattering and search for new physics in events with two same-sign leptons and two jets". In: *Phys. Rev. Lett.* 114.5 (2015), p. 051801. DOI: 10.1103/PhysRevLett.114.051801. arXiv: 1410.6315 [hep-ex].

[19] Christiane Lefèvre. "The CERN accelerator complex." 2008. URL: https://cds.cern.ch/record/1260465.

[20] ATLAS Collaboration. "Improved luminosity determination in *pp* collisions at $\sqrt{s} = 7$ TeV using the ATLAS detector at the LHC". In: *Eur. Phys. J. C* 73 (2013), p. 2518. DOI: 10.1140/epjc/s10052-013-2518-3. arXiv: 1302.4393 [hep-ex].

[21] ATLAS Collaboration. "The ATLAS Experiment at the CERN Large Hadron Collider". In: *JINST* 3 (2008), S08003. DOI: 10.1088/1748-0221/3/08/S08003.

[22] Joao Pequenao. "Computer generated image of the whole ATLAS detector". 2008. URL: https://cds.cern.ch/record/1095924.

[23] Regina Caputo and John D. Hobbs. "A Search for First Generation Leptoquarks at the ATLAS detector." PhD thesis. Stony Brook U., 2011.

[24] Joao Pequenao and Paul Schaffner. "An computer generated image representing how ATLAS detects particles". 2013. URL: https://cds.cern.ch/record/1505342.

[25] Joao Pequenao. "Computer generated image of the ATLAS inner detector". 2008. URL: https://cds.cern.ch/record/1095926.

[26] P. Morettini. "Commissioning of the ATLAS Silicon Tracker with Cosmic Rays and Beam Data". In: CERN. Geneva: CERN, 2010. URL: http://cdsweb.cern.ch/record/1254882/files/ATL-INDET-PROC-2010-009.pdf.

[27] M Capeans et al. *ATLAS Insertable B-Layer Technical Design Report*. Tech. rep. CERN-LHCC-2010-013. ATLAS-TDR-19. Geneva: CERN, 2010. URL: https://cds.cern.ch/record/1291633.

[28] Joao Pequenao. "Computer generated images of the Pixel, part of the ATLAS inner detector." 2008. URL: https://cds.cern.ch/record/1095925.

[29] "ATLAS inner detector: Technical design report. Vol. 1". In: (1997).

[30] N Barlow. *Operation of the ATLAS Semiconductor Tracker*. Tech. rep. ATL-INDET-PROC-2010-003. Geneva: CERN, 2010. URL: https://cds.cern.ch/record/1237401.

[31] J Degenhardt. *Performance of the ATLAS Transition Radiation Tracker with Cosmic Rays and First High Energy Collisions at the LHC*. Tech. rep. ATL-INDET-PROC-2010-040. Geneva: CERN, 2010. URL: https://cds.cern.ch/record/1308426.

[32] A Vogel. *ATLAS Transition Radiation Tracker (TRT): Straw Tube Gaseous Detectors at High Rates*. Tech. rep. ATL-INDET-PROC-2013-005. Geneva: CERN, 2013. URL: https://cds.cern.ch/record/1537991.

[33] "ATLAS liquid argon calorimeter: Technical design report". In: (1996).

[34] Joao Pequenao. "Computer Generated image of the ATLAS calorimeter". 2008. URL: https://cds.cern.ch/record/1095927.

[35] Antonio Salvucci. "Measurement of muon momentum resolution of the ATLAS detector". In: *EPJ Web Conf.* 28 (2012), p. 12039. DOI: 10.1051/epjconf/20122812039. arXiv: 1201.4704 [physics.ins-det].

[36] Joao Pequenao. "Computer generated image of the ATLAS Muons subsystem". 2008. URL: https://cds.cern.ch/record/1095929.

[37] ATLAS Collaboration. "Commissioning of the ATLAS Muon Spectrometer with cosmic rays". In: *Eur. Phys. J. C* 70 (2010), p. 875. DOI: 10.1140/epjc/s10052-010-1415-2. arXiv: 1006.4384 [hep-ex].

[38] A. Airapetian et al. "ATLAS: Detector and physics performance technical design report. Volume 1". In: (1999).

[39] Frank Siegert. "Monte-Carlo event generation for the LHC." PhD thesis. Durham University., 2010. URL: http://etheses.dur.ac.uk/484.

[40] J. Pumplin et al. "New generation of parton distributions with uncertainties from global QCD analysis". In: *JHEP* 0207 (2002), p. 012. DOI: 10.1088/1126-6708/2002/07/012. arXiv: hep-ph/0201195 [hep-ph].

[41] A. D. Martin et al. "Parton distributions for the LHC". In: *Eur. Phys. J.* C63 (2009), pp. 189–285. DOI: 10.1140/epjc/s10052-009-1072-5. arXiv: 0901.0002 [hep-ph].

[42] Richard D. Ball et al. “Parton distributions with LHC data”. In: *Nucl. Phys.* B867 (2013), pp. 244–289. DOI: 10.1016/j.nuclphysb.2012.10.003. arXiv: 1207.1303 [hep-ph].

[43] Andy Buckley et al. “General-purpose event generators for LHC physics”. In: *Phys. Rept.* 504 (2011), pp. 145–233. DOI: 10.1016/j.physrep.2011.03.005. arXiv: 1101.2599 [hep-ph].

[44] G. Corcella et al. “HERWIG 6: An Event generator for hadron emission reactions with interfering gluons (including supersymmetric processes)”. In: *JHEP* 0101 (2001), p. 010. DOI: 10.1088/1126-6708/2001/01/010. arXiv: hep-ph/0011363 [hep-ph].

[45] T. Gleisberg et al. “Event generation with SHERPA 1.1”. In: *JHEP* 0902 (2009), p. 007. DOI: 10.1088/1126-6708/2009/02/007. arXiv: 0811.4622 [hep-ph].

[46] Torbjorn Sjöstrand, Stephen Mrenna, and Peter Z. Skands. “PYTHIA 6.4 Physics and Manual”. In: *JHEP* 0605 (2006), p. 026. DOI: 10.1088/1126-6708/2006/05/026. arXiv: hep-ph/0603175.

[47] Torbjorn Sjostrand, Stephen Mrenna, and Peter Z. Skands. “A Brief Introduction to PYTHIA 8.1”. In: *Comput.Phys.Commun.* 178 (2008), pp. 852–867. DOI: 10.1016/j.cpc.2008.01.036. arXiv: 0710.3820 [hep-ph].

[48] M. Bahr et al. “Herwig++ Physics and Manual”. In: *Eur. Phys. J.* C58 (2008), pp. 639–707. DOI: 10.1140/epjc/s10052-008-0798-9. arXiv: 0803.0883 [hep-ph].

[49] Johannes Bellm et al. “Herwig 7.0/Herwig++ 3.0 release note”. In: *Eur. Phys. J.* C76.4 (2016), p. 196. DOI: 10.1140/epjc/s10052-016-4018-8. arXiv: 1512.01178 [hep-ph].

[50] Michelangelo L. Mangano et al. “ALPGEN, a generator for hard multiparton processes in hadronic collisions”. In: *JHEP* 0307 (2003), p. 001. DOI: 10.1088/1126-6708/2003/07/001. arXiv: hep-ph/0206293 [hep-ph].

[51] Borut Paul Kersevan and Elzbieta Richter-Was. “The Monte Carlo event generator AcerMC versions 2.0 to 3.8 with interfaces to PYTHIA 6.4, HERWIG 6.5 and ARIADNE 4.1”. In: Comput. Phys. Commun. 184 (2013), p. 919. DOI: 10.1016/j.cpc.2012.10.032. arXiv: hep-ph/0405247 [hep-ph].

[52] Stefano Frixione and Bryan R. Webber. "Matching NLO QCD computations and parton shower simulations". In: *JHEP* 06 (2002), p. 029. DOI: 10.1088/1126-6708/2002/06/029. arXiv: hep-ph/0204244 [hep-ph].

[53] Paolo Nason. "A New method for combining NLO QCD with shower Monte Carlo algorithms". In: *JHEP* 0411 (2004), p. 040. DOI: 10.1088/1126-6708/2004/11/040. arXiv: hep-ph/0409146 [hep-ph].

[54] Stefano Frixione, Paolo Nason, and Carlo Oleari. "Matching NLO QCD computations with Parton Shower simulations: the POWHEG method". In: *JHEP* 0711 (2007), p. 070. DOI: 10.1088/1126-6708/2007/11/070. arXiv: 0709.2092 [hep-ph].

[55] S. Agostinelli et al. "GEANT4: A Simulation toolkit". In: *Nucl. Instrum. Meth.* A506 (2003), pp. 250–303. DOI: 10.1016/S0168-9002(03)01368-8.

[56] W. Lukas. "Fast Simulation for ATLAS: Atlfast-II and ISF". In: CERN. Geneva: CERN, 2012. URL: http://cdsweb.cern.ch/record/1458503/files/ATL-SOFT-PROC-2012-065.pdf.

[57] Hung-Liang Lai et al. "New parton distributions for collider physics". In: *Phys. Rev.* D82 (2010), p. 074024. DOI: 10.1103/PhysRevD.82.074024. arXiv: 1007.2241 [hep-ph].

[58] Stefan Höche et al. "QCD matrix elements and truncated showers". In: *JHEP* 0905 (2009), p. 053. DOI: 10.1088/1126-6708/2009/05/053. arXiv: 0903.1219 [hep-ph].

[59] Tanju Gleisberg and Stefan Höche. "Comix, a new matrix element generator". In: *JHEP* 0812 (2008), p. 039. DOI: 10.1088/1126-6708/2008/12/039. arXiv: 0808.3674 [hep-ph].

[60] Steffen Schumann and Frank Krauss. "A Parton shower algorithm based on Catani-Seymour dipole factorisation". In: *JHEP* 0803 (2008), p. 038. DOI: 10.1088/1126-6708/2008/03/038. arXiv: 0709.1027 [hep-ph].

[61] Charalampos Anastasiou et al. "High precision QCD at hadron colliders: Electroweak gauge boson rapidity distributions at NNLO". In: *Phys. Rev.* D69 (2004), p. 094008. DOI: 10.1103/PhysRevD.69.094008. arXiv: hep-ph/0312266 [hep-ph].

[62] J Butterworth et al. *Single Boson and Diboson Production Cross Sections in pp Collisions at sqrts=7 TeV*. Tech. rep. ATL-COM-PHYS-2010-695. Geneva: CERN, 2010. URL: https://cds.cern.ch/record/1287902.

[63] Peter Zeiler Skands. "Tuning Monte Carlo Generators: The Perugia Tunes". In: *Phys. Rev.* D82 (2010), p. 074018. DOI: 10.1103/PhysRevD.82.074018. arXiv: 1005.3457 [hep-ph].

[64] Matteo Cacciari et al. "Top-pair production at hadron colliders with next-to-next-to-leading logarithmic soft-gluon resummation". In: *Phys. Lett.* B710 (2012), pp. 612–622. DOI: 10.1016/j.physletb.2012.03.013. arXiv: 1111.5869 [hep-ph].

[65] M. Beneke et al. "Hadronic top-quark pair production with NNLL threshold resummation". In: *Nucl. Phys.* B855 (2012), pp. 695–741. DOI: 10.1016/j.nuclphysb.2011.10.021. arXiv: 1109.1536 [hep-ph].

[66] Peter BÃđrnreuther, Michal Czakon, and Alexander Mitov. "Percent Level Precision Physics at the Tevatron: First Genuine NNLO QCD Corrections to $q\bar{q} \to t\bar{t} + X$". In: *Phys. Rev. Lett.* 109 (2012), p. 132001. DOI: 10.1103/PhysRevLett.109.132001. arXiv: 1204.5201 [hep-ph].

[67] Michal Czakon and Alexander Mitov. "NNLO corrections to top-pair production at hadron colliders: the all-fermionic scattering channels". In: *JHEP* 12 (2012), p. 054. DOI: 10.1007/JHEP12(2012)054. arXiv: 1207.0236 [hep-ph].

[68] Michal Czakon and Alexander Mitov. "NNLO corrections to top pair production at hadron colliders: the quark-gluon reaction". In: *JHEP* 01 (2013), p. 080. DOI: 10.1007/JHEP01(2013)080. arXiv: 1210.6832 [hep-ph].

[69] MichaÅĆ Czakon, Paul Fiedler, and Alexander Mitov. "Total Top-Quark Pair-Production Cross Section at Hadron Colliders Through $\mathcal{O}(\alpha_S^4)$". In: *Phys. Rev. Lett.* 110 (2013), p. 252004. DOI: 10.1103/PhysRevLett.110.252004. arXiv: 1303.6254 [hep-ph].

[70] Michal Czakon and Alexander Mitov. "Top++: A Program for the Calculation of the Top-Pair Cross-Section at Hadron Colliders". In: *Comput. Phys. Commun.* 185 (2014), p. 2930. DOI: 10.1016/j.cpc.2014.06.021. arXiv: 1112.5675 [hep-ph].

[71] Michiel Botje et al. "The PDF4LHC Working Group Interim Recommendations". In: (2011). arXiv: 1101.0538 [hep-ph].

[72] A. D. Martin et al. "Uncertainties on alpha(S) in global PDF analyses and implications for predicted hadronic cross sections". In: *Eur. Phys. J.* C64 (2009), pp. 653–680. DOI: 10.1140/epjc/s10052-009-1164-2. arXiv: 0905.3531 [hep-ph].

[73] Jun Gao et al. "CT10 next-to-next-to-leading order global analysis of QCD". In: *Phys. Rev.* D89.3 (2014), p. 033009. DOI: 10.1103/PhysRevD.89.033009. arXiv: 1302.6246 [hep-ph].

[74] Nikolaos Kidonakis. "Next-to-next-to-leading-order collinear and soft gluon corrections for t-channel single top quark production". In: *Phys. Rev.* D83 (2011), p. 091503. DOI: 10.1103/PhysRevD.83.091503. arXiv: 1103.2792 [hep-ph].

[75] Nikolaos Kidonakis. "NNLL resummation for s-channel single top quark production". In: *Phys. Rev.* D81 (2010), p. 054028. DOI: 10.1103/PhysRevD.81.054028. arXiv: 1001.5034 [hep-ph].

[76] Nikolaos Kidonakis. "Two-loop soft anomalous dimensions for single top quark associated production with a W- or H-". In: *Phys. Rev.* D82 (2010), p. 054018. DOI: 10.1103/PhysRevD.82.054018. arXiv: 1005.4451 [hep-ph].

[77] John M. Campbell and R. K. Ellis. "MCFM for the Tevatron and the LHC". In: *Nucl. Phys. Proc. Suppl.* 205-206 (2010), pp. 10–15. DOI: 10.1016/j.nuclphysbps.2010.08.011. arXiv: 1007.3492 [hep-ph].

[78] J.M. Butterworth, Jeffrey R. Forshaw, and M.H. Seymour. "Multiparton interactions in photoproduction at HERA". In: *Z. Phys.* C72 (1996), pp. 637–646. DOI: 10.1007/s002880050286. arXiv: hep-ph/9601371 [hep-ph].

[79] ATLAS Collaboration. *New ATLAS event generator tunes to 2010 data*. ATL-PHYS-PUB-2011-008. 2011. URL: http://cds.cern.ch/record/1345343.

[80] T Cornelissen et al. *Concepts, Design and Implementation of the ATLAS New Tracking (NEWT)*. Tech. rep. ATL-SOFT-PUB-2007-007. ATL-COM-SOFT-2007-002. Geneva: CERN, 2007. URL: https://cds.cern.ch/record/1020106.

[81] R. Fruhwirth. "Application of Kalman filtering to track and vertex fitting". In: *Nucl. Instrum. Meth.* A262 (1987), pp. 444–450. DOI: 10.1016/0168-9002(87)90887-4.

[82] ATLAS Collaboration. *Performance of primary vertex reconstruction in proton–proton collisions at $\sqrt{s}$ = 7 TeV in the ATLAS experiment*. ATLAS-CONF-2010-069. 2010. URL: http://cdsweb.cern.ch/record/1281344.

[83] W Lampl et al. *Calorimeter Clustering Algorithms: Description and Performance*. Tech. rep. ATL-LARG-PUB-2008-002. ATL-COM-LARG-2008-003. Geneva: CERN, 2008. URL: https://cds.cern.ch/record/1099735.

[84] ATLAS Collaboration. "Electron reconstruction and identification efficiency measurements with the ATLAS detector using the 2011 LHC proton–proton collision data". In: *Eur. Phys. J. C* 74 (2014), p. 2941. DOI: 10.1140/epjc/s10052-014-2941-0. arXiv: 1404.2240 [hep-ex].

[85] ATLAS Collaboration. "Measurement of the muon reconstruction performance of the ATLAS detector using 2011 and 2012 LHC proton–proton collision data". In: *Eur. Phys. J. C* 74 (2014), p. 3130. DOI: 10.1140/epjc/s10052-014-3130-x. arXiv: 1407.3935 [hep-ex].

[86] ATLAS Collaboration. *Muon Reconstruction Performance*. ATLAS-CONF-2010-064. 2010. URL: http://cdsweb.cern.ch/record/1281339.

[87] ATLAS Collaboration. *Jet energy scale and its systematic uncertainty for jets produced in proton–proton collisions at $\sqrt{s} = 7$ TeV and measured with the ATLAS detector*. ATLAS-CONF-2010-056. 2010. URL: http://cdsweb.cern.ch/record/1281329.

[88] Matteo Cacciari, Gavin P. Salam, and Gregory Soyez. "The anti-k_t jet clustering algorithm". In: *JHEP* 04 (2008), p. 063. DOI: 10.1088/1126-6708/2008/04/063. arXiv: 0802.1189 [hep-ph].

[89] J.J Goodson. "Search for Supersymmetry in States with Large Missing Transverse Momentum and Three Leptons including a Z-Boson." PhD thesis. Stony Brook U., 2012.

[90] Yuri L. Dokshitzer et al. "Better jet clustering algorithms". In: *JHEP* 08 (1997), p. 001. DOI: 10.1088/1126-6708/1997/08/001. arXiv: hep-ph/9707323 [hep-ph].

[91] Bogdan Malaescu et al. *Determination of jet calibration and energy resolution in proton-proton collisions at $\sqrt{s} = 8$ TeV using the ATLAS detector*. Tech. rep. ATL-COM-PHYS-2015-1086. Geneva: CERN, 2015. URL: https://cds.cern.ch/record/2048678.

[92] Georges Aad et al. "Performance of pile-up mitigation techniques for jets in pp collisions at $\sqrt{s} = 8$ TeV using the ATLAS detector". In: (2015). arXiv: 1510.03823 [hep-ex].

[93] ATLAS Collaboration. *b-tagging in dense environments*. ATL-PHYS-PUB-2014-014. 2014. URL: https://atlas.web.cern.ch/Atlas/GROUPS/PHYSICS/PUBNOTES/ATL-PHYS-PUB-2014-014.

[94] ATLAS Collaboration. "Performance of b-Jet Identification in the ATLAS Experiment". In: *JINST* 11.04 (2016), P04008. DOI: 10.1088/1748-0221/11/04/P04008. arXiv: 1512.01094 [hep-ex].

[95] ATLAS Collaboration. *Calibration of the performance of b-tagging for c and light-flavour jets in the 2012 ATLAS data*. ATLAS-CONF-2014-046. 2014. URL: http://cdsweb.cern.ch/record/1741020.

[96] ATLAS Collaboration. *Electron efficiency measurements with the ATLAS detector using the 2012 LHC proton–proton collision data*. ATLAS-CONF-2014-032. 2014. URL: http://cdsweb.cern.ch/record/1706245.

[97] ATLAS Collaboration. "Jet energy measurement with the ATLAS detector in proton–proton collisions at $\sqrt{s} = 7$ TeV". In: *Eur. Phys. J. C* 73 (2013), p. 2304. DOI: 10.1140/epjc/s10052-013-2304-2. arXiv: 1112.6426 [hep-ex].

[98] ATLAS Collaboration. "Jet energy measurement and its systematic uncertainty in proton–proton collisions at $\sqrt{s} = 7$ TeV with the ATLAS detector". In: *Eur. Phys. J. C* 75 (2015), p. 17. DOI: 10.1140/epjc/s10052-014-3190-y. arXiv: 1406.0076 [hep-ex].

[99] Jonathan M. Butterworth et al. "Jet Substructure as a New Higgs-Search Channel at the Large Hadron Collider". In: *Phys. Rev. Lett.* 100 (24 2008), p. 242001. DOI: 10.1103/PhysRevLett.100.242001. URL: http://link.aps.org/doi/10.1103/PhysRevLett.100.242001.

[100] ATLAS Collaboration. *Performance of Missing Transverse Momentum Reconstruction in ATLAS studied in Proton–Proton Collisions recorded in 2012 at* $\sqrt{s} = 8$ *TeV*. ATLAS-CONF-2013-082. 2013. URL: http://cdsweb.cern.ch/record/1570993.

[101] *MET Recommendations for 2012*. URL: https://twiki.cern.ch/twiki/bin/view/AtlasProtected/EtmissRecommendations2012.

[102] ATLAS Collaboration. *Performance of the ATLAS Electron and Photon Trigger in pp Collisions at* $\sqrt{s} = 7$ *TeV in 2011*. ATLAS-CONF-2012-048. 2012. URL: http://cdsweb.cern.ch/record/1450089.

[103] ATLAS Collaboration. "Performance of the ATLAS muon trigger in *pp* collisions at $\sqrt{s} = 8$ TeV". In: *Eur. Phys. J. C* 75 (2015), p. 120. DOI: 10.1140/epjc/s10052-015-3325-9. arXiv: 1408.3179 [hep-ex].

[104] W.H. Bell et al. *Measurement of top quark pair differential cross section with ATLAS in pp collisions at* $\sqrt{s} = 7$ *TeV*. ATL-COM-PHYS-2012-1137 (support note). URL: https://cds.cern.ch/record/1470588.

[105] *ttH, H->bb Analysis for Moriond 2013*. URL: https://twiki.cern.ch/twiki/bin/viewauth/AtlasProtected/TTH2bbWinter2013#ttbar_Powheg_Pythia_reweghting.

[106] Georges Aad et al. "Measurement of the $WW + WZ$ cross section and limits on anomalous triple gauge couplings using final states with one lepton, missing transverse momentum, and two jets with the ATLAS detector at $\sqrt{s} = 7$ TeV". In: *JHEP* 01 (2015), p. 049. DOI: 10.1007/JHEP01(2015)049. arXiv: 1410.7238 [hep-ex].

[107] *Final 2012 Recommendations for Jet Uncertainties*. URL: https://twiki.cern.ch/twiki/bin/view/AtlasProtected/JetUncertainties2012Final.

[108] *Jet Substructure Recommendations*. URL: https://twiki.cern.ch/twiki/bin/view/AtlasProtected/JetSubstructureRecommendations.

[109] F Bertolucci et al. *Measurement of the WW and WZ production cross section and limits on anomalous trilinear gauge couplings in the semileptonic final state in 4.7 fb-1 of pp collisions with the ATLAS detector at* $\sqrt{\mathbf{s}} = \mathbf{7}$ *TeV*. ATL-COM-PHYS-2013-1516 (support note). URL: https://cds.cern.ch/record/1626582.

[110] ATLAS Collaboration. "Measurement of the $WW + WZ$ cross section and limits on anomalous triple gauge couplings using final states with one lepton, missing transverse momentum, and two jets with the ATLAS detector at $\sqrt{s} = 7$ TeV". In: *JHEP* 1501 (2015), p. 049. DOI: 10.1007/JHEP01(2015)049. arXiv: 1410.7238 [hep-ex].

[111] Glen Cowan et al. "Asymptotic formulae for likelihood-based tests of new physics". In: *Eur.Phys.J.* C71 (2011), p. 1554. DOI: 10.1140/epjc/s10052-011-1554-0,10.1140/epjc/s10052-013-2501-z. arXiv: 1007.1727 [physics.data-an].

Appendices

A Summary tables of MC samples

Table 25: Information about MC samples used in this analysis. All samples begin with "mc12_8TeV," which has been omitted to simplify the table. The "Filter Eff." column lists the filter efficiency from AMI. The overall effective cross-section of each sample can be obtained by multiplying the "xSec," "K-factor," and "Filter Eff." columns together.

Sample	tag	xSec (pb)	K-factor	Filter Eff.
$t\bar{t}$				
117050.PowhegPythia_P2011C_ttbar	e1727_a188_a171_r3549_p1575	252.890	1.0	0.5430
Single-top				
110101.AcerMCPythia_P2011CCTEQ6L1_singletop_tchan_l	e2096_a188_a171_r3549_p1575	28.440	1.0	1.0
110119.PowhegPythia_P2011C_st_schan_lep	e1720_a188_a171_r3549_p1575	1.8180	1.0	1.0
110140.PowhegPythia_P2011C_st_Wtchan_incl_DR	e1743_a188_a171_r3549_p1575	22.370	1.0	1.0
Di-boson				
183585.Sherpa_CT10_ZWtoeeqq_MassiveCB	e2370_s1581_s1586_r4485_r4540_p1575	1.4648	1.050	1.0
183586.Sherpa_CT10_ZZtoeeqq_MassiveCB	e2370_a220_a205_r4540_p1575	0.24672	1.0	1.0
183587.Sherpa_CT10_ZWtomumuqq_MassiveCB	e2370_s1581_s1586_r4485_r4540_p1575	1.4634	1.050	1.0
183588.Sherpa_CT10_ZZtomumuqq_MassiveCB	e2370_a220_a205_r4540_p1575	0.24757	1.0	1.0
183589.Sherpa_CT10_ZWtotautauqq_MassiveCB	e2370_s1581_s1586_r4485_r4540_p1575	1.4523	1.050	1.0
183590.Sherpa_CT10_ZZtotautauqq_MassiveCB	e2370_s1581_s1586_r4485_r4540_p1575	0.24167	1.0	1.0
183734.Sherpa_CT10_WWtoenuqq_MassiveCB	e2347_s1581_s1586_r4485_r4540_p1575	7.2854	1.060	1.0
183735.Sherpa_CT10_WZtoenuqq_MassiveCB	e2347_s1581_s1586_r4485_r4540_p1575	1.9036	1.050	1.0
183736.Sherpa_CT10_WWtomunuqq_MassiveCB	e2347_s1581_s1586_r4485_r4540_p1575	7.2974	1.060	1.0
183737.Sherpa_CT10_WZtomunuqq_MassiveCB	e2347_s1581_s1586_r4485_r4540_p1575	1.9057	1.050	1.0
183738.Sherpa_CT10_WWtotaunuqq_MassiveCB	e2347_s1581_s1586_r4485_r4540_p1575	7.2741	1.060	1.0
183739.Sherpa_CT10_WZtotaunuqq_MassiveCB	e2347_s1581_s1586_r4485_r4540_p1575	1.9152	1.050	1.0
145161.Sherpa_CT10_eegammaPt10	e1434_s1499_s1504_r3658_r3549_p1575	32.260	1.0	1.0
145162.Sherpa_CT10_mumugammaPt10	e1434_s1499_s1504_r3658_r3549_p1575	32.3170	1.0	1.0
146436.AlpgenJimmy_AUET2CTEQ6L1_WgammaNp0_LeptonPhotonFilter	e1601_s1499_s1504_r3658_r3549_p1575	229.880	1.150	0.313720
146437.AlpgenJimmy_AUET2CTEQ6L1_WgammaNp1_LeptonPhotonFilter	e1601_s1499_s1504_r3658_r3549_p1575	59.5180	1.150	0.448710
146438.AlpgenJimmy_AUET2CTEQ6L1_WgammaNp2_LeptonPhotonFilter	e1601_s1499_s1504_r3658_r3549_p1575	21.390	1.150	0.544610
146439.AlpgenJimmy_AUET2CTEQ6L1_WgammaNp3_LeptonPhotonFilter	e1601_s1499_s1504_r3658_r3549_p1575	7.12030	1.150	0.629740
146434.AlpgenJimmy_AUET2CTEQ6L1_WgammaNp4	e1601_s1499_s1504_r3658_r3549_p1575	2.12240	1.150	1.0
146435.AlpgenJimmy_AUET2CTEQ6L1_WgammaNp5	e1601_s1499_s1504_r3658_r3549_p1575	0.466120	1.150	1.0

Table 26: Information about MC samples used in this analysis. All samples begin with "mc12_8TeV," which has been omitted to simplify the table. The "Filter Eff." column lists the filter efficiency from AMI. The overall effective cross-section of each sample can be obtained by multiplying the "xSec," "K-factor," and "Filter Eff." columns together.

Sample	tag	xSec (pb)	K-factor	Filter Eff.
W + jets				
mc12_8TeV.167740.Sherpa_CT10_WenuMassiveCBPt0_BFilter	e1585_a159_a171_r3549_p1562	140.34	1.10	1.0
mc12_8TeV.167741.Sherpa_CT10_WenuMassiveCBPt0_CJetFilterBVeto	e1585_a159_a171_r3549_p1562	537.84	1.10	1.0
mc12_8TeV.167742.Sherpa_CT10_WenuMassiveCBPt0_CJetVetoBVeto	e1585_a159_a171_r3549_p1562	10295	1.10	1.0
mc12_8TeV.167743.Sherpa_CT10_WmunuMassiveCBPt0_BFilter	e1585_a159_a171_r3549_p1562	140.39	1.10	1.0
mc12_8TeV.167744.Sherpa_CT10_WmunuMassiveCBPt0_CJetFilterBVeto	e1585_a159_a171_r3549_p1562	466.47	1.10	1.0
mc12_8TeV.167745.Sherpa_CT10_WmunuMassiveCBPt0_CJetVetoBVeto	e1585_a159_a171_r3549_p1562	10368	1.10	1.0
mc12_8TeV.167746.Sherpa_CT10_WtaunuMassiveCBPt0_BFilter	e1585_a159_a171_r3549_p1562	140.34	1.10	1.0
mc12_8TeV.167747.Sherpa_CT10_WtaunuMassiveCBPt0_CJetFilterBVeto	e1585_a159_a171_r3549_p1562	506.45	1.10	1.0
mc12_8TeV.167748.Sherpa_CT10_WtaunuMassiveCBPt0_CJetVetoBVeto	e1585_a159_a171_r3549_p1562	10327	1.10	1.0
mc12_8TeV.180534.Sherpa_CT10_WenuMassiveCBPt40_70_BFilter	e1867_a188_a171_r3549_p1575	652.820	1.10	0.034473
mc12_8TeV.180535.Sherpa_CT10_WenuMassiveCBPt40_70_CJetFilterBVeto	e1867_a188_a171_r3549_p1575	652.830	1.10	0.171420
mc12_8TeV.180536.Sherpa_CT10_WenuMassiveCBPt40_70_CJetVetoBVeto	e1867_a188_a171_r3549_p1562	653.160	1.10	0.793350
mc12_8TeV.180537.Sherpa_CT10_WmunuMassiveCBPt40_70_BFilter	e1867_a188_a171_r3549_p1575	652.730	1.10	0.034565
mc12_8TeV.180538.Sherpa_CT10_WmunuMassiveCBPt40_70_CJetFilterBVeto	e1867_a188_a171_r3549_p1575	653.140	1.10	0.165990
mc12_8TeV.180539.Sherpa_CT10_WmunuMassiveCBPt40_70_CJetVetoBVeto	e1867_a188_a171_r3549_p1562	653.060	1.10	0.799830
mc12_8TeV.180540.Sherpa_CT10_WtaunuMassiveCBPt40_70_BFilter	e1867_a188_a171_r3549_p1575	652.840	1.10	0.034574
mc12_8TeV.180541.Sherpa_CT10_WtaunuMassiveCBPt40_70_CJetFilterBVeto	e1867_a188_a171_r3549_p1575	652.580	1.10	0.169310
mc12_8TeV.180542.Sherpa_CT10_WtaunuMassiveCBPt40_70_CJetVetoBVeto	e1867_a188_a171_r3549_p1562	652.990	1.10	0.796160
mc12_8TeV.167761.Sherpa_CT10_WenuMassiveCBPt70_140_BFilter	e1620_a159_a171_r3549_p1562	250.550	1.10	0.045931
mc12_8TeV.167762.Sherpa_CT10_WenuMassiveCBPt70_140_CJetFilterBVeto	e1620_a159_a171_r3549_p1562	250.710	1.10	0.200990
mc12_8TeV.167763.Sherpa_CT10_WenuMassiveCBPt70_140_CJetVetoBVeto	e1620_a159_a171_r3549_p1562	250.620	1.10	0.752660
mc12_8TeV.167764.Sherpa_CT10_WmunuMassiveCBPt70_140_BFilter	e1714_a159_a171_r3549_p1562	250.550	1.10	0.045919
mc12_8TeV.167765.Sherpa_CT10_WmunuMassiveCBPt70_140_CJetFilterBVeto	e1714_a159_a171_r3549_p1575	250.570	1.10	0.195060
mc12_8TeV.167766.Sherpa_CT10_WmunuMassiveCBPt70_140_CJetVetoBVeto	e1714_a159_a171_r3549_p1562	250.790	1.10	0.758650
mc12_8TeV.167767.Sherpa_CT10_WtaunuMassiveCBPt70_140_BFilter	e1714_s1581_s1586_r3658_r3549_p1562	250.570	1.10	0.045942
mc12_8TeV.167768.Sherpa_CT10_WtaunuMassiveCBPt70_140_CJetFilterBVeto	e1714_s1581_s1586_r3658_r3549_p1562	250.610	1.10	0.198890
mc12_8TeV.167769.Sherpa_CT10_WtaunuMassiveCBPt70_140_CJetVetoBVeto	e1714_s1581_s1586_r3658_r3549_p1562	250.560	1.10	0.754760
mc12_8TeV.167770.Sherpa_CT10_WenuMassiveCBPt140_280_BFilter	e1620_a159_a171_r3549_p1562	31.1630	1.10	0.063113
mc12_8TeV.167771.Sherpa_CT10_WenuMassiveCBPt140_280_CJetFilterBVeto	e1620_a159_a171_r3549_p1562	31.1890	1.10	0.221960
mc12_8TeV.167772.Sherpa_CT10_WenuMassiveCBPt140_280_CJetVetoBVeto	e1620_a159_a171_r3549_p1562	31.1120	1.10	0.714960

Table 27: Information about MC samples used in this analysis. All samples begin with "mc12_8TeV," which has been omitted to simplify the table. The "Filter Eff." column lists the filter efficiency from AMI. The overall effective cross-section of each sample can be obtained by multiplying the "xSec," "K-factor," and "Filter Eff." columns together.

Sample	tag	xSec (pb)	K-factor	Filter Eff.
$W+$jets				
mc12_8TeV.167773.Sherpa_CT10_WmunuMassiveCBPt140_280_BFilter	e1741_a159_a171_r3549_p1562	31.1680	1.10	0.063142
mc12_8TeV.167774.Sherpa_CT10_WmunuMassiveCBPt140_280_CJetFilterBVeto	e1714_a159_a171_r3549_p1562	31.1650	1.10	0.216470
mc12_8TeV.167775.Sherpa_CT10_WmunuMassiveCBPt140_280_CJetVetoBVeto	e1714_a159_a171_r3549_p1575	31.1730	1.10	0.72030
mc12_8TeV.167776.Sherpa_CT10_WtaunuMassiveCBPt140_280_BFilter	e1741_s1581_s1586_r3658_r3549_p1562	31.1630	1.10	0.063169
mc12_8TeV.167777.Sherpa_CT10_WtaunuMassiveCBPt140_280_CJetFilterBVeto	e1714_s1581_s1586_r3658_r3549_p1562	31.1510	1.10	0.220150
mc12_8TeV.167778.Sherpa_CT10_WtaunuMassiveCBPt140_280_CJetVetoBVeto	e1714_s1581_s1586_r3658_r3549_p1575	31.1760	1.10	0.716090
mc12_8TeV.167779.Sherpa_CT10_WenuMassiveCBPt280_500_BFilter	e1714_s1581_s1586_r3658_r3549_p1575	1.83980	1.10	0.082992
mc12_8TeV.167780.Sherpa_CT10_WenuMassiveCBPt280_500_CJetFilterBVeto	e1714_s1581_s1586_r3658_r3549_p1562	1.8370	1.10	0.234540
mc12_8TeV.167781.Sherpa_CT10_WenuMassiveCBPt280_500_CJetVetoBVeto	e1714_s1581_s1586_r3658_r3549_p1562	1.84260	1.10	0.6820
mc12_8TeV.167782.Sherpa_CT10_WmunuMassiveCBPt280_500_BFilter	e1714_s1581_s1586_r3658_r3549_p1575	1.8380	1.10	0.082902
mc12_8TeV.167783.Sherpa_CT10_WmunuMassiveCBPt280_500_CJetFilterBVeto	e1714_s1581_s1586_r3658_r3549_p1562	1.83950	1.10	0.228450
mc12_8TeV.167784.Sherpa_CT10_WmunuMassiveCBPt280_500_CJetVetoBVeto	e1714_s1581_s1586_r3658_r3549_p1575	1.84330	1.10	0.687760
mc12_8TeV.167785.Sherpa_CT10_WtaunuMassiveCBPt280_500_BFilter	e1714_s1581_s1586_r3658_r3549_p1562	1.83860	1.10	0.083054
mc12_8TeV.167786.Sherpa_CT10_WtaunuMassiveCBPt280_500_CJetFilterBVeto	e1714_s1581_s1586_r3658_r3549_p1575	1.83950	1.10	0.232710
mc12_8TeV.167787.Sherpa_CT10_WtaunuMassiveCBPt280_500_CJetVetoBVeto	e1714_s1581_s1586_r3658_r3549_p1575	1.83680	1.10	0.683970
mc12_8TeV.167788.Sherpa_CT10_WenuMassiveCBPt500_BFilter	e1620_a159_a171_r3549_p1562	0.101740	1.10	0.099524
mc12_8TeV.167789.Sherpa_CT10_WenuMassiveCBPt500_CJetFilterBVeto	e1620_a159_a171_r3549_p1562	0.101010	1.10	0.24440
mc12_8TeV.167790.Sherpa_CT10_WenuMassiveCBPt500_CJetVetoBVeto	e1620_a159_a171_r3549_p1562	0.100930	1.10	0.657410
mc12_8TeV.167791.Sherpa_CT10_WmunuMassiveCBPt500_BFilter	e1714_s1581_s1586_r3658_r3549_p1575	0.101630	1.10	0.100040
mc12_8TeV.167792.Sherpa_CT10_WmunuMassiveCBPt500_CJetFilterBVeto	e1714_s1581_s1586_r3658_r3549_p1562	0.10210	1.10	0.238520
mc12_8TeV.167793.Sherpa_CT10_WmunuMassiveCBPt500_CJetVetoBVeto	e1714_s1581_s1586_r3658_r3549_p1562	0.101860	1.10	0.658370
mc12_8TeV.167794.Sherpa_CT10_WtaunuMassiveCBPt500_BFilter	e1714_s1581_s1586_r3658_r3549_p1575	0.101790	1.10	0.099729
mc12_8TeV.167795.Sherpa_CT10_WtaunuMassiveCBPt500_CJetFilterBVeto	e1714_s1581_s1586_r3658_r3549_p1562	0.101390	1.10	0.242210
mc12_8TeV.167796.Sherpa_CT10_WtaunuMassiveCBPt500_CJetVetoBVeto	e1714_s1581_s1586_r3658_r3549_p1562	0.102010	1.10	0.660040
EWK $W+$jets				
129915.Sherpa_CT10_Wenu2JetsEW1JetQCD15GeV_min_n_tchannels	e1557_s1499_s1504_r3658_r3549_p1575	4.21140	1.0	1.0
129916.Sherpa_CT10_Wmunu2JetsEW1JetQCD15GeV_min_n_tchannels	e1557_s1499_s1504_r3658_r3549_p1575	4.21280	1.0	1.0
129917.Sherpa_CT10_Wtaunu2JetsEW1JetQCD15GeV_min_n_tchannels	e1557_s1499_s1504_r3658_r3549_p1575	4.21240	1.0	1.0

Table 28: Information about MC samples used in this analysis. All samples begin with "mc12_8TeV," which has been omitted to simplify the table. The "Filter Eff." column lists the filter efficiency from AMI. The overall effective cross-section of each sample can be obtained by multiplying the "xSec," "K-factor," and "Filter Eff." columns together.

Sample	tag	xSec (pb)	K-factor	Filter Eff.
Z + jets				
mc12_8TeV.167749.Sherpa_CT10_ZeeMassiveCBPt0_BFilter	e1585_s1773_s1776_r4485_r4540_p1770	1110.0	1.120	0.027969
mc12_8TeV.167750.Sherpa_CT10_ZeeMassiveCBPt0_CFilterBVeto	e1585_s1773_s1776_r4485_r4540_p1770	1109.60	1.120	0.283220
mc12_8TeV.167751.Sherpa_CT10_ZeeMassiveCBPt0_CVetoBVeto	e1585_s1773_s1776_r4485_r4540_p1770	1110.10	1.120	0.68860
mc12_8TeV.167752.Sherpa_CT10_ZmumuMassiveCBPt0_BFilter	e1585_s1773_s1776_r4485_r4540_p1770	1110.0	1.120	0.027960
mc12_8TeV.167753.Sherpa_CT10_ZmumuMassiveCBPt0_CFilterBVeto	e1585_s1773_s1776_r4485_r4540_p1770	1110.30	1.120	0.283530
mc12_8TeV.167754.Sherpa_CT10_ZmumuMassiveCBPt0_CVetoBVeto	e1585_s1773_s1776_r4485_r4540_p1770	1110.0	1.120	0.688720
mc12_8TeV.167755.Sherpa_CT10_ZtautauMassiveCBPt0_BFilter	e1585_s1773_s1776_r4485_r4540_p1770	1110.0	1.120	0.027935
mc12_8TeV.167756.Sherpa_CT10_ZtautauMassiveCBPt0_CFilterBVeto	e1587_s1773_s1776_r4485_r4540_p1770	1110.10	1.120	0.28330
mc12_8TeV.167757.Sherpa_CT10_ZtautauMassiveCBPt0_CVetoBVeto	e1587_s1773_s1776_r4485_r4540_p1770	1109.80	1.120	0.688930
mc12_8TeV.167797.Sherpa_CT10_ZeeMassiveCBPt70_140_BFilter	e1714_a159_a171_r3549_p1575	29.4940	1.120	0.082517
mc12_8TeV.167798.Sherpa_CT10_ZeeMassiveCBPt70_140_CFilterBVeto	e1714_a159_a171_r3549_p1575	29.4870	1.120	0.354970
mc12_8TeV.167799.Sherpa_CT10_ZeeMassiveCBPt70_140_CVetoBVeto	e1714_a159_a171_r3549_p1575	29.4910	1.120	0.562620
mc12_8TeV.167800.Sherpa_CT10_ZmumuMassiveCBPt70_140_BFilter	e1620_a159_a171_r3549_p1575	29.4910	1.120	0.082585
mc12_8TeV.167801.Sherpa_CT10_ZmumuMassiveCBPt70_140_CFilterBVeto	e1620_a159_a171_r3549_p1575	29.4470	1.120	0.354880
mc12_8TeV.167802.Sherpa_CT10_ZmumuMassiveCBPt70_140_CVetoBVeto	e1620_a159_a171_r3549_p1575	29.5210	1.120	0.561960
mc12_8TeV.167803.Sherpa_CT10_ZtautauMassiveCBPt70_140_BFilter	e1714_s1581_s1586_r3658_r3549_p1575	29.4890	1.120	0.082563
mc12_8TeV.167804.Sherpa_CT10_ZtautauMassiveCBPt70_140_CFilterBVeto	e1714_s1581_s1586_r3658_r3549_p1575	29.4990	1.120	0.355090
mc12_8TeV.167805.Sherpa_CT10_ZtautauMassiveCBPt70_140_CVetoBVeto	e1714_s1581_s1586_r3658_r3549_p1575	29.4940	1.120	0.562470
mc12_8TeV.167809.Sherpa_CT10_ZeeMassiveCBPt140_280_BFilter	e1714_a159_a171_r3549_p1575	3.98770	1.120	0.095263
mc12_8TeV.167810.Sherpa_CT10_ZeeMassiveCBPt140_280_CFilterBVeto	e1714_a159_a171_r3549_p1575	3.98110	1.120	0.369190
mc12_8TeV.167811.Sherpa_CT10_ZeeMassiveCBPt140_280_CVetoBVeto	e1714_a159_a171_r3549_p1575	3.9890	1.120	0.534310
mc12_8TeV.167812.Sherpa_CT10_ZmumuMassiveCBPt140_280_BFilter	e1620_a159_a171_r3549_p1575	3.98420	1.120	0.095389
mc12_8TeV.167813.Sherpa_CT10_ZmumuMassiveCBPt140_280_CFilterBVeto	e1620_a159_a171_r3549_p1575	3.99110	1.120	0.369990
mc12_8TeV.167814.Sherpa_CT10_ZmumuMassiveCBPt140_280_CVetoBVeto	e1620_a159_a171_r3549_p1575	3.98410	1.120	0.534410
mc12_8TeV.167815.Sherpa_CT10_ZtautauMassiveCBPt140_280_BFilter	e1714_s1581_s1586_r3658_r3549_p1575	3.98870	1.120	0.095456
mc12_8TeV.167816.Sherpa_CT10_ZtautauMassiveCBPt140_280_CFilterBVeto	e1714_s1581_s1586_r3658_r3549_p1575	3.9880	1.120	0.369530
mc12_8TeV.167817.Sherpa_CT10_ZtautauMassiveCBPt140_280_CVetoBVeto	e1714_s1581_s1586_r3658_r3549_p1575	3.98710	1.120	0.533280

Table 29: Information about MC samples used in this analysis. All samples begin with "mc12_8TeV," which has been omitted to simplify the table. The "Filter Eff." column lists the filter efficiency from AMI. The overall effective cross-section of each sample can be obtained by multiplying the "xSec," "K-factor," and "Filter Eff." columns together.

Sample	tag	xSec (pb)	K-factor	Filter Eff.
Z + jets				
mc12_8TeV.167821.Sherpa_CT10_ZeeMassiveCBPt280_500_BFilter	e1714_s1581_s1586_r3658_r3549_p1575	0.24160	1.120	0.107060
mc12_8TeV.167822.Sherpa_CT10_ZeeMassiveCBPt280_500_CFilterBVeto	e1741_s1581_s1586_r3658_r3549_p1575	0.241280	1.120	0.387440
mc12_8TeV.167823.Sherpa_CT10_ZeeMassiveCBPt280_500_CVetoBVeto	e1714_s1581_s1586_r3658_r3549_p1575	0.241580	1.120	0.506170
mc12_8TeV.167824.Sherpa_CT10_ZmumuMassiveCBPt280_500_BFilter	e1714_s1581_s1586_r3658_r3549_p1575	0.242190	1.120	0.108020
mc12_8TeV.167825.Sherpa_CT10_ZmumuMassiveCBPt280_500_CFilterBVeto	e1741_s1581_s1586_r3658_r3549_p1575	0.241690	1.120	0.386430
mc12_8TeV.167826.Sherpa_CT10_ZmumuMassiveCBPt280_500_CVetoBVeto	e1714_s1581_s1586_r3658_r3549_p1575	0.242720	1.120	0.505490
mc12_8TeV.167827.Sherpa_CT10_ZtautauMassiveCBPt280_500_BFilter	e1714_s1581_s1586_r3658_r3549_p1575	0.24190	1.120	0.107180
mc12_8TeV.167828.Sherpa_CT10_ZtautauMassiveCBPt280_500_CFilterBVeto	e1741_s1581_s1586_r3658_r3549_p1575	0.241020	1.120	0.384810
mc12_8TeV.167829.Sherpa_CT10_ZtautauMassiveCBPt280_500_CVetoBVeto	e1714_s1581_s1586_r3658_r3549_p1575	0.241470	1.120	0.50720
mc12_8TeV.167833.Sherpa_CT10_ZeeMassiveCBPt500_BFilter	e1714_s1581_s1586_r3658_r3549_p1575	0.013235	1.120	0.115730
mc12_8TeV.167834.Sherpa_CT10_ZeeMassiveCBPt500_CFilterBVeto	e1714_s1581_s1586_r3658_r3549_p1575	0.013454	1.120	0.398460
mc12_8TeV.167835.Sherpa_CT10_ZeeMassiveCBPt500_CVetoBVeto	e1714_s1581_s1586_r3658_r3549_p1575	0.013307	1.120	0.48480
mc12_8TeV.167836.Sherpa_CT10_ZmumuMassiveCBPt500_BFilter	e1620_a159_a171_r3549_p1575	0.013161	1.120	0.114080
mc12_8TeV.167837.Sherpa_CT10_ZmumuMassiveCBPt500_CFilterBVeto	e1620_a159_a171_r3549_p1575	0.013480	1.120	0.398570
mc12_8TeV.167838.Sherpa_CT10_ZmumuMassiveCBPt500_CVetoBVeto	e1620_a159_a171_r3549_p1575	0.013264	1.120	0.486890
mc12_8TeV.167839.Sherpa_CT10_ZtautauMassiveCBPt500_BFilter	e1714_s1581_s1586_r3658_r3549_p1575	0.013285	1.120	0.116260
mc12_8TeV.167840.Sherpa_CT10_ZtautauMassiveCBPt500_CFilterBVeto	e1714_s1581_s1586_r3658_r3549_p1575	0.013308	1.120	0.393160
mc12_8TeV.167841.Sherpa_CT10_ZtautauMassiveCBPt500_CVetoBVeto	e1714_s1581_s1586_r3658_r3549_p1575	0.013284	1.120	0.485620

Table 30: Information about MC samples used in this analysis. All samples begin with "mc12_8TeV," which has been omitted to simplify the table. The "Filter Eff." column lists the filter efficiency from AMI. The overall effective cross-section of each sample can be obtained by multiplying the "xSec," "K-factor," and "Filter Eff." columns together.

Sample	tag	xSec (pb)	K-factor	Filt Eff
WV VBS Signal				
185721.WhizardPythia8_AU2_CT10_WVsemileptonic_km_a4_0_a5_0	e3030_a220_a205_r4540_p1575	0.67608	1.	1.
185722.WhizardPythia8_AU2_CT10_WVsemileptonic_km_a4_00_a5_01	e3030_a220_a205_r4540_p1575	0.71426	1.0	1.0
185723.WhizardPythia8_AU2_CT10_WVsemileptonic_km_a4_00_a5_02	e3030_a220_a205_r4540_p1575	0.772485	1.	1.
185724.WhizardPythia8_AU2_CT10_WVsemileptonic_km_a4_00_a5_m01	e3030_a220_a205_r4540_p1575	0.72116	1.0	1.0
185725.WhizardPythia8_AU2_CT10_WVsemileptonic_km_a4_00_a5_m02	e3030_a220_a205_r4540_p1575	0.77983	1.0	1.0
185726.WhizardPythia8_AU2_CT10_WVsemileptonic_km_a4_01_a5_00	e3030_a220_a205_r4540_p1575	0.71374	1.0	1.0
185727.WhizardPythia8_AU2_CT10_WVsemileptonic_km_a4_01_a5_01	e3030_a220_a205_r4540_p1575	0.76323	1.0	1.0
185728.WhizardPythia8_AU2_CT10_WVsemileptonic_km_a4_01_a5_m02	e3030_a220_a205_r4540_p1575	0.73422	1.0	1.0
185729.WhizardPythia8_AU2_CT10_WVsemileptonic_km_a4_01_a5_m04	e3030_a220_a205_r4540_p1575	0.88084	1.0	1.0
185730.WhizardPythia8_AU2_CT10_WVsemileptonic_km_a4_02_a5_m03	e3030_a220_a205_r4540_p1575	0.78435	1.0	1.0
185731.WhizardPythia8_AU2_CT10_WVsemileptonic_km_a4_03_a5_m02	e3030_a220_a205_r4540_p1575	0.78191	1.0	1.0
185732.WhizardPythia8_AU2_CT10_WVsemileptonic_km_a4_03_a5_m06	e3030_a220_a205_r4540_p1575	0.961	1.0	1.0
185733.WhizardPythia8_AU2_CT10_WVsemileptonic_km_a4_m01_a5_00	e3030_a220_a205_r4540_p1575	0.72011	1.0	1.0
185734.WhizardPythia8_AU2_CT10_WVsemileptonic_km_a4_m01_a5_02	e3030_a220_a205_r4540_p1575	0.73466	1.0	1.0
185735.WhizardPythia8_AU2_CT10_WVsemileptonic_km_a4_m01_a5_04	e3030_a220_a205_r4540_p1575	0.87209	1.0	1.0
185736.WhizardPythia8_AU2_CT10_WVsemileptonic_km_a4_m01_a5_m01	e3030_a220_a205_r4540_p1575	0.77243	1.0	1.0
185737.WhizardPythia8_AU2_CT10_WVsemileptonic_km_a4_m02_a5_03	e3030_a220_a205_r4540_p1575	0.78402	1.0	1.0
185738.WhizardPythia8_AU2_CT10_WVsemileptonic_km_a4_m03_a5_02	e3030_a220_a205_r4540_p1575	0.79853	1.0	1.0
185739.WhizardPythia8_AU2_CT10_WVsemileptonic_km_a4_m03_a5_06	e3030_a220_a205_r4540_p1575	0.9581	1.0	1.0
185740.WhizardPythia8_AU2_CT10_WVsemileptonic_km_a4_01_a5_m01	e3030_a220_a205_r4540_p1575	0.70146	1.0	1.0
185741.WhizardPythia8_AU2_CT10_WVsemileptonic_km_a4_m01_a5_01	e3030_a220_a205_r4540_p1575	0.70569	1.0	1.0
185742.WhizardPythia8_AU2_CT10_WVsemileptonic_km_a4_005_a5_005	e3030_a220_a205_r4540_p1575	0.70918	1.0	1.0
185743.WhizardPythia8_AU2_CT10_WVsemileptonic_km_a4_005_a5_0	e3030_a220_a205_r4540_p1575	0.68855	1.0	1.0
185744.WhizardPythia8_AU2_CT10_WVsemileptonic_km_a4_005_a5_m005	e3030_a220_a205_r4540_p1575	0.68384	1.0	1.0
185745.WhizardPythia8_AU2_CT10_WVsemileptonic_km_a4_00_a5_005	e3030_a220_a205_r4540_p1575	0.69112	1.0	1.0
185746.WhizardPythia8_AU2_CT10_WVsemileptonic_km_a4_00_a5_m005	e3030_a220_a205_r4540_p1575	0.69072	1.0	1.0
185747.WhizardPythia8_AU2_CT10_WVsemileptonic_km_a4_m005_a5_005	e3030_a220_a205_r4540_p1575	0.68389	1.0	1.0
185748.WhizardPythia8_AU2_CT10_WVsemileptonic_km_a4_m005_a5_0	e3030_a220_a205_r4540_p1575	0.69274	1.0	1.0
185749.WhizardPythia8_AU2_CT10_WVsemileptonic_km_a4_m005_a5_m005	e3030_a220_a205_r4540_p1575	0.71448	1.0	1.0
185750.WhizardPythia8_AU2_CT10_WVsemileptonic_km_a4_03_a5_03	e3030_a220_a205_r4540_p1575	1.02982	1.0	1.0

Table 31: Information about MC samples used in this analysis. All samples begin with "mc12_8TeV," which has been omitted to simplify the table. The "Filter Eff." column lists the filter efficiency from AMI. The overall effective cross-section of each sample can be obtained by multiplying the "xSec," "K-factor," and "Filter Eff." columns together.

Sample	tag	xSec (pb)	K-factor	Filt Eff
WV VBS Signal				
185751.WhizardPythia8_AU2_CT10_WVsemileptonic_km_a4_03_a5_0	e3030_a220_a205_r4540_p1575	0.840242	1.	1.
185752.WhizardPythia8_AU2_CT10_WVsemileptonic_km_a4_03_a5_m03	e3030_a220_a205_r4540_p1575	0.81024	1.0	1.0
185753.WhizardPythia8_AU2_CT10_WVsemileptonic_km_a4_00_a5_03	e3030_a220_a205_r4540_p1575	0.8448	1.0	1.0
185754.WhizardPythia8_AU2_CT10_WVsemileptonic_km_a4_00_a5_m03	e3030_a220_a205_r4540_p1575	0.85536	1.0	1.0
185755.WhizardPythia8_AU2_CT10_WVsemileptonic_km_a4_m03_a5_03	e3030_a220_a205_r4540_p1575	0.82033	1.0	1.0
185756.WhizardPythia8_AU2_CT10_WVsemileptonic_km_a4_m03_a5_0	e3030_a220_a205_r4540_p1575	0.86255	1.0	1.0
185757.WhizardPythia8_AU2_CT10_WVsemileptonic_km_a4_m03_a5_m03	e3030_a220_a205_r4540_p1575	1.06203	1.0	1.0
ZV VBS Signal				
185758.WhizardPythia8_AU2_CT10_ZVsemileptonic_km_a4_0_a5_0	e3030_a220_a205_r4540_p1575	0.0946094	1.	1.
185759.WhizardPythia8_AU2_CT10_ZVsemileptonic_km_a4_00_a5_01	e3030_a220_a205_r4540_p1575	0.10648	1.0	1.0
185760.WhizardPythia8_AU2_CT10_ZVsemileptonic_km_a4_00_a5_02	e3030_a220_a205_r4540_p1575	0.126686	1.	1.
185761.WhizardPythia8_AU2_CT10_ZVsemileptonic_km_a4_00_a5_m01	e3030_a220_a205_r4540_p1575	0.10908	1.0	1.0
185762.WhizardPythia8_AU2_CT10_ZVsemileptonic_km_a4_00_a5_m02	e3030_a220_a205_r4540_p1575	0.1312	1.0	1.0
185763.WhizardPythia8_AU2_CT10_ZVsemileptonic_km_a4_01_a5_00	e3030_a220_a205_r4540_p1575	0.10764	1.0	1.0
185764.WhizardPythia8_AU2_CT10_ZVsemileptonic_km_a4_01_a5_01	e3030_a220_a205_r4540_p1575	0.11845	1.0	1.0
185765.WhizardPythia8_AU2_CT10_ZVsemileptonic_km_a4_01_a5_m02	e3030_a220_a205_r4540_p1575	0.12041	1.0	1.0
185766.WhizardPythia8_AU2_CT10_ZVsemileptonic_km_a4_01_a5_m04	e3030_a220_a205_r4540_p1575	0.17695	1.0	1.0
185767.WhizardPythia8_AU2_CT10_ZVsemileptonic_km_a4_02_a5_m03	e3030_a220_a205_r4540_p1575	0.14836	1.0	1.0
185768.WhizardPythia8_AU2_CT10_ZVsemileptonic_km_a4_03_a5_m02	e3030_a220_a205_r4540_p1575	0.14896	1.0	1.0
185769.WhizardPythia8_AU2_CT10_ZVsemileptonic_km_a4_03_a5_m06	e3030_a220_a205_r4540_p1575	0.22998	1.0	1.0
185770.WhizardPythia8_AU2_CT10_ZVsemileptonic_km_a4_m01_a5_00	e3030_a220_a205_r4540_p1575	0.10876	1.0	1.0
185771.WhizardPythia8_AU2_CT10_ZVsemileptonic_km_a4_m01_a5_02	e3030_a220_a205_r4540_p1575	0.12016	1.0	1.0
185772.WhizardPythia8_AU2_CT10_ZVsemileptonic_km_a4_m01_a5_04	e3030_a220_a205_r4540_p1575	0.17332	1.0	1.0
185773.WhizardPythia8_AU2_CT10_ZVsemileptonic_km_a4_m01_a5_m01	e3030_a220_a205_r4540_p1575	0.12369	1.0	1.0
185774.WhizardPythia8_AU2_CT10_ZVsemileptonic_km_a4_m02_a5_03	e3030_a220_a205_r4540_p1575	0.14849	1.0	1.0
185775.WhizardPythia8_AU2_CT10_ZVsemileptonic_km_a4_m03_a5_02	e3030_a220_a205_r4540_p1575	0.1546	1.0	1.0
185776.WhizardPythia8_AU2_CT10_ZVsemileptonic_km_a4_m03_a5_06	e3030_a220_a205_r4540_p1575	0.2258	1.0	1.0
185777.WhizardPythia8_AU2_CT10_ZVsemileptonic_km_a4_01_a5_m01	e3030_a220_a205_r4540_p1575	0.11004	1.0	1.0
185778.WhizardPythia8_AU2_CT10_ZVsemileptonic_km_a4_m01_a5_01	e3030_a220_a205_r4540_p1575	0.10992	1.0	1.0

Table 32: Information about MC samples used in this analysis. All samples begin with "mc12_8TeV," which has been omitted to simplify the table. The "Filter Eff." column lists the filter efficiency from AMI. The overall effective cross-section of each sample can be obtained by multiplying the "xSec," "K-factor," and "Filter Eff." columns together.

Sample	tag	xSec (pb)	K-factor	Filt Eff
ZV VBS Signal				
185779.WhizardPythia8_AU2_CT10_ZVsemileptonic_km_a4_005_a5_005	e3030_a220_a205_r4540_p1575	0.1034	1.0	1.0
185780.WhizardPythia8_AU2_CT10_ZVsemileptonic_km_a4_005_a5_0	e3030_a220_a205_r4540_p1575	0.09943	1.0	1.0
185781.WhizardPythia8_AU2_CT10_ZVsemileptonic_km_a4_005_a5_m005	e3030_a220_a205_r4540_p1575	0.09963	1.0	1.0
185782.WhizardPythia8_AU2_CT10_ZVsemileptonic_km_a4_00_a5_005	e3030_a220_a205_r4540_p1575	0.09814	1.0	1.0
185783.WhizardPythia8_AU2_CT10_ZVsemileptonic_km_a4_00_a5_m005	e3030_a220_a205_r4540_p1575	0.09838	1.0	1.0
185784.WhizardPythia8_AU2_CT10_ZVsemileptonic_km_a4_m005_a5_005	e3030_a220_a205_r4540_p1575	0.09896	1.0	1.0
185785.WhizardPythia8_AU2_CT10_ZVsemileptonic_km_a4_m005_a5_0	e3030_a220_a205_r4540_p1575	0.10055	1.0	1.0
185786.WhizardPythia8_AU2_CT10_ZVsemileptonic_km_a4_m005_a5_m005	e3030_a220_a205_r4540_p1575	0.10564	1.0	1.0
185787.WhizardPythia8_AU2_CT10_ZVsemileptonic_km_a4_03_a5_03	e3030_a220_a205_r4540_p1575	0.19902	1.0	1.0
185788.WhizardPythia8_AU2_CT10_ZVsemileptonic_km_a4_03_a5_0	e3030_a220_a205_r4540_p1575	0.147518	1.	1.
185789.WhizardPythia8_AU2_CT10_ZVsemileptonic_km_a4_03_a5_m03	e3030_a220_a205_r4540_p1575	0.16189	1.0	1.0
185790.WhizardPythia8_AU2_CT10_ZVsemileptonic_km_a4_00_a5_03	e3030_a220_a205_r4540_p1575	0.15279	1.0	1.0
185791.WhizardPythia8_AU2_CT10_ZVsemileptonic_km_a4_00_a5_m03	e3030_a220_a205_r4540_p1575	0.15682	1.0	1.0
185792.WhizardPythia8_AU2_CT10_ZVsemileptonic_km_a4_m03_a5_03	e3030_a220_a205_r4540_p1575	0.16402	1.0	1.0
185793.WhizardPythia8_AU2_CT10_ZVsemileptonic_km_a4_m03_a5_0	e3030_a220_a205_r4540_p1575	0.154	1.0	1.0
185794.WhizardPythia8_AU2_CT10_ZVsemileptonic_km_a4_m03_a5_m03	e3030_a220_a205_r4540_p1575	0.20961	1.0	1.0

In order to model the dependence of the signal on the aQGCs, signal samples were generated at 45 different points in (α_4, α_5) space. The cross-sections of the generated samples are summarized in Table 33 (for WV samples) and Table 34 (for ZV samples). More details about the datasets are given in Tables 28-29.

α_4	α_5	Dataset ID	Cross-section (fb)
0	0	185721	676.1
0	0.1	185722	714.3
0	0.2	185723	772.5
0	-0.1	185724	721.2
0	-0.2	185725	779.8
0.1	0	185726	713.7
0.1	0.1	185727	763.2
0.1	-0.2	185728	734.2
0.1	-0.4	185729	880.8
0.2	-0.3	185730	784.3
0.3	-0.2	185731	781.9
0.3	-0.6	185732	961.0
-0.1	0	185733	720.1
-0.1	0.2	185734	734.7
-0.1	0.4	185735	872.1
-0.1	-0.1	185736	772.4
-0.2	0.3	185737	784.0
-0.3	0.2	185738	798.5
-0.3	0.6	185739	958.1
0.1	-0.1	185740	701.5
-0.1	0.1	185741	705.7
0.05	0.05	185742	709.2
0.05	0	185743	688.5
0.05	-0.05	185744	683.8
0	0.05	185745	691.1
0	-0.05	185746	690.7
-0.05	0.05	185747	683.9
-0.05	0	185748	692.7
-0.05	-0.05	185749	714.5
0.3	0.3	185750	1029.8
0.3	0	185751	840.2
0.3	-0.3	185752	810.2
0	0.3	185753	844.8
0	-0.3	185754	855.4
-0.3	0.3	185755	820.3
-0.3	0	185756	862.5
-0.3	-0.3	185757	1062.0
0.03	0.03	207266	689.6
0.03	0	207267	683.5
0.03	-0.03	207268	680.6
0	0.03	207269	682.1
0	-0.03	207270	680.9
-0.03	0.03	207271	675.9
-0.03	0	207272	686.8
-0.03	-0.03	207273	697.7

α_4	α_5	Dataset ID	Cross-section (fb)
0	0	185758	94.6
0	0.1	185759	106.5
0	0.2	185760	126.7
0	-0.1	185761	109.1
0	-0.2	185762	131.2
0.1	0	185763	107.6
0.1	0.1	185764	118.4
0.1	-0.2	185765	120.4
0.1	-0.4	185766	176.9
0.2	-0.3	185767	148.4
0.3	-0.2	185768	149.0
0.3	-0.6	185769	230.0
-0.1	0	185770	108.8
-0.1	0.2	185771	120.2
-0.1	0.4	185772	173.3
-0.1	-0.1	185773	123.7
-0.2	0.3	185774	148.5
-0.3	0.2	185775	154.6
-0.3	0.6	185776	225.8
0.1	-0.1	185777	110.0
-0.1	0.1	185778	109.9
0.05	0.05	185779	103.4
0.05	0	185780	99.4
0.05	-0.05	185781	99.6
0	0.05	185782	98.1
0	-0.05	185783	98.4
-0.05	0.05	185784	99.0
-0.05	0	185785	100.6
-0.05	-0.05	185786	105.6
0.3	0.3	185787	199.0
0.3	0	185788	147.5
0.3	-0.3	185789	161.9
0	0.3	185790	152.8
0	-0.3	185791	156.8
-0.3	0.3	185792	164.0
-0.3	0	185793	154.0
-0.3	-0.3	185794	209.6
0.03	0.03	207274	98.6
0.03	0	207275	96.7
0.03	-0.03	207276	95.2
0	0.03	207277	96.2
0	-0.03	207278	96.0
-0.03	0.03	207279	97.5
-0.03	0	207280	98.3
-0.03	-0.03	207281	99.8

B SM cross-section significance

The Standard Model (SM) signal cross-section is small compared to the backgrounds like W + jets and $t\bar{t}$. It is also difficult to find variables to cut on that strongly suppress the backgrounds. The best variable for discriminating SM signal from the main backgrounds tends to be $m_{\mathrm{jj,tag}}$. In order to get a feeling for the possible sensitivity to the SM signal, we look at the expected statistical significance, defined as $\frac{s}{\sqrt{b}}$, where s is the number of signal events passing the cuts and b is the number of total backgrounds passing the cuts. In Table 35, the $\frac{s}{\sqrt{b}}$ is shown for different cut values on $m_{\mathrm{jj,tag}}$. The $\frac{s}{\sqrt{b}}$ is always less than 1. Even more troublesome, the S/B is small, at the few percent level.

$m_{\mathrm{jj,tag}}$ cut	Selection	signal	Bkg	$\frac{s}{\sqrt{b}}$
200	Resolved	77.9	16700	0.6
	Merged	3.4	613	0.14
500	Resolved	45	5053	0.63
	Merged	2.1	196	0.15
800	Resolved	25.9	1916	0.59
	Merged	1.1	80	0.13
1000	Resolved	17.1	1049	0.53
	Merged	0.9	44	0.13
1500	Resolved	5.9	237	0.38
	Merged	0.5	10	0.15

Table 35: Sensitivity for SM signal for resolved and merged selections for different $m_{\mathrm{jj,tag}}$ cut values. Apart form $m_{\mathrm{jj,tag}}$, otherwise loose VBS plus $\mathrm{p_T}(W_{\mathrm{lep}}) > 150$ GeV cuts have been applied.

C aTGC studies

In this analysis, only anomalous quartic gauge couplings were considered and it was assumed that there is no anomalous triple gauge coupling contributions. This approach has been pursued by same-sign WW analysis looking at a VBS-like topology [15]. This is motivated by the fact that our final state is insensitive to aTGC parameters. The semileptonic WW+WZ analysis [109] had set limits on the aTGC parameters. The signal significance was investigated for the aTGC samples used in that analysis in the optimized selection region of the current analysis. The sensitivity is defined as the ratio of aQGC/aTGC contribution on top of SM expectation to the uncertainty in the background yield. The aTGC sensitivity is very small compared to that of aQGC as seen in Tab. 36.

Selection	lepton	Bkg	Bkg uncert.	aQGC sig (0,0)	aQGC sig (0,0.1)	|sig(0,0.1)-sig(0,0)|/Bkg uncert.	WW QCD SM	WW aTGC ($g_Z^1 = 0.1$)	|WW SM-WW aTGC)|/Bkg uncert.
resolved	e	86.4	3.1	1.2	9.1	2.5	4.8	5.0	0.06
	μ	78.0	3.1	1.3	8.1	2.2	2.6	2.7	0.03
merged	e	49.2	2.2	0.5	7.9	3.4	0.55	0.56	0.0
	μ	49.6	2.2	0.5	7.1	3.0	1.15	1.17	0.01

Table 36: Sensitivity for aQGC and aTGC samples. For aTGC samples all the parameters except for g_Z^1 has been set to zero.

D Efficiency of resolved and merged V_{had} reconstruction

Traditionally, hadronically-decaying W or Z bosons are reconstructed as two distinct jets, one jet associated with each of the quarks. This becomes difficult if the W/Z boson (V_{had}) has high p_{T}, because the two jets become highly collimated. A rough rule of thumb is that the separation between the decay products of the V_{had} is $\Delta R \sim \frac{2m(V_{\text{had}})}{\text{p}_{\text{T}}(V_{\text{had}})}$. A popular solution to this problem is to reconstruct the V_{had} decay products as a single large-radius jet.

In this section, we compare the efficiency for reconstructing the V_{had} as two jets to the efficiency for reconstructing it as a single large-R jet. We calculate the efficiency for $W \to qq'$ in a Whizard VBS sample with $\alpha_4 = 0.3$, $\alpha_5 = 0$. For this study, we define "efficiency" as the percentage of V_{had} decays for which two small-R jets (or a single large-R jet) are reconstructed that are truth-matched to the V_{had}. The following truth-matching definition is used:

- Resolved case: there are small-R jets within $\Delta R = 0.4$ of the true quarks from the true V_{had}. We require the two matched jets to have an invariant mass of $50 < m_{\text{jj}} < 110$GeV.
- Merged case: there is a large-R jet with $\text{p}_{\text{T}}(J) > 200$GeV and $70 < m(J) < 100$GeV that is within $\Delta R = 0.5$ of the true V_{had}.

The study uses basic pre-selection cuts, and in addition we require the truth-level objects to pass the following cuts:

- zero b-quarks at the matrix-element level, which enhances the VBS-like portion of the signal sample.
- true $\text{p}_{\text{T}}(\ell) > 30$GeV, true $\text{p}_{\text{T}}(\nu) > 30$GeV.
- both quarks from $V \to qq'$ and both of the "tagging" quarks should have $\text{p}_{\text{T}} > 30$GeV and $|\eta| < 4.1$.
- The "tagging" quarks should have $m(qq) > 500$GeV.

The results are shown in Fig. 79. The efficiency of the resolved and merged jet reconstruction is given as a function of the p_{T} of the true V_{had}. The resolved jet reconstruction starts to fall off dramatically for $\text{p}_{\text{T}}(V_{\text{had}}) > 350$GeV, while the merged jet reconstruction remains high.

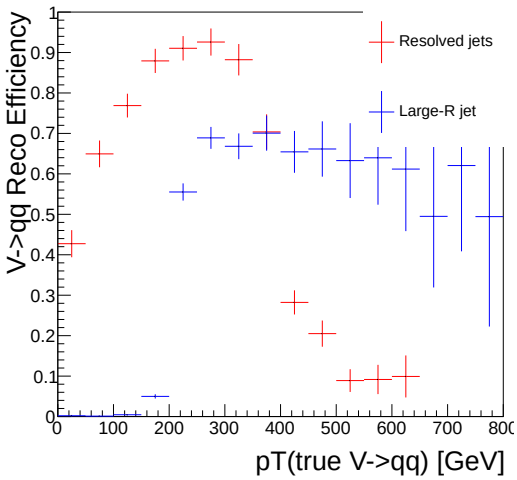

Figure 79: The efficiency for reconstructing a $W \to qq'$ decay as two resolved small-R jets, or as a single large-R jet, as a function of the true $\mathrm{p_T}(W)$. The definition of the reconstruction efficiency is given in the text.

E Kinematics of VBS tagging jets

For VBS-like events the "VBS tagging" jets are expected to have large di-jet invariant mass and should be separated by a large pseudorapidity gap, $\Delta\eta(\mathrm{jj})$. Also, the tagging jets tend to be in the forward direction. This tendency is even more striking for the aQGC samples with a striking gap in the central region as seen in Figure 80. This distinction between signal and background however largely disappears with the application of an $m_{\mathrm{jj,tag}}$ cut of 500 GeV as seen in Figure 81, as the background samples also tend to develop the gap in the central region. As a result, additional cuts on the pseudorapidities of the tagging jets can only provide a small improvement to the analysis.

In this analysis, in contrast, we have decided to cut on the boson centrality, ζ_V which combines the η of the tagging jets and the η of the reconstructed vector-boson candidates. Early studies showed that ζ_V gave slightly better discrimination power than $\Delta\eta(\mathrm{jj})$, and so it was decided to focus on ζ_V for the nominal analysis (cutting on *both* variables would serve little purpose, since the two variables are highly correlated).

The boson centrality is strongly correlated with $\Delta\eta(\mathrm{jj})$, and in fact, the

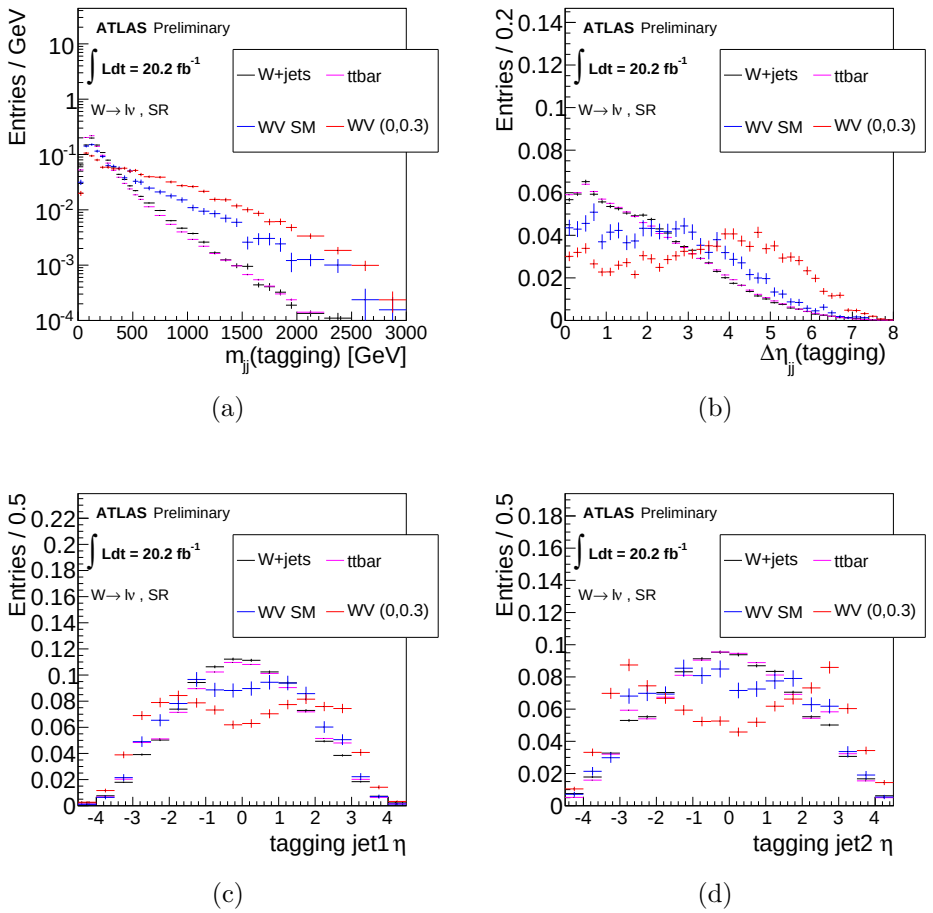

(a) (b) (c) (d)

Figure 80: Distributions for resolved jet selection with no cut on $m_{\mathrm{jj,tag}}$. Otherwise loose VBS cuts are in place (a) Tag jet di-jet mass, (b) tag jet $\Delta\eta$, (c) Tag-jet1 $|\eta|$, (d) Tag-jet2 $|\eta|$.

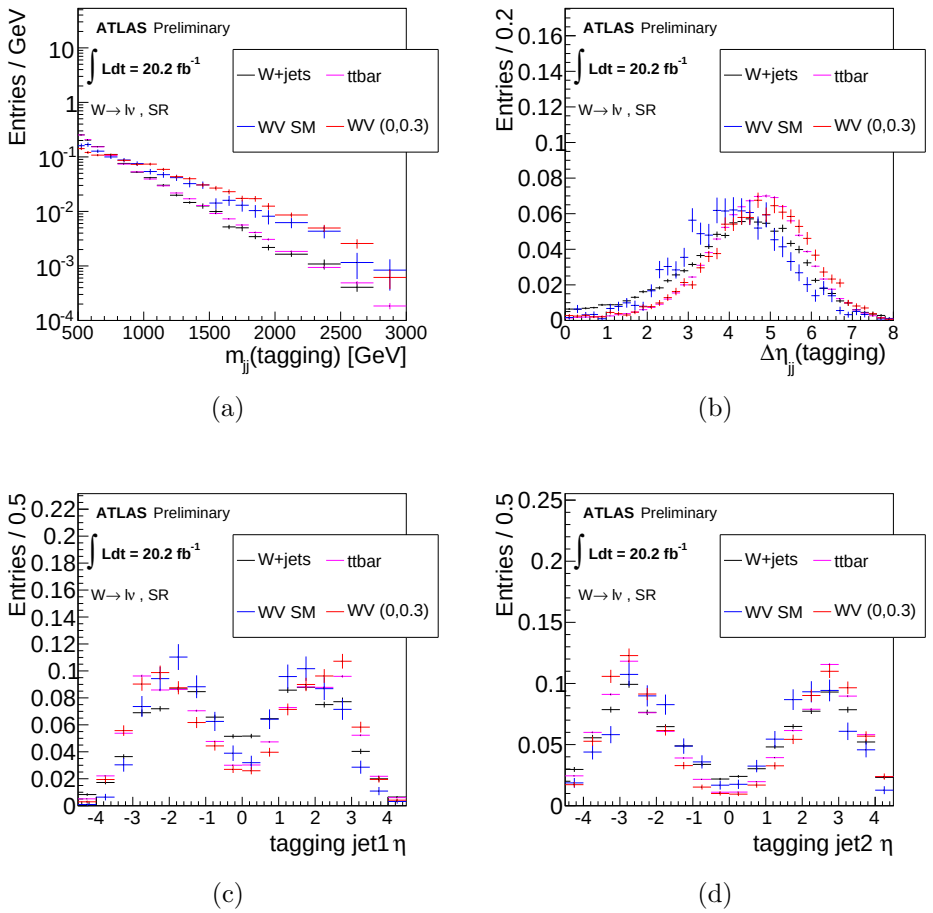

Figure 81: Distributions for resolved jet selection with $m_{\mathrm{jj,tag}}$ >500. Loose VBS cuts are in place. (a) Tag jet di-jet mass, (b) tag jet $\Delta\eta$, (c) Tag-jet1 $|\eta|$, (d) Tag-jet2 $|\eta|$.

following mathematical relation between the two variables exists:

$$\Delta\eta(\mathrm{jj}) \geq 2\ \zeta_V\ . \tag{65}$$

This relation can be seen from the 2D ($\Delta\eta(\mathrm{jj})$ versus ζ_V) plots shown in Fig. 82. Therefore, a cut of $\zeta_V > X_0$ implies necessarily a cut of $\Delta\eta(\mathrm{jj}) > 2X_0$. So, even though this analysis does not *directly* cut on $\Delta\eta(\mathrm{jj})$, there is an *implicit* cut on $\Delta\eta(\mathrm{jj})$. This is illustrated in Fig. 83, which shows the $\Delta\eta$ between the tagging jets, after application of the ζ_V cut.

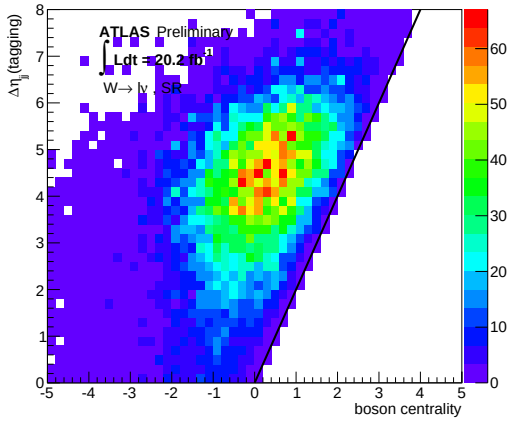

Figure 82: A 2D plot of $\Delta\eta(\mathrm{jj})$ versus ζ_V for W + jets events in the resolved SR. Loose VBS cuts are applied. The black line shows $\Delta\eta(\mathrm{jj}) = 2\ \zeta_V$.

As a cross-check of our optimized analysis cuts (which include cuts on ζ_V), we re-did the cut optimization procedure described in Sec. 9.2, using a background systematic uncertainty of 20%, except including $\Delta\eta(\mathrm{jj})$ in the cut optimization instead of ζ_V. Using this setup, we found slightly (11%) worse limits for the resolved selection and slightly (2%) better limits for the merged selection, as compared to the limits found using cuts on ζ_V.

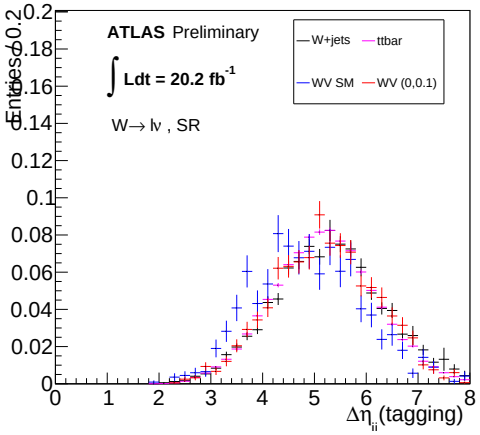

Figure 83: the $\Delta\eta$ between the tagging jets, after application of the ζ_V cut with otherwise loose VBS cuts.

F n-1 cut distributions

In subsections 7.3 and 7.2 data-MC comparisons were shown for different important distribution with loose VBS cuts in place. In this section variables that were used to define the optimized selection for aQGC studies are considered. Distributions are shown in Fig. 84- 86 after removing the cut on the variable itself but otherwise optimized selection has been applied.

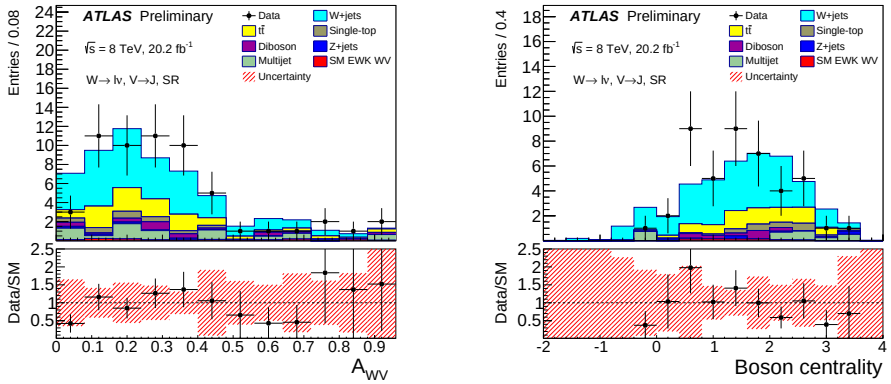

(a)

(b)

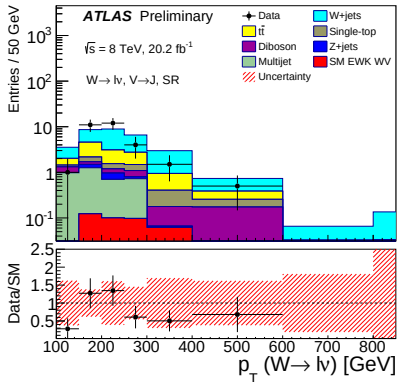

(c)

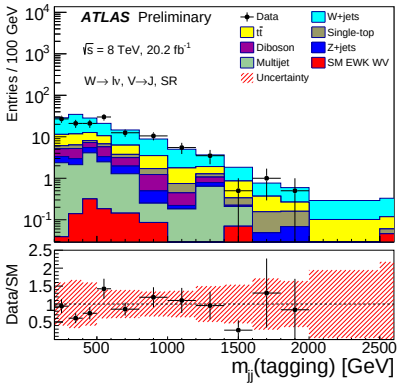

(d)

Figure 84: Various distributions in the merged (V→ J) signal region for optimized selection except the cut on the variable itself has been removed. (a) Diboson p_T balance, A_{WV}, (b) boson centrality, (c) $p_T(W_{lep})$ and (d) $m_{jj,tag}$.

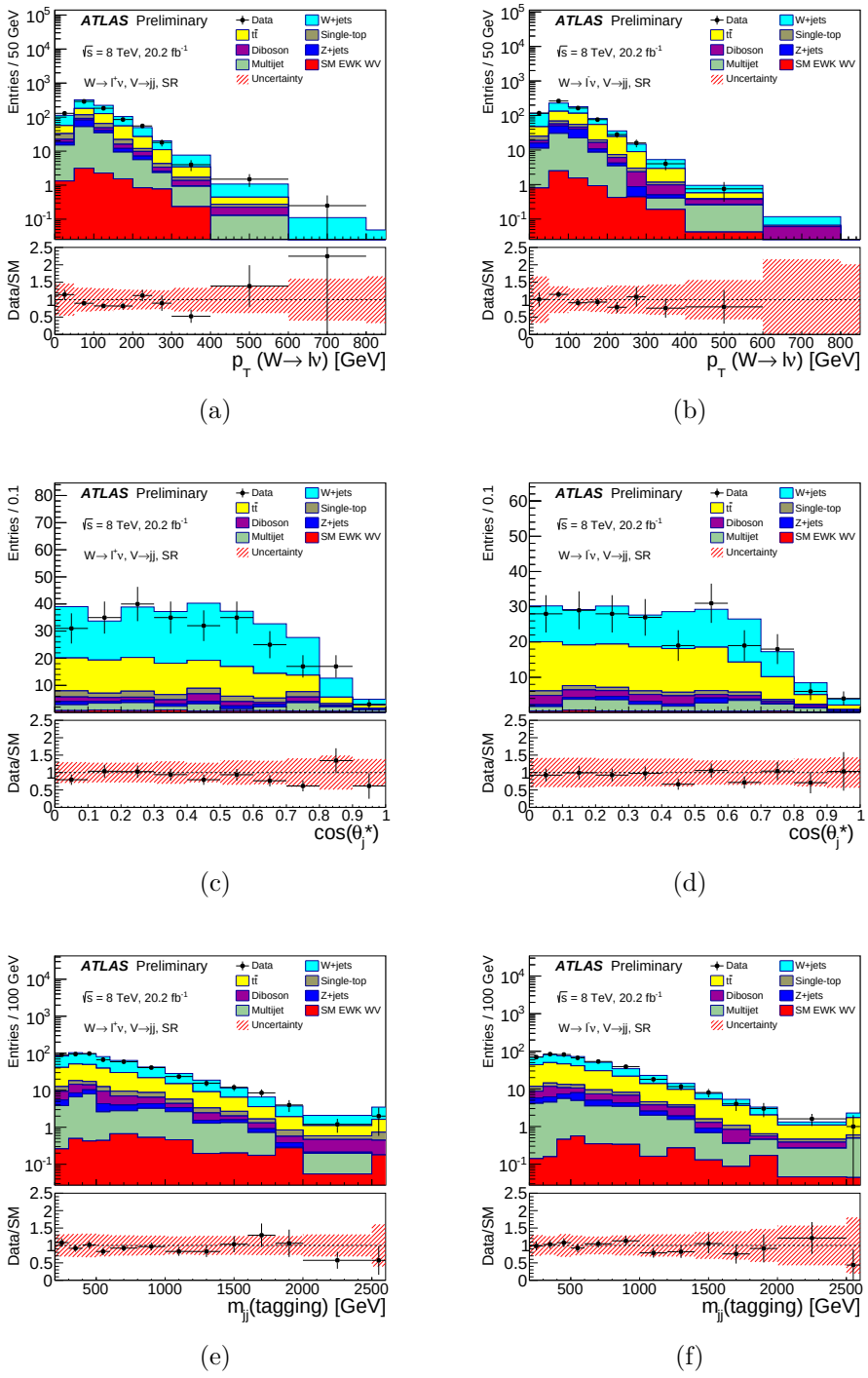

Figure 85: Various distributions in resolved (V→ jj) signal region for optimized selection except the cut on the variable itself has been removed. The left plots are for anti-lepton channel and right are for lepton channel. (a) and (b) show $p_T(W_{lep})$, (c) and (d) show $\cos\left(\theta^*_j\right)$, and (e) and (f) show $m_{jj,tag}$.

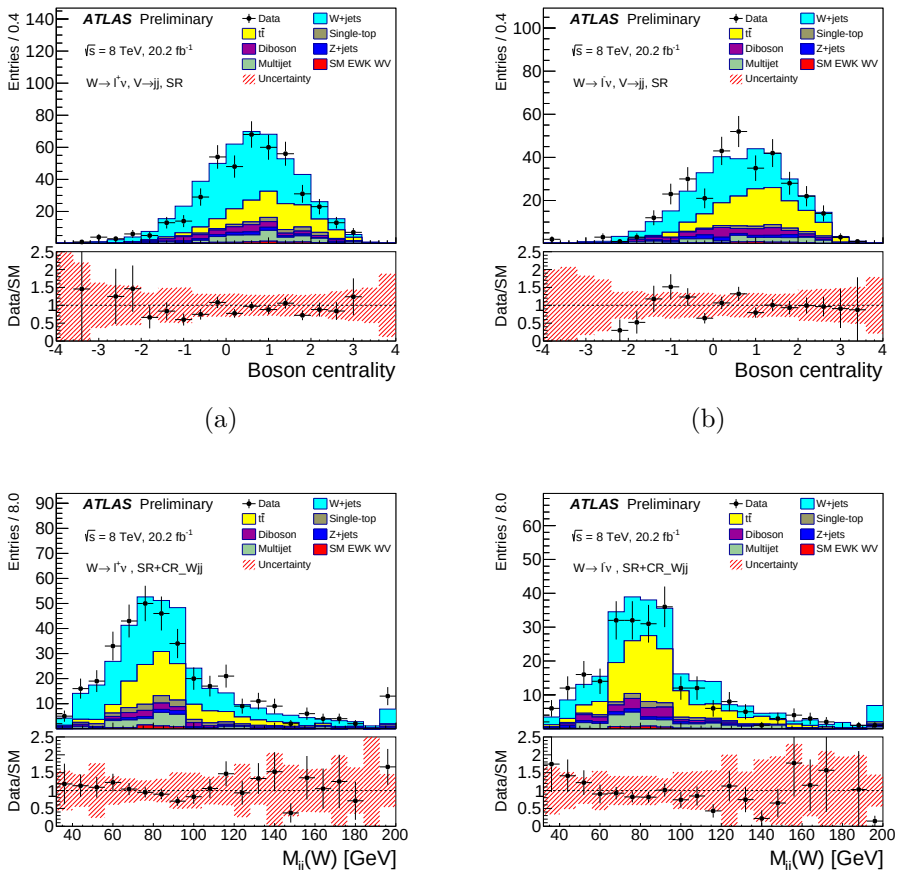

Figure 86: Various distributions in resolved jet selection with optimized cuts except the cut on the variable itself has been removed. The left plots are for anti-lepton channel and right are for lepton channel. (a) and (b) show boson centrality in signal region. (c) and (d) show m(V_{had}) where signal and W + jets control regions have been merged.

G Powheg $t\bar{t}$ reweighting code

The following piece of code is used to introduce the $t\bar{t}$ reweighting factors.

```
Float_t ttbarPt_NOMINAL[4] = { 0.0409119, -0.0121258, -0.188448,
    -0.316183 };
Float_t ttbarPtUpBins[4]= { 40.e3, 170.e3, 340.e3, 1000.e3 };
float GetTTbarPtWeight_Powheg(float pT) {
  int index=3;
  for (unsigned int i=0; i<4; i++) {
    if (pT < ttbarPtUpBins[i]) {
      index=i;
      break;
    }
  }
  return 1 + ttbarPt_NOMINAL[index];
}
```

And the following piece of code is used to introduce the sequential top p_T reweighting factors.

```
Float_t sequential_topPt_NOMINAL[7] = { 0.0139729, 0.0128711,
    0.00951743, 0.00422323, -0.0352631, -0.0873852, -0.120025};
Float_t sequential_topPtUpBins[7]= { 50.e3, 100.e3, 150.e3,
    200.e3, 250.e3, 350.e3, 800.e3 };
float GetSequentialTopPtWeight_Powheg(float pT) {
  int index=6;
  for (unsigned int i=0; i<7; i++) {
    if (pT < sequential_topPtUpBins[i]) {
      index=i;
      break;
    }
  }
  return 1 + sequential_topPt_NOMINAL[index];
}
```

H $m_{\mathrm{T}}(WV)$ shape for different aQGC values

Figure 87 shows the shape of the $m_{\mathrm{T}}(WV)$ of signal events for a variety of different α_4 and α_5 values.

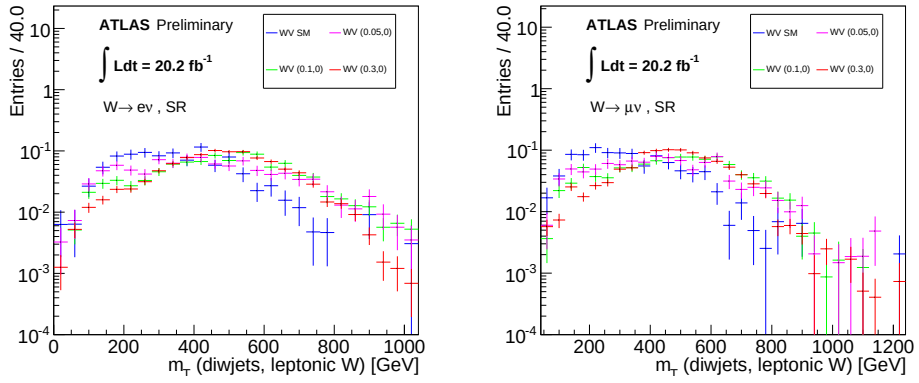

(a)

(b)

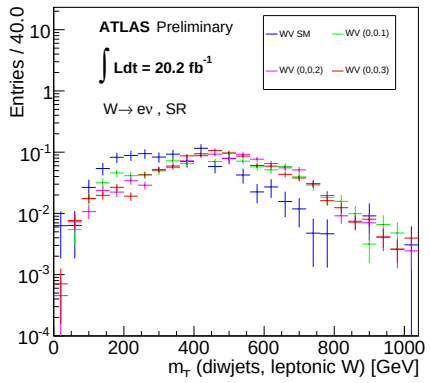

(c)

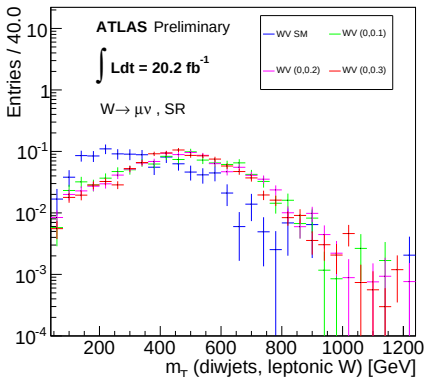

(d)

Figure 87: Probability distributions for the $m_{\mathrm{T}}(WV)$ variable for resolved jet selection. All distributions are normalized to 1. Loose plus $\mathrm{p_T}(W_{\mathrm{lep}})>$ 150 GeV cuts are in place. (a) e channel, α_5 fixed at zero, (b) μ channel, α_5 fixed at zero, (c) e channel, α_4 fixed at zero, (d) μ channel, α_4 fixed at zero.

I Correlations of Systematic Uncertainties

In this appendix, we show the correlations between the systematic uncertainties in different $m_{\mathrm{T}}(WV)$ bins. In Section 9.3, the C-matrix was defined (Equations 60-62), which describes the fractional uncertainty on the number of background and signal events in each $m_{\mathrm{T}}(WV)$ bin, and the correlations between these uncertainties.

The C-matrix itself is difficult to visualize, because most of the elements are close to zero. Instead, we plot the correlation matrix ρ, given by:

$$\rho_{i,j} = \frac{C_{i,j}}{\sqrt{C_{i,i}}\sqrt{C_{j,j}}}\,, \tag{66}$$

whose elements are always in the range $[-1, 1]$. A reminder that this matrix is $2m \times 2m$, where m is the total number of bins in the analysis. The factor of 2 accounts for the fact that the systematics on the background and signal are considered separately. In this analysis, $m_{\mathrm{T}}(WV)$ is fit in three channels, labeled 0, 1, and 2 in Sec. 9.4, which contain 4, 5, and 5 bins, respectively. So, in total there are $m = 14$ bins. This means ρ is a 28×28 matrix. In Figs. 88-89, we plot the ρ matrix for the total sum of systematic uncertainties, and also for particular groups of systematic uncertainties:

- The W/Z + jets modeling (Sherpa parameter variation) uncertainties.
- The signal modeling (scales, PDF, parton shower) uncertainties.
- The $t\bar{t}$ modeling (generator, parton shower, ISR/FSR) uncertainties.
- The uncertainty on the W + jets scale-factor (derived from the $Wjet$ control region).
- The JES and JER uncertainties (for both small-R and large-R jets).
- The multi-jet background uncertainty (100% uncertainty).

In Figs. 90-91, we plot the fractional size of different groups of systematic uncertainties, as a function of bin number, separately for signal and for background.

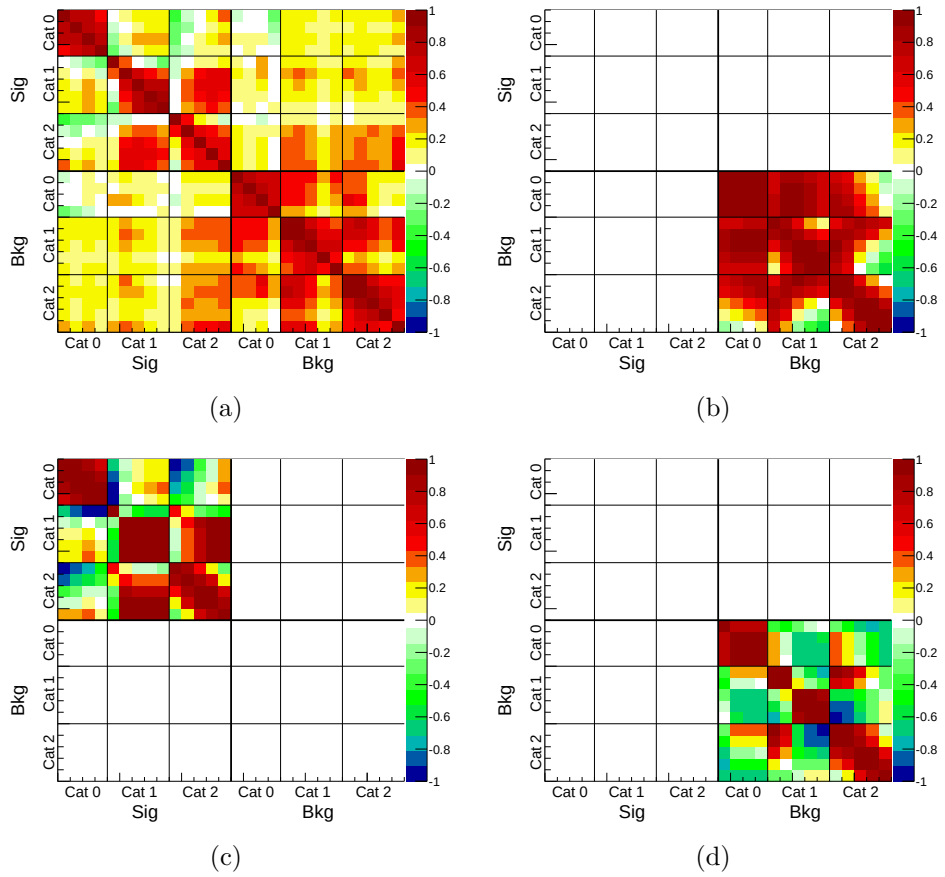

Figure 88: Correlation matrices ρ for (a) the full systematics, (b) W + jets modeling, (c) signal modeling, (d) $t\bar{t}$ modeling. Each bin refers to an entry in the 28×28 ρ matrix. The labels in the plots indicate how the matrix is organized into signal and background. The bins are to be read from left-to-right and from top-to-bottom. The bins are organized into "Cat 0,1,2" referring to the fit channels 0, 1, and 2 defined in Section 9.4.

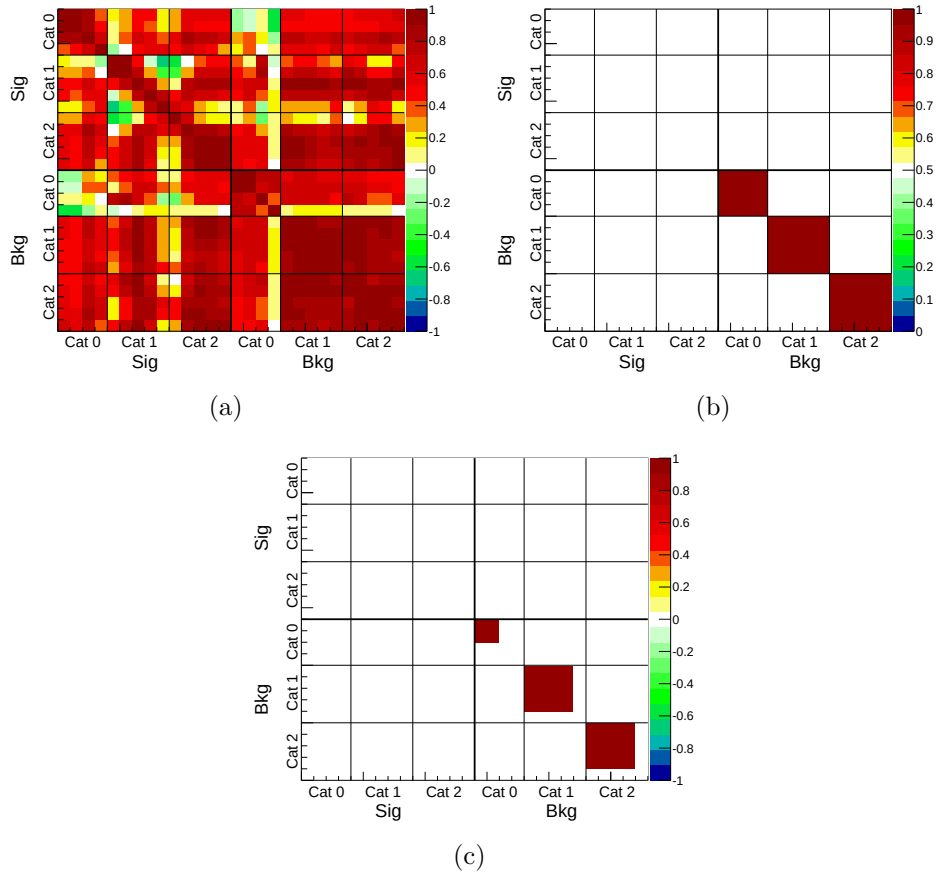

Figure 89: Correlation matrices ρ for (a) JES and JER uncertainties, (b) the W + jets scale-factor, and (c) the multi-jet uncertainty.

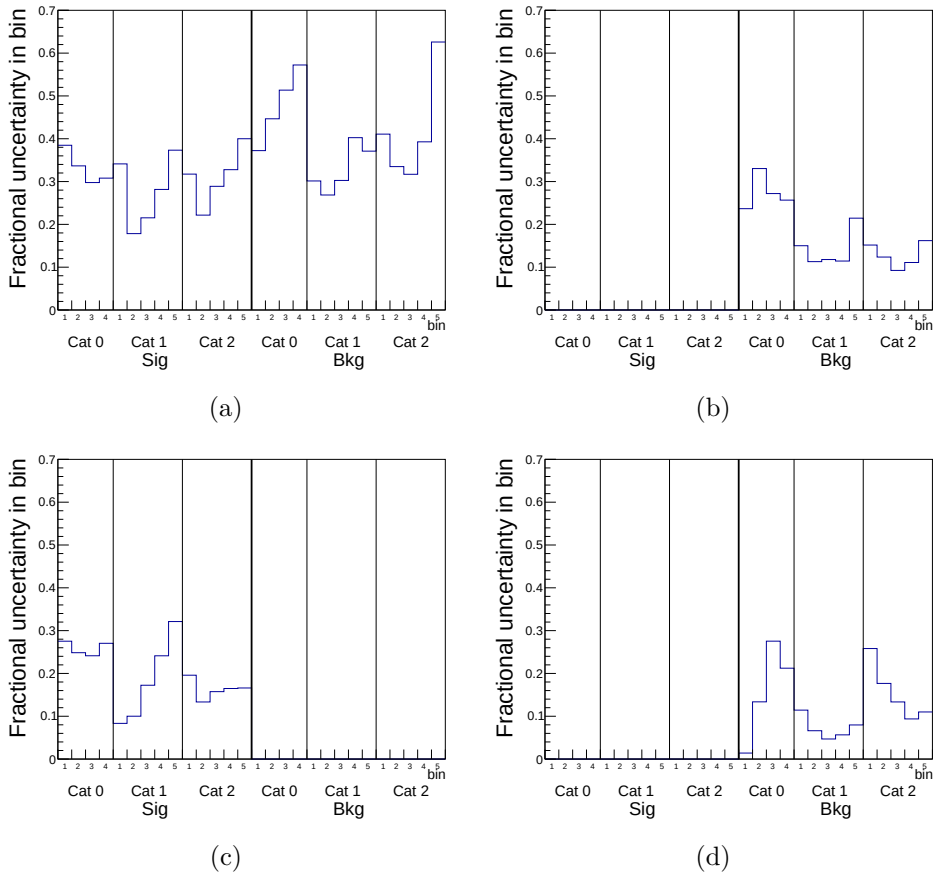

Figure 90: The fractional systematic uncertainty on the signal and background, as a function of bin number. The different plots show the systematic uncertainties for (a) the full systematics, (b) W + jets modeling, (c) signal modeling, and (d) $t\bar{t}$ modeling. The bins are organized into "Cat 0,1,2" referring to the fit channels 0, 1, and 2 defined in Section 9.4.

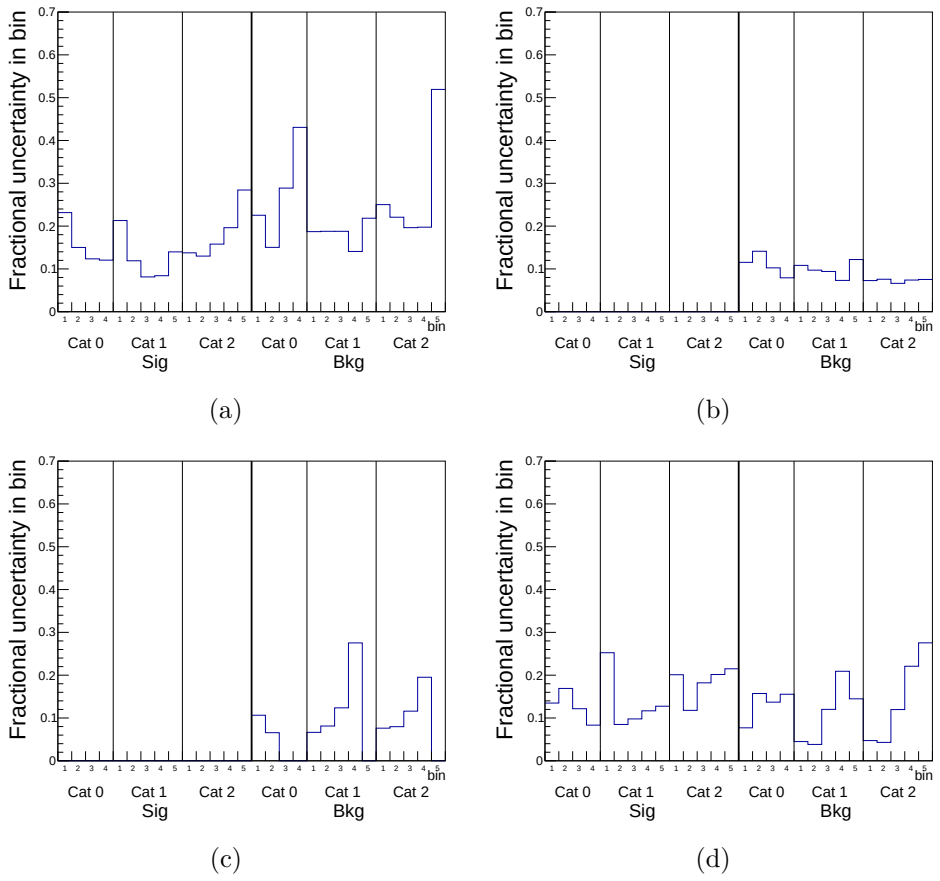

Figure 91: The fractional systematic uncertainty on the signal and background, as a function of bin number. The different plots show the systematic uncertainties for (a) JES and JER uncertainties, (b) the W+jets scale-factor, (c) the multi-jet uncertainty, and (d) the statistical uncertainty on the signal and background predictions. The bins are organized into "Cat 0,1,2" referring to the fit channels 0, 1, and 2 defined in Section 9.4.